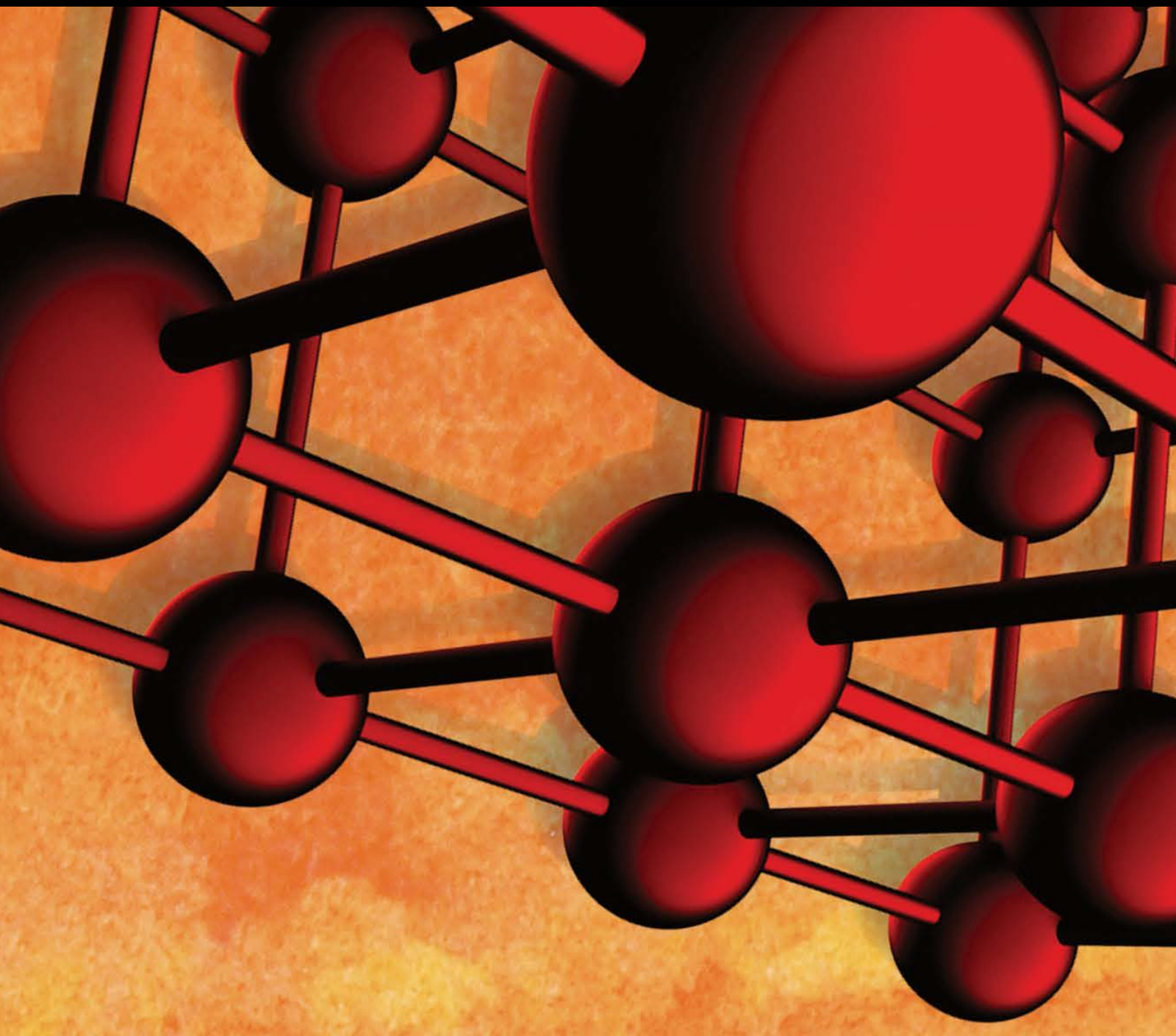


Advances in Materials Science and Engineering

Earth Materials and Environmental Applications 2016

Guest Editors: Zhaohui Li, Guocheng Lv, and Jianxi Zhu





**Earth Materials and Environmental
Applications 2016**

Advances in Materials Science and Engineering

**Earth Materials and Environmental
Applications 2016**

Guest Editors: Zhaohui Li, Guocheng Lv, and Jianxi Zhu



Copyright © 2017 Hindawi Publishing Corporation. All rights reserved.

This is a special issue published in “Advances in Materials Science and Engineering.” All articles are open access articles distributed under the Creative Commons Attribution License, which permits unrestricted use, distribution, and reproduction in any medium, provided the original work is properly cited.

Editorial Board

M. S.A. Abdel-Mottaleb, Egypt
Michael Aizenshtein, Israel
J. Aktaa, Germany
K. G. Anthymidis, Greece
Amit Bandyopadhyay, USA
Arun Bansil, USA
Massimiliano Barletta, Italy
Mikhael Bechelany, France
Jozef Bednarcik, Germany
Avi Bendavid, Australia
Jamal Berakdar, Germany
Giovanni Berselli, Italy
Patrice Berthod, France
Didier Blanchard, Denmark
Susmita Bose, USA
H.-G. Brokmeier, Germany
Steve Bull, UK
Peter Chang, Canada
Daolun Chen, Canada
Gianluca Cicala, Italy
Gabriel Cuello, France
Narendra B. Dahotre, USA
João P. Davim, Portugal
Angela De Bonis, Italy
Francesco Delogu, Italy
Seshu B. Desu, USA
Guru P. Dinda, USA
Yong Ding, USA
N. Tzankova Dintcheva, Italy
Kaveh Edalati, Japan
Philip Eisenlohr, USA
Paolo Ferro, Italy
Massimo Fresta, Italy
Eric Freysz, France
Sergi Gallego, Spain
Santiago Garcia-Granda, Spain
Filippo Giannazzo, Italy

Daniel Guay, Canada
Hiroki Habazaki, Japan
Joke Hadermann, Belgium
Satoshi Horikoshi, Japan
David Houivet, France
Rui Huang, USA
Michele Iafisco, Italy
Katsuyuki Kida, Japan
Jae-Ho Kim, Republic of Korea
Akihiko Kimura, Japan
Takayuki Kitamura, Japan
Hongchao Kou, China
Prashant Kumta, USA
Luciano Lamberti, Italy
Heinrich Lang, Germany
Pavel Lejcek, Czech Republic
Cristina Leonelli, Italy
Ying Li, USA
Jun Liu, China
Meilin Liu, Georgia
Wei Liu, France
Yunqi Liu, China
Fernando Lusquiños, Spain
Peter Majewski, Australia
Philippe Miele, France
Hossein Moayedi, Iran
Paul Munroe, Australia
Rufino M. Navarro, Spain
Luigi Nicolais, Italy
Hiroschi Noguchi, Japan
Chérif Nouar, France
José L. Ocaña, Spain
Tsutomu Ohzuku, Japan
Olanrewaju Ojo, Canada
Gianfranco Palumbo, Italy
A. Maria Paradowska, Australia
Matthew Peel, UK

Gianluca Percoco, Italy
Giorgio Pia, Italy
Jean-Francois Pierson, France
Simon C. Potter, Canada
Manijeh Razeghi, USA
Yuri Ribakov, Israel
Anna Richelli, Italy
Antonio Riveiro, Spain
Pascal Roussel, France
Timo Sajavaara, Finland
Antti Salminen, Finland
F.H. Samuel, Canada
Carlo Santulli, Italy
Franz-Josef Schmitt, Germany
Fridon Shubitidze, USA
Maria A. Signore, Italy
Donato Sorgente, Italy
Charles C. Sorrell, Australia
Costas M. Soukoulis, USA
Sam-Shajing Sun, USA
Kohji Tashiro, Japan
Achim Trampert, Germany
Filip Tuomisto, Finland
Krystyn Van Vliet, USA
Qiang Wang, China
Rong Wang, USA
Rui Wang, China
Lu Wei, China
J. M. K. Wiezorek, USA
Wei Wu, USA
Hemmige S. Yathirajan, India
Wenbin Yi, China
Belal F. Yousif, Australia
Jinghuai Zhang, China
Li Zhang, China
Ming-Xing Zhang, Australia
Wei Zhou, China

Contents

Earth Materials and Environmental Applications 2016

Zhaohui Li, Guocheng Lv, and Jianxi Zhu
Volume 2017, Article ID 6251354, 2 pages

Properties of Crushed Red-Bed Soft Rock Mixtures Used in Subgrade

Huayan Yao, Shanpo Jia, Wenning Gan, Zhenhua Zhang, and Kunlin Lu
Volume 2016, Article ID 9624974, 8 pages

Solidification/Stabilization of Fly Ash from a Municipal Solid Waste Incineration Facility Using Portland Cement

Qiang Tang, Yang Liu, Fan Gu, and Ting Zhou
Volume 2016, Article ID 7101243, 10 pages

Stress Analysis of CFG Pile Composite Foundation in Consolidating Saturated Mine Tailings Dam

Jinxing Lai, Houquan Liu, Junling Qiu, Haobo Fan,
Qian Zhang, Zhinan Hu, and Junbao Wang
Volume 2016, Article ID 3948754, 12 pages

An Experimental Study on the Water-Induced Strength Reduction in Zigong Argillaceous Siltstone with Different Degree of Weathering

Yu-chuan Yang, Jia-wen Zhou, Fu-gang Xu, and Hui-ge Xing
Volume 2016, Article ID 4956986, 12 pages

Comparison of Effects of Using Geosynthetics and Lime Stabilization to Increase Bearing Capacity of Unpaved Road Subgrade

Erhan Burak Pancar and Muhammet Vefa Akpınar
Volume 2016, Article ID 7129356, 8 pages

Sulfur Fixation by Chemically Modified Red Mud Samples Containing Inorganic Additives: A Parametric Study

Yang Liu, Yang Li, Feng-shan Zhou, Ying-mo Hu, and Yi-he Zhang
Volume 2016, Article ID 9817969, 9 pages

Application of Coal Ash to Postmine Land for Prevention of Soil Erosion in Coal Mine in Indonesia: Utilization of Fly Ash and Bottom Ash

Shinji Matsumoto, Shunta Ogata, Hideki Shimada, Takashi Sasaoka, Ginting J. Kusuma, and Rudy S. Gautama
Volume 2016, Article ID 8386598, 8 pages

Weathering Influence on Properties of Siltstones from Istria, Croatia

Martina Vivoda Prodan and Željko Arbanas
Volume 2016, Article ID 3073202, 15 pages

The Effects of High Alkaline Fly Ash on Strength Behaviour of a Cohesive Soil

A. Binal
Volume 2016, Article ID 3048716, 11 pages

Influence of Alkali Treatment on the Surface Area of Aluminium Dross

N. S. Ahmad Zauzi, M. Z. H. Zakaria, R. Bains, M. R. Rahman, N. Mohamed Sutan, and S. Hamdan
Volume 2016, Article ID 6306304, 4 pages

Graphite Intended for Green Engineering Developed by Noncontaminant Reverse Abrasion

Roberto Baca Arroyo

Volume 2016, Article ID 7016457, 6 pages

Soil Erosion Estimation Using Remote Sensing Techniques in Wadi Yalamlam Basin, Saudi Arabia

Jarbou A. Bahrawi, Mohamed Elhag, Amal Y. Aldhebiani, Hanaa K. Galal, Ahmad K. Hegazy, and Ebtisam Alghailani

Volume 2016, Article ID 9585962, 8 pages

Effect of Kinetin on Physiological and Biochemical Properties of Maize Seedlings under Arsenic Stress

Haijuan Wang, Biyu Dai, Xiaogang Shu, Hongbin Wang, and Ping Ning

Volume 2015, Article ID 714646, 7 pages

Editorial

Earth Materials and Environmental Applications 2016

Zhaohui Li,^{1,2} Guocheng Lv,¹ and Jianxi Zhu³

¹Beijing Key Laboratory of Materials Utilization of Nonmetallic Minerals and Solid Wastes, National Laboratory of Mineral Materials, School of Materials Science and Technology, China University of Geosciences, Beijing, 29 Xueyuan Road, Beijing 100083, China

²Geosciences Department, University of Wisconsin-Parkside, Kenosha, WI 53144, USA

³Guangzhou Institute of Geochemistry, CAS 511 Kehua Street, Tianhe, Guangzhou 510640, China

Correspondence should be addressed to Zhaohui Li; li@uwp.edu

Received 5 January 2017; Accepted 5 January 2017; Published 26 January 2017

Copyright © 2017 Zhaohui Li et al. This is an open access article distributed under the Creative Commons Attribution License, which permits unrestricted use, distribution, and reproduction in any medium, provided the original work is properly cited.

Since the publication of the 1st special issue on Earth Materials and Environmental Applications in *Adv. Mater. Sci. Eng.* in 2015, positive feedbacks and needs to expand the scope of research lead to the call for papers and eventually publication of this special issue. In this special issue, we have a collection of 13 papers selected among 29 submitted manuscripts. This special issue focuses more on engineering applications, including from soil erosion prevention and evaluation of fly ash use to mine tailing control.

In the area of controlling soil erosion in arid land such as Saudi Arabia, remote sensing techniques in combination with Geographic Information Systems (GIS) were applied to reclassify soil erosion risk maps, confirming the role of Revised Universal Soil Loss Equation for calculating and predicting soil erosion. Lime stabilization of clayey road base soil with high water content and its improvement with geosynthetics reinforcement and comparisons of these two different improvement methods were made. And the method of improvement with lime and then reinforcement with geosynthetics yields better results on these types of soils. Siltstones from flysch rock masses, Istria Peninsula, Croatia, are highly susceptible to weathering, which causes rapid changes in the geotechnical properties and durability. Laboratory testing showed that the standardized slake durability index was not sufficient enough to classify the durability of weak rock masses such as siltstones. Therefore, the durability of siltstone samples of different weathering grades was quantified from the fragment size distribution after each of five slaking cycles.

Proper dispose of fly ash with high lime content is an issue. Mixing the fly ash collected from Yeniköy thermal power plants in Turkey with local soil Ankara clay could change the geotechnical properties of the clay, resulting in an increase in cohesion value and decrease of free swelling index. Similarly, application of coal ash from Indonesia to postmine land could reduce the soil erosion significantly with an enhanced water retention capacity. As fly ash, used as a binder for Portland cement, often contains heavy metals, the leachability of the heavy metals decreased with increasing curing time.

Engineering tests were conducted to evaluate the use of cement fly ash gravel (CFG) composite foundation in consolidating saturated mine tailings dam. The distribution of earth pressure and pile stress is relatively homogeneous and stable over depth and load, while the development of CFG composite foundation bearing capacity is insufficient, in which the developed bearing capacity of CFG piles is less than 50% of its characteristic value. The deformation modulus and thickness of cushion exert significant influence on pile-soil stress ratio and integral bearing capacity of CFG composite foundation.

Compacting tests, the resilient modulus tests, the California bearing ratio tests, and permeability tests were carried out on crushed red-bed soft rock mixtures to evaluate their use as materials for highway construction. Studies on mechanical properties of red soil in Sichuan showed that the water-softening effect is more obvious with higher degree of weathering and the changes of the microstructure and

material composition seem to be the key parameters for the reduction of its mechanical strength.

Aluminum dross is an industrial waste from aluminum refining industry and classified as toxic substances. However, the disposal of dross as a waste is a burden to aluminum manufacturer industries due to its negative effects to the ecosystem, surface, and ground water. A study on the utilization of aluminum dross by alkali treatment showed that it had the potential to be converted into other useful material such as catalyst and absorbent. In addition, sulfur retention ability of Bayer red mud from an alumina plant was improved by fusel salt and waste mother liquor of sodium ferrocyanide as the main sulfur fixation agent and the calcium based natural mineral materials as servicing additives.

The effects of different levels of kinetin (KT) application on the growth, biomass, contents of chlorophyll (Chl a, Chl b, and carotenoid), arsenic uptake, and activities of antioxidant enzymes in maize seedlings under arsenic (As) stress were investigated by a hydroponic experiment. The results showed that KT supplementation increased the biomass in terms of root length, root number, fresh weight, and seedling length, and KT treatments also improved the contents of Chl a, As uptake, and Chl a : b ratio compared to cases with As treatment alone.

Finally, graphite intended for green engineering was synthesized by noncontaminant reverse abrasion, which consists of graphite layers assembled with thickness controlled on SiC sandpaper as insulating substrate. Phase formation of the graphite layers was validated by X-ray diffraction studies and its finished profile by Atomic Force Microscopy.

Acknowledgments

We would like to thank all the authors who have submitted their papers to this special issue and also to all the reviewers for their invaluable contributions to the reviewing process.

*Zhaohui Li
Guocheng Lv
Jianxi Zhu*

Research Article

Properties of Crushed Red-Bed Soft Rock Mixtures Used in Subgrade

Huayan Yao,^{1,2} Shanpo Jia,³ Wenning Gan,^{1,2} Zhenhua Zhang,^{1,2} and Kunlin Lu^{1,2}

¹School of Civil and Hydraulic Engineering, Hefei University of Technology, Hefei, Anhui 230009, China

²Anhui Key Laboratory of Civil Engineering and Materials, Hefei, Anhui 230009, China

³School of Urban Construction, Yangtze University, Jingzhou 434023, China

Correspondence should be addressed to Shanpo Jia; jiashanporsm@163.com

Received 4 January 2016; Accepted 6 December 2016

Academic Editor: Carlo Santulli

Copyright © 2016 Huayan Yao et al. This is an open access article distributed under the Creative Commons Attribution License, which permits unrestricted use, distribution, and reproduction in any medium, provided the original work is properly cited.

Slaking red-bed soft rocks are widely distributed in the south of Anhui Province, China, and several highways will go through this area. It is important to evaluate their physical and mechanical characteristics for the purpose of using this kind of soft rocks as materials for road construction. In this paper, the compacting tests, the resilient modulus tests, the California bearing ratio (CBR) tests, and permeability tests have been carried out on crushed red-bed soft rock mixtures. The test results showed that, for a given degree of compaction, the resilient modulus decreases linearly with the increase of moisture content. For a given moisture content, the resilient modulus and CBR values increase linearly with the increase of compaction degree, while the soaking swelling, water absorption capacity, and permeability coefficient decrease linearly. In other words, the strength and water stability are enhanced with the increase of the degree of compaction. The results demonstrate that the crushed red-bed soft rock mixtures can be directly used as materials for the highway construction by taking corresponding measures.

1. Introduction

Soft rock is one of the rock types encountered frequently in geotechnical engineering, which is less than the uniaxial compressive strength of 25 MPa, covering a series of sedimentary rocks, such as sandstone, mudstone, argillaceous sandstone, sandy mudstone, and siltstone. Generally, soft rocks are prone to slaking, swelling, collapse, breaking, softening, and argillization in the presence of humidity [1–6]. Such phenomenon can be quite crucial for various geotechnical hazards in roads, slopes, tunnels, and other engineering projects [7–10]. For example, when these soft rocks are used to fill subgrade, it is difficult to ensure the quality of the construction, often leading to excessive settlement, failure of embankments, and slope collapse.

Therefore, soft rocks are considered to be of very poor quality used for subgrade filling materials. In general, the soft rocks should be replaced with soil with better mechanical properties for subgrade filling, but this process will cause additional project costs and possibly extend the construction

duration. Moreover, a large number of such rocks removed as excavated earth have an adverse effect on surrounding environment. Therefore, if soft rocks can be used for subgrade filling, not only can it save a great deal of investment and earthwork, but also substantial economic and environmental benefits can be achieved.

Some studies have focused on the physical and mechanical properties of the crushed soft rocks used as filling materials. The authors of [11] have conducted a staged compression-immersion-direct shear test on the compacted samples of crushed mudstone aggregates, and the compressive and shear behaviors were discussed with attention to cementation effects. The authors of [12] have studied water-induced granular decomposition and its effects on geotechnical properties of crushed soft rocks. The authors of [13] have carried out cyclic loading tests on sandstone and limestone shale aggregates used in unbound forest roads.

Some researchers have paid attention to the techniques to make use of soft rocks as subgrade filling. The authors of [14]

carried out research on the physical and mechanical properties of soft rocks after slaking, and research results show that the indexes of those slaked materials with compacting factor 95% can reach the requirement of embankment. And the subgrade construction technology with the core of “preslaking/raking pressure/rolling pressure,” construction quality control methods and detection measures were adopted in order to ensure the feasibility of using red sandstone as a subgrade filling.

In China, residential land development and transportation networks have been extended to mountainous areas due to rapid economic and population growth. Accordingly, road constructions have been carried out in many soft rock regions. In these regions, many sedimentary soft rocks, such as sandstone or mudstone, are distributed widely. Huangshan city, which exists in the southern mountains of Anhui Province, China, is one of the typical areas covered with many slaking soft rocks. The rocks in this area are red, dark red, or brown resulting from being rich in iron oxides. Some scholars have called them “red-bed soft rocks” [15, 16]. Some construction measures, such as preslaking or adding lime, have been adopted to make full use of the red-bed soft rock as subgrade fillings [14, 17]. But those measures potentially extend the construction duration and increase the costs of the road projects. If the crushed red-bed soft rock in these areas can be directly used as subgrade fillings, the construction duration and investments of the road projects can be reduced.

Accordingly, the purpose of this study is to assess the applicability of crushed red-bed soft rock mixtures to road construction. In particular, the resilient modulus tests, the California bearing ratio (CBR) tests, and permeability tests were carried out on crushed soft rock mixtures with variable moisture contents or compaction degrees.

2. Experimental Materials and Experimental Schemes

2.1. Experimental Material. Naturally weathered red-bed soft rocks were obtained from a typical area of the quarry for the Jixi-Huangshan highway, in southern Anhui Province, China, as shown in Figure 1. These soft rocks include argillaceous feldspar quartz fine sandstone, calcareous argillaceous siltstone, argillaceous siltstone, iron-stain argillaceous calcareous siltstone, iron-stain argillaceous calcareous feldspar lithic sandstone, and mudstone.

In natural conditions, uniaxial compressive strength of the red-bed soft rocks generally ranges from 1.24 to 12.32 MPa, and the strength reduces sharply after they are soaked. Large blocks of rock samples were crushed resulting in coarse-grained soils in laboratory.

Due to the differences in their geological locations, the red-bed soft rock’s chemical composition and physical characteristics are different even with the same weathering degree, which directly affect the mechanical properties. The structures of the samples mainly consist of silty-fine structure, silty structure, cryptocrystalline structure, argillaceous structure, pebbly silty-calcareous-argillaceous structure, and argillaceous structure (see Figure 2). The cemented form between the grains is dominated by a basal type cementation.



FIGURE 1: Representative red-bed sandstone sample.

The cementation matters are mainly argillaceous and calcareous, with low strength. The main mineral compositions of the soft rock samples used in this study are summarized in Table 1.

2.2. Experimental Scheme. In the light of the construction duration, it is accepted in the construction process that soft rocks are crushed directly by machine instead of preslaking. For simulating the mechanical crushing process, the soft rock samples were artificially broken with a maximum diameter less than 20 mm (see Figure 3). Then, a series of mechanical tests were carried out according to Test Methods of Soil for Highway Engineering [18].

Firstly, the modified Proctor test compaction was used for the compaction in order to obtain the maximum dry density and optimum moisture content. Then, the resilient modulus test, California Bearing Ratio (CBR) test, and permeability test were carried out with different moisture contents or compaction degrees.

3. Experimental Result

3.1. Compaction Properties. The Proctor compaction test can determine the optimal moisture content (OWC) at which a given soil type becomes the most dense and achieves its maximum dry density. After the obtained rock samples underwent artificial mechanical crushing into small pieces, the aggregates were compacted in the steel mold with an inner diameter of 152 mm and height of 120 mm. The compaction was performed in the way that the aggregates were placed into the mold in three layers; in each layer compaction was conducted using a 4.5 kg rammer, and the compaction energies were 2677.2 kJ/m³.

The relation curve between dry density ρ_d and moisture content w is shown in Figure 4. The maximum dry density is 2.107 g/cm³, and the optimum moisture content, OWC, is 8.8%. Assessment of aggregates compaction is measured by the degree of compaction (K), which is defined as the ratio of the current dry density and maximum dry density.

The coarse aggregates of the red-bed soft rocks will become smaller or transform into fine-grained soil during the rolling process. In this study, in order to investigate the moisture content and compaction effect on grains, particle

TABLE 1: Main mineral composition.

Rock sample number	Main compositions (%)								
	Quartz	Feldspar	Debris	Dolomite	Opaque mineral	Micrite gravel	Calcite	Iron-stain clay mineral + sericite	Calcareous
1#	35	20	5	<1	<1	—	3	30	7
2#	30	15	8	—	<1	3	10	33	—
3#	3	—	—	—	—	—	—	97	—
4#	40	15	5	<1	<1	—	8	31	—
5#	40	10	5	1	1	—	—	30	13
6#	38	12	5	1	<1	—	—	30	13
7#	50	10	—	5	—	—	20	15	—
8#	55	10	1	1	3	—	15	15	—
9#	4	—	—	—	—	—	40	56	—
10#	50	10	—	1	3	1	20	15	—
11#	38	8	19	3	—	—	20	10	—
12#	40	12	23	<1	—	—	15	10	—

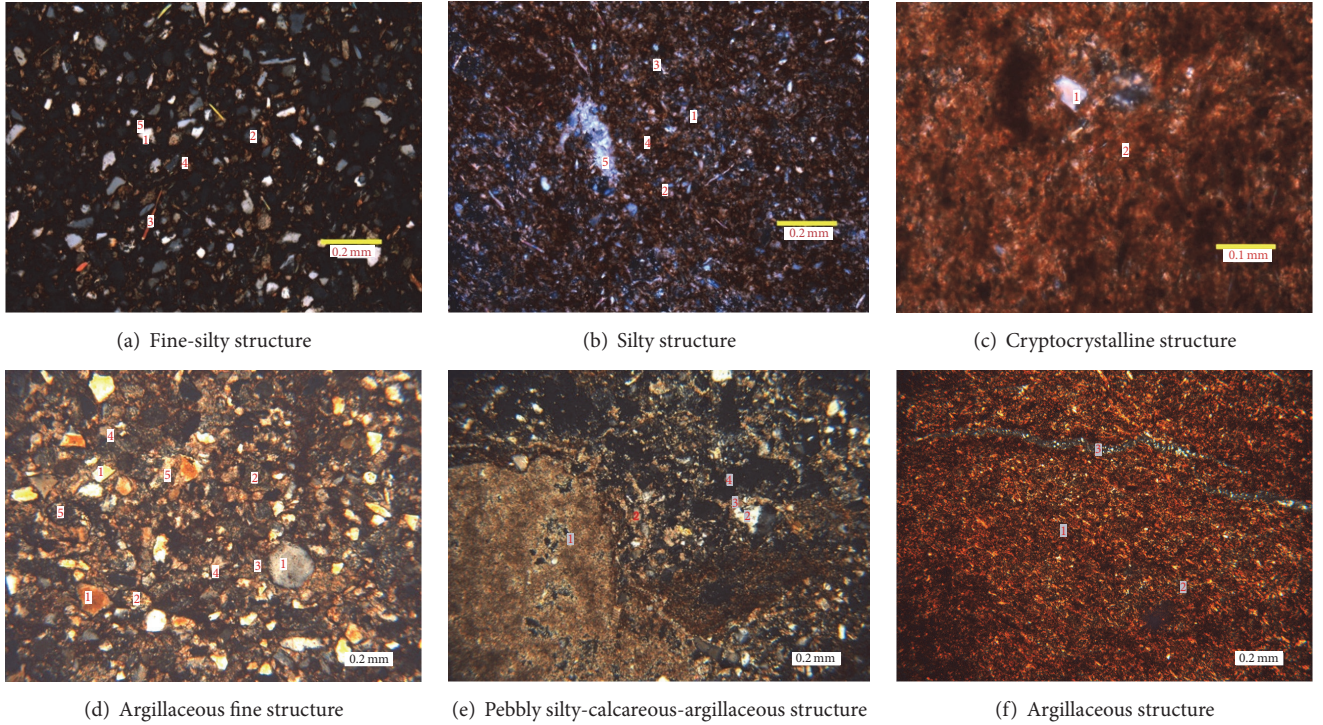


FIGURE 2: Microscopic structure diagram of representative red-bed soft rock.

size distribution tests were performed for the dry crushed soft rock mixtures and three compacted specimens with the moisture content of 5%, 8%, and 9% respectively, as shown in Figure 5. And the uniformity coefficient C_u and gradation coefficient C_c of each curve were calculated, as shown in Table 2.

The uniformity coefficient C_u is defined as

$$C_u = \frac{D_{60}}{D_{10}}. \quad (1)$$

The gradation coefficient C_c is defined as

$$C_c = \frac{(D_{30})^2}{D_{60} \cdot D_{10}}, \quad (2)$$

where D_{60} , D_{30} , and D_{10} are diameter through which 60%, 30%, and 10% of the total soil mass are passing, respectively.

It can be seen from Table 2 that the coarse-grained soil has the uniformity coefficient C_u greater than 5, and the gradation coefficient C_c is in the range 1–3 after compaction,



FIGURE 3: The crushed red-bed soft rock mixtures.

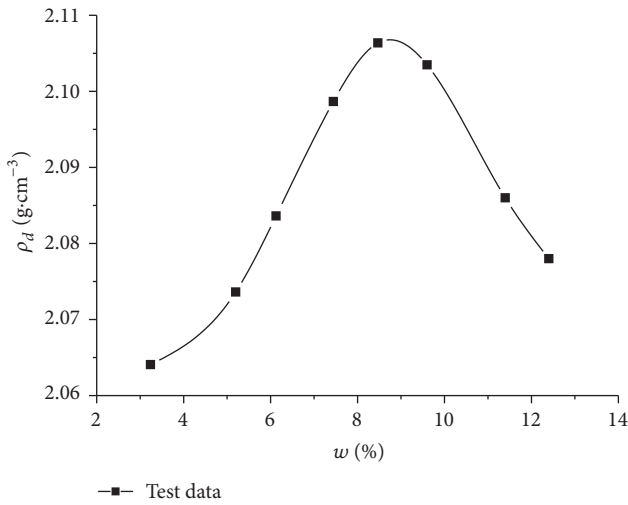


FIGURE 4: Relation between dry density ρ_d and moisture content w .

TABLE 2: Uniformity coefficient C_u and gradation coefficient C_c .

Test group	D_{60}	D_{30}	D_{10}	C_u	C_c
Before compaction	9.4	5.3	1.2	7.83	2.49
$w = 9\%$	4.8	1.8	0.23	20.87	2.93
$w = 8\%$	4.1	1.3	0.16	25.63	2.58
$w = 5\%$	3	0.55	0.09	33.33	1.12

which shows the aggregates have a good size distribution. It is worthwhile to note that the uniformity coefficients of compacted crushed rock mixtures have become greater than that without compaction. In other words, the compaction and other construction technologies executed on broken soft rock mixtures can improve the particle grading, which leads to good engineering properties, such as smaller porosity, higher density, and large bearing capacity.

3.2. *Test on Resilient Modulus.* Resilient modulus E_r is one of the mechanical parameters used to characterize subgrade soil strength, which is a vital parameter for pavement design. The most commonly applied resilient modulus models are the so-called universal models that relate the modulus to the deviatoric stress, confining pressure, or a combination

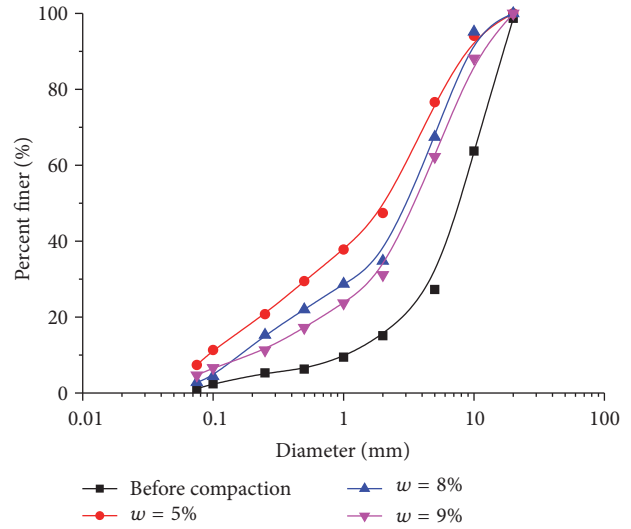


FIGURE 5: Particle size grading of crushed red-bed soft rock mixtures before and after compaction.

of them [19]. In this paper, the resilient modulus model in China’s specification [18] is adopted and the modulus of the soil can be obtained by the Plate Load tests. The relationships between the resilient modulus and moisture content, as well as the compaction degree, are discussed.

Moisture is one of the main factors affecting the subgrade resilient modulus. The specimens with a compaction degree of 96% and moisture contents of 4.8%, 7.0%, 8.3%, 7.0%, and 12.4% were prepared for the tests on resilient modulus. The results are shown in Figure 6.

Figure 6 reflects the influences of moisture content (w) on the resilient modulus (E_r). It can be seen that the resilient modulus has close relation with moisture content, decreasing with the increase of moisture content, and the general decline trend is approximately linear; around the optimum moisture content $w = 8.8\%$, the resilient modulus is not less than 90 MPa, which meets the requirement of national standard [20], in which the resilient modulus larger than 40 MPa is demanded. However, the resilient modulus is 13.69 MPa in the case of moisture content of 12.4%. Therefore, the moisture content should be controlled close to the optimum moisture content. Based on the test results, the moisture content in the construction period is suggested to be no more than 11%, so as to fulfill the strength performance of the subgrade filling required.

With the same moisture content of 9.0%, the specimens with a compaction degree of 99.7%, 97.1%, and 95.0% were prepared for the tests on the resilient modulus. Figure 7 illustrates the relation between the resilient modulus (E_r) and the degree of compaction (K). It can be seen that the resilient modulus gradually increases with the increase of the compaction degree.

3.3. *Test on CBR.* CBR is used to assess the strength indexes of subgrade and pavement materials. In the CBR test, load and penetration reading of plunger were observed at a rate of 1.25 mm/minute; the load for 2.5 mm and 5 mm were

TABLE 3: The results of CBR tests under different degrees of compaction.

Sample number	Number of blows	Dry density $\rho_d/(g\cdot cm^{-3})$	Compaction degree $K/\%$	CBR %	Soaking swelling $Q/\%$	Water absorbing X/g
(1)	98	2.104	99.9	61.24	0.088	28
(2)		2.102	99.7	57.14	0.074	25
(4)	50	2.060	97.7	49.71	0.108	49
(5)		2.053	97.5	48.76	0.102	48
(7)	30	2.010	95.4	35.14	0.164	108
(8)		2.006	95.2	34.00	0.155	99

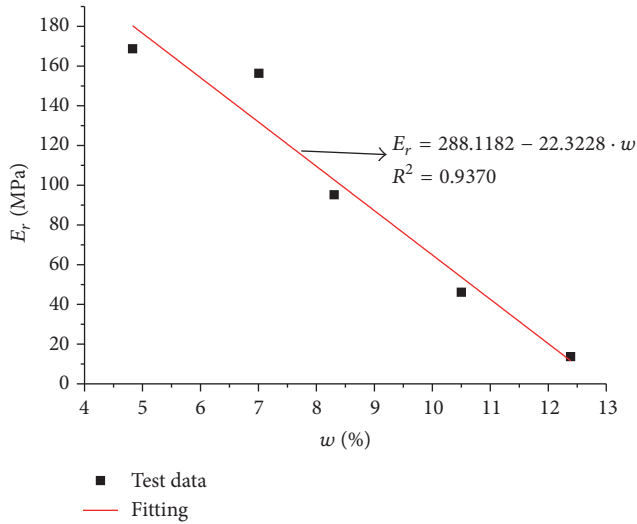


FIGURE 6: Relation between resilient modulus E_r and moisture content w .

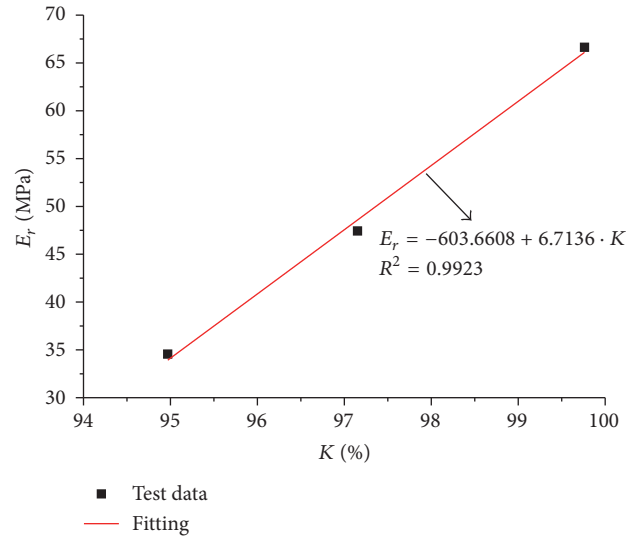


FIGURE 7: Relation between resilient modulus E_r and compaction degree K .

observed. CBR value is the comparison between applied piston loads on a soil sample and the standard loads.

Typically, CBR value is calculated by the load for 2.5 mm as follows:

$$CBR = \frac{P}{7000} \times 100, \quad (3)$$

where p is applied stress, kPa.

At the same time, CBR value is calculated by the load for 5 mm as follows:

$$CBR = \frac{P}{10500} \times 100. \quad (4)$$

If the value from (4) is greater than that from (3), the test should be carried out once more. If the result is still like that, CBR value calculated by the load for 5 mm would be adopted.

The specimens with different degrees of compaction were prepared with each layer having blows of 30, 50, and 98 with the same moisture content 9.0%, to explore the influences of compaction degree K on CBR, the soaking swelling Q , and water adsorption X , which were evaluated by the Chinese Industrial Standard [18]. The test results are shown in Table 3 and Figures 8–10.

Figure 8 shows the relationship between CBR and compaction degree (K). It can be seen that (1) all the compacted

specimens with different dry densities have higher CBR values; for example, the CBR value of the specimen with 95% compaction degree can reach up to 30% or more, which shows that the compacted specimens have a strong ability to resist damage; (2) with the increase of the compaction degree, the CBR value presents a linear increasing trend. According to the national standard [20] of China, the CBR of the fillings for highway should not be lower than 8% when the 96% degree of compaction is proposed. The results suggest that the compacted specimens fully meet the requirements of national standard [20].

Figures 9 and 10 give the relationship of the soaking swelling (Q) and the water adsorption (X) with the degree of compaction (K), respectively. It can be seen that the compaction degree has basically the same influence on the soaking swelling and the water adsorption. The higher the compaction degree is, the smaller the soaking swelling and water adsorption become, which show that the water stability is gradually enhanced with the increase of compaction degree. This is mainly due to higher compaction degree leading to a decrease of porosity among the soil particles. In other words, the water storage space of specimens is reduced, characterized by declining of the water absorbing capacity.

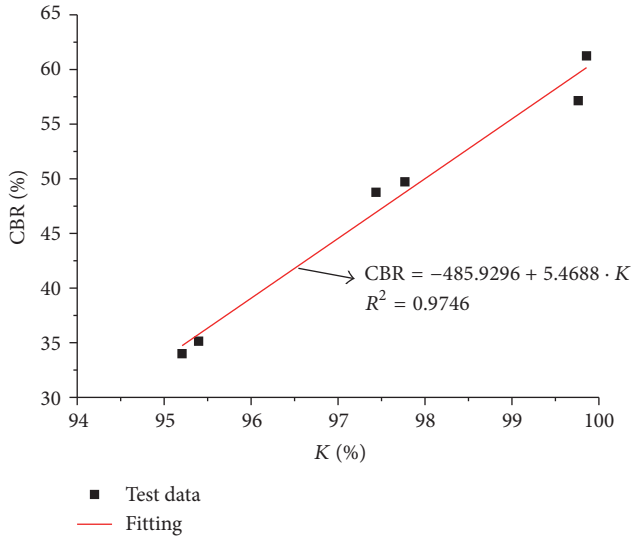


FIGURE 8: Relation between CBR and compaction degree K .

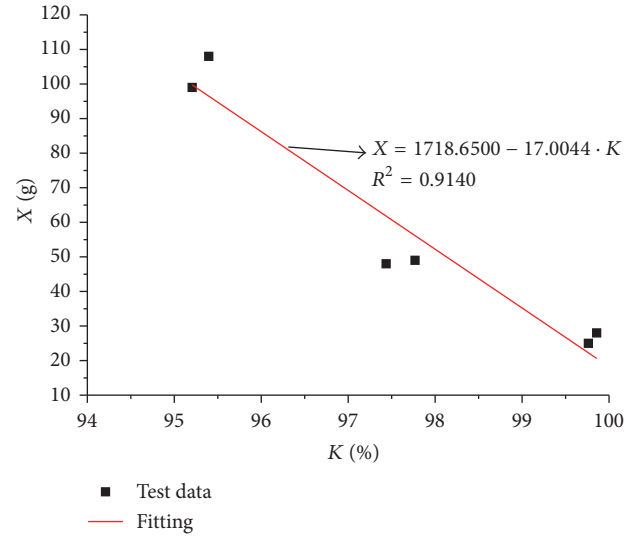


FIGURE 10: Relation between water absorbing X and compaction degree K .

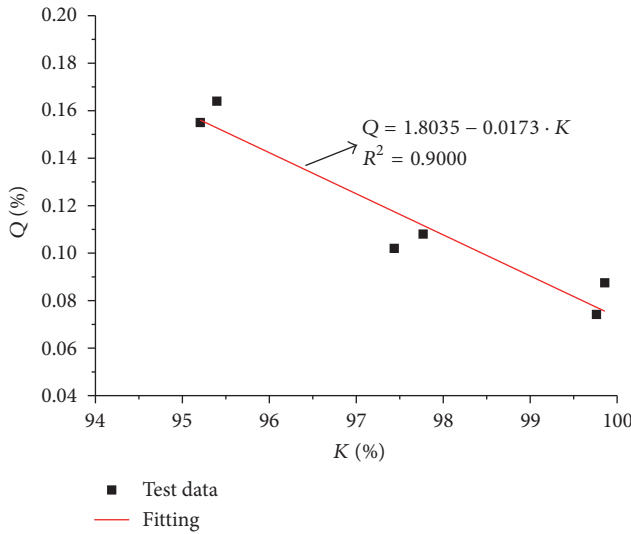


FIGURE 9: Relation between soaking swelling Q and compaction degree K .

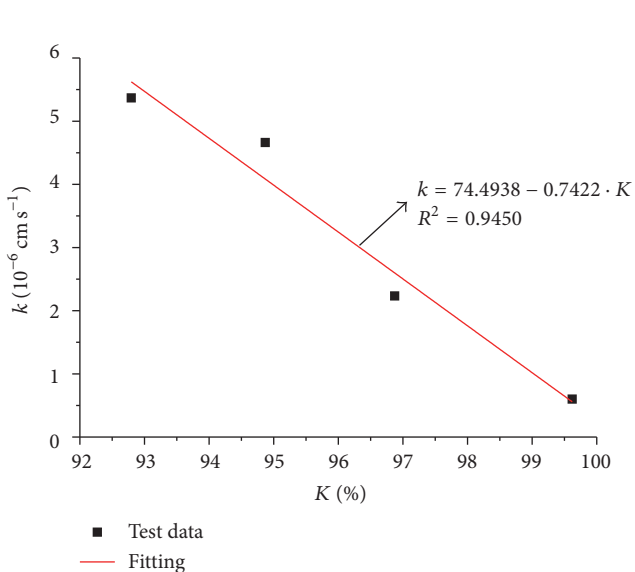


FIGURE 11: Relation between permeability coefficient k and compaction degree K .

From the long-term stability of the roadbed, the compaction of red-bed sandstone fillings should be controlled as well as possible. In this condition, the adverse effect of water on the strength of the roadbed can be reduced significantly.

3.4. Test on Permeability. In order to study the relationship between the permeability coefficient (k) and the compaction degree (K), a variable water head method was adopted for the seepage experiment of the saturated specimens with varied compaction degrees ($K = 99.6\%$, 96.9% , 94.9% , and 96.9%). The results are shown in Figure 11.

Figure 11 reflects the influences of compaction degree on permeability. It can be seen that (1) the permeability coefficients of the filling decrease linearly with the increase of the compaction degree; with the increasing of the compaction degree, the porosity becomes smaller, and the pore water

pressure increases; so, the flowing of free water among soil particles slows down or even stops due to the capillary effect, which leads to the decreasing of the permeability coefficient; (2) with the compaction degree of 92% to 100%, the permeability coefficients k are less than $1.0 \times 10^{-6} \text{ cm/s}$, showing a good antipermeability performance and thus proving that the compaction degree has an effective controlling effect on the porosity and permeability coefficients.

4. Discussion

The special properties of red-bed soft rocks, such as slaking or softening in water, should be full considered in materials for road construction. Based on the above physical and

mechanical properties of crushed soft rock matrix, the red-bed soft rocks have good engineering properties for subgrade after being crushed and compacted. The red-bed soft rocks mixtures become fine-grained soil during the rolling process. The compaction and other construction technologies can improve the particle grading, which leads to good engineering properties.

Compaction degree is a key factor to ensure that the mechanical properties of the crushed rock mixtures meet the requirements. So, the compaction degree should be selected as the main quality control index for the red-bed roadbed construction in practice.

When the compaction degree of the crushed red-bed rock mixtures is above 90%, the permeability is very small, similar to that of clay. The moisture has great influences on the mechanical properties, and some waterproof measures should be taken on the subgrade slope in the actual highway construction project.

5. Conclusions

- (1) The red-bed soft rocks in the southern mountains of Anhui Province, China, have complex and diversified lithology and structure. The clay mineral contents are higher with a mud-calcium cementation, minimal strength, and weak weathering resistance.
- (2) The moisture has great influences on the resilient modulus of the red-bed crushed soft rock mixtures. The resilient modulus decreases with the increase of moisture content. Therefore, the moisture content of the mixtures should be controlled close to the OWC when rolling to ensure the subgrade resilient modulus meeting the requirements of road construction.
- (3) The compaction degree has close relationship with the filling's strength and water stability. With the increase of the compaction degree, the resilient modulus and CBR of the compacted specimens show linear increasing trends, while the soaking swelling, water absorbing capacity, and permeability coefficient present linear decreasing trends.
- (4) The laboratory experimental results show that, under certain key control indices such as moisture content or degree compaction, the engineering properties of the crushed red-bed soft rock mixtures can meet the demands of highway construction.

Competing Interests

The authors declare that they have no competing interests.

Acknowledgments

The work reported in this paper has received financial support from the National Natural Science Foundation of China (no. 51579063). This support is gratefully acknowledged.

References

- [1] J. A. Franklin and R. Chandra, "The slake-durability test," *International Journal of Rock Mechanics and Mining Sciences and*, vol. 9, no. 3, pp. 325–328, 1972.
- [2] G. Dhakal, T. Yoneda, M. Kato, and K. Kaneko, "Slake durability and mineralogical properties of some pyroclastic and sedimentary rocks," *Engineering Geology*, vol. 65, no. 1, pp. 31–45, 2002.
- [3] M. A. Kanji, "Critical issues in soft rocks," *Journal of Rock Mechanics and Geotechnical Engineering*, vol. 6, no. 3, pp. 186–195, 2014.
- [4] D. Wu, H. Liu, and G. Wang, "Laboratory experimental study of slaking characteristics of soft rock," *Chinese Journal of Rock Mechanics and Engineering*, vol. 29, supplement 2, pp. 4173–4179, 2010 (Chinese).
- [5] M. He, "Latest progress of soft rock mechanics and engineering in China," *Journal of Rock Mechanics and Geotechnical Engineering*, vol. 6, no. 3, pp. 165–179, 2014.
- [6] P. Azadan and K. Ahangari, "Evaluation of the new dynamic needle penetrometer in estimating uniaxial compressive strength of weak rocks," *Arabian Journal of Geosciences*, vol. 7, no. 8, pp. 3205–3216, 2014.
- [7] X. Li and Q. Jin, "Compacting deformation engineering characteristics of weathered soft rock mixture in subgrade," *Journal of China University of Geosciences*, vol. 19, no. 3, pp. 298–306, 2008.
- [8] P. Mišćević and G. Vlastelica, "Impact of weathering on slope stability in soft rock mass," *Journal of Rock Mechanics and Geotechnical Engineering*, vol. 6, no. 3, pp. 240–250, 2014.
- [9] H. Zhou, C. Zhang, Z. Li, D. Hu, and J. Hou, "Analysis of mechanical behavior of soft rocks and stability control in deep tunnels," *Journal of Rock Mechanics and Geotechnical Engineering*, vol. 6, no. 3, pp. 219–226, 2014.
- [10] H. Cetin, M. Laman, and A. Ertunç, "Settlement and slaking problems in the world's fourth largest rock-fill dam, the Ataturk Dam in Turkey," *Engineering Geology*, vol. 56, no. 3-4, pp. 225–242, 2000.
- [11] N. Yoshida and K. Hosokawa, "Compression and shear behavior of mudstone aggregates," *Journal of Geotechnical and Environmental Engineering*, vol. 130, no. 5, pp. 519–525, 2004.
- [12] M. Aziz, I. Towhata, S. Yamada, M. U. Qureshi, and K. Kawano, "Water-induced granular decomposition and its effects on geotechnical properties of crushed soft rocks," *Natural Hazards and Earth System Science*, vol. 10, no. 6, pp. 1229–1238, 2010.
- [13] M. Rodgers, G. Hayes, and M. G. Healy, "Cyclic loading tests on sandstone and limestone shale aggregates used in unbound forest roads," *Construction and Building Materials*, vol. 23, no. 6, pp. 2421–2427, 2009.
- [14] M. H. Zhao, J. Y. Deng, and W. G. Cao, "Study of the disintegration character of red sandstone and the construction techniques of red sandstone embankment," *China Journal of Highway and Transport*, vol. 16, no. 7, pp. 1–5, 2003 (Chinese).
- [15] H. Peng, "Perspectives on the red beds landforms in humid area of Southern China and some related problems," *Geographical Research*, vol. 30, no. 10, pp. 1739–1752, 2011 (Chinese).
- [16] Y.-C. Guo, Q. Xie, and J.-Q. Wen, "Red beds distribution and engineering geological problem in China," *Hydrogeology and Engineering Geology*, vol. 6, pp. 67–71, 2007 (Chinese).
- [17] X.-S. Mao, L.-G. Zhou, B. Ma, X.-Z. Zheng, and W.-Y. Zhao, "Research on improvement technology of filling subgrade with highly-weathered phyllite," *China Journal of Highway and Transport*, vol. 25, no. 2, pp. 20–26, 2012 (Chinese).

- [18] The Ministry of Communications of the People's Republic of China, *Test Methods of Soil for Highway Engineering (JTG E40-2007)*, The Ministry of Communications of the People's Republic of China, Beijing, China, 2007 (Chinese).
- [19] A. J. Puppala, *Estimating Stiffness of Subgrade and Unbound Materials for Pavement Design*, NCHRP Synthesis 382, Transportation Research Board, National Research Council, Washington, DC, USA, 2007.
- [20] The Ministry of Communications of the People's Republic of China, "Technical specification for construction of highway subgrade," Tech. Rep. JTG F10, 2006 (Chinese).

Research Article

Solidification/Stabilization of Fly Ash from a Municipal Solid Waste Incineration Facility Using Portland Cement

Qiang Tang,^{1,2,3} Yang Liu,¹ Fan Gu,⁴ and Ting Zhou¹

¹School of Urban Rail Transportation, Soochow University, Soochow, China

²Key Laboratory of Ministry of Education for Geomechanics and Embankment Engineering, Hohai University, Nanjing, China

³Jiangsu Research Center for Geotechnical Engineering Technology, Hohai University, Nanjing, China

⁴Texas A&M Transportation Institute, Texas A&M University, College Station, TX, USA

Correspondence should be addressed to Fan Gu; tracygufan@tamu.edu

Received 10 April 2016; Accepted 8 September 2016

Academic Editor: Jun Liu

Copyright © 2016 Qiang Tang et al. This is an open access article distributed under the Creative Commons Attribution License, which permits unrestricted use, distribution, and reproduction in any medium, provided the original work is properly cited.

This study investigated the solidification/stabilization of fly ash containing heavy metals using the Portland cement as a binder. It is found that both the cement/fly ash ratio and curing time have significant effects on the mechanical (i.e., compressive strength) and leaching behaviors of the stabilized fly ash mixtures. When the cement/fly ash ratio increases from 4 : 6 to 8 : 2, the increase of compressive strength ratio raises from 42.24% to 80.36%; meanwhile, the leaching amount of heavy metals decreases by 2.33% to 85.23%. When the curing time increases from 3 days to 56 days, the compressive strength ratio of mixtures raises from 240.00% to 414.29%; meanwhile, the leaching amount of heavy metals decreases by 16.49% to 88.70%. The decrease of compressive strength with the lower cement/fly ash ratios and less curing time can be attributed to the increase of fly ash loading, which hinders the formation of ettringite and destroys the structure of hydration products, thereby resulting in the pozzolanic reaction and fixation of water molecules. Furthermore, the presence of cement causes the decrease of leaching, which results from the formation of ettringite and the restriction of heavy metal ion migration in many forms, such as C-S-H gel and adsorption.

1. Introduction

Incineration, as an effective method to energy recovery and reduction of the volume and weight of waste, has been widely adopted for the treatment of solid waste around the world [1, 2]. According to the Eurostat yearbook, the incineration percentages of solid waste in Germany and France were as high as 32% [3]. In Holland, the incineration percentage of solid waste already reached 40% in 2000, while such incineration percentage was around 60% in Sweden, Denmark, and Luxembourg, even up to 77% and 80% in Japan and Switzerland [4, 5]. During the incineration process, heavy metals in the waste were accumulated through absorption by fly ash along the evaporation of the water and the decrease in waste volume, and the concentration of heavy metals eventually reaches a relative high level. The heavy metal contents of fly ash from various districts worldwide are detailed in Table 1. The upper limits of designated heavy metals in soils, defined by three listed standards individually

implemented by European union, Canada, and China, are also shown in Table 1. Thus, fly ash is regarded as hazardous waste in Code 19.01.13 of the Council of the European Union and has to be pretreated according to ASTM STP 1123 and 40 CFR 261.24 [1, 6–8]. Similar to pozzolana, the composition of fly ash also includes high content of Si and Ca, which provide the potential possibility for further utilization, such as cement and concrete products, structural fill, cover material, and roadway and pavement utilization [9]. In Germany, 50% of the ash produced from the incinerated waste was used in the manufacture of sound insulating walls along highways and the sublayers of city roads. In Denmark, over 72% of the ash is reused in the construction of parking lots, cycling tracks, and other roads [10].

For the reutilization in the civil and environmental engineering fields, the fly ash should meet the requirement in both the mechanical and leaching properties of heavy metals. According to Choi et al. and Song et al.'s research, cement can be utilized as a binder to effectively reduce the leachability

TABLE 1: Heavy metals in fly ash from various districts and countries.

	Heavy metal content (mg/kg)							References
	Cr	Pb	Cu	Zn	Cd	Ni	Hg	
Standard								
EU	100	100	100	300	1	50	—	[20]
CCME	64	70	63	200	1.4	50	—	[21]
GB	150	280	50	200	0.3	70	0.25	[22]
China								
Wuhan	282	1276	899	4187	36	—	—	[23]
Shanghai	180	2710	990	4530	90	70	—	[24]
Shenzhen	566.2	1356.4	3080.8	37383.5	77.8	1583.9	—	[25]
Spain	790	398	156	15900	≤6	90	<60	[2]
Poland	152.9	185.7	240.0	4660.0	87.5	78.6	—	[26]
Japan	235	3750	1800	21000	225	—	4.5	[27]
Portugal	185	2462	586	—	83.4	61	—	[28]
Italy	109	964	173	—	85	45	—	[29]
Denmark	99.0	2710	749.1	22400	97.6	—	—	[30]
Austria	500	4500	890	19000	350	94	—	[31]
India	120	35	100	—	—	150	—	[32]
Belgium	100	2900	500	9400	300	100	<100	[33]

Note: EU = European Union Standards (2009); CCME = Canadian Environmental Quality Guidelines (1999); GB = Environmental Quality Standards for Soils of China (2009).

of As and Pb in mine tailing [11–14]. Furthermore, Voglar and Leštan's and Patel and Pandey's findings indicated that, with the presence of cement in sludge and contaminated soils, the mechanical properties (i.e., compressive strength) were also greatly improved [15, 16]. Considering all above, in this study, the ordinary Portland cement (OPC) was selected as a binder material utilized for the solidification/stabilization (S/S) treatment towards the fly ash. Compressive strength test and TCLP (Toxicity Characteristic Leaching Procedure) tests were conducted to the cement-stabilized fly ash mixtures. This study investigated the mechanical behavior of the mixtures and the leaching behaviors of heavy metal ions (e.g., Cr, Cd, Pb, Ni, Cu, and Mn). The influence factors taken into account in this study include the cement/fly ash ratio, moisture content, fly ash-water reaction, and curing time. Visual MINTEQ was used to simulate the experimental conditions. The calculation results were used to analyze the leaching behaviors of heavy metals. Based on the calculation results, further discussions were made towards the S/S mechanisms and the leaching behaviors of heavy metals with the assistance of X-ray diffraction (XRD) pattern and X-ray fluorescence (XRF) results.

2. Materials and Methods

2.1. Materials. Since incineration can provide a substantial reduction in volume and weight of the waste, landfills usually equipped incineration facilities to cut down the cost of waste disposal. The fly ash used in this study was collected from municipal solid waste (MSW) incineration facility in the Qizi Mountain landfill site, Suzhou, China. The landfill has a total storage capacity of 4.7 million m³. Approximately 5000



FIGURE 1: MSWI fly ash sample collection.

tons (t)/day of MSW was deposited at this location. Among them, around 3550 t/day MSW was incinerated for electricity generation, and the incineration temperature inside the incinerator was controlled at 900°C–1100°C. During the incineration, the flue gases were successively purified by an alkaline absorbent spray system (acid gases removal), an activated carbon injection system (heavy metals and dioxin removal), and a fabric filter (dust removal and fly ash generation). In Qizi Mountain landfill site, over 100 t/day fly ashes were produced during MSW incineration. With the assistance of the staff there, original fly ash samples utilized in this study were collected as shown in Figure 1. As the binder material, the commercially available OPC P.O 42.5 was prepared, which consisted of 6%–15% active additive and 85%–94% cement.

N_2 -BET adsorption tests were conducted on fly ash to analyze several parameters, including the specific surface area, total pore volume, micropore volume (diameter < 102.12 nm), and average pore size (NOVA2000e, Quantachrome, US). Moisture content and water retention capacity were measured following JIS A 1203 and JGS 0151, respectively [17]. The maximum and minimum density and the granule density of the fly ash were determined according to JGS 0162, JIS A 1224, and JIS A 1202, respectively [17]. Plastic limit was determined according to JIS A 1205 [17]. Following GB/T50123-1999, liquid limit was determined by Photoelectric Liquid-Plastic Tester (GYS-2, Turangyiqi, China) [18]. In accordance with JIS A 1218, hydraulic conductivity was determined using a permeameter (TST-55, Jingkeyusheng, China) [17]. In addition, swell index and grain size distribution test of fly ash were conducted according to ASTM D5890-06 [19] and GB/T50123-1999 [18], respectively. The chemical composition and mineral composition of fly ash and OPC were analyzed by XRF (JSX-3400R, JEOL, Japan) and XRD (RAD-2B, Rigaku Corporation, Japan). The electrical conductivity (EC) and pH of the samples were measured using a pH/EC meter (PH-2603, Lohand, China), following JGS 0212 and JGS 0211, respectively [17].

2.2. Preparation of Samples. Fly ash and OPC samples were oven dried at 105°C for 24 hours (h) (101-A, Leao, China) to ensure the accurate quality during the experiment, since there might be some moisture content in them. Subsequently, they were cooled to room temperature in a desiccator. In order to mix evenly, the fly ash was first homogenized with the cement at five different ratios of cement/fly ash (8 : 2, 7 : 3, 6 : 4, 5 : 5, and 4 : 6 by dry mass) manually for 4-5 minutes (min) in the vessel [1]. Then distilled water, which was produced by a water distillation apparatus (JYCS-0.02T, China), was added slowly into the dry mix for the mixing process.

To determine the optimum water content or water/cement ratio, two preliminary tests were carried out as follows. Fly ash was mixed with water with the initial moisture contents maintained at 42.86%, 66.67%, 100%, 150.00%, 233.33%, and 400% (preliminary test 1); 10%, 20%, 30%, 40%, 50%, 60%, 70%, 80%, 90%, and 100% (preliminary test 2). During the test period, one mixture was exposed to the air in preliminary test 1; meanwhile another mixture was sealed by a polyethylene membrane in preliminary test 2. Then the final moisture contents were determined after 15 min (preliminary test 1) and 6 h (preliminary test 2), and the results are presented in Figures 2 and 3, respectively. From Figure 2, the initial water content decreased by 2.78%–13.00% within 15 min, which indicates that 3.25%–6.67% water evaporated due to the heat released by the reaction between fly ash and water. In preliminary test 1, the reaction between water and fly ash was neglected since the relative short period. As shown in Figure 3, the initial water content decreased by 4.17%–11.0% after 6 h, which indicates 7.22%–53.00% water has reacted with fly ash. Since the samples were all sealed by a polyethylene membrane during experiment period, the evaporation can be neglected in preliminary test 2. Considering the above and the hydration reaction of cement, the water-cement ratio was therefore maintained at 1 : 1.

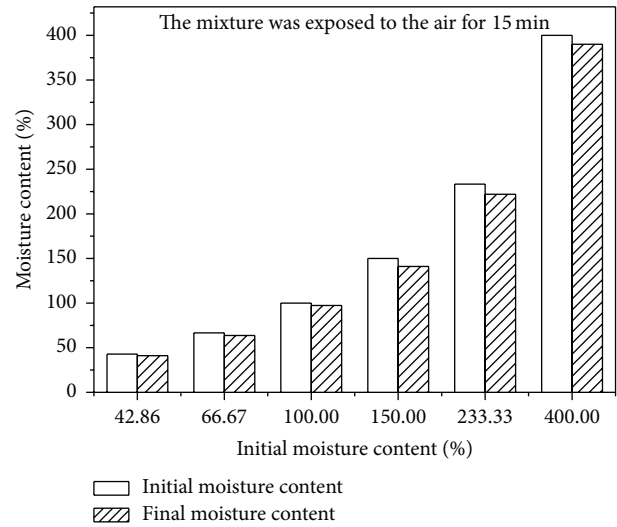


FIGURE 2: Moisture content before and after preliminary test 1.

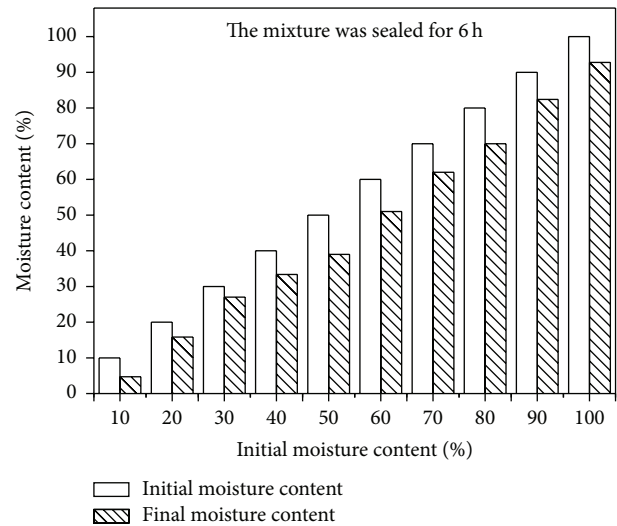


FIGURE 3: Moisture content before and after preliminary test 2.

After the mixing procedure, the mixture was transferred into the moulds (100 mm × 100 mm × 100 mm, Jianyi, China), which were then sealed with a polyethylene membrane to avoid severe dehydration. Afterwards, the mixtures were left undisturbed for 24 h at room temperature ($23 \pm 2^\circ\text{C}$) and high relative humidity ($>50\%$). Three replicates were analyzed for each trial. After the period of the initial setting, the mixtures were demoulded and cured ($\geq 95\%$ humidity, $20 \pm 2^\circ\text{C}$) for 3, 7, 14, 28, and 56 days in a curing box (HBY-15B, Donghua, China).

2.3. Compressive Strength Test Method. Microcomputer Controlled Electronic Testing Machine (LDS-50, Chenda, China) was used to obtain the compressive strength of samples. The loading platform's diameter was 15 cm and the range was fixed at 0–30 kN during the test. Total maximum loads were recorded at the point of fracture and the compressive strength was determined using the formula $P = F/A$, where P is

TABLE 2: Properties of fly ash.

Property	Units	Standard	Values
Moisture content	%	JIS A 1203	6.110
Water retention capacity	%	JGS 0151	117.8
Maximum density	g/cm ³	JGS 0162	0.67
Minimum density	g/cm ³	JIS A 1224	0.49
Granule density	g/cm ³	JIS A 1202	2.528
Plastic limit	%	JIS A 1205	15.96
Liquid limit	%	GB/T50123-1999	47.66
Swell index	mL/2g-solid	ASTM D 5890-06	3.00
Hydraulic conductivity	m/s	JIS A 1218	1.55×10^{-7}
pH	—	JGS 0211	12.15
EC	mS/cm	JGS 0212	57.68
Grain size distribution		GB/T 50123-1999	
Sand fraction (2–0.075 mm)	%		12.10
Silt fraction (0.075–0.005 mm)	%		84.26
Clay fraction (≤ 0.005 mm)	%		3.64
Uniformity coefficient	—		4.02
Coefficient of curvature	—		1.12
N ₂ -BET			
Correlation coefficient (R^2)	—		0.999
Specific surface area	m ² /g		7.944
Average pore size	Å		114.2
Total pore volume	mL/g		2.710×10^{-2}
Micropore volume (diameter < 102.12 nm)	mL/g		2.516×10^{-2}

the compressive strength (MPa), F is the total maximum load (N), and A is the area of loaded surface (mm²) [34, 35]. All of samples were prepared in triplicate.

2.4. Leaching Test Method for Heavy Metals. First of all, the extraction buffer was prepared using 1 mol/L acetic acid and 1 mol/L sodium hydroxide (pH 2.88 ± 0.05). The crushed samples collected after the compressive strength test were oven dried at 105°C for 24 h. Then the dried samples were further crushed manually until the particle size was less than 9.5 mm. The crushed samples were then leached using the previously prepared extraction buffer at a liquid/solid ratio of 20:1. Subsequently, the extraction was performed using Flip-Automatic Extraction Oscillator (KB-W08, Marina Bay, China) for 18 ± 2 h at 23 ± 2 °C and the rotational speed was fixed at 30 ± 2 r/min. After the extraction, the leachate samples were filtered through a 0.45 μm borosilicate glass fiber filter and the resultant TCLP (US EPA Test Method 1311) extract (filtrate) was analyzed for heavy metals by Atomic Absorption Spectroscopy (AAS) (TAS-990, Persee General, China) [36]. All the samples were prepared in duplicate.

3. Results and Discussion

3.1. Characterization of the Materials. The properties of fly ash are detailed in Table 2. As shown in Table 2, the moisture content of fly ash is 6.110%. The maximum and minimum

density are 0.67 and 0.49 g/cm³, respectively. The granule density of fly ash is 2.528 g/cm³, which is lower than that of the clay utilized in Tran et al. (i.e., the granule density of fly ash is 2.7 g/cm³) [37]. The plastic limit and liquid limit of fly ash are 15.96% and 47.66%, respectively. The swell index is 3.00 mL/2 g solid, almost the same as the Fukakusa clay utilized in Tang et al., which demonstrates that the fly ash used in the experiment contains little expansive constitute [38]. As observed in the grain size accumulation curve of fly ash presented in Figure 4, the curve is steep when the particle size ranges from 0.067 to 0.1 mm, which indicates that the particle size distribution is dense within this range. The uniformity coefficient and coefficient of curvature are 4.02 and 1.12, respectively [39]. This indicates that the particle size distribution is relatively uniform. The hydraulic conductivity of fly ash is 1.55×10^{-7} m/s, two orders of magnitude higher than that of the clay used in Tran et al. [37]. The diverse hydraulic conductivities can be attributed to the difference in the particle size. The pH value of fly ash is 12.15 because of its alkaline nature. The EC value of fly ash is 57.68 mS/cm, which is 287 times higher than for the soil used in Taghipour and Jalali [40]. This demonstrates that a large amount of soluble salt exists in fly ash and thus increases the difficulty in immobilization.

The specific surface area of the fly ash used in this experiment is 7.944 m²/g. This is much higher than the pozzolana utilized in Ghrici et al., which is 0.42 m²/g [41].

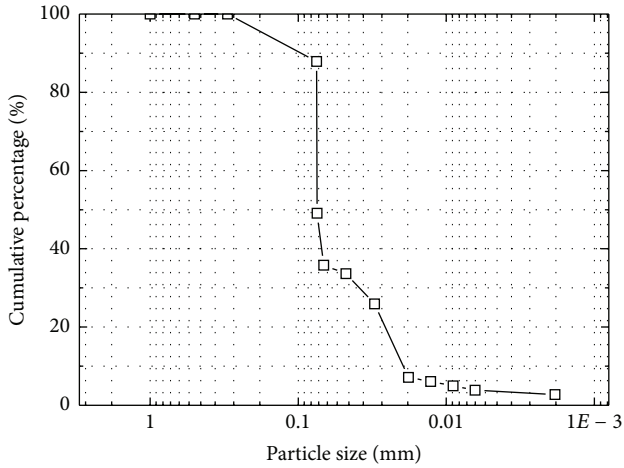


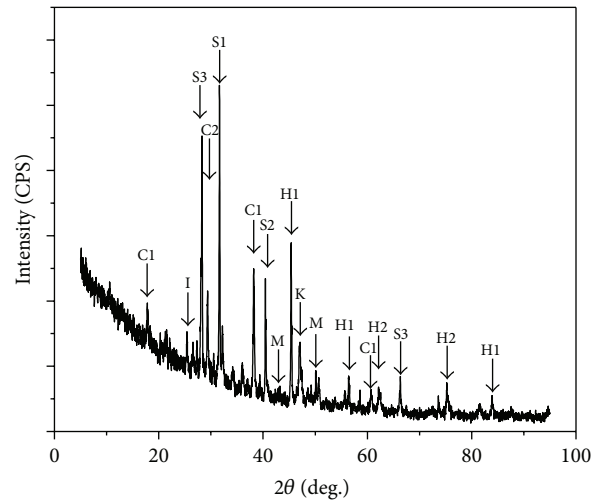
FIGURE 4: Grain size distribution curve of fly ash.

TABLE 3: Chemical compositions of fly ash and OPC.

Chemical composition	Unit	Fly ash	OPC
SiO ₂	%	11.53	20.85
Al ₂ O ₃	%	7.89	5.71
Fe ₂ O ₃	%	2.57	3.33
CaO	%	41.80	60.48
MgO	%	2.27	2.28
SO ₃	%	3.25	2.84
Na ₂ O	%	2.58	1.43
K ₂ O	%	5.74	0.73
TiO ₂	%	0.68	0.31
Cl	%	10.89	0.26
ZnO	%	1.30	—
PbO	%	0.55	—
CdO	%	0.07	—
MnO	%	0.07	—
CuO	%	0.25	—
Cr ₂ O ₃	%	0.01	—

This may be because the particle size of fly ash is smaller than that of the pozzolana. In addition, the specific surface area of the fly ash is smaller than that of the bentonite utilized in Hua, which is 34.4 m²/g. The reason for this is due to the special microstructure of bentonite, which consists of irregular groups that have an average diameter of approximately 0.1 to 10 μm [42]. These groups are composed of a certain number of particles whose lateral dimensions range from 8 to 10 nm. At the same time, these particles are made up of 5 to 10 layers, whose dimensions are 100 to 200 nm in diameter and only 1 nm in thickness [43]. Additionally, the average pore size of fly ash is 114.2 Å. The total pore volume and micropore volume of the fly ash are 2.710 × 10⁻² mL/g and 2.516 × 10⁻² mL/g, respectively.

XRF results of untreated fly ash and OPC are displayed in Table 3. Based on the XRD pattern shown in Figure 5, untreated fly ash is composed of calcite (CaCO₃) and calcium chlorite hydrate (Ca(ClO)₂·4H₂O), which are



- C1: calcium chlorite hydrate
- C2: calcite
- H1: halite
- H2: hematite
- I: iron manganese titanium oxide
- K: kyanite
- M: maghemite
- S1: silicon chloride
- S2: silicon titanium
- S3: sylvite

FIGURE 5: XRD pattern of fly ash.

observed at $2\theta = 29.36^\circ$ and ($17.80^\circ, 38.20^\circ, 60.73^\circ$). XRF results corroborate the presence of these two substances and CaO accounts for 41.80% of the total contents. According to Anastasiadou et al.'s study, the calcite was also observed [1]. From Table 3, fly ash contains 11.53% SiO₂, 10.89% Cl, and 5.71% Al₂O₃. The presences of kyanite (Al₂O₃·SiO₂) and silicon chlorite (SiCl₄) are verified at $2\theta = 47.09^\circ$ and 31.64° as well. Faleschini et al. also demonstrated that kyanite exists in fly ash [44]. Considering the existence of Na₂O and K₂O shown by XRF results, the characteristic peaks at $2\theta = (45.38^\circ, 56.41^\circ, 83.92^\circ)$ and ($28.30^\circ, 66.34^\circ$) shown in the XRD pattern indicate the presence of halite (NaCl) and sylvite (KCl). This also agrees with Liu et al.'s study [45]. In addition, hematite (Fe₂O₃), maghemite (Fe₃O₄), iron manganese titanium oxide (Fe₂MnTi₃O₁₀), and silicon titanium (TiSi₂) appearing at $2\theta = (62.14^\circ, 75.22^\circ), (43.27^\circ, 50.14^\circ), 25.42^\circ$, and 40.45° are in accordance with XRF analysis, in which 2.57% Fe₂O₃, 0.68% Ti₂O, and 0.07% MnO are detected.

3.2. Compressive Strength Test Results. The compressive strength values of the cement-based fly ash mixtures under different curing periods are presented in Figure 6. At cement/fly ash ratios of 4 : 6, 5 : 5, 6 : 4, 7 : 3, and 8 : 2, the compressive strengths are 0.45–1.53 MPa, 0.63–2.57 MPa, 0.49–2.52 MPa, 0.60–2.59 MPa, and 0.75–2.67 MPa, respectively. Compared to 3 days of curing, the compressive strength of mixtures with 28 days of curing time increases by 157.8% (4 : 6), 84.1% (5 : 5), 179.6% (6 : 4), 175.0% (7 : 3), and 120.0% (8 : 2), respectively. These results were in good agreement with the Anastasiadou et al.'s study, where the compressive strength of mixtures increased by 200.0% (4 : 6), 700.0% (5 : 5), and 404.0% (6 : 4) by comparing the values after 28 days of curing with 1 day of curing [1]. All values of compressive strength for the test mixtures exceed the standard (ASTM

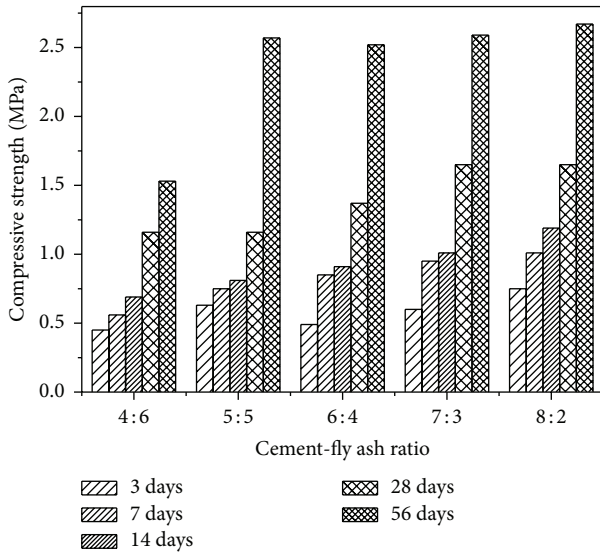


FIGURE 6: Compressive strength of cemented solidified fly ash.

STP 1123) stipulated for solidified waste to be landfilled, which is 0.414 MPa [1, 7].

Figure 6 shows that the compressive strength of mixtures increases with the curing time. This is because the hydration reaction will be more complete when the curing time is longer. Two processes are involved during the period of cement hydration reaction. One is through-solution hydration, which involves several factors including dissolution of anhydrous compounds into their ionic constituents, formation of hydrates in the solution, and eventual precipitation of hydrates from the supersaturated solution. The other is solid-state hydration of cement and the reactions occurring directly at the surface of the anhydrous cement compounds. During this period, no compounds dissolve into solution. In the early stage of cement hydration, through-solution hydration is dominant. At the poststage of cement hydration, the hydration of residual cement particles may occur by the solid-state reactions and the migration of ions in the solution becomes restricted [46].

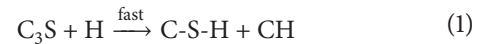
For cement/fly ash ratio, the attributes of the mixture will be closer to the pure OPC when cement/fly ash ratio is larger. Therefore, the compressive strength decreases as the cement/fly ash ratio is reduced. This phenomenon can be analyzed from four aspects, specifically, the formation of ettringite (AFt), the structure of products of hydration, pozzolanic reaction, and the fixation of water molecules. Firstly, when the addition of fly ash increases, the formation of AFt, which supports the development of the early strength, will be reduced [47]. Due to the presence of fly ash, a part of the aluminate, which should participate in the formation of AFt, is seized to form Friedel's salt. It is inferred that the more the fly ash that is added, the more the aluminate that reacts to form Friedel's salt and the larger the decrease in magnitude of strength. Regarding the AFt, a more concrete discussion will be given in Section 3.3.

Secondly, the residues in fly ash that are not completely burnt also influence the compressive strength of the solidified

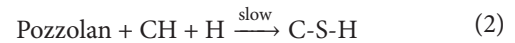
matrix. The products of cement hydration are lapped and bound by the multiple gravitation. This is the reason why cement blocks have a high compressive strength. However, the high levels of residues in fly ash not only reduce the concentration of products from cement hydration, which have connection effect, but also destroy the structure of products of hydration [48]. This also explains the phenomenon that the compressive strength of mixtures decreases with the increase of fly ash loading.

Thirdly, when fly ash is added to OPC, it will undergo the pozzolanic reaction. Due to similar chemical composition, fly ash can be classified as a pozzolan, which is one of two main components used in production of concrete. The other is cement [26]. When added to OPC, fly ash, as a pozzolan, undergoes the pozzolanic reaction with calcium hydroxide, which is slow, and the rate of strength development will accordingly slow down. Regarding the hydration reaction, a comparison between Portland cement and Portland-pozzolan cement is given as follows.

Portland cement:



Portland-pozzolan cement:



where C, S, and H represents CaO, SiO₂, and H₂O, respectively [46]. When the cement/fly ash ratio is low, the hydration of Portland-pozzolan cement has the higher tendency to take place following (2). This is another reason for the decrease of compressive strength associated with the decrease of cement/fly ash ratio.

Fourthly, fly ash will bind water, which should participate in the hydration of cement, due to its strong ability to fix water molecules. Based on the work by Mitchell and Soga, the surface charges of fly ash particles, along with hydrogen bonds on the particle surface and van Der Waals forces between water molecules and fly ash particles, contribute to the fixation of water molecules [49]. As shown in Table 2, the specific surface area of fly ash is 7.944 m²/g, which provides a favorable condition for attracting water, considering the interaction between water and fly ash particles. That is expected by the results of the preliminary tests in Section 2.2. For the samples with various initial moisture contents, 7.22%–53.00% water reacted with fly ash. The ability to strongly fix water molecules is also corroborated by the water retention capacity displayed in Table 2. When the water is bound by fly ash, the hydration reaction is incomplete. This is why fly ash loading leads to a decrease of compressive strength. Obviously, the more fly ash is added, the more water is attracted. Thereby, the compressive strength of fly ash mixtures decreases accordingly.

3.3. Leaching Test Results. The TCLP leaching amounts of fly ash samples after 3, 7, 14, 28, and 56 days of curing are displayed in Table 4. For treated fly ash, the final leaching amount of all measured metals is lower than the US EPA standard (40 CFR 261.24) [8]. Compared to the untreated

TABLE 4: Summary of TCLP leaching results for solidified fly ash samples.

Cement/fly ash	Curing time	Concentration of metals in leachate (mg/L)					
		Cr	Cd	Pb	Ni	Cu	Mn
Untreated fly ash		0.85	6.40	15.50	1.04	0.19	—
40 CFR 261.24		5	1	5	100	100	—
8:2	3 d	0.722	0.084	0.821	0.188	0.115	0.113
	7 d	0.601	0.076	0.688	0.182	0.092	0.094
	14 d	0.541	0.073	0.465	0.176	0.084	0.040
	28 d	0.433	0.056	0.255	0.169	0.009	0.034
	56 d	0.455	0.057	0.236	0.157	0.013	0.045
7:3	3 d	0.843	0.148	0.907	0.200	0.189	0.194
	7 d	0.547	0.106	0.741	0.190	0.167	0.145
	14 d	0.472	0.069	0.669	0.156	0.109	0.037
	28 d	0.361	0.044	0.321	0.140	0.099	0.034
	56 d	0.367	0.048	0.189	0.138	0.098	0.014
6:4	3 d	0.823	0.094	1.014	0.218	0.131	0.157
	7 d	0.746	0.092	0.547	0.207	0.112	0.148
	14 d	0.486	0.073	0.493	0.198	0.092	0.116
	28 d	0.450	0.045	0.448	0.176	0.087	0.097
	56 d	0.530	0.057	0.494	0.188	0.097	0.078
5:5	3 d	0.798	0.106	0.893	0.245	0.173	0.152
	7 d	0.493	0.088	0.684	0.236	0.096	0.132
	14 d	0.444	0.066	0.220	0.225	0.079	0.046
	28 d	0.423	0.048	0.142	0.214	0.045	0.021
	56 d	0.480	0.069	0.238	0.205	0.034	0.013
4:6	3 d	0.828	0.104	0.944	0.241	0.123	0.147
	7 d	0.601	0.092	0.644	0.221	0.098	0.129
	14 d	0.490	0.080	0.480	0.213	0.086	0.071
	28 d	0.357	0.070	0.390	0.215	0.062	0.031
	56 d	0.341	0.067	0.342	0.213	0.088	0.033

Note: “—” = not available.

fly ash from Table 4, the leaching amounts of heavy metals after 3 days of curing decrease by approximately 98.33% (Cd), 94.09% (Pb), and 79.00% (Ni). The decreases of the leaching amounts of Cr and Cu are 0.82%–15.06% and 0.53%–39.47%, respectively. After 56 days of curing, the decreases of the leaching amounts of heavy metals are approximately 98.91% (Cd), 98.52% (Pb), 82.17% (Ni), 37.65%–59.88% (Cr), and 48.42%–93.16% (Cu). The leaching amount of all heavy metals decreases with the increase of curing time. This finding is also proved by Anastasiadou et al. [1]. In Anastasiadou et al.'s research, comparing the samples after 1 day of curing, the leaching-out heavy metal amount from samples after 28 days decreases by a wide margin. For example, Cr, Ni, Cu, Cd, and Pb decrease by 28.9%, 30.6%, 30.6%, 57.1%, and 64.5% [1]. According to Table 4, however, the leaching amounts of some heavy metals such as Cr (5:5, 6:4) and Cu (4:6, 6:4, and 8:2) after 56 days of curing are higher than those after 28 days of curing. It indicates that a part of heavy metals have released from the material again after 28 days of curing, and two reasons can be concluded as given below. First of all, as mentioned in Section 2.2, the humidity during the curing process is relatively high ($\geq 95\%$). Therefore,

the carbon dioxide in the air tends to dissolve in water and forms carbonic acid, resulting in the decrease of alkalinity. According to Beaudoin and Brown, C-S-H gel is unstable when pH is lower than 10.0 [50]. Thus, it is rational to judge that the barriers provided by C-S-H, especially covered at the outward surface, have the tendency to be destroyed due to the decrease in alkalinity as the curing period increased and caused the release of fixed heavy metals. In addition, carbonic acid also redissolves heavy metal ion precipitates, making heavy metals exist in free ion form. Table 4 also shows that the leaching amount of Cr is much higher than that of Cu(II). According to the results calculated by Visual MINTEQ as shown in Table 5, that may be attributed to the soluble form of Cr(VI) in the alkaline environment. Table 5 shows that 100% Cr exists in the form of soluble ions (CrO_4^{2-} or HCrO_4^-) when pH ranges from 10.0 to 12.0, while 0.466%–11.594% Cu exists as the precipitate ($\text{Cu}(\text{OH})_2$). The similar phenomenon is also observed by Mulligan et al., in which Cr(VI) is found hard to transform into a low soluble hydroxide [51].

The mechanisms of S/S can be generally divided into two processes: physical encapsulation and chemical immobilization. The former provides barriers generated on the surface

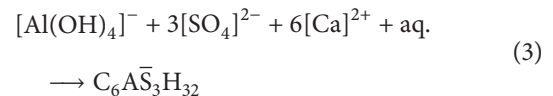
TABLE 5: The percentage of possible ion forms of Cu(II) and Cr(VI).

	pH	Percentage of possible ion forms (%)					
		A	B	C	D	E	F
Cr(VI)	10.0	CrO ₄ ²⁻	HCrO ₄ ⁻	—	—	—	—
		99.987	0.013	—	—	—	—
	11.0	CrO ₄ ²⁻	—	—	—	—	—
		99.999	—	—	—	—	—
	12.0	CrO ₄ ²⁻	—	—	—	—	—
		100	—	—	—	—	—
Cu(II)	10.0	CuOH ⁺	Cu(OH) ₃ ⁻	Cu(OH) ₂	Cu ₂ (OH) ₂ ²⁺	Cu ₃ (OH) ₄ ²⁺	—
		0.036	0.262	0.466	0.155	99.081	—
	11.0	CuOH ⁺	Cu(OH) ₄ ²⁻	Cu(OH) ₃ ⁻	Cu(OH) ₂	Cu ₂ (OH) ₂ ²⁺	Cu ₃ (OH) ₄ ²⁺
		0.016	0.236	11.594	2.065	0.030	86.059
	12.0	Cu(OH) ₄ ²⁻	Cu(OH) ₃ ⁻	Cu(OH) ₂	Cu ₃ (OH) ₄ ²⁺	—	—
		16.717	81.539	1.443	0.300	—	—

of the waste to restrict contaminant migration by mechanical processes or chemical reactions. The latter refers to the processes that keep heavy metals in a certain form by chemical reactions to reduce the leachability. The related mechanisms are also validated by Sobiecka et al. [26]. The importance of fly ash solidification/stabilization can be specifically expounded using the following three aspects. Firstly, the migration of heavy metal ions is hindered by the products of the cement hydration reactions. The solidification processes result in the formation of C-S-H gel on the surface of the stabilized fly ash particles. C-S-H gel acts as a barrier between the immobilized solid wastes and the surrounding liquids and controls the potential adsorption of ions present in the liquids onto the surface of the solid waste, as well as the immobilization of heavy metals in the resulting products [52]. Based on the aforementioned theory, it can be inferred that the hydration reaction of OPC is more sufficient and the amount of C-S-H gel is larger by prolonging the curing time. That can explain why the leaching amount of heavy metals decreases with the increase of curing time.

Secondly, heavy metal ions are absorbed by the products of the cement hydration reaction. The absorption can be divided into the physical absorption and chemical absorption. Physical absorption is caused by van Der Waals forces between particles, while chemical absorption is the result of chemical bond formation [53]. Due to the porous structure and small crystal particles, the specific surface area of cement hydration reaction products ranges from 10 to 50 m²/g [54]. This creates a favorable condition for physical absorption. As mentioned before, with the increase in cement/fly ash ratio, the products of cement hydration reaction also increase, and the effect of physical absorption will therefore be more remarkable. This is corroborated in Table 4, which demonstrates that the highest leaching levels of heavy metals occur at the smallest cement/fly ash ratio (4 : 6). However, according to Liu et al., Cr cannot be effectively removed through the physical absorption when pH is over 10.0 [55]. Given the alkaline environment during the cement hydration reaction, this can help explain why the immobilization of Cr is not very efficient.

Thirdly, the Ca(II) in the structure of AFt can be replaced by divalent heavy metal ions, including Zn(II), Cd(II), Pb(II), and Ni(II), through isomorphous replacement. Similarly, the Al(III) can be replaced by trivalent or tetravalent heavy metal ions, including Cr(III), Mn(III), Ti(III), and Ti(IV) [54]. These reactions have a certain relationship with the ionic radius. For instance, the ionic radii of some divalent heavy metal ions are 0.074 nm (Zn(II)), 0.095 nm (Cd(II)), and 0.069 nm (Ni(II)), which are relatively smaller and denser than that of Ca(II) (0.1 nm). Therefore, these heavy metal ions have the tendency to replace Ca(II) in the AFt due to the stronger attractive force. However, with an increase in fly ash loading, the formation of AFt will be hindered. The calcium sulfate and chloride in fly ash can influence the hydration of cement at the same time. On the one hand, the calcium sulfate in fly ash tends to react with aluminate in cement to generate AFt. The chemical reaction can be expressed as follows:



where C, A, $\bar{\text{S}}$, and H represent CaO, Al₂O₃, SO₃, and H₂O. On the other hand, the large amount of chloride in fly ash dissolves into the solution existing in the pores of cement and tends to form calcium chloride, which can react with aluminate in cement and generate Friedel's salt. The impacts on the hydration reaction of aluminate are the opposite, resulting in a competition between the two reactions. As a matter of fact, compared with the pure cement paste, only a small amount of aluminate may react with sulfate. This indicates that the latter reaction is dominant in the process [44]. Therefore, the addition of fly ash reduces the formation of AFt. This explains why the maximum leaching amount of heavy metal ion occurs at the minimum cement/fly ash ratio (4 : 6).

4. Conclusions

In this study, compressive strength test and TCLP test were conducted on the cement-stabilized fly ash. The mechanical

behavior of the fly ash mixtures and the leaching behaviors of heavy metal ions (Cr, Cd, Pb, Ni, Cu, and Mn) were investigated. According to the compressive strength test results, the compressive strength of the mixtures grew with the increase of cement/fly ash ratio and curing time. For the TCLP test results, it was shown that the leaching amounts of heavy metals decreased with the increase of cement/fly ash ratio and curing time. After the cement S/S treatment, the final leaching amounts of heavy metals were effectively controlled, which is lower than the US EPA standard. Combined with the XRF and XRD analysis, it was found that the formation of AFt was hindered due to the presence of fly ash and thereby reduced the compressive strength and blocked the immobilization of heavy metals. In addition, fly ash loading destroyed the structure of the products of cement hydration. This resulted in the pozzolanic reaction and fixation of water molecules, which further increased the compressive strength of test samples. The formation of C-S-H gel, along with the adsorption of products, restricted the migration of ions and ultimately reduced the total amount of leachate.

Competing Interests

The authors declare that they have no competing interests.

Acknowledgments

The research presented herein is supported by the National Nature Science Foundation of China (Grant no. 41630633), China Postdoctoral Science Foundation funded project (Grant no. 2016M591756), and the Open Project Program of MOE Key Laboratory of Soft Soils and Geoenvironmental Engineering, Zhejiang University (Grant no. 2016P03). The research is also supported by Jiangsu Provincial Transport Bureau, Bureau of Housing and Urban-Rural Development of Suzhou, and Soft Science Research Program from Suzhou Association for Science and Technology.

References

- [1] K. Anastasiadou, K. Christopoulos, E. Mousios, and E. Gidaracos, "Solidification/stabilization of fly and bottom ash from medical waste incineration facility," *Journal of Hazardous Materials*, vol. 207-208, no. 6, pp. 165-170, 2012.
- [2] Y. L. Galiano, C. F. Pereira, and J. Vale, "Stabilization/solidification of a municipal solid waste incineration residue using fly ash-based geopolymers," *Journal of Hazardous Materials*, vol. 185, no. 1, pp. 373-381, 2011.
- [3] European Commission, *Eurostat Yearbook 2011*, Eurostat, 2011.
- [4] H.-U. Hartenstein and M. Horvay, "Overview of municipal waste incineration industry in west Europe (based on the German experience)," *Journal of Hazardous Materials*, vol. 47, no. 1-3, pp. 19-30, 1996.
- [5] "Waste treatment in Japan," Ministry of Environment, Waste Management and Recycling Unit, 2011 (Japanese).
- [6] Q. Tang, X. Tang, M. Hu, Z. Li, Y. Chen, and P. Lou, "Removal of Cd(II) from aqueous solution with activated Firmiana Simplex Leaf: behaviors and affecting factors," *Journal of Hazardous Materials*, vol. 179, no. 1-3, pp. 95-103, 2010.
- [7] American Society for Testing and Materials, "Stabilization and solidification of hazardous, radioactive, and mixed wastes," ASTM STP 1123, 1992.
- [8] US Environmental Protection Agency, *Definition of Solid Waste and Hazardous Waste Recycling*, 2001.
- [9] M. Ahmaruzzaman, "A review on the utilization of fly ash," *Progress in Energy and Combustion Science*, vol. 36, no. 3, pp. 327-363, 2010.
- [10] L. Reijnders, "Disposal, uses and treatments of combustion ashes: a review," *Resources, Conservation and Recycling*, vol. 43, no. 3, pp. 313-336, 2005.
- [11] W.-H. Choi, S.-R. Lee, and J.-Y. Park, "Cement based solidification/stabilization of arsenic-contaminated mine tailings," *Waste Management*, vol. 29, no. 5, pp. 1766-1771, 2009.
- [12] F. Y. Song, L. Gu, N. W. Zhu, and H. P. Yuan, "Leaching behavior of heavy metals from sewage sludge solidified by cement-based binders," *Chemosphere*, vol. 92, no. 4, pp. 344-350, 2013.
- [13] I. G. Richardson and G. W. Groves, "The incorporation of minor and trace elements into calcium silicate hydrate (C-S-H) gel in hardened cement pastes," *Cement and Concrete Research*, vol. 23, no. 1, pp. 131-138, 1993.
- [14] F. Ziegler, A. M. Scheidegger, C. A. Johnson, R. Dáhn, and E. Wieland, "Sorptions mechanisms of zinc to calcium silicate hydrate: X-ray absorption fine structure (XAFS) investigation," *Environmental Science and Technology*, vol. 35, no. 7, pp. 1550-1555, 2001.
- [15] G. E. Voglar and D. Leštan, "Solidification/stabilisation of metals contaminated industrial soil from former Zn smelter in Celje, Slovenia, using cement as a hydraulic binder," *Journal of Hazardous Materials*, vol. 178, no. 1-3, pp. 926-933, 2010.
- [16] H. Patel and S. Pandey, "Evaluation of physical stability and leachability of Portland Pozzolona Cement (PPC) solidified chemical sludge generated from textile wastewater treatment plants," *Journal of Hazardous Materials*, vol. 207-208, pp. 56-64, 2012.
- [17] ISBN, 2nd edition.
- [18] Ministry of Housing and Urban-Rural Development of the People's Republic of China, *Standard for Soil Test Method*, 1999.
- [19] American Society for Testing and Materials, "Standard test method for swell index of clay mineral component of geosynthetic clay liners," ASTM D5890-06, ASTM International, West Conshohocken, Pa, USA, 2006.
- [20] European Union, *Heavy Metals in Wastes*, European Commission on Environment, 2009.
- [21] Canadian Environmental Council of Ministers of the Environment, *Soil Quality Guidelines for the Protection of Environmental and Human Health*, 1999.
- [22] Ministry of Environmental Protection of the People's Republic of China, *Environmental Quality Standards for Soils*, 2009.
- [23] J. Yu, Y. Qiao, L. Jin, C. Ma, N. Paterson, and L. Sun, "Removal of toxic and alkali/alkaline earth metals during co-thermal treatment of two types of MSWI fly ashes in China," *Waste Management*, vol. 46, pp. 287-297, 2015.
- [24] Y. Y. Hu, P. F. Zhang, J. P. Li, and D. Z. Chen, "Stabilization and separation of heavy metals in incineration fly ash during the hydrothermal treatment process," *Journal of Hazardous Materials*, vol. 299, pp. 149-157, 2015.
- [25] F.-H. Wang, F. Zhang, Y.-J. Chen, J. Gao, and B. Zhao, "A comparative study on the heavy metal solidification/stabilization performance of four chemical solidifying agents in municipal solid waste incineration fly ash," *Journal of Hazardous Materials*, vol. 300, pp. 451-458, 2015.

- [26] E. Sobiecka, A. Obraniak, and B. Antizar-Ladislao, "Influence of mixture ratio and pH to solidification/stabilization process of hospital solid waste incineration ash in Portland cement," *Chemosphere*, vol. 111, pp. 18–23, 2014.
- [27] M. Kamon, T. Katsumi, and Y. Sano, "MSW fly ash stabilized with coal ash for geotechnical application," *Journal of Hazardous Materials*, vol. 76, no. 2-3, pp. 265–283, 2000.
- [28] A. T. Lima, L. M. Ottosen, and A. B. Ribeiro, "Assessing fly ash treatment: remediation and stabilization of heavy metals," *Journal of Environmental Management*, vol. 95, pp. S110–S115, 2012.
- [29] F. Lombardi, T. Mangialardi, L. Piga, and P. Sirini, "Mechanical and leaching properties of cement solidified hospital solid waste incinerator fly ash," *Waste Management*, vol. 18, no. 2, pp. 99–106, 1998.
- [30] G. M. Kirkelund, C. Magro, P. Guedes, P. E. Jensen, A. B. Ribeiro, and L. M. Ottosen, "Electrodialytic removal of heavy metals and chloride from municipal solid waste incineration fly ash and air pollution control residue in suspension—test of a new two compartment experimental cell," *Electrochimica Acta*, vol. 181, pp. 73–81, 2015.
- [31] B. Nowak, P. Aschenbrenner, and F. Winter, "Heavy metal removal from sewage sludge ash and municipal solid waste fly ash—a comparison," *Fuel Processing Technology*, vol. 105, pp. 195–201, 2013.
- [32] S. Sushil and V. S. Batra, "Analysis of fly ash heavy metal content and disposal in three thermal power plants in India," *Fuel*, vol. 85, no. 17-18, pp. 2676–2679, 2006.
- [33] B. Van Der Bruggen, G. Vogels, P. Van Herck, and C. Vandecasteele, "Simulation of acid washing of municipal solid waste incineration fly ashes in order to remove heavy metals," *Journal of Hazardous Materials*, vol. 57, no. 1-3, pp. 127–144, 1998.
- [34] F. Gu, Y. Zhang, C. V. Drodody, R. Luo, and R. L. Lytton, "Development of a new mechanistic empirical rutting model for unbound granular material," *Journal of Materials in Civil Engineering*, vol. 28, no. 8, Article ID 4016051, 2016.
- [35] F. Gu, H. Sahin, X. Luo, R. Luo, and R. L. Lytton, "Estimation of resilient modulus of unbound aggregates using performance-related base course properties," *Journal of Materials in Civil Engineering*, vol. 27, no. 6, Article ID 04014188, 2015.
- [36] U.S. Environmental Protection Agency, "Toxicity characteristic leaching procedure," US EPA Test Method 1311, 1984.
- [37] T. D. Tran, Y.-J. Cui, A. M. Tang, M. Audiguier, and R. Cojean, "Effects of lime treatment on the microstructure and hydraulic conductivity of Héricourt clay," *Journal of Rock Mechanics and Geotechnical Engineering*, vol. 6, no. 5, pp. 399–404, 2014.
- [38] Q. Tang, T. Katsumi, T. Inui, and Z. Li, "Membrane behavior of bentonite-amended compacted clay," *Soils and Foundations*, vol. 54, no. 3, pp. 329–344, 2014.
- [39] T. Qiang, K. Heejong, E. Kazuto, K. Takeshi, and I. Toru, "Size effect on lysimeter test evaluating the properties of construction and demolition waste leachate," *Soils and Foundations*, vol. 55, no. 4, pp. 720–736, 2015.
- [40] M. Taghipour and M. Jalali, "Effect of clay minerals and nanoparticles on chromium fractionation in soil contaminated with leather factory waste," *Journal of Hazardous Materials*, vol. 297, pp. 127–133, 2015.
- [41] M. Ghrici, S. Kenai, and M. Said-Mansour, "Mechanical properties and durability of mortar and concrete containing natural pozzolana and limestone blended cements," *Cement and Concrete Composites*, vol. 29, no. 7, pp. 542–549, 2007.
- [42] J. Hua, "Synthesis and characterization of bentonite based inorgano-organo-composites and their performances for removing arsenic from water," *Applied Clay Science*, vol. 114, pp. 239–246, 2015.
- [43] H. Han and Y. Zhu, "Study on modification and application of bentonite," *Inorganic Chemicals Industry*, vol. 43, pp. 5–8, 2011 (Chinese).
- [44] F. Faleschini, M. A. Zanini, K. Brunelli, and C. Pellegrino, "Valorization of co-combustion fly ash in concrete production," *Materials and Design*, vol. 85, pp. 687–694, 2015.
- [45] Y. Q. Liu, W. P. Zhu, and E. H. Yang, "Alkali-activated ground granulated blast-furnace slag incorporating incinerator fly ash as a potential binder," *Construction and Building Materials*, vol. 112, pp. 1005–1012, 2016.
- [46] P. K. Mehta and P. J. M. Monteiro, *Concrete: Microstructure, Properties, and Materials*, McGraw-Hill Education, 4th edition, 2014.
- [47] S. Rémond, D. P. Bentz, and P. Pimienta, "Effects of the incorporation of municipal solid waste incineration fly ash in cement pastes and mortars: II: modeling," *Cement and Concrete Research*, vol. 32, no. 4, pp. 565–576, 2002.
- [48] H.-Q. Liu, G.-X. Wei, S.-G. Zhang, and J.-J. Cai, "Effect of activated carbon on cement solidification of hospital waste incineration fly ash," *The Chinese Journal of Process Engineering*, vol. 8, no. 5, pp. 953–956, 2008 (Chinese).
- [49] J. K. Mitchell and K. Soga, *Fundamentals of Soil Behavior*, John Wiley & Sons, New York, NY, USA, 3rd edition, 2005.
- [50] J. J. Beaudoin and P. W. Brown, "The structure of hardened cement paste," in *Proceedings of the 9th International Congress on the Chemistry of Cement*, pp. 1485–1525, 1992.
- [51] C. N. Mulligan, R. N. Yong, and B. F. Gibbs, "Remediation technologies for metal-contaminated soils and groundwater: an evaluation," *Engineering Geology*, vol. 60, no. 1–4, pp. 193–207, 2001.
- [52] A. Pariatamby, C. Subramaniam, S. Mizutani, and H. Takatsuki, "Solidification and stabilization of fly ash from mixed hazardous waste incinerator using ordinary Portland cement," *Environmental Sciences*, vol. 13, no. 5, pp. 289–296, 2006.
- [53] Q. Tang, X. W. Tang, Z. Z. Li et al., "Zn(II) removal with activated firmiana simplex leaf: kinetics and equilibrium studies," *Journal of Environmental Engineering*, vol. 138, no. 2, pp. 190–199, 2012.
- [54] X. He, H. Hou, and D. Zhang, "Study on cement solidification of municipal solid waste incineration fly ash," *Environmental Pollution and Control*, vol. 28, pp. 425–428, 2006 (Chinese).
- [55] H. Liu, S. Liang, J. Gao et al., "Enhancement of Cr(VI) removal by modifying activated carbon developed from *Zizania caduciflora* with tartaric acid during phosphoric acid activation," *Chemical Engineering Journal*, vol. 246, pp. 168–174, 2014.

Research Article

Stress Analysis of CFG Pile Composite Foundation in Consolidating Saturated Mine Tailings Dam

Jinxing Lai,¹ Houquan Liu,¹ Junling Qiu,¹ Haobo Fan,¹
Qian Zhang,² Zhinan Hu,² and Junbao Wang³

¹School of Highway, Chang'an University, Xi'an 710064, China

²School of Civil Engineering, Shijiazhuang Tiedao University, Shijiazhuang 050043, China

³School of Civil Engineering, Xi'an University of Architecture and Technology, Xi'an 710055, China

Correspondence should be addressed to Jinxing Lai; 373159626@qq.com and Haobo Fan; 739512276@qq.com

Received 27 January 2016; Revised 2 August 2016; Accepted 18 August 2016

Academic Editor: Antonio Riveiro

Copyright © 2016 Jinxing Lai et al. This is an open access article distributed under the Creative Commons Attribution License, which permits unrestricted use, distribution, and reproduction in any medium, provided the original work is properly cited.

Cement fly-ash gravel (CFG) pile is a widely used ground reinforcement technique. This paper aims to address the mechanical characteristics of CFG composite foundation in consolidating saturated mine tailings (MTs) dam. The field static load tests were employed to explore the bearing capacity of the CFG composite foundation, and finite element (FE) models in three dimensions validated through comparison with experimental results were used to discuss the pile-soil stress distribution and pile-soil stress ratio of the CFG composite foundation. The results indicate that the distribution of earth pressure and pile stress is relatively homogeneous and stable over depth and load, while the development of CFG composite foundation bearing capacity is insufficient, in which the developed bearing capacity of CFG piles is less than 50% of its characteristic value. Additionally, compared with the laboratory model test results, the pile-soil stress ratio decreases with the increasing of the load in FEM results proved to better conform to the actual engineering conditions. Furthermore, the deformation modulus and thickness of cushion exert significant influence on pile-soil stress ratio and integral bearing capacity of CFG composite foundation.

1. Introduction

Recently, as a common foundation type, composite foundation reinforcement technology has been implemented in varied engineering fields in China, such as building foundation engineering and subgrade engineering [1–5]. Simultaneously, CFG pile composite foundation has been applied in various foundation treatments engineering due to its virtue of wide application scope, quick construction, and low engineering cost [6–8]. In highway engineering, CFG pile composite foundation is commonly used in flexible foundation reinforcement; however, CFG pile composite foundation under flexible foundation will bear incomplete development of pile bearing capacity and insufficient bearing capacity of the composite foundation [9–12]. Thus, it is important to study the mechanical behaviors of composite foundation, such as load-transferring mechanism, pile-soil load sharing ratio, and pile-soil stress ratio, which can improve the bearing capacity of composite foundation.

Over the recent years, a substantial amount of studies including analytical, experimental, and numerical approaches have been conducted on CFG pile composite foundation under flexible foundation to address its mechanical behaviors. In terms of theoretical analysis, for instance, Wang et al. [13] studied the determination approach of bearing capacity of CFG pile composite foundation under railway flexible foundation. Dan et al. [14] used simple and convergent approach to deduce the computational formula for pile-soil stress ratio of CFG pile composite foundation. There are many experimental studies: for example, Han and Ren et al. [15, 16] explored the pile-soil stress ratio and pile-soil load sharing ratio through *in situ* test. Zeng et al. [17] discussed the stress distribution and friction distribution at the round of pile of CFG composite foundation in high speed railway. Ding et al. [18] researched the bearing capacity characteristics of large-size oil tank group through *in situ* test. Xue et al. [19] investigated the effects of different influence factors on the pile-soil stress ratio based on the laboratory model test.

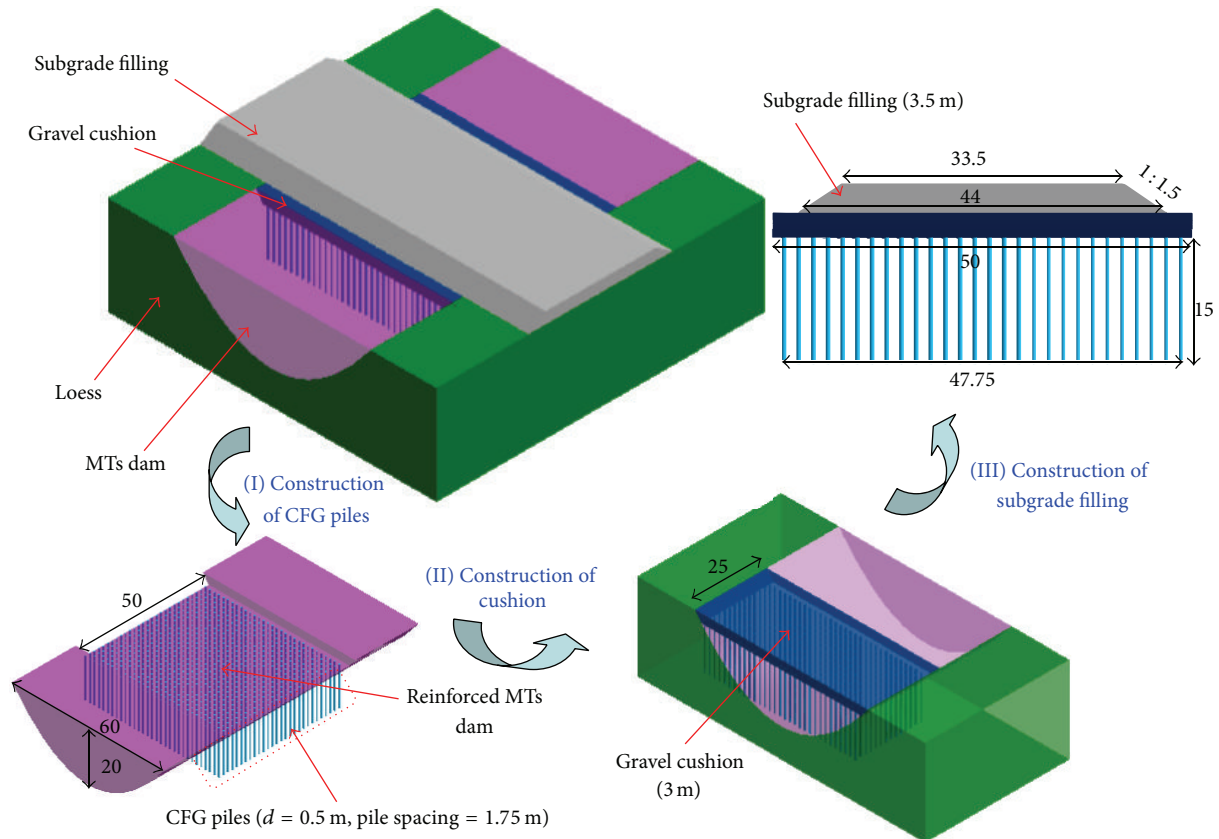


FIGURE 1: Diagram of CFG pile composite foundation (unit: m).

Numerical investigation has also been launched to study the CFG composite foundation: for instance, Wang et al. [20] conducted numerical analysis on the joint function mechanism of pile and soil and analyzed the stress distribution. Huang and Zhou [21, 22] studied the influence of different cushion parameters on pile-soil stress ratio based on FEM. The aforementioned research greatly promoted the development of CFG pile composite foundation. However, the theoretical studies and field tests on the reinforcement of saturated MTs dam are considered as a deficiency with the use of CFG pile composite foundation [23, 24]. Hence, this paper conducts a detailed analysis on the mechanical behaviors of CFG pile composite foundation in the consolidation of saturated MTs dam under embankment flexible load of an expressway.

2. Field Test of CFG Pile Composite Foundation

2.1. Engineering Overview. Shanxi Wangcheng expressway links Wangzhuangbao and Fanshi. The route design standard is bidirectional with six lanes; the design speed is 100 km/h; the subgrade width is 33.5 m, and the separate subgrade width is 16.75 m. The high demand construction quality is proposed to avoid the uncontrolled deformation.

The whole route has nine sections drilling through or passing near saturated MTs dam area, in which Yuehong

magnetic plant saturated MTs dam (a “V”-shaped MTs dam, see Figure 1) from K55 + 650 to K55 + 770 was reinforced by CFG pile composite foundation. The CFG pile length is 15 m and the pile diameter is 0.5 m with the pile spacing of 1.75 m, and the piles are distributed in square shape. Besides, the bearing capacity characteristic values were provided by the design department in the document of construction drawing according to the geological survey report and relevant criterion [26–28], in which bearing capacity characteristic value of composite foundation should not be less than 280 kPa and that of single pile should not be less than 400 kN, and the limit value of bearing capacity of soil among piles should not be less than 200 kPa. However, due to the high quality requirements of the project, the composite foundation field static load tests, including bearing capacity test of single pile composite foundation, bearing capacity test of single pile, and bearing capacity test of soil among piles, were imperative and were thus performed to explore the bearing capacity characteristics of CFG pile composite foundation. The diagram of CFG pile composite foundation is presented in Figure 1. Figure 2 shows the *in situ* conditions in various stages of construction.

2.2. Results of Field Test

2.2.1. Bearing Capacity of Composite Foundation. Static load test is presented in Figure 3. In this test, fourteen groups of CFG piles were selected to investigate the bearing capacity of

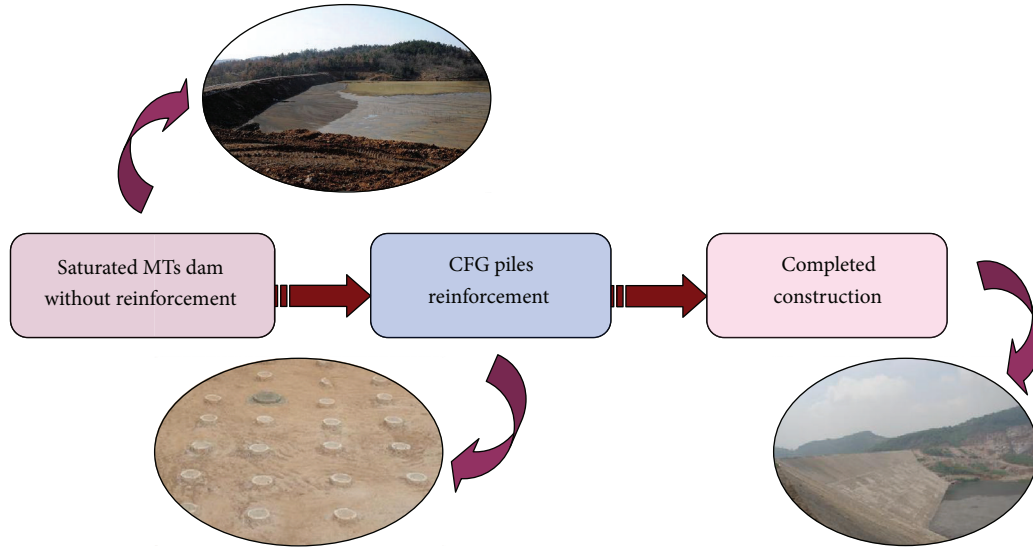


FIGURE 2: *In situ* diagrams in various construction stages.

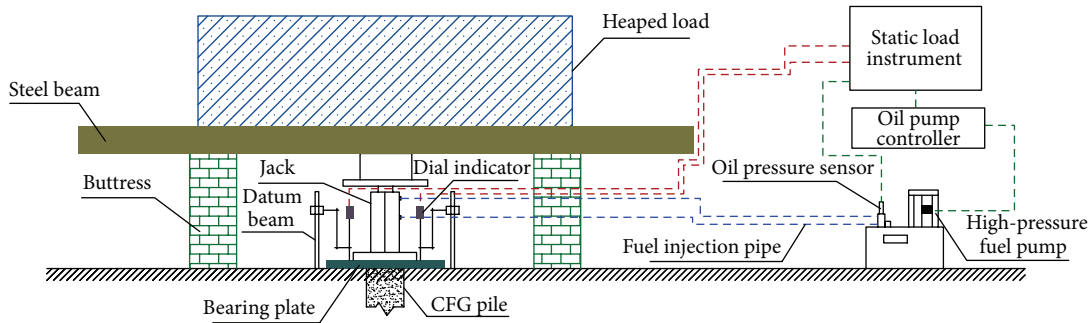


FIGURE 3: Diagram of static load test of composite foundation.

the composite foundation, and two of fourteen groups were chosen for the analysis in this study [29]. The bearing plate for the test was a square steel plate at a size of 1.75×1.75 m; loading devices were hydraulic jack, and four dial indicators were used to measure settlement. Loading increased step by step, and the loading of each step was 1/10 of total loading (2 times of designed bearing capacity); additionally, loading of the first step was two times of step loading. When the loading increased to the maximum value of 560 kPa, there was no obvious settlement; hence, loading was stopped and unloading subsequently. The P - S curve (Figure 4) illustrates that the settlement curve of CFG piles composite foundation is stable and changes slowly. According to the “JGJ79-2012, Technical Code for Treatment of Buildings” [30], the bearing capacity characteristic value of composite foundation can be determined by relative settlement approach. When the CFG piles are located at foundation of thick medium sand, the parameter $S/b = 0.008$ (where “ S ” is settlement and “ b ” represents the width of bearing plate) can be obtained. The width of bearing plate in this test is $b = 1.75$ m, and the corresponding settlement is $S = 14$ mm in Figure 4; hence,

the bearing capacity characteristic value ($f_{spk} = 526$ kPa) of CFG composite foundation can be determined based on the loading towards $S = 14$ mm. Obviously, the characteristic value of bearing capacity is much more than the designed value (280 kPa). Obviously, the design is too conservative, which will result in the increased technical inputs, higher cost of construction, and other negative results [31].

2.2.2. Bearing Capacity of Single Pile. Three groups of CFG piles were selected to carry out the single pile vertical static load test. Hydraulic jack was employed to loading step by step, and steel beam was used as antforce device. The loading of each step was 1/10 of the predicted maximum load (1500 kN). The settlement of the first nine steps was stable, while sharp settlement, sharp oil pressure fall, and pile damage occurred when loading tenth. This indicates that CFG pile is at ultimate limit state when the load reaches 1500 kN. According to the “JGJ94-2008, Technical Code for Building Pile Foundations” [28] ($R_a = Q_{uk}/K$, where Q_{uk} is single pile ultimate bearing capacity of 1350 kPa in this test and K is safety factor of 2), the bearing capacity characteristic value of single pile is

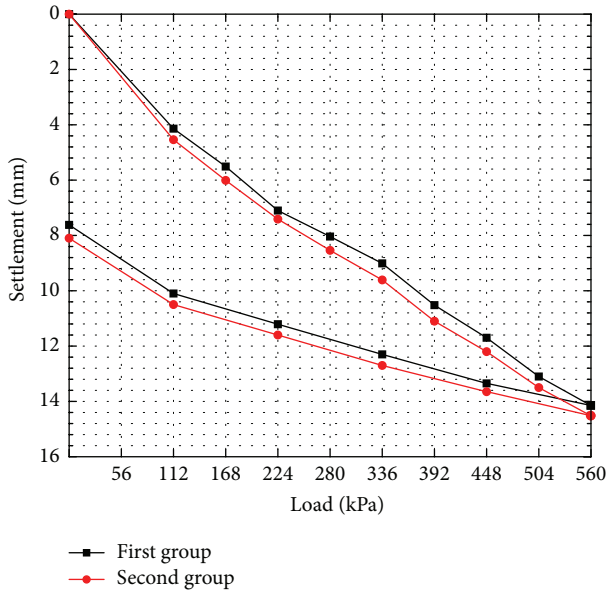


FIGURE 4: P - S curve of single pile CFG composite foundation.

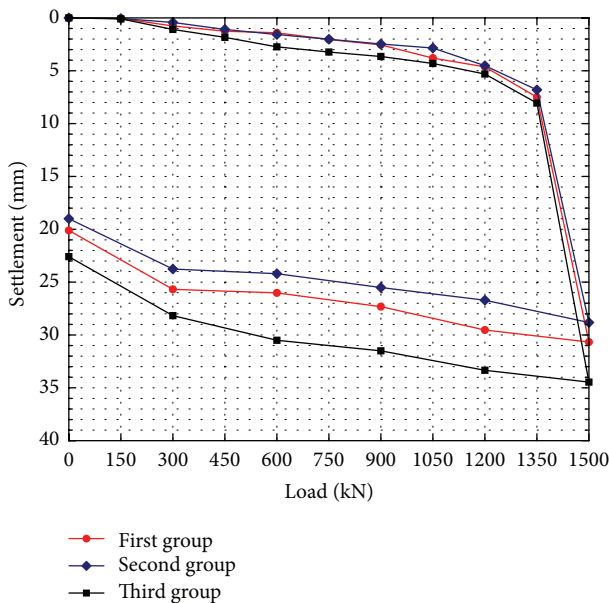


FIGURE 5: The Q - S curve of single CFG pile.

$R_a = 675 \text{ kN}$ ($>400 \text{ kN}$). The design requirements are satisfied. The Q - S curve of single CFG pile is plotted in Figure 5.

2.2.3. Bearing Capacity of Soil among Piles. Shallow plate load test was conducted to the three groups of the soil among piles. The bearing plate used in this test was a square steel plate at a size of $0.8 \times 0.8 \text{ m}$. No more than 20 mm thick coarse sand was laid under the bearing plate. Load was applied through slow loading method, and the loading of each step was 20 kPa which was 1/10 of total loading (2 times of designed bearing capacity). The first loading was two times of step loading, the maximum load was 220 kPa, and load was applied by



FIGURE 6: Field diagram of shallow flat plate static load test.

50 t oil jack. Four dial indicators were used to measure the settlement, and the field test diagram is shown in Figure 6. When the load reached 220 kPa, settlement rate of soil among piles was stable, and no sharp drop occurred. Since this load had exceeded the limit value in design (200 kPa), loading was stopped and unloading subsequently. The P - S curve of soil among piles (Figure 7) depicts that the settlement is stable and the ultimate load of soil among piles satisfies the design. However, due to the different bearing capacity of soil between piles at the test sites, a relatively large settlement happens in the second group compared with that in the first and third groups. Furthermore, since settlement sharp drop does not occur and settlement change is stable, the ultimate value of bearing capacity of soil among piles is above the maximum loading force of 220 kPa. According to “GB50007-2002, Code for Design of Building Foundation” [32], the bearing capacity characteristic value of soil among piles is $f_{sk} = 110 \text{ kPa}$ after reinforcement.

3. Numerical Analysis of CFG Pile Composite Foundation

3.1. Numerical Modeling. In this paper, MIDAS-GTS (Geotechnical and Tunnel Analysis System) software [33], which was generally employed for geotechnical analysis, was used to develop the FE analysis. MIDAS-GTS software is FEM analysis software which is developed by the MIDAS Information Technology Co., Ltd., based on the visual C++ and Windows. MIDAS-GTS software can provide the users with various analysis types, which includes nonlinear elastic plastic and construction stage analysis, unsteady seepage and stress-seepage coupling analysis, consolidation analysis, and earthquake and dynamic analysis. In this software, the graphic user interface (GUI) environment is supported during the modeling process, and the complex geometric model can be constructed in a visual environment.

To investigate the pile-soil stress and stress ratio of CFG pile composite foundation under vertical load, a three-dimensional FE modeling at a size of $14 \times 10 \times 31.5 \text{ m}$ is constructed, in which displacements are restricted at the model boundaries in the normal direction to their respective planes. In the FE modeling (Figure 8(a)), the saturated MTs and loess layers are at a depth of 25 m in total; gravel cushion is 3 m and subgrade filling is 3.5 m. Figure 8(b)

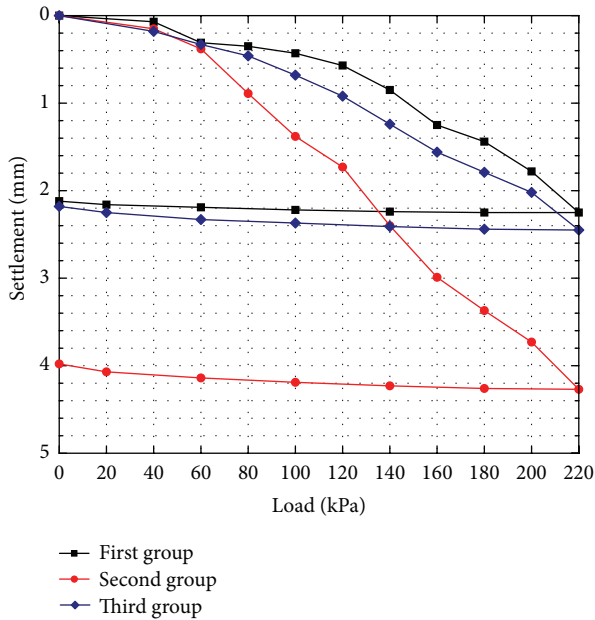


FIGURE 7: The P - S curve of soil among piles.

shows the total simulated 35 CFG piles, in which the length of CFG pile is 15 m, pile diameter is 0.5 m, and pile spacing is 1.75 m. On the other hand, the interface of all soil layers was simplified to be plane, and the soil strata in this modeling were modeled as elastoplastic materials following a Mohr-Coulomb criterion [34, 35], while the piles were assumed to be linearly elastic material. Besides, contact element was constructed between pile and soil. Analyses were performed for loading intensities of 50, 100, and 150 kPa. Furthermore, in order to study the influence of cushion parameters on pile-soil stress, different cushion thickness and deformation modulus were set to analyze pile-soil stress ratio. Soil strata parameters in this study were derived from field tests [25], and the CFG piles input parameters were typical values [21]. Modulus of deformation was employed for soil, and modulus of elasticity was used for the CFG piles. Consolidation behavior was not considered. The material properties of the various components are summarized in Table 1. Figure 8 shows integral modeling of CFG composite foundation.

3.2. Pile Stress Analysis. The FEM results of CFG piles stress and axial force distribution under the loading of 150 kPa are shown in Figure 9, in which stress of central pile, intermediate pile, side pile, and corner pile (cf. Figure 10) were selected for analysis. The variations of the CFG piles with depth and pile position are presented in Figures 11 and 12, respectively. Accordingly, the stress of single CFG pile increases and then decreases with depth increasing and the stress on pile top and pile bottom is relatively small (Figure 11). Specifically, the stress tends to increase rapidly near the top of the piles and decrease rapidly at the bottom but presents a relatively small increment at the middle of the piles. In addition, the maximum value is near pile bottom, and the position of maximum pile stress gradually moves up when the distance to

the central pile increases (Figure 9). Additionally, compared with other piles, the stress of central pile is comparatively small under the same conditions, while corner pile stress changes greatly and has the maximum stress of about 1102 kPa (Figure 11). On the other hand, as can be seen in Figure 12, the analogous stress of CFG piles is displayed at the same depth. Generally, the stress of CFG piles is uniform and stable among depth and position. However, compared to the bearing capacity characteristic value of single pile obtained from field test, it is evident that the bearing capacity utilization of CFG piles rate is less than 50%. As reported in [21], the utilization rate of bearing capacity of CFG piles only accounts for 35.3% of the ultimate bearing capacity under flexible foundation. The foregoing analysis indicates that it is difficult to make full use of the bearing capacity of CFG piles in composite foundation under flexible foundation.

3.3. Earth Pressure Analysis. The FEM results of various soil layers pressure of 150 kPa load are shown in Figure 13. The isoclines distribution in FEM results evince that the earth pressure of various soil layers is consistent and stable. Therefore, the earth pressure of the different soil layers near the central pile was selected to analyze the variation of earth pressure. The earth pressure distribution is illustrated in Figure 14. The results demonstrate that, under the different loads, the earth pressure in saturated MTs area reinforced by CFG piles shows an approximate straight-line increase with the increase of depth, and the increasing range tends to reduce with the increase of depth. Furthermore, the earth pressure in reinforced saturated MTs area causes a relatively small change during the three times loading (i.e., 50, 100, and 150 kPa), and the average value of that is 128, 139, and 165 kPa, respectively, which is smallest among the various soil layers. Hence, it is apparent that the CFG piles in saturated MTs layer have shared a certain load and obtained a good reinforcement effect. At the gravel cushion and subgrade filling layers, the soil pressure builds up with the depth at a relatively stable increasing range about 10 kPa. However, the earth pressure decreases with depth at the depth of 0.5 m to the pile top, which is because of the penetration of piles to the cushion, that is, a part of the load has been transferred to the CFG piles. Besides, at the MTs and loess layers which locate below the bottom of pile, earth pressure builds up greatly with the increase of depth compared with the reinforced MTs layer, and the increase range reaches up to around 50 kPa with the load increasing. Overall, the earth pressure of the different soil layers is stable and consistent with the change of depth and load. On the other hand, the average increasing range of earth pressure, which occurs at soil between piles during the loading for three times, is stable at 6 kPa, 11 kPa, and 26 kPa, respectively. This means that the soil between piles carries much more loads at the later period of loading, which is consistent with the results reported in [36–39]. According to the FEM results in this paper, the load sharing ratio of pile and soil is only 23%: that is, the soil among piles bears most of the loads, and the piles fail to develop their bearing capacity sufficiently. In the previous research, it is discovered that the effect of changing CFG pile parameters to improve the

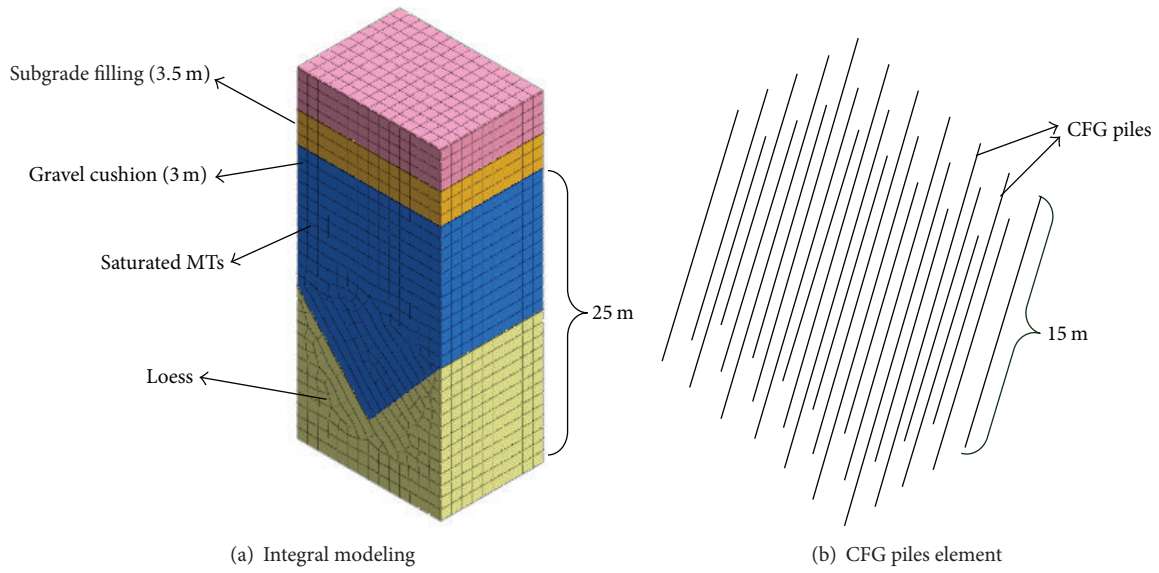


FIGURE 8: FE modeling of composite foundation and pile element.

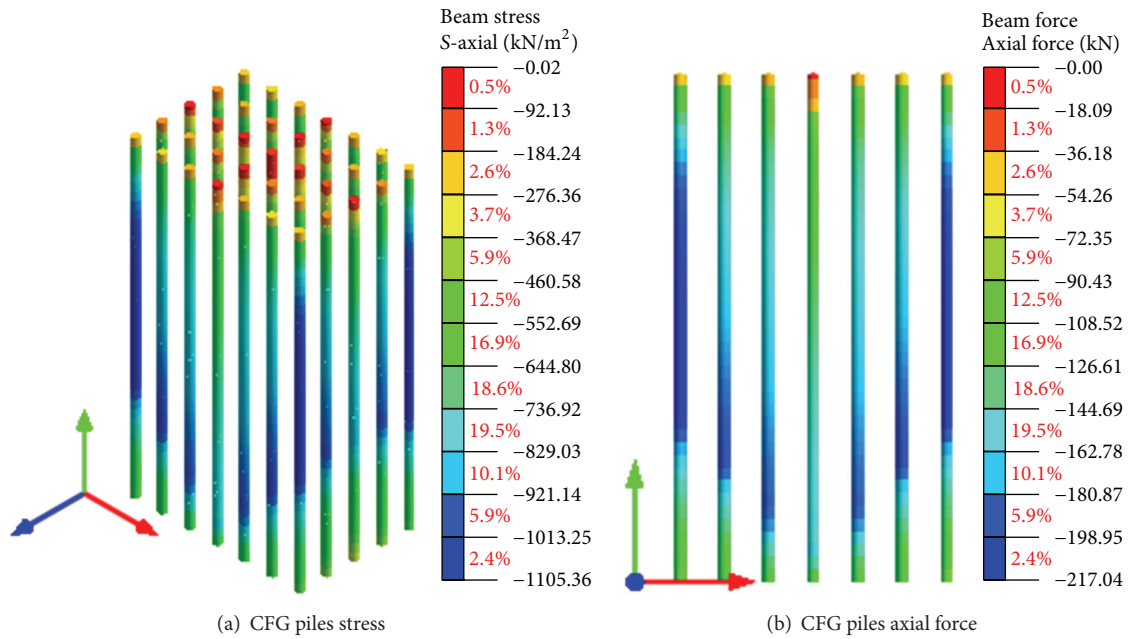


FIGURE 9: FEM results of CFG piles stress and axial force under the loading of 150 kPa.

TABLE 1: Geotechnical properties of CFG pile and soil layers [25].

Number	Material types	Modulus/MPa	Poisson's ratio	Soil unit weight/(kN/m ³)	Cohesion/kPa	Angle of internal friction/(°)
1	CFG pile	1600	0.25	21.5	900	35
2	Saturated MTs	2	0.32	18.7	7	40
3	Loess	40	0.25	20	35	45
4	Gravel cushion	140	0.16	20	0	36
5	Subgrade filling	100	0.2	19	15	20

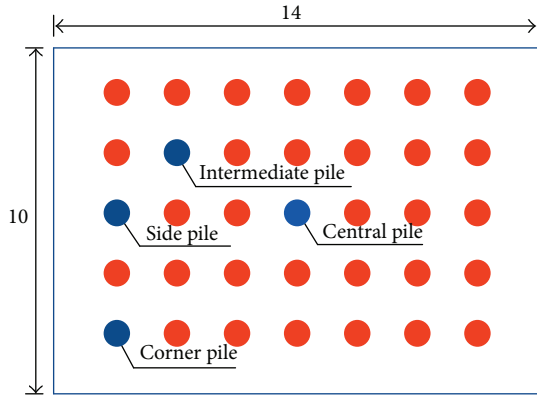


FIGURE 10: Distribution of CFG piles (unit: m).

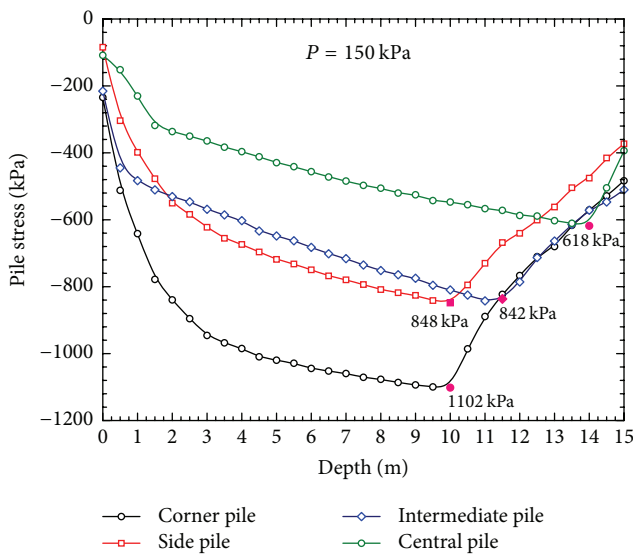


FIGURE 11: Distribution of the CFG piles stress with depth.

bearing capacity of composite foundation is not significant under flexible foundation [40–42]. However, improving the parameters of soft soil foundation and enhancing the material properties of soft soil foundation can improve the bearing capacity of composite foundation effectively. In addition, altering the connecting type of pile-cushion system will also enhance bearing capacity of composite foundation [43].

4. Comparison of the Results in Laboratory Model Test and FEM on Pile-Soil Stress Ratio

Based on the saturated MTs dam at K55 + 650–K55 + 770 sections of Wangzhuangbu-Fanshi Expressway in Shanxi, China, Xing [25] had launched laboratory model test (the model trough is at a size of $2 \times 2 \times 2$ m) on the CFG pile composite foundation with a geometric similarity ratio α_l of 10. In the laboratory model test, five different test areas were selected to study the pile-soil stress ratio of composite foundation (cf. Figure 15). The accumulation load method

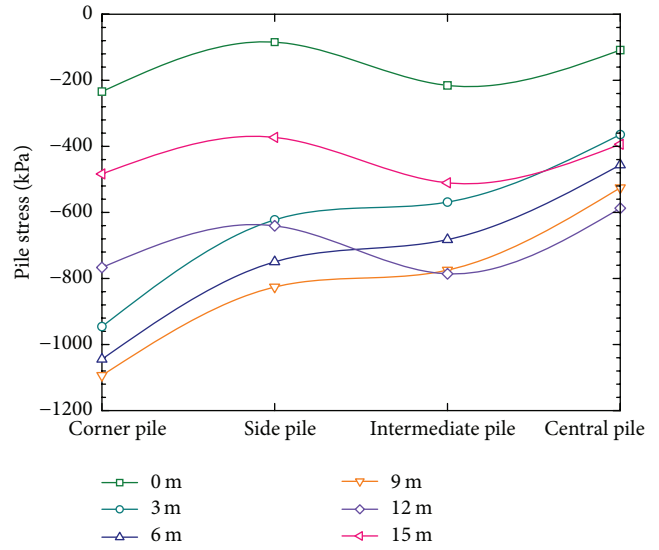


FIGURE 12: Distribution of the CFG piles stress with pile positions.

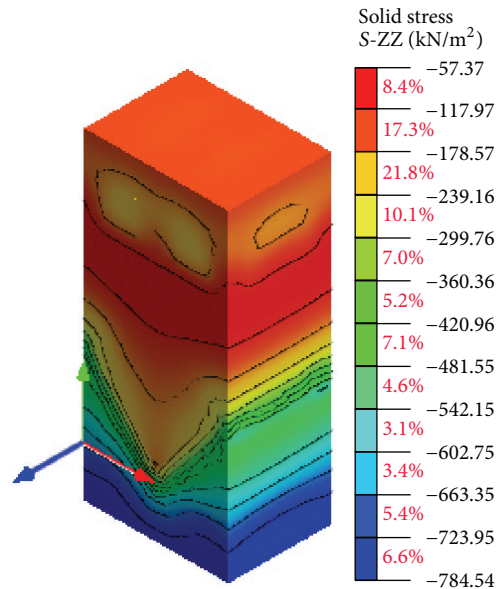


FIGURE 13: FEM results of earth pressure under the loading of 150 kPa.

was used for loading of three times, and the loads were converted based on *in situ* loads according to the similarity ratio in the model test. Figure 16 shows some of the diagrams in the model test construction. The results of pile-soil stress ratio in laboratory test are compared with that in FEM, which is shown in Figure 17.

In the laboratory model test (Figure 17), the pile-soil stress ratio increases with the increase of load and the average value of stress ratio in different test areas for three times loading is 2.0, 2.1, and 3.7, respectively. It is apparent that the increasing range of pile-soil stress ratio in later period of loading is larger than that in earlier period, which indicates that the load shared by the pile increases gradually with the increase of loading, and the bearing capacity of pile

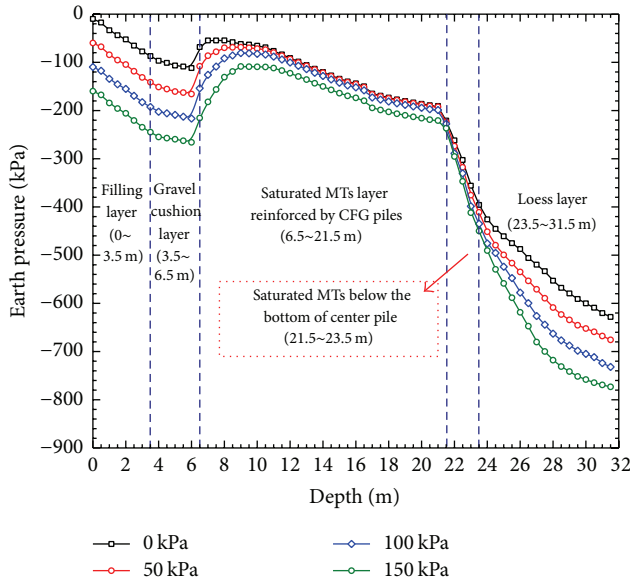


FIGURE 14: Distribution of the earth pressure with depth.

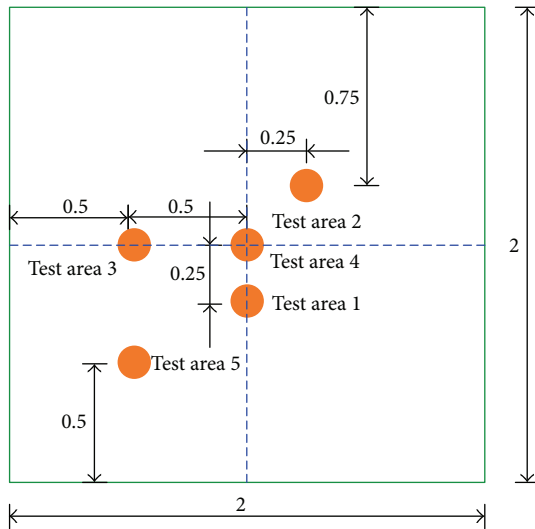


FIGURE 15: Diagram of CFG pile model test area (unit: m).

is gradually developed. While in the FEM results, pile-soil stress ratio gradually reduces with the increase of load, and the average value of stress ratio in the various test areas for three times loading is 3.6, 3.1, and 2.3, respectively. The pile-soil stress ratio is much larger at the earlier period of loading, while it tends to decrease with the increase of loading, which has a good agreement with the results reported in [36, 37]. Furthermore, field measurement result of the pile-soil stress ratio is 1.1~1.7, 1.1~1.6, and 1.18~2.26, respectively [44~46], and the recommended value in “JTJ 017-96, technical specifications for design construction of highway embankment on soft ground” is 3~6 [47]. Thus, the pile-soil stress ratio in laboratory model test and FEM are close to the actual conditions. On the other hand, the pile-soil stress ratio is variable among different test areas with

a small change in the laboratory model test, in which the maximum value of pile-soil stress ratio occurs in test area 3, while the minimum value happens in test areas 1 and 2. Simultaneously, the pile-soil stress ratio in FEM increases gradually with the increase of the distance to the central pile, and the pile-soil stress ratio of central pile (test area 3) is the smallest. According to the results in the laboratory model test and FEM, the settlement increases with the distance to central pile decrease [25, 48]. The greater settlement will result in a wider scope of negative friction area, and more loads will be carried by soil among piles [36, 37]. Hence, the pile-soil stress ratio increases with the increase of distance to the central pile in FEM which conforms to practical engineering situation.

Overall, there is a great difference of the variation of pile-soil stress ratio between the laboratory model test and FEM, in which the opposite variation trend with load is observed. The thickness of gravel cushion in actual engineering is 3 m, while that in actual engineering in laboratory model test is 0.05 m. However, based on geometric similarity ratio ($\alpha_l = 10$), the thickness of cushion in model test should be 0.3 m, with the addition of the indeterminacy of model test. Hence, it is concluded that the FEM results are closer to the actual situations by referring to the previous research results. Furthermore, based on the results in laboratory model test and FEM, the pile-soil stress of composite foundation is smaller than the recommended value 3~6 [47]. Hence, the development of bearing capacity of CFG pile in composite foundation of saturated MTs dam after CFG pile treatment can be further improved.

5. Influence of Cushion Parameters on the Properties of Bearing Capacity of CFG Pile Composite Foundation

It is effective to improve the development of CFG piles bearing capacity in composite foundation by changing the parameters of cushion [49~52]. Therefore, in order to investigate the influence of cushion parameters on pile-soil stress ratio, variations of pile-soil stress ratio in test areas 4 (smallest stress ratio, cf. Figure 15) and 5 (largest stress ratio) are discussed.

5.1. The Influence of the Cushion Thickness on Bearing Capacity of CFG Composite Foundation. Pile-soil stress ratio decreases with the increase of cushion thickness (cf. Figure 18, the cushion deformation modulus is $E_0 = 140$ MPa). And when the thickness reaches about 1 m, the whole curve has an obvious inflection point, which demonstrates that when the range of cushion thickness is between 0.1 and 1 m, pile-soil stress ratio decreases greatly with the increase of thickness, and the amplitude decreases with the increase of thickness. However, when the cushion thickness is 1~3 m, the changes of pile-soil stress ratio are sufficiently small with increase of thickness, which illustrates that the bearing capacity of pile obtains a better exertion with a thinner thickness. Hence, the 3 m thickness of cushion in design plan should be decreased to about 1 m, which can not only satisfy the waterproof requirement of highway subgrade, but also improve the

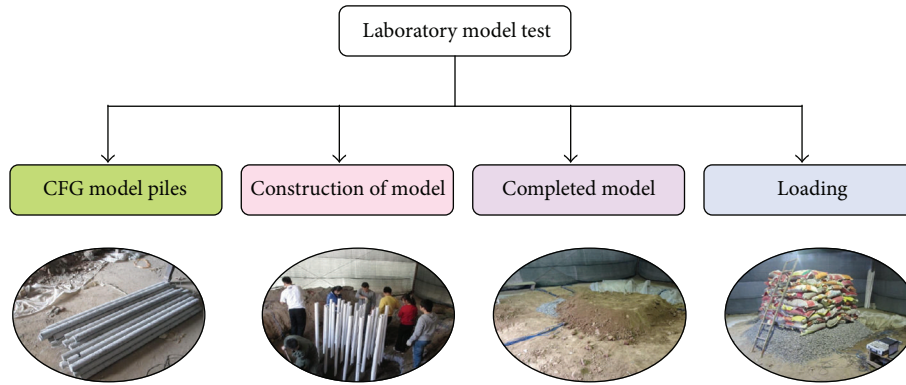


FIGURE 16: Construction of laboratory model test [25].

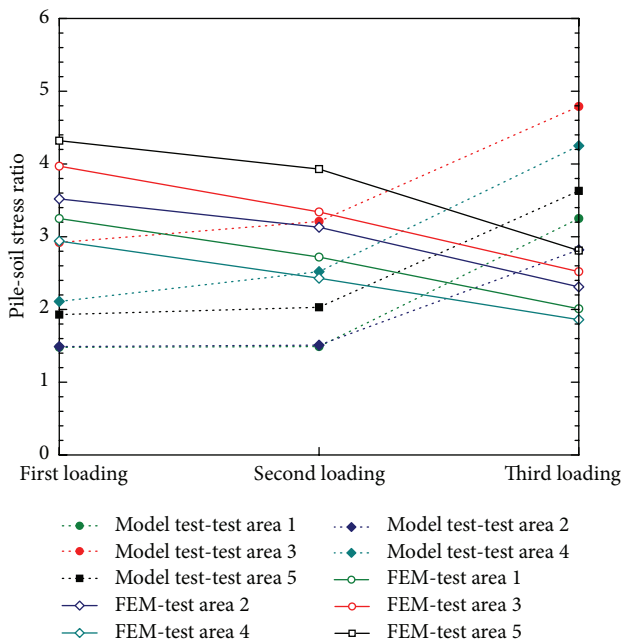


FIGURE 17: The results of pile-soil stress ratio in model test and FEM.

bearing capacity of composite foundation greatly. On the other hand, the influence of cushion thickness on the pile-soil stress ratio in later loading period is greater than that in earlier loading period, and the influence of cushion thickness on the pile-soil stress ratio in test area 5 is smaller than that in test area 4. This is because of the negative friction of pile which has more effect in test area 4. Therefore, it is recommended that the bearing capacity of composite foundation can be improved by enhancing the compactness in test area 4 (the central area of subgrade, cf. Figure 15).

5.2. *The Influence of Cushion Deformation Modulus on the Bearing Capacity of CFG Composite Foundation.* Curve of pile-soil stress ratio over cushion deformation modulus (Figure 19, cushion thickness is 1 m) demonstrates that pile-soil stress ratio increases with the increase of cushion deformation modulus, which is small relatively when deformation

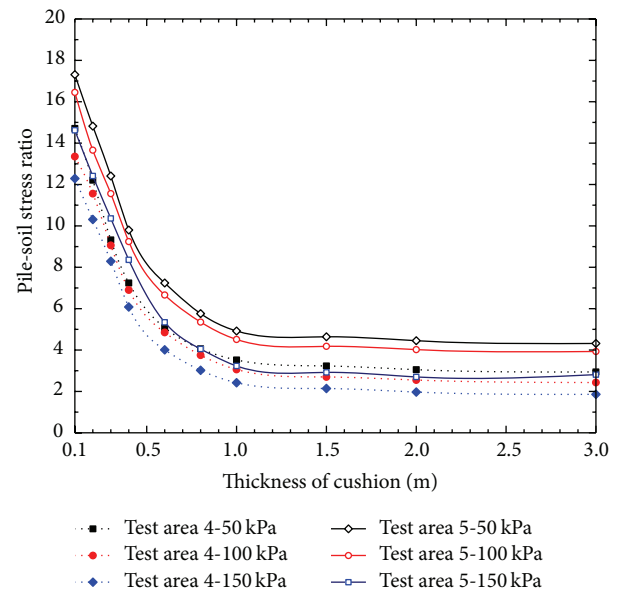


FIGURE 18: Effect of cushion thickness on pile-soil stress ratio curve.

modulus is below 120 MPa and then increases rapidly when the deformation modulus range is between 120 and 160 MPa. When the deformation modulus is larger than 160 MPa, the increasing range is relatively small and the pile-soil stress ratio tends to be stable. As the cushion deformation modulus gradually increases, the effect of pile negative friction gradually decreases, and the loads gradually transform to pile; hence, the pile-soil ratio gradually increases. Furthermore, when the cushion deformation modulus is small relatively, the effect of negative friction is much great and the influence of deformation modulus on the pile-soil ratio is unobvious. However, when the deformation modulus increases to about 120 MPa, the effect of negative friction becomes small gradually, and the increasing range of pile-soil stress ratio became larger. When the deformation modulus reaches about 180 MPa, the effect of negative friction is sufficiently small; thus, the pile-soil stress ratio tends to be stable with the further increase of cushion deformation modulus. These results demonstrate that bearing capacity of CFG pile can

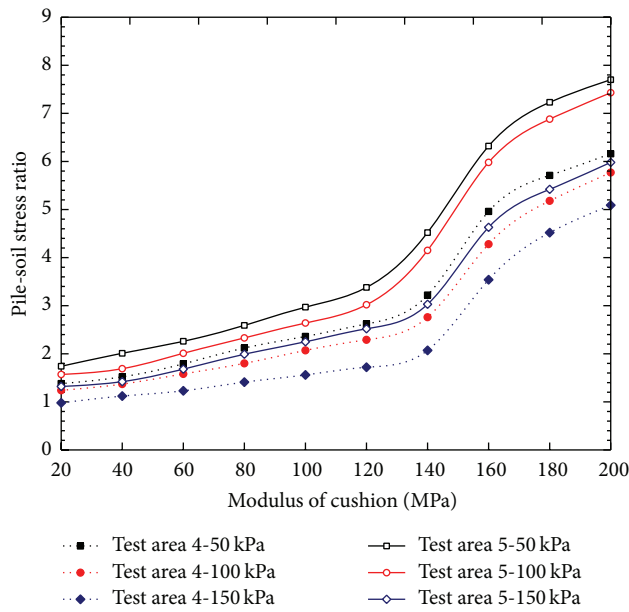


FIGURE 19: Effect of cushion thickness on pile-soil stress ratio.

be enhanced by improving cushion deformation modulus. However, the influence of cushion deformation modulus on the bearing capacity is not obvious when the cushion deformation modulus increases to a certain extent. It is reasonable to increase the cushion deformation modulus to about 200 MPa. Thus, the deformation modulus of gravel cushion adopted in construction is relatively small, which is unfavorable for the development of bearing capacity of CFG pile.

6. Conclusions

This paper studied the mechanical characteristics of CFG composite foundation in the application of saturated MTs dam. The field static load tests were carried out to investigate the bearing capacity of the CFG composite foundation, and FE modeling in three dimensions validated through comparison with experimental results were used to discuss the pile-soil stress distribution and pile-soil stress ratio of the CFG composite foundation. Furthermore, the effects of cushion on the CFG composite foundation pile-soil ratio were studied. Based on the foregoing mechanical characteristics studies, some of the main findings are summarized as follows.

(1) In the field tests, the bearing capacity characteristic value of CFG composite foundation is $f_{spk} = 526$ kPa and that of single pile is $R_a = 675$ kN, which are proved to be much more than the designed value. The results uncover the fact that the development the bearing capacity of CFG composite foundation is insufficient because of the relatively conservative designed value.

(2) According to the FEM results, it is confirmed that the distribution of CFG piles stress is uniform and stable over depth and position, stress on pile top and pile bottom is small, and the maximum value is near pile bottom. Furthermore, the exertion degree of bearing capacity of pile is lower than 50%.

On the other hand, the earth pressure is homogeneous with depth and load in each soil layer. Especially in the reinforced MTs area, due to the good reinforcement effect of CFG piles, the reinforced MTs layer has a more small earth pressure and increase range. Furthermore, load sharing ratio of soil between piles at the later period of loading is much larger than that at the earlier period of loading.

(3) Comparing the results in FEM and laboratory model test, the magnitude of pile-soil stresses is similar, while their changes trends with load are opposite and the pile-soil stress ratio decreases with the increase of load in FEM which is much close to the actual engineering.

(4) According to the FEM results, when the thickness of cushion is less than 1 m, it exhibits significant influence on the pile-soil stress ratio, and the stress decreases approximately linearly with the increase of thickness. However, when the thickness is more than 1 m, pile-soil stress ratio has slight changes with thickness. Therefore, the bearing capacity of CFG composite foundation can be improved when the cushion thickness reduces to about 1 m.

(5) Cushion deformation modulus has significant influence on the pile-soil stress ratio, which increases with the increasing of cushion deformation modulus. Furthermore, the influence of cushion deformation modulus on pile-soil stress ratio is different due to the different effect degree of negative friction. Large cushion deformation modulus around 200 MPa should be set to improve the pile-soil stress ratio in the CFG composite foundation, simultaneously, to enhance the bearing capacity of composite foundation.

Although the utilization of CFG composite foundation in saturated MTs dam has obtained a good consolidation effect, the bearing capacity of CFG composite foundation can be further improved in pursuit of a more effective consolidation according to the results in this study. Additionally, increasing of strength and rigidity of CFG pile has little effect on improving the bearing capacity of composite foundation, while improving the material parameters of soft foundation and changing the connecting type among cushion; pile and soil are effective in the improvement of bearing capacity of composite foundation. Hence, further research should focus on the aforementioned two aspects.

Competing Interests

The authors declare that there is no conflict of interests regarding the publication of this paper.

Acknowledgments

This work is financially supported by the Special Fund for Basic Scientific Research of Central Colleges of Chang'an University (Grant no. 310821165011) and the Key Industrial Research Project of Shaanxi Provincial Science and Technology Department (Grant no. 2015GY185) and the Integrated Innovation Project of Shaanxi Provincial Science and Technology Department (Grant no. 2015KTZDGY01-05-02) and the Brainstorm Project on Social Development of Shaanxi

Provincial Science and Technology Department (Grant no. 2016SF-412).

References

- [1] F. Song, J.-M. Zhang, and G.-R. Cao, "Experimental investigation of asymptotic state for anisotropic sand," *Acta Geotechnica*, vol. 10, no. 5, pp. 571–585, 2015.
- [2] A. Hegde and T. G. Sitharam, "3-Dimensional numerical modelling of geocell reinforced sand beds," *Geotextiles and Geomembranes*, vol. 43, no. 2, pp. 171–181, 2015.
- [3] M. Zhou, W. C. Yuan, and Y. Zhang, "Seismic material properties of reinforced concrete and steel casing composite concrete in elevated pile-group foundation," *Polish Maritime Research*, vol. 22, no. 1, pp. 141–148, 2015.
- [4] X. L. Weng, Y. T. Nie, and J. Y. Lu, "Strain monitoring of widening cement concrete pavement subjected to differential settlement of foundation," *Journal of Sensors*, vol. 2015, Article ID 679549, 7 pages, 2015.
- [5] C. Zhang, X. Chen, W. Fan, and J. Zhao, "A new unified failure criterion for unsaturated soils," *Environmental Earth Sciences*, vol. 74, no. 4, pp. 3345–3356, 2015.
- [6] X. N. Gong, "Development of composite foundation in China," in *Soil Mechanics and Geotechnical Engineering*, vol. 1, p. 201, A A Balkema, 1999.
- [7] M. L. Yan, C. L. Wu, and J. Yang, "Study on the composite foundation with cement-flyash-gravel pile," *Chinese Journal of Geotechnical Engineering*, vol. 18, no. 2, pp. 56–62, 1996.
- [8] C. L. Zhang, G. L. Jiang, X. F. Liu, and Z. Wang, "Deformation performance of cement-fly ash-gravel pile-supported embankments over silty clay of medium compressibility: a case study," *Arabian Journal of Geosciences*, vol. 8, no. 7, pp. 4495–4507, 2014.
- [9] J. W. Duan, X. N. Gong, and G. X. Zeng, "Load transfer behavior of cement treated soil column," *Chinese Journal of Geotechnical Engineering*, vol. 16, no. 4, pp. 2–7, 1994.
- [10] J. T. Shahu, M. R. Madhav, and S. Hayashi, "Analysis of soft ground-granular pile-granular mat system," *Computers and Geotechnics*, vol. 27, no. 1, pp. 45–62, 2000.
- [11] H. F. Schweiger and G. N. Pande, "Numerical analysis of stone column supported foundations," *Computers and Geotechnics*, vol. 2, no. 6, pp. 347–372, 1986.
- [12] Y. R. Lv, H. L. Liu, C. W. W. Ng, X. Ding, and A. Gunawan, "Three-dimensional numerical analysis of the stress transfer mechanism of XCC piled raft foundation," *Computers and Geotechnics*, vol. 55, pp. 365–377, 2014.
- [13] L. Wang, G. Ding, S. Liu, X. Chen, and Y. Shen, "Study on the determination method for the bearing capacity of CFG pile composite foundation under the flexible foundation in railway," *China Railway Science*, vol. 29, no. 6, pp. 12–17, 2008.
- [14] H. Dan, L. Li, L. Zhao, and F. Wang, "Calculation and influence factors analysis on pile-soil stress ratio of CFG pile composite foundation," *China Railway Science*, vol. 29, no. 5, pp. 7–12, 2008.
- [15] Y. S. Han, H. X. Bai, and R. W. Lian, "Cushion influence on bearing capacity of composite foundation with cement-flyash-gravel piles," *Chinese Journal of Rock Mechanics and Engineering*, vol. 23, no. 20, pp. 3498–3403, 2004.
- [16] P. Ren, R.-G. Deng, and Z.-Q. Yu, "Experimental research on composite foundations with CFG piles," *Rock and Soil Mechanics*, vol. 29, no. 1, pp. 81–86, 2008.
- [17] C. J. Zeng, J. W. Zhang, and X. D. Tong, "In-situ test of stress characteristics of CFG pile composite foundation of high-speed railway," *Journal of the China Railway Society*, vol. 33, no. 5, pp. 92–95, 2011.
- [18] X. J. Ding, X. Wang, and Y. J. Zhang, "Experimental study of bearing and deformation features of CFG-pile composite ground for large oil storage tanks," *Chinese Journal of Rock Mechanics and Engineering*, vol. 32, no. 9, pp. 1852–1856, 2013.
- [19] X. H. Xue, Y. X. Wei, G. X. Yang et al., "Laboratory model test study on CFG pile composite foundation," *China Railway Science*, vol. 33, no. 2, pp. 8–12, 2012.
- [20] S. J. Wang, M. C. He, C. Z. Zhu et al., "Research on bearing properties of composite foundation integrated by CFG piles and gravel piles," *Rock and Soil Mechanics*, vol. 33, no. 2, pp. 2632–2636, 2008.
- [21] S.-G. Huang, "Test study and finite element analysis of CFG composite foundation," *Rock and Soil Mechanics*, vol. 29, no. 5, pp. 1275–1279, 2008.
- [22] A.-J. Zhou and B. Li, "Experimental study and finite element analysis of cushion in CFG pile composite foundation," *Rock and Soil Mechanics*, vol. 31, no. 6, pp. 1803–1808, 2010.
- [23] R. Chen, I. Lee, and L. Y. Zhang, "Biopolymer stabilization of mine tailings for dust control," *Journal of Geotechnical and Geoenvironmental Engineering*, vol. 141, no. 2, Article ID 04014100, 2015.
- [24] R. Chen, L. Y. Zhang, and M. Budhu, "Biopolymer stabilization of mine tailings," *Journal of Geotechnical and Geoenvironmental Engineering*, vol. 139, no. 10, pp. 1802–1807, 2013.
- [25] Y. R. Xing, *The model test of saturated tailing ore foundation which treated by CFG piles [Ph.D. thesis]*, Chang'an University, Xi'an, China, 2014.
- [26] *Construction Drawing Document of Shanxi Wangcheng Expressway Engineering Project*, CCCC First Highway Consultants, Xi'an, China, 2011.
- [27] *Geological Survey Report of Shanxi Wangcheng Expressway Engineering Project*, CCCC First Highway Consultants Co. Ltd, Xi'an, China, 2011.
- [28] JGJ94-2008, *Technical Code for Building Pile Foundations*, China Architecture & Building Press, Beijing, China, 2008.
- [29] Z. Li, "Analysis of bearing capacity of CFG pile composite foundation by in-situ test," Research Report, Chang'an University, Xi'an, China, 2014.
- [30] JGJ79-2012, *Technical Code for Treatment of Buildings*, China Architecture & Building Press, Beijing, China, 2012.
- [31] L. Zhang, "Study of method for determining bearing capacity of composite foundation by in-situ loading test," *Rock and Soil Mechanics*, vol. 35, no. 2, pp. 241–249, 2014.
- [32] GB50007-2002, *Code for Design of Building Foundation*, China Architecture & Building Press, Beijing, China, 2002.
- [33] Midas, *Midas/GTS (Geotechnical and Tunnel Analysis System) Reference Manual for Modeling, Integrated Design and Analysis*, Midas Corporation, 2013.
- [34] H. Jiang, "Failure criteria for cohesive-frictional materials based on Mohr-Coulomb failure function," *International Journal for Numerical and Analytical Methods in Geomechanics*, vol. 39, no. 13, pp. 1471–1482, 2015.
- [35] J. X. Lai, S. Mao, J. L. Qiu et al., "Investigation progresses and applications of fractional derivative model in geotechnical engineering," *Mathematical Problems in Engineering*, vol. 2016, Article ID 9183296, 15 pages, 2016.
- [36] J. C. Ekstrom, J. A. Berntsson, and G. B. Sallfors, "Test fills of clays stabilized with cement columns," in *Proceedings of the*

13th International Conference on Soil Mechanics and Foundation Engineering (ICSMFE '94), pp. 1183–1186, New Delhi, India, 1994.

- [37] Y. K. Chow, J. T. Chin, and S. L. Lee, “Negative skin friction on pile groups,” *International Journal for Numerical and Analytical Methods in Geomechanics*, vol. 14, no. 2, pp. 75–91, 1990.
- [38] J. X. Lai, J. L. Qiu, Z. H. Feng, J. Chen, and H. Fan, “Prediction of soil deformation in tunnelling using artificial neural networks,” *Computational Intelligence and Neuroscience*, vol. 2016, Article ID 6708183, 16 pages, 2016.
- [39] J. Lai, H. Fan, J. Chen, J. Qiu, and K. Wang, “Blasting vibration monitoring of undercrossing railway tunnel using wireless sensor network,” *International Journal of Distributed Sensor Networks*, vol. 2015, Article ID 703980, 7 pages, 2015.
- [40] X.-N. Gong, “Generalized composite foundation theory and engineering application,” *Chinese Journal of Geotechnical Engineering*, vol. 29, no. 1, pp. 1–13, 2007.
- [41] W. J. Xue, L. B. Wang, and D. Wang, “A prototype integrated monitoring system for pavement and traffic based on an embedded sensing network,” *IEEE Transactions on Intelligent Transportation Systems*, vol. 16, no. 3, pp. 1380–1390, 2015.
- [42] W. J. Xue, E. Weaver, L. B. Wang, and Y. Wang, “Influence of tyre inflation pressure on measured pavement strain responses and predicted distresses,” *Road Materials and Pavement Design*, vol. 17, no. 2, pp. 328–344, 2016.
- [43] J.-J. Zheng, S. W. Abusharar, and X.-Z. Wang, “Three-dimensional nonlinear finite element modeling of composite foundation formed by CFG-lime piles,” *Computers and Geotechnics*, vol. 35, no. 4, pp. 637–643, 2008.
- [44] G.-W. Li and T. Yang, “Field experimental study on pile-soil stress ratio of composite ground under flexible foundation,” *Rock and Soil Mechanics*, vol. 26, no. 2, pp. 265–269, 2005.
- [45] H. M. Wu and X. N. Gong, “Model tests on composite ground under soft and stiff foundation,” *China Civil Engineering Journal*, vol. 34, no. 5, pp. 81–83, 2002.
- [46] H. Zhang, Y. F. Zhou, B. A. Wan et al., “In-situ test of pile-soil stress ratio of CFG pile composite foundation under embankment load,” *Journal of Highway and Transportation Research and Development*, vol. 28, no. 9, pp. 6–10, 2011.
- [47] JTJ017-96, *Technical Specifications for Design and Construction of Highway Embankment on Soft Ground*, China Communications Press, Beijing, China, 1996.
- [48] J. Lai, H. Liu, J. Qiu, and J. Chen, “Settlement analysis of saturated tailings dam treated by CFG pile composite foundation,” *Advances in Materials Science and Engineering*, vol. 2016, Article ID 7383762, 10 pages, 2016.
- [49] F.-Y. Liang, L.-Z. Chen, and X.-G. Shi, “Numerical analysis of composite piled raft with cushion subjected to vertical load,” *Computers and Geotechnics*, vol. 30, no. 6, pp. 443–453, 2003.
- [50] W. J. Xue and E. Weaver, “Influence of tyre configuration on pavement response and predicted distress,” *International Journal of Pavement Engineering*, vol. 16, no. 6, pp. 538–548, 2015.
- [51] G.-L. Ding, L.-J. Wang, and S.-C. Liu, “Effect of cushion thickness on deformation characteristics of CFG pile composite foundation with caps under flexible load,” *Chinese Journal of Geotechnical Engineering*, vol. 31, no. 7, pp. 997–1001, 2009.
- [52] Y. Xie and X. Yang, “Characteristics of a new-type geocell flexible retaining wall,” *Journal of Materials in Civil Engineering*, vol. 21, no. 4, pp. 171–175, 2009.

Research Article

An Experimental Study on the Water-Induced Strength Reduction in Zigong Argillaceous Siltstone with Different Degree of Weathering

Yu-chuan Yang,¹ Jia-wen Zhou,¹ Fu-gang Xu,² and Hui-ge Xing³

¹State Key Laboratory of Hydraulics and Mountain River Engineering, Sichuan University, Chengdu 610065, China

²College of Water Resources and Hydropower, Sichuan University, Chengdu 610065, China

³College of Architecture and Environment, Sichuan University, Chengdu 610065, China

Correspondence should be addressed to Hui-ge Xing; hgxing@scu.edu.cn

Received 13 April 2016; Accepted 14 August 2016

Academic Editor: Giorgio Pia

Copyright © 2016 Yu-chuan Yang et al. This is an open access article distributed under the Creative Commons Attribution License, which permits unrestricted use, distribution, and reproduction in any medium, provided the original work is properly cited.

The water-softening property of soft rocks is a key problem in geotechnical engineering. A typical red-bed soft rock (the Zigong argillaceous siltstones) with different weathering degree is selected as an example to study the water-softening property and the influence of degree of weathering. A series of mechanical and microstructure tests are carried out to analyze the weathering characteristics and mechanism of the Zigong argillaceous siltstones. The results of mechanical experiments reveal that the water content and the weathering degree of rock specimens both have a weakening effect on the compressive and shear strengths. According to the results of present microstructure tests, the mechanical properties of the Zigong argillaceous siltstones are closely correlated with their physical properties, including internal microstructure and material composition for highly weathered rocks or moderately weathered rocks (in both natural and saturation conditions). Finally, experimental results indicate that the changes of microstructure and internal materials are two main factors that influence rock strength parameters after contacting with water and that these properties reflect the rock weathering degree. In a word, when red-bed soft rocks are encountered in geotechnical engineering, special attention should be paid to presence of water.

1. Introduction

There are many types of red-bed soft rocks such as red siltstone and red mudstone, which are widely distributed at the Sichuan basin, the Shanganning basin, the Yunnan plateau, and other places in China [1]. The Sichuan Province belongs to typical inland basin known as “Red Basin,” and the elevations of the inland basin are about 200 m to 750 m with hilly regions as the main geomorphic units. It is generally believed that the iron element in rocks is oxidized to trivalent iron due to the strong oxidation, which is the reason of forming the red appearance [2, 3]. Among these areas, the basis formation condition of red-bed rocks is the proper geomorphological environment with dry and hot paleoclimate, weathering conditions, and rich sediments source from mountains. The different forming conditions, tectonic activity, and climate lead

to the differences of the red-bed rocks in colors, microstructure, mineral composition, weathering degree, and others [3]. The widely distributed red-bed rocks have special mechanical properties (especially for the soft rocks) and are often encountered during the construction process of civil engineering. However, the red-bed soft rocks are mostly exposed below the ground surface and are sensitive to the water; therefore the water-softening and weathering are two main problems for the red-bed soft rocks.

In geotechnical engineering, the water-softening effect on mechanical properties of the soft rock is one of the important theoretical and practical problems. Among Southwest China, most red beds belong to soft rocks' category because its physical and mechanical properties are very poor relatively [1, 2, 4]. Such rocks have lower strength (saturated uniaxial compressive strength of rock mass less than 30 MPa), larger porosity,

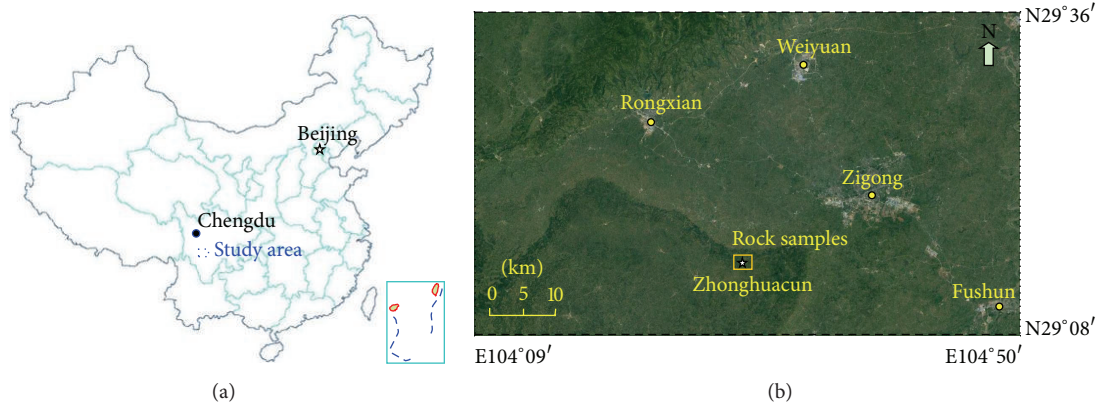


FIGURE 1: Location of the test samples for red-bed soft rock: (a) site location of the study area and (b) the Zigong argillaceous siltstone samples are collected from the Zhonghuacun reservoir area.

and poorer cementation degree than hard rocks [4]. The lithologies of red beds are mainly sandstone, siltstone, silty mudstone, argillaceous siltstone, shale, or claystone. When they encounter water, the red beds commonly develop many engineering problems such as erosion, seepage, and softening [2, 3, 5]. With the development of engineering construction in the red-bed areas, more researchers begin to pay more attention to the physical and mechanical properties of soft rocks [2, 5–10]. For example, Arnould (2006) analyzed the reasons of mudstone easily disintegrating from the perspective of mudstone internal mineral composition and microstructure [6]. Chen et al. (2014) studied a shallow progressive landslide developed in loose deposits of red beds by analyzing mechanical properties of the main slip zone and its microstructure using polarising microscopy (PM) and scanning electron microscope (SEM) techniques [2]. In order to study the features of rock-water interaction of natural soft rock, Guo et al. (2015) analyzed the hydrophilic characteristics at high stress state combining X-ray diffraction and mercury injection tests [7].

Previous studies have revealed that water is the most notable factor lowering rock strength, but few works focused on the relationship of the water-softening properties with the microscopic softening mechanism, which can be analyzed based on its microstructure change law for rock mass with different degree of weathering. This paper treated the Zigong argillaceous siltstone as a special example of red-bed soft rock, which is a common soft rock encountered in geotechnical engineering. A series of mechanical and microstructure tests were carried out to study the water-softening properties of the Zigong argillaceous siltstone under different degree of weathering, some useful conclusions are presented in this paper.

2. Material and Methods

2.1. Material. The argillaceous siltstone is selected from the Zhonghuacun reservoir (E104°32'56'', N29°15'8''), locating at Zhonghuacun, Gongjing District, Zigong City, Sichuan Province, China (as shown in Figure 1). The Zhonghuacun

dam site lies about 25 km from the Zigong City. The reservoir is a small water project offering emergency backup water source of Gongjing District, Zigong City. The irrigation area of the reservoir is $6.986 \times 10^6 \text{ m}^2$.

By some test pits and vertical boreholes, horizontal geological tunnels for geological survey works, the Zigong argillaceous siltstone was collected in different drilling depths. According to drilling results, the drilling depths of the highly and moderately weathered argillaceous siltstones are about 5–13 m and 15–25 m as shown in Figures 2(b) and 2(c), respectively. The diagenesis of natural argillaceous siltstones is poor, so it is easy to cause weathering fissures for depositional interface. When water enters its internal pores, the rock can produce inflation and softening phenomenon easily.

Furthermore, the physical and mechanical properties of rock mass often depend on its material compositions. Test results indicate that the elemental composition of the highly and moderately weathered Zigong argillaceous siltstones contain a lot of soluble salts, and there are many soluble cements with chemically active elements such as K, Na, and Fe (as shown in Figure 3). The argillaceous siltstones mainly consist of the ten elements such as O, Si, C, Ca, Al, Fe, K, Mg, Na, and Ti. For the moderately weathered rock, the content of four elements O, Si, C, and Ca reaches 89.22% and the minimum content is 3.25% for the four elements K, Mg, Na, and Ti (Figure 3(a)). For the highly weathered rock, the content of three elements O, Al, and Fe increases to 64.52% from 55.26%, while the content of two elements C and Ca decreased significantly to 7.43% from 16.92% because of the destruction of some carbon skeletons and decomposition of calcium carbonate (Figure 3(b)). Elemental compositions results show that the elemental composition changes with the degree of weathering significantly.

When the argillaceous siltstones encounter water, these soluble cements are easy to react with water that will lead to lost connectivity between rock particles. After some materials dissolve in the water, rock pore solution is easy to cause the interaction with its internal clay minerals again. That means the water can cause great effect on the physical and mechanical properties of the Zigong argillaceous siltstone. Below, we

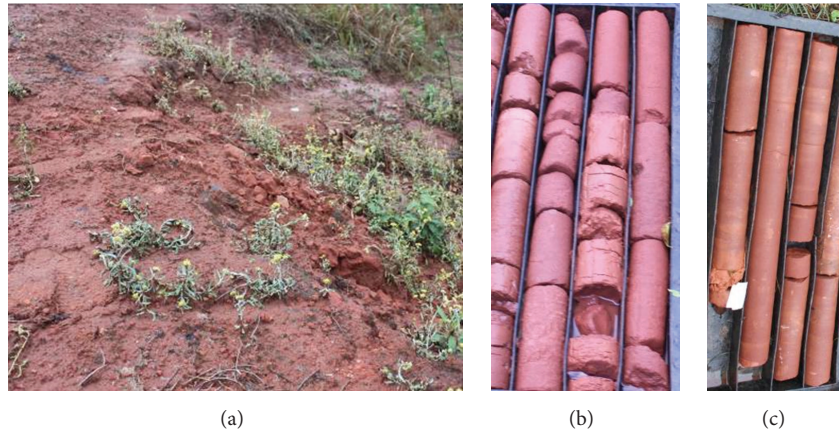


FIGURE 2: Site photos of the Zigong argillaceous siltstone: (a) completely weathered at the shallow surface (a type of silty clay); (b) borehole core samples of the highly weathered argillaceous siltstone and (c) borehole core samples of the moderately weathered argillaceous siltstone.

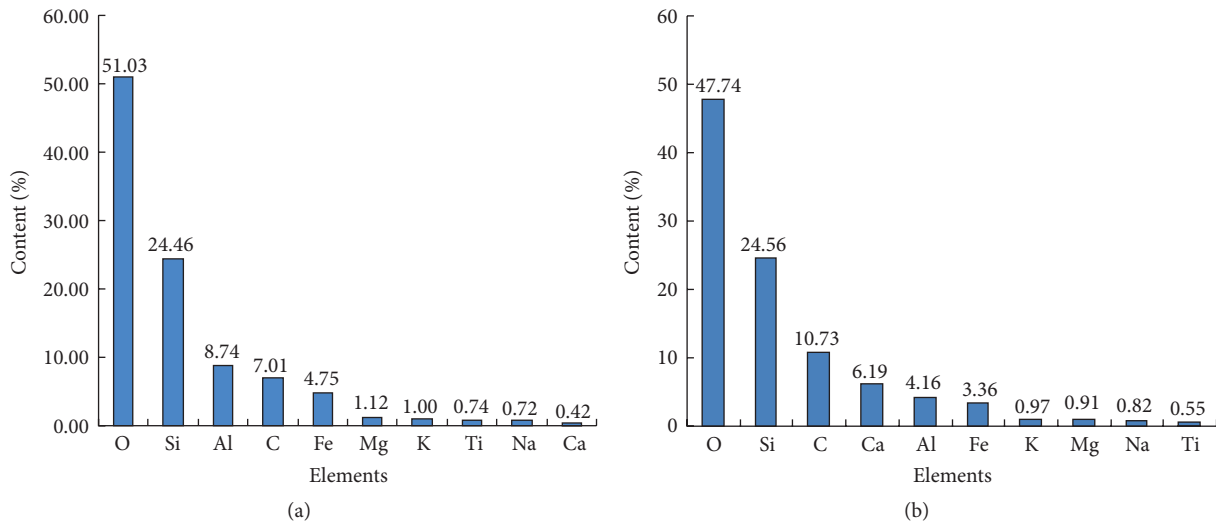


FIGURE 3: Elemental composition of the Zigong argillaceous siltstone with different weathered degrees: (a) highly weathered and (b) moderately weathered.

used different mechanical experiments and microtechniques to study the strength characteristics of the argillaceous siltstone with different moisture content and degree of weathering.

2.2. Laboratory Experiments. In general, rock strength parameters often show a decreasing trend as water content increases. The accurate estimation of rock strength parameters is of great importance in many engineering practices, especially for the stability assessment of dam foundations and soft rock roadways [8, 9, 11]. The microstructure and material composition of rock mass can reflect rock physical and mechanical properties. Therefore, it is meaningful to analyze the change of its internal structure and composition with different moisture content and degree of weathering. Here, the Zigong argillaceous siltstone was selected for sampling. These samples of the argillaceous siltstone were separated into four typical groups, which were natural highly weathered,

saturated highly weathered, natural moderately weathered, and saturated moderately weathered. The moderately weathered siltstone appears mauve, and the rock mass contains some joints and cracks, resulting in its low strength. As for the highly weathered siltstone, it is deep purple with lower strength, and some parts can be crushed in hand.

Parts of rock samples with different degree of weathering were immersed into water fully for 48 h to ensure those samples to absorb as much water as possible which can be regarded as saturation state in the present study. As shown in Figure 4, the average density of the natural highly weathered rock samples is lower than the natural moderately weathered rock from 1.98 g/m^3 to 2.38 g/m^3 , and the average density increases about 5% from natural condition to saturated condition.

Aimed to study the water-softening for mechanical properties of the Zigong argillaceous siltstones under different degree of weathering, this paper selected three types of

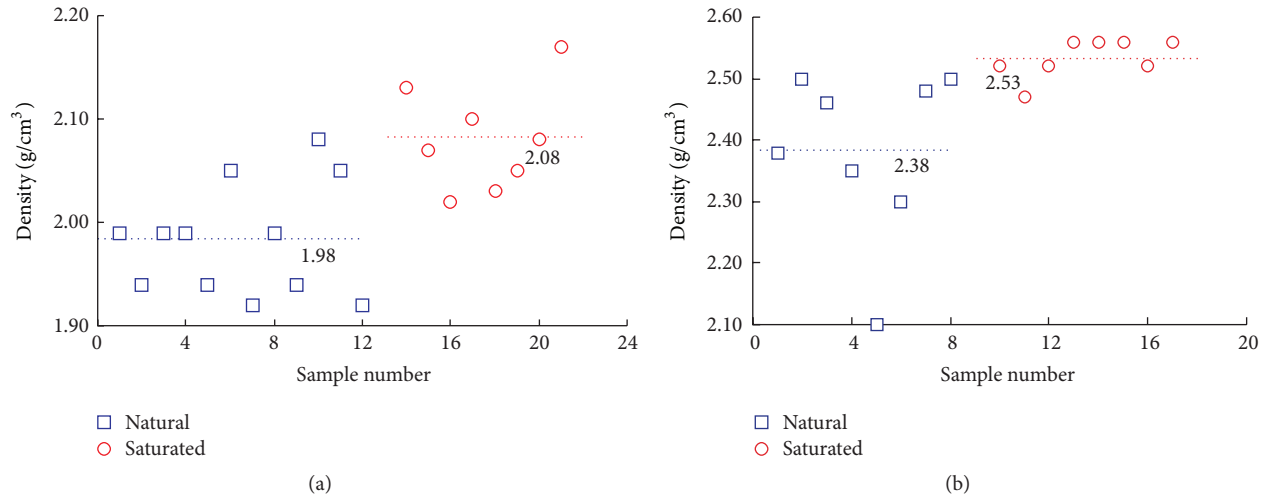


FIGURE 4: Test results for the density of the Zigong argillaceous siltstone under different conditions: (a) highly weathered and (b) moderately weathered.

mechanical tests: uniaxial compression test, triaxial compression test, and direct shear test. In addition, the differences of internal microstructural characteristics and material composition were also analyzed using scanning electron microscope (SEM) and energy dispersive X-ray microanalysis (EDXMA).

2.2.1. Mechanical Tests. In order to study the strength parameters of the above four typical Zigong argillaceous siltstones, two kinds of standard cylindrical samples dimensions (50 mm in diameter and 100 mm in length and 50 mm in diameter and 50 mm in length) were cut and weighted (as shown in Figure 5(a)). These specimens were separated into two typical groups (Figure 5(b)), the samples of dimensions (50 mm in diameter and 100 mm in length) were tested to measure their uniaxial and triaxial compressive strengths using MTS 815 rock mechanics test systems, and the samples of dimensions (50 mm in diameter and 50 mm in length) were tested to measure shear strength using a direct shear testing machine. MTS 815 rock mechanics test systems can test many types of samples from soft sandstone to high-strength brittle rock using a three-axis stabilized pressure system and control system (Figure 5(c)). These systems combine versatile servohydraulic load frames with precise digital controls, flexible software, and specialized accessories for uniaxial and triaxial compressive tests. The direct shear testing machine includes a loading frame, a shear box, two oil pressure power supplies, a control system, a data acquisition, and display system (as shown in Figure 5(d)). The maximum normal force of the shear testing system is 500 kN, and the maximum tangential force is 300 kN. The testing time and the testing load (including the normal and tangential forces) of each specimen can be recorded directly during the testing process.

According to the requirements of international rock mechanics regulations [8, 12–14], rock samples of the above four typical groups were chosen to measure their uniaxial compressive strength and stress-strain curve by controlling displacement speed as 0.1 mm/min. To gain the triaxial

strength of natural argillaceous siltstone, four confining pressures were applied: 0 MPa, 1.0 MPa, 2.0 MPa, and 3 MPa. The deviator stress $\sigma_1 - \sigma_3$ was obtained from the ratio of the applied axial load after the designated hydrostatic confining pressure was reached for the cross-sectional area of these specimens. The maximum principal stress σ_1 can also be calculated by the summation of the deviator stress $\sigma_1 - \sigma_3$ and the confining stress σ_3 .

For direct shear test, 20 rock samples (the test sample is a cylinder with diameter 50 mm and height of 50 mm) were performed to determine the shear strength of the Zigong argillaceous siltstones with different moisture content and degree of weathering.

2.2.2. Microstructure and Material Composition Tests. According to the surface morphology and material composition of rock samples, scanning electron microscope tests were carried out by JSM-7500 housed in the Analytical & Testing Center Sichuan University (Chengdu), China, which can analyze material micromorphology including surface morphology, fracture morphology, and phase structure analysis. Here, the microscopic images were collected from fracture surfaces of the soft rock samples. By scanning electron microscope, the microstructural differences of rock samples were determined. Finally, combined with the results of the above three mechanical tests, rocks' surface microstructure can be used to explain the water-softening mechanism of the Zigong argillaceous siltstone.

The physical and mechanical properties of rock mass depend largely on its material composition; especially when encountering water, some minerals can be easy to react with water which can change rock microstructure and decrease rock strength. For the red-bed soft rocks of Sichuan basin, quartz, calcite, and clay minerals are the major components, and the minor ingredients are feldspar, mica, gypsum, and others, where various specific minerals are composed of a series of oxides in rocks. For example, silica (SiO_2) is present

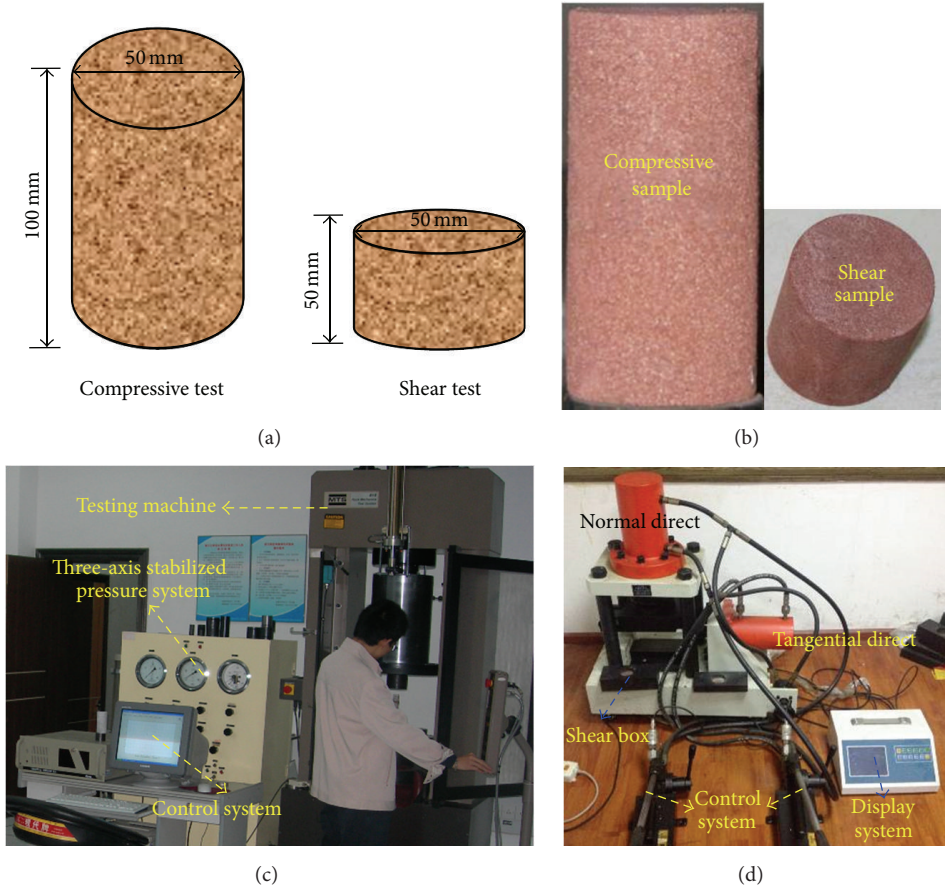


FIGURE 5: Laboratory test sample size and apparatus: (a) sample size used for the laboratory tests; (b) two natural rock samples for different test; (c) compressive test device (MTS 815 rock mechanics test systems); and (d) direct shear strength test device.

in the form of complex clay minerals including montmorillonite and kaolinite, primary silicates, and silica-free. Alumina (Al_2O_3) is the basic component of complex clay minerals and primary silicates, and calcium oxide (CaO) mainly exists in carbonates form. Besides, iron oxide (Fe_2O_3) has great influence on the color of red-bed soft rocks. Potassium and sodium oxide (K_2O and Na_2O) are absorbed by clay minerals in the form of potassium and sodium ions, respectively, which are the components of hydromica and clay-mica. Therefore, the paper analyzed the difference of the oxides' composition for the Zigong argillaceous siltstone with different degree of weathering by scanning material surface using energy dispersive X-ray microanalysis (EDXMA).

3. Results

Rock strength parameters are very important for engineering design, such as rock slopes and roadways, which often decrease with the increase of moisture content and degree of weathering [2, 11, 15, 16]. In general, rock strength shows a decreasing trend with the increase of water content [10, 13, 17, 18], mainly due to water adsorption and subsequent expansion, which can cause failure and collapse for rock mass ultimately.

3.1. Evolution of Compressive Strength. Compressive strength is the most widely used parameter in the rock engineering [13, 16]. In general, the greater water content often means the lower compressive strength of rock mass. The above four typical specimens were tested to determine the uniaxial compressive strength based on the requirements of international rock mechanics regulations. The test results reveal clearly that water can significantly affect rock compressive strength, and the softening coefficients are 0.46 and 0.58 for the moderately and highly weathered Zigong argillaceous siltstones, respectively (Table 1). As shown in Table 1, the average uniaxial compressive strength (UCS) of moderately weathered rock (20.46 MPa) is larger than the highly weathered rock (6.87 MPa) under natural condition, and the corresponding softening degree is smaller.

Test results can reveal that the Zigong argillaceous siltstone is much sensitive to water. Figure 6(a) shows the stress-strain curves of the highly and moderately weathered Zigong argillaceous siltstones during uniaxial compression tests. As shown in Figure 6(a), the axial strain of the highly weathered rock is greater than the moderately weathered with the rising of the axial stress. According to the failure phenomena of rock samples (Figure 6(b)), the splitting failure occurred in rock samples of the argillaceous siltstones, and the deformation

TABLE 1: The uniaxial compressive strength of the argillaceous siltstone samples.

Condition	Sample	Highly weathered		Moderately weathered		
		UCS (MPa)	Average (MPa)	Sample	UCS (MPa)	Average (MPa)
Natural	t1-N-1	7.19	6.87	t2-N-1	19.21	20.46
	t1-N-2	6.52		t2-N-2	21.53	
	t1-N-3	6.91		t2-N-3	20.65	
Saturated	t1-S-1	2.63	3.13	t2-S-1	10.89	11.86
	t1-S-2	2.23		t2-S-2	13.43	
	t1-S-3	4.53		t2-S-3	11.26	

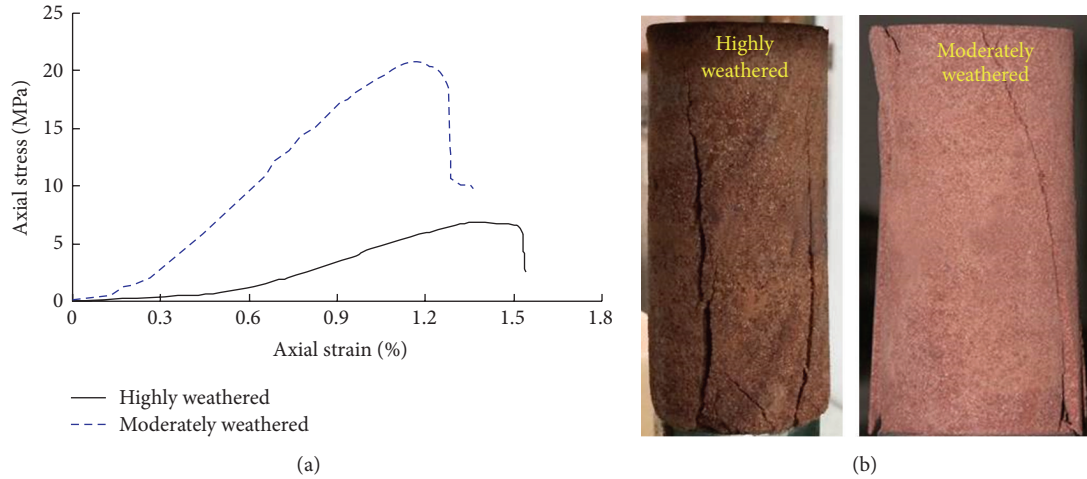


FIGURE 6: The results of the uniaxial compressive tests: (a) stress-strain curves and (b) the failure types of the Zigong argillaceous siltstone with different degree of weathering.

is more obvious with the increasing degree of weathering (Figure 6(a)).

The highly and moderately weathered rocks showed some characteristics of plastic and soft rock deformation. With the increase of axial stress, axial strain of the two group rocks increased gradually. Comparing the two deformation curves (as shown in Figure 6(a)), the average elastic modulus of the highly weathered rock sample is far lower than the moderately weathered rock sample, which proves that the degree of weathering has great influence on their deformation properties. By comparing the compressive strength and deformation characteristics, the moisture content and degree of weathering also have great effect on the Zigong argillaceous siltstones; that is to say, the increase with moisture content and degree of weathering of the argillaceous siltstone leads to its compressive strength reduction.

3.2. Shear Strength Parameters. MTS 815 rock mechanics test systems are available to support triaxial testing, including compression, creep, extension, and deformational stress pathways. The paper only chose one group totally 4 cylindrical samples of dimensions 50 mm \times 50 mm of the natural highly weathered argillaceous siltstone. For the triaxial compressive test, four confining pressures were applied, and the confining pressure σ_3 was 0 MPa, 1.0 MPa, 2.0 MPa, and 3.0 MPa. In the present study, the deviator stress $\sigma_1 - \sigma_3$ can

be obtained from the ratio of the applied axial load after the designated hydrostatic confining pressure is reached to the cross-sectional area. The peak compressive strength σ_1 can be obtained by the summation of the deviator stress $\sigma_1 - \sigma_3$ and the confining pressure σ_3 . According to Mohr-Coulomb criterion [19], the cohesion (c) and the internal friction angle (φ) can be calculated based on the geometric relationship of the confining pressure σ_3 and the peak compressive strength σ_1 (Figure 7(a)). The test results are that the cohesion is equal to 1.604 MPa and the internal friction angle is 38.06°, and rock samples showed typical shear failure characteristics as shown in Figure 7(b).

For the direct shear test, the above four typical specimens were tested using five different normal pressures. The axial forces were 0.2 kN, 0.5 kN, 0.8 kN, 1.1 kN, and 1.5 kN for the saturated highly weathered argillaceous siltstone because its strength is very low; for the other three groups, the axial forces were 0.5 kN, 1.0 kN, 1.5 kN, and 2.0 kN, respectively. The relationship between normal stresses and shear stresses can be drawn in a figure and used to determine the shear strength parameters of rock. Figure 8 shows the direct shear test results of the Zigong argillaceous siltstone under different conditions.

The criteria values of rock physics index can be considered same as the rock mass, but rock shear strength parameters must be reduced as shear strength of rock mass

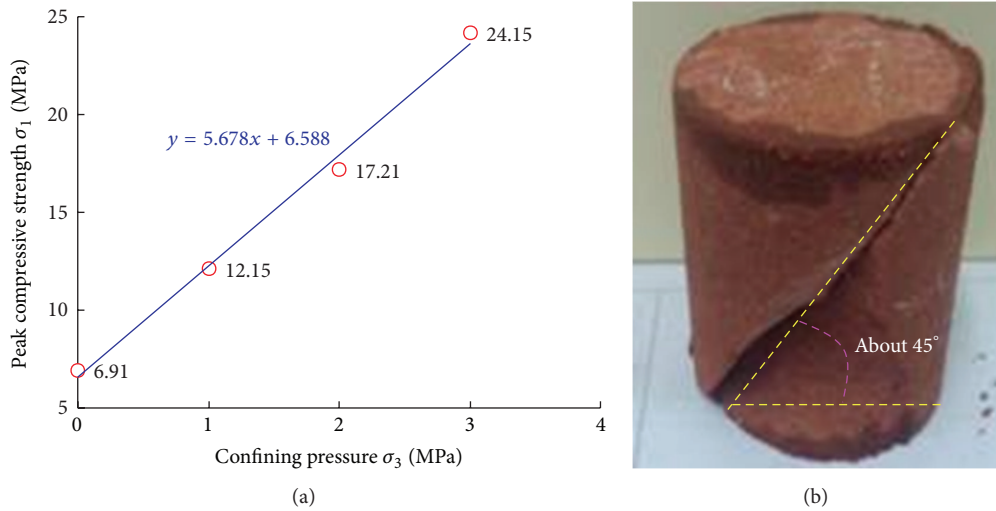


FIGURE 7: The results of the triaxial compressive test: (a) relationship between the confining stress and the failure stress of rock sample and (b) the failure pattern of the natural highly weathered Zigong argillaceous siltstone.

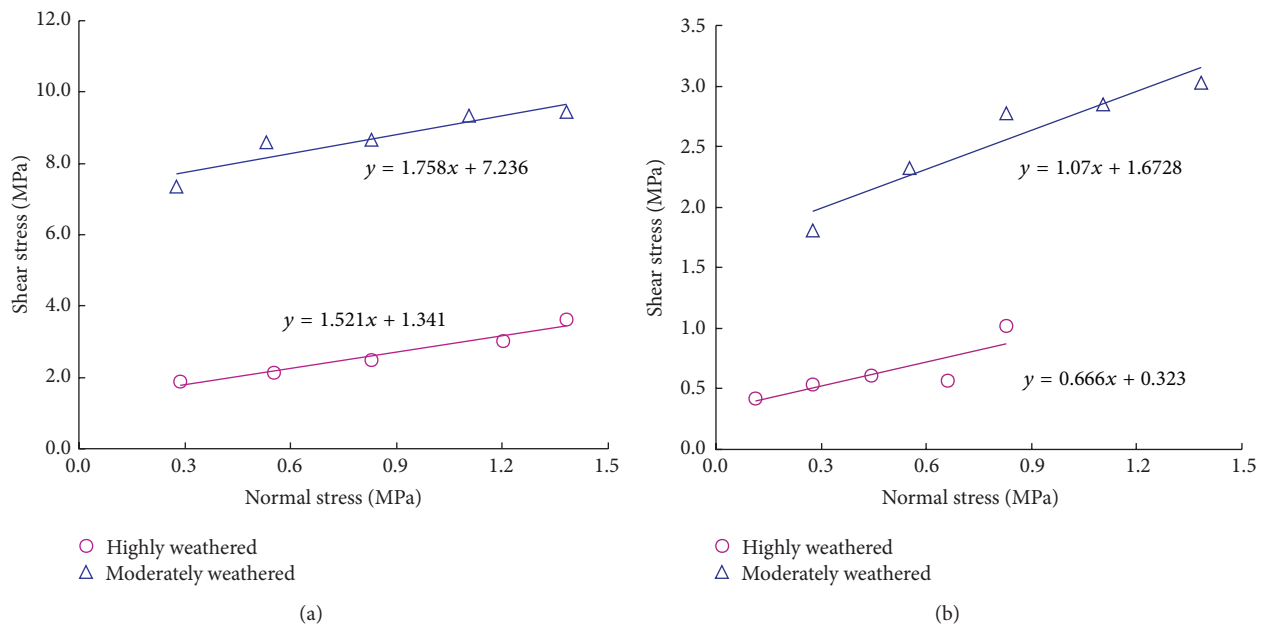


FIGURE 8: The results of the direct shear tests: (a) natural rock samples and (b) saturated rock samples.

[12, 20, 21]: reducing the rock internal friction angle to 80–95 percent based on the rock mass integrity and reducing the rock cohesion to 20–30 percent. According to Figure 8 and the above principles, the shear strength parameters were calculated including the cohesion (c) and the internal friction angle (φ) (Table 2).

For the natural Zigong argillaceous siltstone, the cohesion of the highly weathered rock was significantly lower than the moderately weathered rock decreasing from 1.447 MPa to 0.335 MPa and the internal friction angle lower by about 22% from 48.30° to 37.55°. After contacting with water,

the shear strength reduces significantly such that the cohesion decreases about 80% for the highly and moderately weathered rocks. As shown in Table 2, the cohesion of the red-bed soft rock is more sensitive encountering water than the internal friction angle. Above all, the shear strength reduces significantly which proves water can soften the red-bed soft rock obviously. According to the test results, the shear strength of the Zigong argillaceous siltstone is also sensitive to water, perhaps because water can decrease frictional shearing resistance or change the characteristics of clay mineral constituents of the red-bed soft rock.

TABLE 2: Shear strength parameters of the silty mudstones under different condition.

Samples	Natural condition		Saturated condition	
	c (MPa)	φ (°)	c (MPa)	φ (°)
Highly weathered	0.335	37.55	0.065	26.94
Moderately weathered	1.447	48.30	0.268	45.34

4. Discussions

Water-rock interaction is one of the frontier topics in geotechnical engineering. Under certain seepage pressure and hydrodynamic condition, rock can produce the physicochemical action and mechanical process, which are the basic reasons of engineering rock deformation and failure occurring [5, 10–16, 18, 22, 23]. Especially for some soft rocks, where intact, they have good mechanical properties under natural conditions, and yet, there will be the rapid expansion, disintegration, and softening in water saturation, which results in significant reductions of the mechanical properties of the rock.

4.1. Effect of Water on the Mechanical Properties of Soft Rock. Soft rocks can produce various changes of physical, chemical, and mechanical properties when encountering water, which is among the most important factors affecting rock strength, and rock strength reduction has been the chief technique problem controlling the stability of surrounding rock in underground engineering. In the field of mining, coal mine tunnel traverses mostly soft rocks' strata and its water stability is poor. Under high temperature, high stress, and high pressure conditions, the softening property of soft rocks is more obvious [7]. And, water-induced strength softening effect has been analyzed based on correlation between water content and rock mechanical properties including UCS and modulus of elasticity [14, 18, 24, 25].

The test results in our studies reveal that the cohesion and internal friction angle of the natural Zigong argillaceous siltstone are larger than those of the corresponding saturated rocks (Table 2). Therefore, the presence of water in rock samples can be concluded to weaken the shear strengths of the red-bed soft rock. And its deformation decreases from highly weathered to moderately weathered. Water often plays a key parameter in the water-weakening to cause the reduction of rock strength [10, 16, 22]. Risnes et al. (2003) studied the water-weakening effect on chalk. They performed compressive tests and Brazilian tests revealing that the variations in mechanical strength are correlated with the activity of water in the brines. They observed a linear trend between reduction of water activity and the corresponding increase in strength [26]. In addition, Zhou et al. (2005) ran a series of tests to obtain the mechanical property of silt mudstones in different saturation times (1 month, 3 months, 6 months, and 12 months) and drew a conclusion that the uniaxial compressive strength, cleave tensile strength, and shear strength conformed to an exponent curve after different saturated time on which the point in 6 months was the critical time for mechanical properties changing from gradually declining to stable state [10].

According to the results of the above mechanical tests, water and degree of weathering both have great effect on the mechanical properties of the red-bed soft rock. Aiming at rocks with different degree of weathering and saturation condition, rocks often exhibit a big difference in mechanical characteristics. In general, rock strength is larger with a lower weathering degree and moisture contents. Of course, some researchers have also studied the effect of water on rock strength and internal structure. First, the presence of water can reduce uniaxial compressive strength (UCS) in many sedimentary rocks and even some metamorphic rocks experimentally [13, 16]. Water can influence significantly the compressive strength and deformability of rocks, even though the water contents of rocks are not high for the natural and saturated rocks. And the reduction of strength by water content is found to be related to a reduction of friction angle and cohesion in the Mohr-Coulomb failure criterion. Li et al. (2012) thought the critical factors influencing rock strength and stiffness include material factors, such as constituent mineral composition, porosity, anisotropy, and discontinuity, and environment factors such as water content, temperature, and confining pressure [12]. Besides, it is quite difficult to evaluate and correlate these influencing factors by using only one index. So the paper also analyzed the microstructure and material composition for the above tested rock samples to study the water-softening mechanism and the influence of weathering degree.

4.2. Water-Softening Mechanism. The Zigong argillaceous siltstone is a sedimentary rock and is mainly composed of silt particles. With the help of scanning electron technique, the microstructures of fracture surfaces were determined for the above four typical rock samples (Figure 9). According to the microstructures' results, the natural red-bed soft rocks with different degree of weathering present a slab structure, and the phenomenon of the moderately weathered is more obvious that the fracture surface of the fragment is blocky with regular edges (Figures 9(a) and 9(c)). As shown in Figures 9(b) and 9(d), the Zigong argillaceous siltstone shows good water permeability performance and the rock shows granular structure at a magnification of $\times 70$ and $\times 100$.

The differences of microstructure are obvious for the above typical rock samples with different conditions. According to mechanical tests, the shear strength of the triaxial test is bigger than the direct shear test. The possible reason was that the existing of the confining pressure (σ_3) improves the loose structure of the highly weathered argillaceous siltstone as observed in Figure 9(a). When encountering water to saturation condition, there are big differences between natural and saturated rocks. For example, the fracture surfaces of the natural argillaceous siltstone are smoother and the shape of the fragment is more irregular than the saturated rock. Combined with the microstructure imageries, the phenomenon of water swell occurred in the saturated rocks. Figure 9 can help explain the cause of the change in the strength parameter that there are remarkable differences with its different water content and degree of weathering for the argillaceous siltstones. For the saturated rock, the fracture surfaces show the irregular scatter of silt particle because

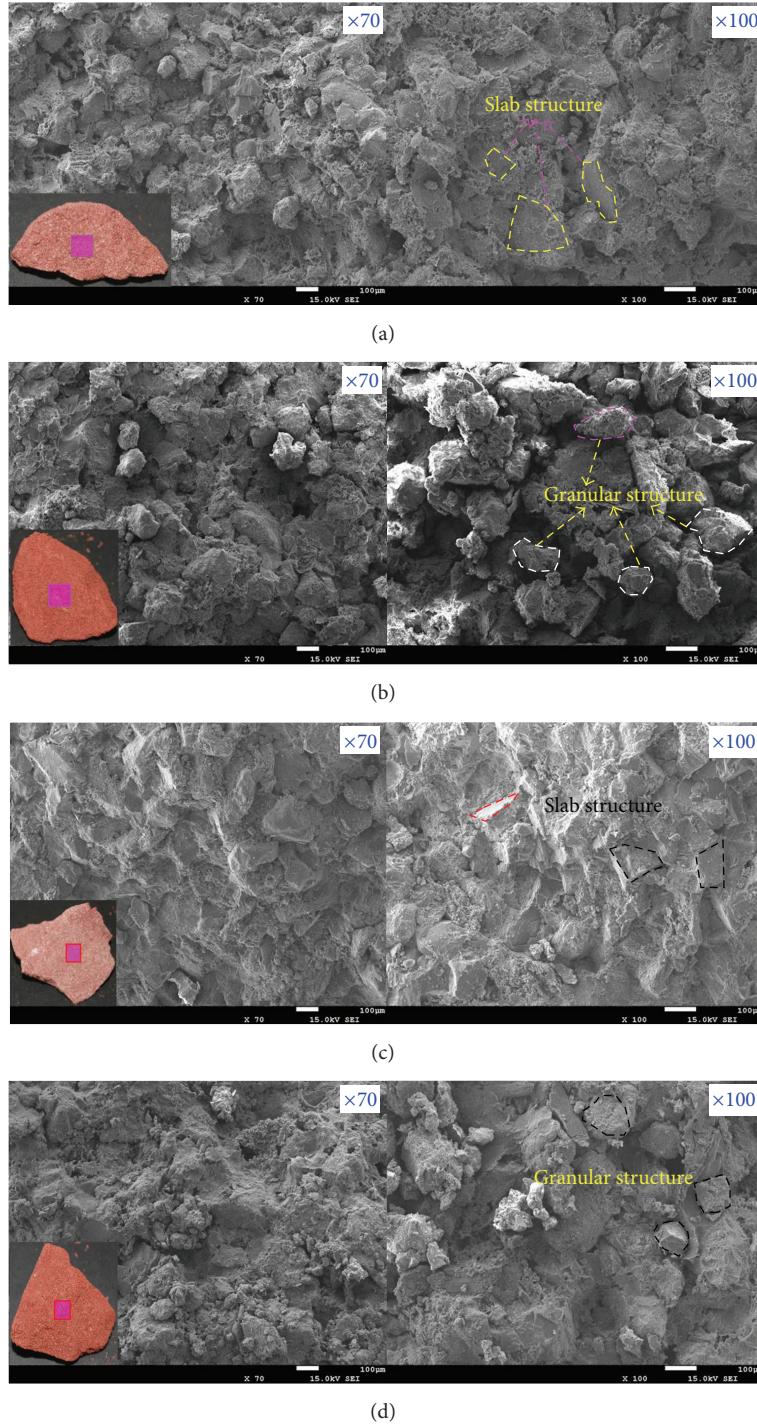


FIGURE 9: Microstructural characteristics of the Zigong argillaceous siltstone with different degree of weathering (SEM images): (a) natural highly weathered; (b) saturated highly weathered; (c) natural moderately weathered; and (d) saturated moderately weathered.

these soluble materials dissolve in the water leading to loosening of the structure. For the triaxial compressive test, the original loose structure became compact structure with the aid of the confining pressure σ_3 (Figure 9(a)); therefore, the shear strength parameters are bigger than the direct shear test for the highly weathered argillaceous siltstone. Combined with Figure 9, the monolithic turned into pieces and the fracture

surface produced some microscopic pores for the saturated rocks. Changes in microstructure eventually lead to reduced density, development of the pore system, and increased degree of argillation. As reported in literature [2, 11, 20, 27–30], it can be inferred that the changes in microstructure may be an important reason for rock softening and deterioration.

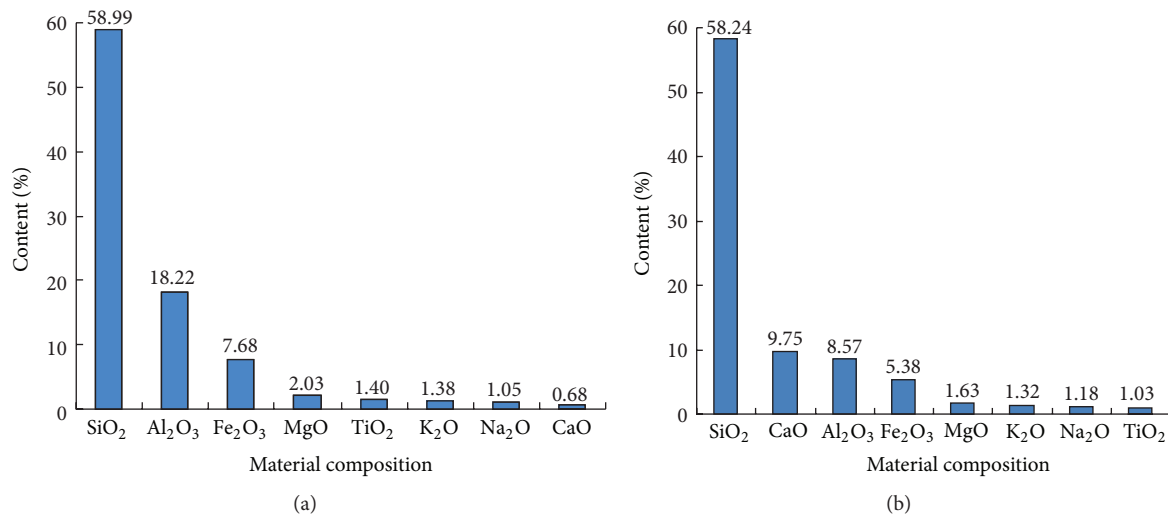


FIGURE 10: Material compositions of the natural Zigong argillaceous siltstone with different degree of weathering: (a) highly weathered and (b) moderately weathered.

From the above analysis, the argillaceous siltstone is sensitive to water, likely because the rock contains some clay minerals and soluble materials. According to Figure 10, the content of silica (SiO₂) is the highest in all oxides, accounting for about 60%, which indicates that the argillaceous siltstone contains many complex clay minerals, primary silicate minerals, and free silica. Besides, for the moderately weathered argillaceous siltstone, calcium oxide (CaO) and alumina (Al₂O₃) account for about 10% and 9%, respectively, (as shown in Figure 10(b)), which prove that there are a lot of carbonates and complex clay minerals in the red-bed soft rock. Comparing with Figure 6(b), its content of calcium oxide (CaO) and alumina (Al₂O₃) is very different from Figure 6(a), which indicates the content of clay minerals is higher, and the carbonate content is obviously decreased in the highly weathered argillaceous siltstone. The increase of clay minerals makes it more sensitive to water than the moderately weathered argillaceous siltstone.

With the aid of pore water pressure, the water can change the characteristics of clay mineral constituents of the red-bed soft rock. When encountering water, these soluble materials of rock samples can easily dissolve in the water which will cause the microstructural change and the reduction of strength parameters. Therefore, some internal materials dissolved in the water which may be the reason why the slab structure becomes granular structure for the microstructure images.

Many researchers thought the existing pores and clay minerals in the microstructure are the strength weakening reasons of soft rock affected by water [10, 11, 16]. The mechanical tests' results show that the shear strength parameters of saturated rocks mass reduced significantly, mainly because water can decrease frictional shearing resistance or change the characteristics of clay mineral constituents of the red-bed soft rock. Therefore, it is necessary to study the physical-chemical softening effect on microstructure and material composition in the future. By analyzing the microscopic

mechanism of water-rock interaction, the difference of rock internal microstructure is the main reason for influencing the water-softening properties, and the soluble oxides such as CaO, K₂O, and Na₂O, are another reason. The Zigong argillaceous siltstones underwent significant changes in microscopic morphology after saturation condition. Due to mineral leaching induced by physicochemical reactions including water flow, water leaching, and other water chemistry reactions, microstructural changes of the Zigong argillaceous siltstone are the main reason of water-softening.

Similar results of water-weakening effect have also been reported by some researchers [13–16, 21, 25, 26] on different kinds of rock such as clay-bearing rock, granite, chalk, shale, sandstone, and gypsum. Some studies have revealed that the loss of strength is most pronounced in clay-rich rock due to softening and expansive effect of hydrated clay [5, 10, 15]. Despite the fact that the harmful effects of water on different types of rock have been investigated extensively, the corresponding fundamental mechanism of water-induced strength reduction and deformability is still not very clear [14]. Compared with all test results of the natural and saturated argillaceous siltstones, the results of the work indicate that the increase of moisture content of the Zigong argillaceous siltstone leads to water interacting with mineral surfaces and altering the microstructure properties, which is the two main reasons for strength reduction.

5. Conclusions

The mechanical tests have been successfully conducted on thirty-six argillaceous siltstone rock samples, in which twenty of them were highly weathered, while sixteen of them were moderately weathered, both including natural and saturation conditions. The UCS of highly weathered rocks were about 6.87 MPa and 3.13 MPa, while that of moderately weathered were about 20.46 MPa and 11.86 MPa for the above two conditions. The shear strength of four typical rocks has also

been obtained. From the present study, the direct shear strength generally reduced with increasing water content and degree of weathering; meanwhile, the deformation of the red-bed soft rock has correlation with the weathered degree.

Present experimental studies have proved that water can influence the uniaxial compressive strength and shear strength of the red-bed soft rock, particularly for highly weathered argillaceous siltstone. The experimental results reveal the mechanical properties are correlated with the physical properties of tested rocks. Water can change not only rock microscopic structure morphology but also its internal material composition. When contacting with water, water will interact with mineral surfaces and alter their surface properties; therefore, the existing soluble materials are the reason for the difference of microstructure characteristics. By observing the surface morphology and pores, the change of microstructure can cause rock instability along weakness planes and decrease rock strength parameters. And high moisture content can also decrease durability and hardness of rock specimens.

Experimental results show that the microstructure characteristics can reflect rock strength well. In addition, the water-softening effect is obvious especially for the red-bed soft rock with higher degree of weathering, so special attention should be paid to the practical engineering when encountering groundwater or rainfall. The most important conclusion that can be drawn from this study is that the changes of the microstructure and material composition seem to be the key parameters in the water-softening mechanism. Therefore, the changes of microstructure and material composition are the main reason for the reduction of rock strength parameters.

Competing Interests

The authors declare that there is no conflict of interests regarding the publication of this paper.

Acknowledgments

This work is supported by the National Natural Science Foundation of China (51209156).

References

- [1] Y. C. Guo, Q. Xie, and J. Q. Wen, "Red beds distribution and engineering geological problem in China," *Chinese Journal of Hydrogeology and Engineering Geology*, vol. 6, pp. 67–71, 2007 (Chinese).
- [2] J. Chen, F. C. Dai, L. Xu et al., "Properties and microstructure of a natural slip zone in loose deposits of red beds, southwestern China," *Engineering Geology*, vol. 183, pp. 53–64, 2014.
- [3] L. T. Jiang, G. N. Chen, R. Grapes, and Z. L. Peng, "Thermal origin of continental red beds in SE China: an experiment study," *Journal of Asian Earth Sciences*, vol. 101, pp. 14–19, 2015.
- [4] G. X. Wu, B. Zhang, Y. X. Yang, and Q. Cheng, "Geology characteristics of red-layer soft rock in western region and its influence to the roadbase construction stability," *Journal of Chongqing Jiaotong University*, vol. 23, no. 6, pp. 53–58, 2004 (Chinese).
- [5] N. Zhang, L. B. Liu, D. W. Hou, M. C. He, and Y. L. Liu, "Geomechanical and water vapor absorption characteristics of clay-bearing soft rocks at great depth," *International Journal of Mining Science and Technology*, vol. 24, no. 6, pp. 811–818, 2014.
- [6] M. Arnould, "Discontinuity networks in mudstones: a geological approach," *Bulletin of Engineering Geology and the Environment*, vol. 65, no. 4, pp. 413–422, 2006.
- [7] H. Y. Guo, X. Y. Lei, Y. M. Zhang, G. X. Yang, and Z. Niu, "Experimental research on hydrophilic characteristics of natural soft rock at high stress state," *International Journal of Mining Science and Technology*, vol. 25, no. 3, pp. 489–495, 2015.
- [8] M. C. He, "Latest progress of soft rock mechanics and engineering in China," *Journal of Rock Mechanics and Geotechnical Engineering*, vol. 6, no. 3, pp. 165–179, 2014.
- [9] G. C. Li, Z. H. Jiang, C. X. Lv, C. Huang, G. Chen, and M. Y. Li, "Instability mechanism and control technology of soft rock roadway affected by mining and high confined water," *International Journal of Mining Science and Technology*, vol. 25, no. 4, pp. 573–580, 2015.
- [10] C.-Y. Zhou, Y.-M. Deng, X.-S. Tan, Z.-Q. Liu, W. Shang, and S. Zhan, "Experimental research on the softening of mechanical properties of saturated soft rocks and application," *Chinese Journal of Rock Mechanics and Engineering*, vol. 24, no. 1, pp. 33–38, 2005 (Chinese).
- [11] X.-T. Feng, S. Li, and S. Chen, "Effect of water chemical corrosion on strength and cracking characteristics of rocks—a review," *Key Engineering Materials*, vol. 261–263, no. II, pp. 1355–1360, 2004.
- [12] D. Y. Li, L. N. Y. Wong, G. Liu, and X. P. Zhang, "Influence of water content and anisotropy on the strength and deformability of low porosity meta-sedimentary rocks under triaxial compression," *Engineering Geology*, vol. 126, pp. 46–66, 2012.
- [13] T. AL-Bazali, "The impact of water content and ionic diffusion on the uniaxial compressive strength of shale," *Egyptian Journal of Petroleum*, vol. 22, no. 2, pp. 249–260, 2013.
- [14] I. Yilmaz, "Influence of water content on the strength and deformability of gypsum," *International Journal of Rock Mechanics and Mining Sciences*, vol. 47, no. 2, pp. 342–347, 2010.
- [15] Z. A. Erguler and R. Ulusay, "Water-induced variations in mechanical properties of clay-bearing rocks," *International Journal of Rock Mechanics and Mining Sciences*, vol. 46, no. 2, pp. 355–370, 2009.
- [16] X.-T. Feng, S. Chen, and S. Li, "Effects of water chemistry on microcracking and compressive strength of granite," *International Journal of Rock Mechanics and Mining Sciences*, vol. 38, no. 4, pp. 557–568, 2001.
- [17] S. Q. Yang, H. W. Jing, Y. S. Li, and L. J. Han, "Experimental investigation on mechanical behavior of coarse marble under six different loading paths," *Experimental Mechanics*, vol. 51, no. 3, pp. 315–334, 2011.
- [18] N. Zhang, M. C. He, and P. Y. Liu, "Water vapor sorption and its mechanical effect on clay-bearing conglomerate selected from China," *Engineering Geology*, vol. 141–142, pp. 1–8, 2012.
- [19] N. Barton, "Shear strength criteria for rock, rock joints, rockfill and rock masses: problems and some solutions," *Journal of Rock Mechanics and Geotechnical Engineering*, vol. 5, no. 4, pp. 249–261, 2013.
- [20] X.-T. Feng, S. Chen, and H. Zhou, "Real-time computerized tomography (CT) experiments on sandstone damage evolution

- during triaxial compression with chemical corrosion,” *International Journal of Rock Mechanics and Mining Sciences*, vol. 41, no. 2, pp. 181–192, 2004.
- [21] P. L. P. Wasantha, W. J. Darlington, and P. G. Ranjith, “Characterization of mechanical behaviour of saturated sandstone using a newly developed triaxial apparatus,” *Experimental Mechanics*, vol. 53, no. 5, pp. 871–882, 2013.
- [22] Y. Mikami, M. Kurashige, and K. Imai, “Mechanical response of a water-saturated core sample under opposite diametrical loadings,” *Acta Mechanica*, vol. 158, no. 1-2, pp. 15–32, 2002.
- [23] B. J. Thomson, J. A. Hurowitz, L. L. Baker et al., “The effects of weathering on the strength and chemistry of Columbia River Basalts and their implications for Mars Exploration Rover Rock Abrasion Tool (RAT) results,” *Earth and Planetary Science Letters*, vol. 400, pp. 130–144, 2014.
- [24] E. Rybacki, A. Reinicke, T. Meier, M. Makasi, and G. Dresen, “What controls the mechanical properties of shale rocks?—part I: strength and Young’s modulus,” *Journal of Petroleum Science and Engineering*, vol. 135, pp. 702–722, 2015.
- [25] S. Taibi, A. Duperret, and J.-M. Fleureau, “The effect of suction on the hydro-mechanical behaviour of chalk rocks,” *Engineering Geology*, vol. 106, no. 1-2, pp. 40–50, 2009.
- [26] R. Risnes, H. Haghghi, R. I. Korsnes, and O. Natvik, “Chalk-fluid interactions with glycol and brines,” *Tectonophysics*, vol. 370, no. 1–4, pp. 213–226, 2003.
- [27] E. Ishii, “Microstructure and origin of faults in siliceous mudstone at the Horonobe Underground Research Laboratory site, Japan,” *Journal of Structural Geology*, vol. 34, pp. 20–29, 2012.
- [28] N. P. Kruyt and L. Rothenburg, “On micromechanical characteristics of the critical state of two-dimensional granular materials,” *Acta Mechanica*, vol. 225, no. 8, pp. 2301–2318, 2014.
- [29] X. R. Liu, Z. J. Wang, Y. Fu, W. Yuan, and L. L. Miao, “Macro/microtesting and damage and degradation of sandstones under dry-wet cycles,” *Advances in Materials Science and Engineering*, vol. 2016, Article ID 7013032, 16 pages, 2016.
- [30] S. M. Brooks, T. Spencer, and S. Boreham, “Deriving mechanisms and thresholds for cliff retreat in soft-rock cliffs under changing climates: rapidly retreating cliffs of the Suffolk coast, UK,” *Geomorphology*, vol. 153-154, pp. 48–60, 2012.

Research Article

Comparison of Effects of Using Geosynthetics and Lime Stabilization to Increase Bearing Capacity of Unpaved Road Subgrade

Erhan Burak Pancar¹ and Muhammet Vefa Akpınar²

¹Department of Architecture, Ondokuz Mayıs University, Samsun, Turkey

²Department of Civil Engineering, Karadeniz Technical University, Trabzon, Turkey

Correspondence should be addressed to Erhan Burak Pancar; erhanpancar@hotmail.com

Received 22 April 2016; Revised 21 July 2016; Accepted 1 August 2016

Academic Editor: Jianxi Zhu

Copyright © 2016 E. B. Pancar and M. V. Akpınar. This is an open access article distributed under the Creative Commons Attribution License, which permits unrestricted use, distribution, and reproduction in any medium, provided the original work is properly cited.

So many soil improvement methods have been developed in order to increase bearing capacity of superstructure of the road to be constructed on the soft clayey road base soils, decrease settlements, and increase other strength specifications (CBR, k , M_R values, etc.). In this paper, lime stabilization of clayey road base soil with high water content and its improvement with geosynthetics (geocell + geotextile) reinforcement and comparisons of these two different improvement methods were made. For this purpose, plate loading experimental comparisons of clayey soil, which had high water content by 10% increasing the optimum water content, were made after it was improved with lime at the rates of 3, 6, and 12%, geotextile reinforcement, geocell reinforcement, geosynthetics reinforcement, and geosynthetics reinforcement + lime stabilization at various rates. It was understood that these improvement methods will not yield sufficient results on clayey soils with high water content on their own, and method of improvement with lime and then reinforcement with geosynthetics yields better results on these types of soils. Only one improvement state among ten different states examined in this study gave the sufficient results for the soil to be used for unpaved roads.

1. Introduction

Subgrade soils may safely withstand the stresses that traffic loads constitute. Soft soils have low shear strength and this causes excessive consolidation settlement and bearing capacity failure when they are used as a road subgrade. Bearing capacity of the soil is generally affected by soil type, water content, and compaction degree. The soils shall support high amount of loading without excessive settlement. It is required to stabilize the subgrade soils that are not appropriate for road superstructure by improving them. With the improvement of the soil, bearing capacity is increased, settlements are decreased, and therefore surfacing thickness is decreased and surfacing performance is increased. A variety of ground improvement techniques including vertical drains, complete soil replacement, grouting, geosynthetic reinforcement, and lime stabilization are used in several structures such as

highways, railways, airports, and embankment to improve the performance of soils [1–6].

Many researchers have reported the ability of lime to change the plasticity of soils. The liquid limit of clay soil decreases when the lime content increases [7]. The plastic limit increases and the plasticity index which is the difference between the liquid limit and the plastic limit decreases with lime stabilization [8]. The pH becomes about 12.4 by mixing soil, lime, and water [9]. It is desired to get this pH value by adding lime to the soil and there is a minimum limit for lime content to achieve this goal. The strength of soil increases if the amount of lime added to the soil increases [10]. Dash and Hussain [2] determined that the optimum lime content was 9% for expansive soils and 5% for residual soil-rich specimens.

Dash and Hussain [2] also stated that when the amount of lime added to the soil increases, the swell potential of soils

decreases at first and then starts to increase after a certain limit of lime content. This content is 5% for fine-grained soils and 9% for coarse-grained soils. It is also known that excessive lime treatments decrease the soil strength. Because of that, calculating the optimum amount of lime is very important for lime stabilization.

Dash and Hussain [11] detected that the effect of lime on reducing the shrinkage potential of high plastic expansive soils is more than low plastic residual soil. The optimum lime content to get minimum shrinkage was calculated as 5%.

In the studies, Kavak et al. [12] reviewed performance of lime stabilization of clay, with high plasticity, on the base soil of the real road. The necessary lime ratio was determined as 5%. Implementation was done on total 40 cm part of the soil. The lime stabilization was applied in 2 layers as 20 cm for each. CBR (California Bearing Ratio) values increased from 11% to 56% after lime stabilization. At the plate loading experiments, maximum settlement decreased to 3.6 mm from 22.2 mm. 8 times increases occurred on dry CBR values of the material to which 5% lime was mixed at the end of 56 days and up to 34 times increases occurred on its wet CBR values compared to the natural material.

Geosynthetic reinforcement has been more used among soil improvement techniques. It gives an advantage of rapid construction at low costs. Zhou and Wen [13] have determined the mechanisms of geosynthetic reinforcement by explaining the confinement, pocket effect, raft foundation effect, and stress dispersion effect in their study.

Latha and Somwanshi [14] demonstrated that the geocell is the most advantageous form of geosynthetic reinforcement (i.e., geocell, planar layers, and randomly distributed mesh elements). Moghaddas Tafreshi and Dawson [4] and Dash et al. [15] also determined that geocell reinforcement is more desirable than planar reinforcement. Moghaddas Tafreshi and Dawson [4] stated that the geocell reinforcement improves the bearing capacity of soil more than 200% and reduces the settlement by 75%.

Zhou and Wen [13] indicated that subgrade reaction coefficient k_{30} can be improved by 3000%, and the deformation can be reduced by 44% by using geocell-reinforced sand cushion. Sireesh et al. [16] and Dash et al. [15] stated that if a planar geogrid is added at the base of the geocell, the bearing capacity of the foundation also increases. Dash et al. [17] detected that this increasing can be 30% more than with geocell alone. The effect of planar reinforcement layer reduces by increasing the height of the geocell mattress.

The overall goal of this study was to demonstrate the benefits of geosynthetics reinforcement and lime stabilization for clayey pavement subgrade with high water content, with the detailed objective of this study being to compare the performance of geocell reinforcement, geotextile reinforcement, and lime stabilization by using these treatments solely and together. This comparison has not been made before in other studies.

2. Cellular Confinement Systems

As seen in Figure 1, cellular confinement systems (geocell, geoweb, neoweb, etc.) are a network having a high resistance



FIGURE 1: Application of geocell in the field.

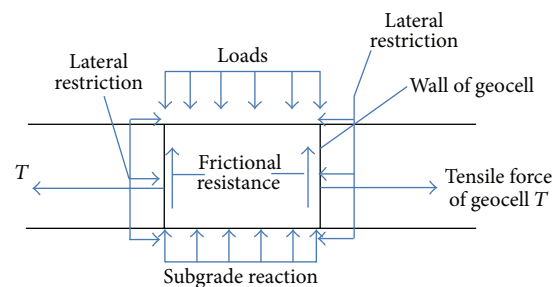


FIGURE 2: Lateral resistance effect of geocell reinforcement.

that was developed with the aim of stabilizing the soil by taking it under control and formed from three-dimensional cells interconnected with nodes in the shape of a honeycomb made from polyethylene. The cellular load bearing systems expand in the construction field and are filled with soil. The filling material completely covers the cell walls and confined the entire environment in the soil. Therefore, it increases load-deformation behavior and resistance of the soil by taking vertical loading stresses at the cell walls and soil resistance at the adjacent cells [18].

Zhao et al. [19] stated the working principle of geocell layer by explaining its three effects: lateral resistance effect, vertical stress dispersion effect, and membrane effect. Zhang et al. [6] explained these aspects in their study. Figure 2 shows the “lateral resistance effect” of geocell reinforcement. The soil above and below the geocell increases the lateral confinement and lower lateral strain.

Figure 3 shows the “vertical stress dispersion effect” of geocell reinforcement. Footing load is distributed over a wider area and the soil pressure decreases on the soft subgrade [6].

Figure 4 shows the “membrane effect” of geocell reinforcement. The loads deflect the geocell and it causes tension forces. The vertical component of the tension force is upward and it reduces the load and pressure on the subgrade soil [6].

In their study, Zhang et al. [6] determined that “vertical stress dispersion effect” and “membrane effect” are effective on increasing the bearing capacity of subgrade soil while “lateral resistance effect” of geocell reinforcement has no

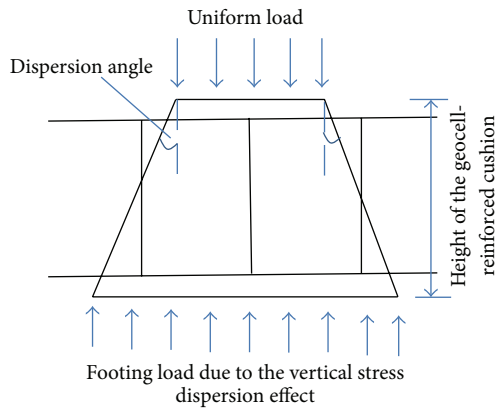


FIGURE 3: Vertical stress dispersion effect of geocell reinforcement.

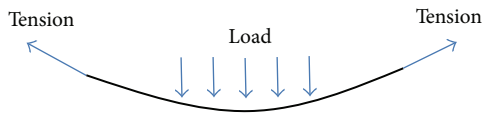


FIGURE 4: Membrane effect of geocell reinforcement.

significant effect. In that study, it is also observed that when the settlement is small, “vertical stress dispersion effect” is more effective than “membrane effect” and “membrane effect” is accepted as almost zero.

In that study, a different method from Koerner’s method was used to draw bearing capacity increment-settlement (Δp - s) curves. It was stated that Δp - s curve from the presented method in that study was more realistic than that from Koerner’s method when the embankment settlement was larger than 5 mm. This is because the influence of tension membrane effect of the reinforcement is not taken into account in Koerner’s method. It was detected that dispersion angle has very significant effects on the calculated Δp - s curve and geocell size, infill material properties, and geocell tensional strength are effective on dispersion angle [6] although Dash et al. [17] stated that the tensile strength of the grid used to fabricate geocell mattress is not effective on geocell.

Dash et al. [17] stated that the footing width is important for pressure-settlement curve and this curve is almost linear up to settlement of half of the footing width. In their study, Moghaddas Tafreshi and Dawson [4] noted that in most of the researches settlement limit criterion is not taken into account and only bearing capacity is considered while dealing with the performance of footing. But settlement is very important in practical design of shallow foundations. The improvement in bearing capacity is estimated to be unreal in some studies [15, 17, 20] because of not considering the acceptable range of settlement. The footing settlement (s) must not be more than 12% of the footing width (B). Using geotextile is very effective on reduction in footing settlement for higher settlements ($s/B > 6\%$) [4].

3. Material and Method

3.1. Method. In this paper, experimental studies were conducted on clayey soil. After sieve analysis, consistency limit experiments and hydrometer analyses, respectively, were done on this material, which was classified according to AASHTO and unified soil classification system. In order to determine optimum water content and dry unit weight of the clay material, also modified proctor experiments were conducted. The experiments that were conducted up to here were done with the aim of determining class and specifications of the soil. In this paper, the experiment model that was mainly wanted to be conducted was plate loading experiment. With this aim, model plate loading experiments were conducted on the mixtures that were prepared from high water content (10% more than optimum water content). In these experiments, the stabilization was done by the way the soil was reinforced with geocell and geotextile without adding anything to the clayey soil and lime was mixed to dry weight of the soil at the rates of 3, 6, and 12% and high water content; in other words, natural water content of the soil was increased 10%.

3.2. Materials Used for the Testing

3.2.1. Soil Used as a Subgrade and Sand Used as an Infill Material for Geocell. The sieve analysis of soil samples is shown in Table 1.

With the aim of classifying the material, consistency limits are given in Table 2. Measurements were made after 3 days’ curing period of lime.

As per ASTM D2487 [21], the soil used as a subgrade was classified as clay with high plasticity (Class CH).

The sand used as an infill material for geocell in this investigation was dry. It was used as a base layer for unreinforced test section. The effective particle size (D_{10}) was 1.2 mm, coefficient of uniformity (C_u) was 2.25, specific gravity was 2.64, and coefficient of curvature (C_c) was 1.05. It is classified as poorly graded sand (SP) according to unified soil classification system [21]. The void ratio of the sand was 0.42 and internal friction angle was 37° .

3.2.2. Geosynthetics. The geocell and planar reinforcement used in this study were both made and supplied by the same company. The type of geotextile was nonwoven. The engineering properties of this geotextile, as listed by the manufacturer, are in Table 3.

The engineering properties of the geocell, as listed by the manufacturer, are in Table 4. There were also drainage holes having 10 mm diameter at geocell cell walls.

3.2.3. Lime. The chemical analysis information belonging to the lime used in this study is given in Table 5.

3.3. Model Plate Loading Experiment

3.3.1. Experiment Tool. Laboratory model loading tests were conducted to compare the influence of geocell and geotextile

TABLE 1: Wet sieve analysis.

Sieve number	Sieve diameter (mm)	Sieve analysis		
		Residue of sieving (gr)	Sieved (gr)	Sieved percent, %
3/8"	9,53	0	420	100
4	4,76	41,3	378,7	90
10	2	29,6	349,1	83
40	0,42	19,4	329,7	79
100		15,2	314,5	75
200	0,074	12,7	301,8	72
Pan		301,8		

TABLE 2: Liquid limit and plastic limit experiments for natural soil and lime state.

	Atterberg (consistency) limits		
	Liquid limit	Plastic limit	Plasticity index
Natural	57	27	30
3% lime	54	32	22
6% lime	51	35	16
12% lime	50	39	11

TABLE 3: Technical properties of nonwoven geotextile.

Properties	Values
Unit weight (gr/m^2)	500
Thickness (mm)	4
Tensile strength (kN/m)	27–29
Breaking elongation (%)	50–80
Static puncture resistance (N)	5500
Dynamical puncture resistance (mm)	3
Water permeability (m/sn)	0.025
Characteristic aperture size (mm)	0.1

TABLE 4: Technical properties of geocell.

Properties	Values
Density (gr/cm^3)	0.94
Welding size (cm)	40
Cell length (mm)	300
Cell width (mm)	250
Thickness (mm)	2
Cell depth (cm)	20

reinforcement and lime stabilization on increasing the bearing capacity of clayey soil in a steel box. The overall inner dimensions of the box were 1.2 m length, 1.2 m width, and 1.2 m height as seen in Figure 5. Unpaved road test sections were constructed inside the box.

The pocket size (d) of the geocell is taken as the diameter of an equivalent circular area of the pocket opening. This diameter was 25 cm in this study. Pocket diameter/footing width (d/B) is reported by Dash et al. [15] to be around 0.8 times the footing width which is found to be the one that gives

TABLE 5: Chemical analysis of the lime (%).

Chemical analysis	%
$\text{Ca}(\text{OH})_2$	80–85
Active CaO	60–65
Total CaO + MgO	85–95
MgO	1–3
Density (gr/lt)	375–500

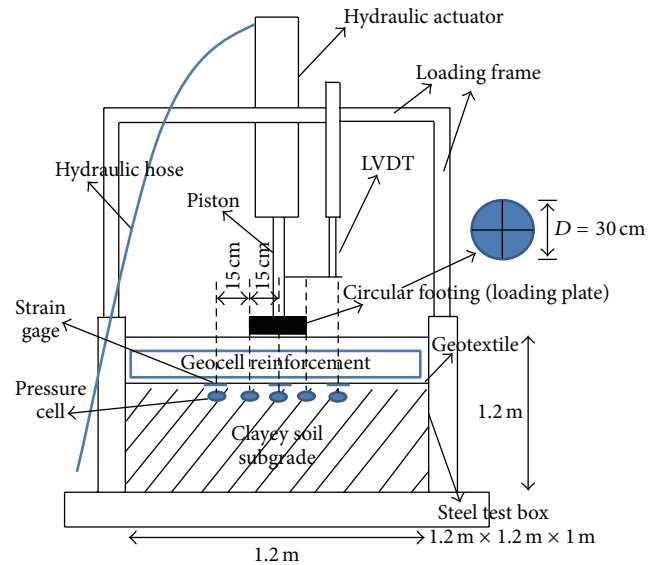


FIGURE 5: Schematic diagram for the set-up of the plate loading test.

maximum performance improvement. Due to this reason, the diameter of circular footing was determined as 30 cm in this experimental tool.

The footing was loaded with a hydraulic actuator and the circular footing was 30 cm in diameter and 3 cm thick. 1 cm thick rubber pad was attached to the bottom of the loading plate to ensure full contact and minimize stress concentrations at the edge of the plate. Dash et al. [17] detected that very good improvement in the footing performance can be obtained even with geocell mattress of width equal to the width of the footing and the optimum width of the geocell layer is around 4 times the footing width. Moghaddas Tafreshi and Dawson [4] determined that

increasing the reinforcement width more than 4.2 times the footing width for the geocell would not provide much additional improvement in bearing pressure and additional reduction in footing settlement. Sireesh et al. [16] and Dash et al. [15] detected the efficient width of the geocell as 4.9 and 5, respectively. In this experiment, geocell layer was chosen as 4 times the footing width. The peak load was selected to simulate a single wheel load of 40 kN (equivalent to an axle load of 80 kN and a tire contact pressure of 550 kPa).

The testing procedures in the experiment are as follows. The subgrade clayey soil was prepared by increasing the optimum water content of the clayey soil by 10% and bringing it to 35% outside the test device. The soil was mixed homogeneously and represented a soil whose bearing capacity was low. The soil also stabilized by lime in proportions of 3, 6, and 12% by total weight of dry soil. The test box was filled with this soil at the depth of 75 cm as a subgrade. The subgrade soil was placed in 3 layers with 25 cm thickness for each layer. The placed layers were compacted in lifts inside a box using a vibratory plate compactor. The top of geocell mattress should be at a depth of 0.1 times the footing width from the bottom of the footing to obtain maximum benefit [4, 17]. In this study, the top of geocell mattress was at a depth of 3 cm from the bottom of the footing.

After preparing the subgrade, three strain gages were installed on the top of the subgrade. Five pressure cells were installed on the surface of the subgrade at the center and 15 cm and 30 cm away from the center of the loading plate, respectively. A linear variable differential transducer (LVDT) was also placed on the footing model to provide the value of footing settlement during the loading (Figure 5).

Ten unpaved road test sections were prepared in the test box. Experiments were conducted on one (natural subgrade and unreinforced base), one (natural subgrade and geotextile reinforced base), one (natural subgrade and geocell-reinforced base), one (natural subgrade and geocell + geotextile reinforced base), three (3, 6, and 12% lime stabilized subgrades and unreinforced bases), and three (3, 6, and 12% lime stabilized subgrades and geocell + geotextile reinforced bases) sections, respectively. Reinforced and unreinforced bases were all 23 cm thick. Unreinforced bases consisted of clayey soil. After installation of pressure cells and strain gages, a layer of geotextile was placed on top of the subgrade and the geocells were placed on top of geotextile for reinforced sections. The geocell used in this experiment was 20 cm thick, top of the geocell mattress was at a depth of 3 cm from the bottom of the footing, and the geocell width was 1.18 m as Moghaddas Tafreshi and Dawson [4] and Dash et al. [17] detected the ratios between footing width, geocell height, and geocell width to get optimum test results.

4. Results and Discussion

4.1. Load-Deformation Findings and Review. Comparison between the improvement of clayey unpaved road subgrade with geosynthetics and lime stabilization was made in the laboratory. Ten different alternatives for road sections were

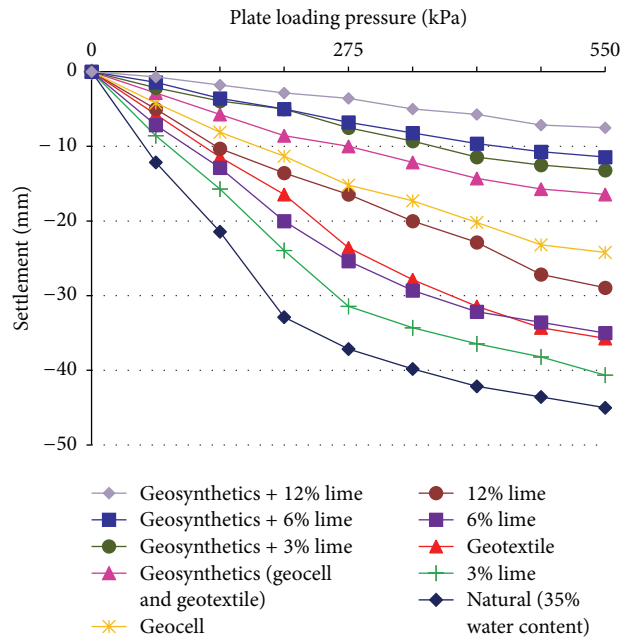


FIGURE 6: Loading-settlement curve.

examined in this study. The loading-settlement relation at different states is in Figure 6. While the maximum settlement in natural state at 550 kPa pressure was 45 mm, this settlement was decreased to 41 mm when soil was stabilized with 3% lime, 36 mm when soil was reinforced with geotextile, 35 mm when soil was stabilized with 6% lime, 29 mm when soil was reinforced with geocell, 16 mm when soil was reinforced with geosynthetics (geocell + geotextile), 13 mm when soil was reinforced with geosynthetics (geocell + geotextile) and subgrade was stabilized with 3% lime, 11 mm when soil was reinforced with geosynthetics (geocell + geotextile) and subgrade was stabilized with 6% lime, and 8 mm when soil was reinforced with geosynthetics (geocell + geotextile) and subgrade was stabilized with 12% lime. It was observed that the effects of geotextile (placed 23 cm under the top surface of the soil) and lime stabilization of soil with 6% lime were similar to each other. The settlement at geotextile reinforcement state was 1.5 times the geocell reinforcement state and 2.1 times the geosynthetics reinforcement under 550 kPa loading. The settlement at natural state was 6 times the settlement at geosynthetics + 12% lime state under the same loading. The authors in [4] stated that the value of footing settlement that equals 12% of footing width is considered absolute upper limit. It was observed that four states (natural, 3% lime, geotextile, and 6% lime) among ten states examined in this study did not meet the requirements of settlement.

4.2. Modulus of Subgrade Reaction. The most popular model in determining the modulus of subgrade reaction (k) is Winkler model. In this model, the subgrade soil is assumed to behave like infinite number of linear elastic springs such that the stiffness of the spring is named as the modulus

TABLE 6: Modulus of subgrade reaction.

States	Modulus of subgrade reaction (k) (kN/m^3)
Natural	6.765
3% lime	9.677
6% lime	12.000
Geotextile	12.608
12% lime	15.000
Geocell	18.330
Geosynthetics	26.000
Geosynthetics + 3% lime	42.000
Geosynthetics + 6% lime	48.300
Geosynthetics + 12% lime	70.000

of subgrade reaction. The direct method to estimate the modulus of subgrade reaction is plate load test that is done with 30–100 cm diameter circular plate or equivalent rectangular plate.

Modulus of subgrade reaction values was calculated with the help of Figure 6 by determining the inclinations of loading-settlement curves. These values are listed in Table 6.

As seen in Table 6, “ k ” value was 6765 kN/m^3 for natural state of the soil which had 35% water content and this value was 70.000 kN/m^3 for soils reinforced with geocell + geotextile and 12% lime stabilized. According to Highways Technical Specifications in Turkey, this value is to be no less than 55.000 kN/m^3 and “geosynthetics + 12% lime” was the only state that met the requirement of Highway Technical Specifications. It was seen that lime stabilization or reinforcement with geosynthetics solely did not meet the requirement of modulus of subgrade reaction in this study. The only acceptable situation was making geosynthetics reinforcement after stabilizing soil with 12% lime. Although Dash and Hussain [2] determined that, for expansive soil dominant samples, the optimum lime content was 9%, in this study 12% lime content was the better proportion among 3, 6, and 12% lime treatments. In Figure 7, the relation between the modulus of subgrade reaction and ratio of lime used to stabilize the soil is seen. In Figure 8, the relation between the modulus of subgrade reaction and geosynthetics reinforcement with lime content in the soil is seen.

4.3. Vertical Stress. Vertical stresses occurring on the subgrade soil were measured by the help of pressure cells used in the experiment. These values were measured at 23 cm lower than the bottom of the loading plate and they are seen in Figure 9. It is detected that geosynthetics reinforcement is more effective than 12% lime stabilization. 12% lime stabilization + geosynthetics reinforcement is much more effective than the other states. The stress value, 23 cm lower and at the center of the plate, of natural soil is about 2.5 times the stress value obtained at 12% lime stabilization + geosynthetics reinforcement.

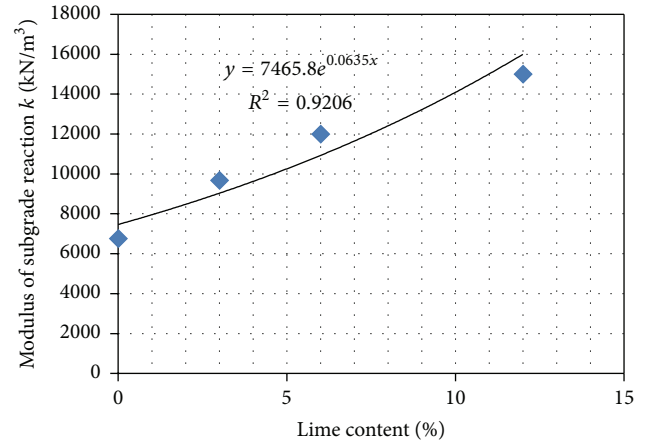


FIGURE 7: Modulus of subgrade reaction with respect to lime content in the soil.

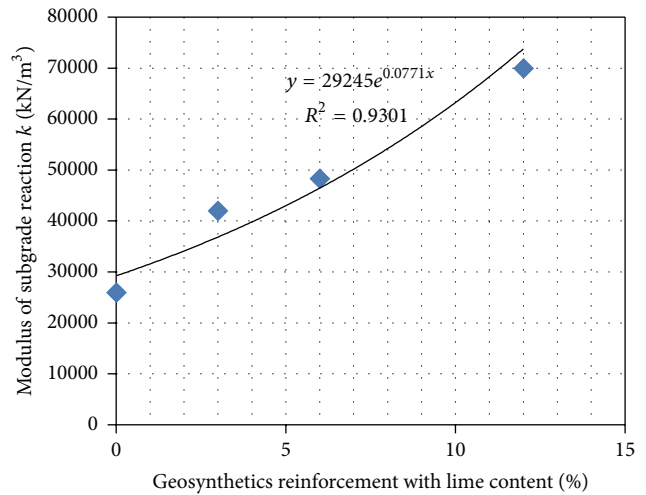


FIGURE 8: Modulus of subgrade reaction with respect to geosynthetics (geocell + geotextile) reinforcement with lime content in the soil.

5. Conclusion

In this paper, the effects of lime stabilization, geotextile reinforcement, geocell reinforcement, geosynthetics (geocell + geotextile) reinforcement, and lime stabilization + geosynthetics reinforcement were researched for unpaved road which has clayey subgrade with high water content. Model plate loading experiments were done in the laboratory for this purpose. Comparisons of these soil improvement methods were made. These comparisons have not been made before in the literature for ten different states examined in this study. This study is important to detect the optimum soil improvement method among lime stabilization, geocell, and geotextile reinforcement for unpaved roads with clayey subgrade which has high water content. Plate loading test was made by considering optimum dimensions obtained from other studies.

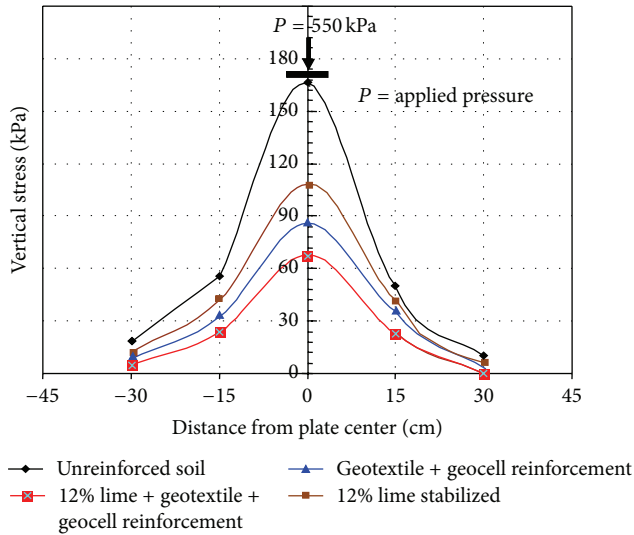


FIGURE 9: The vertical stress values on subgrade.

As a result of plate loading test, lime stabilization achieves decrease in soil settlement. 12% lime stabilization gave better results among 3, 6, and 12% lime treatments for reduction of settlements. Although lime stabilization or geotextile reinforcement decreases settlements, natural clayey soil with high water content (10% more than optimum content), 3 and 6% lime stabilization, and geotextile reinforcement did not meet the settlement requirement which must be at most 12% of the width of footing. 12% lime stabilization, geocell reinforcement, geosynthetics reinforcement, and geosynthetics reinforcement + lime stabilization gave the sufficient values for settlement among ten states in this study. Geosynthetics reinforcement + 12% lime stabilization was the best treatment to get lowest settlement and it was 5.6 times the settlement at natural state under 550 kPa loading pressure. The stress value measured at 23 cm lower than the bottom of the loading plate for natural state was 2.5 times the stress value obtained at 12% lime stabilization + geosynthetics reinforcement.

Lime stabilization and geosynthetics reinforcements all increased the modulus of subgrade reaction (k). But when the natural clayey soil, which has 35% water content by increasing the optimum water content of the clayey soil by 10%, has " k " value of 6765 kN/m^3 , only one state (geosynthetics + 12% lime stabilization) among 10 states applied to improve the soil in this experiment met the Highways Technical Specifications with a value of 70.000 kN/m^3 .

When clayey soil with high plasticity (Class CH), with 10% more water content than optimum water content, is used as an unpaved road base, it does not meet the bearing capacity and modulus of subgrade reaction requirements. Lime stabilization or geosynthetics reinforcements are not enough on their own for this purpose. It is recommended to stabilize the soil with 12% lime content and then reinforce it with geotextile and geocell to improve these types of soils to be used for unpaved roads.

Competing Interests

The authors declare that they have no competing interests.

References

- [1] A. Wilkinson, A. Haque, J. Kodikara, J. Adamson, and D. Christie, "Improvement of problematic soils by lime slurry pressure injection: case study," *Journal of Geotechnical and Geoenvironmental Engineering*, vol. 136, no. 10, pp. 1459–1468, 2010.
- [2] S. K. Dash and M. Hussain, "Lime stabilization of soils: reappraisal," *Journal of Materials in Civil Engineering*, vol. 24, no. 6, pp. 707–714, 2012.
- [3] N. R. Krishnaswamy, K. Rajagopal, and G. Madhavi Latha, "Model studies on geocell supported embankments constructed over a soft clay foundation," *Geotechnical Testing Journal*, vol. 23, no. 1, pp. 45–54, 2000.
- [4] S. N. Moghaddas Tafreshi and A. R. Dawson, "Comparison of bearing capacity of a strip footing on sand with geocell and with planar forms of geotextile reinforcement," *Geotextiles and Geomembranes*, vol. 28, no. 1, pp. 72–84, 2010.
- [5] S. Y. Liu, J. Han, D. W. Zhang, and Z. S. Hong, "A combined DJM-PVD method for soft ground improvement," *Geosynthetics International*, vol. 15, no. 1, pp. 43–54, 2008.
- [6] L. Zhang, M. Zhao, C. Shi, and H. Zhao, "Bearing capacity of geocell reinforcement in embankment engineering," *Geotextiles and Geomembranes*, vol. 28, no. 5, pp. 475–482, 2010.
- [7] F. G. Bell, "Lime stabilization of clay minerals and soils," *Engineering Geology*, vol. 42, no. 4, pp. 223–237, 1996.
- [8] J. E. Barker, C. D. F. Rogers, and D. I. Boardman, "Physiochemical changes in clay caused by ion migration from lime piles," *Journal of Materials in Civil Engineering*, vol. 18, no. 2, pp. 182–189, 2006.
- [9] J. K. Mitchell and K. Soga, *Fundamentals of Soil Behavior*, John Wiley & Sons, Hoboken, NJ, USA, 3rd edition, 2005.
- [10] N. C. Consoli, L. Lopes Jr., P. Prietto, L. Festugato, and R. Cruz, "Variables controlling stiffness and strength of lime-stabilized soils," *Journal of Geotechnical and Geoenvironmental Engineering*, vol. 137, no. 6, pp. 628–632, 2011.
- [11] S. K. Dash and M. Hussain, "Influence of lime on shrinkage behavior of soils," *Journal of Materials in Civil Engineering*, vol. 27, no. 12, Article ID 04015041, pp. 1–9, 2015.
- [12] A. Kavak, A. G. Güngör, C. Aşşar, B. Atbaş, and A. Akyarlı, "A lime stabilization application on a divided road project," in *Zemin Mekaniği ve Temel Mühendisliği Onikinci Ulusal Kongresi*, Selçuk University, Konya, Turkey, October 2008.
- [13] H. Zhou and X. Wen, "Model studies on geogrid- or geocell-reinforced sand cushion on soft soil," *Geotextiles and Geomembranes*, vol. 26, no. 3, pp. 231–238, 2008.
- [14] G. M. Latha and A. Somwanshi, "Effect of reinforcement form on the bearing capacity of square footings on sand," *Geotextiles and Geomembranes*, vol. 27, no. 6, pp. 409–422, 2009.
- [15] S. K. Dash, S. Sireesh, and T. G. Sitharam, "Model studies on circular footing supported on geocell reinforced sand underlain by soft clay," *Geotextiles and Geomembranes*, vol. 21, no. 4, pp. 197–219, 2003.
- [16] S. Sireesh, T. G. Sitharam, and S. K. Dash, "Bearing capacity of circular footing on geocell-sand mattress overlying clay bed with void," *Geotextiles and Geomembranes*, vol. 27, no. 2, pp. 89–98, 2009.

- [17] S. K. Dash, N. R. Krishnaswamy, and K. Rajagopal, "Bearing capacity of strip footings supported on geocell-reinforced sand," *Geotextiles and Geomembranes*, vol. 19, no. 4, pp. 235–256, 2001.
- [18] A. Emersleben and N. Meyer, "Bearing capacity improvement of gravel base layers in road constructions using geocells," in *Proceedings of the 12th International Conference of International Association for Computer Methods and Advances in Geomechanics (IACMAG '08)*, pp. 3538–3545, Goa, India, October 2008.
- [19] M.-H. Zhao, L. Zhang, X.-J. Zou, and H. Zhao, "Research progress in two-direction reinforced composite foundation formed by geocell reinforced mattress and gravel piles," *China Journal of Highway and Transport*, vol. 22, no. 1, pp. 1–10, 2009.
- [20] S. G. Thallak, S. Saride, and S. K. Dash, "Performance of surface footing on geocell-reinforced soft clay beds," *Geotechnical and Geological Engineering*, vol. 25, no. 5, pp. 509–524, 2007.
- [21] ASTM, "Standard practice for classification of soils for engineering purposes (unified soil classification system)," Tech. Rep. D2487, ASTM, West Conshohocken, Pa, USA, 2006.

Research Article

Sulfur Fixation by Chemically Modified Red Mud Samples Containing Inorganic Additives: A Parametric Study

Yang Liu, Yang Li, Feng-shan Zhou, Ying-mo Hu, and Yi-he Zhang

Beijing Key Laboratory of Materials Utilization of Nonmetallic Minerals and Solid Wastes, National Laboratory of Mineral Materials, School of Materials Science and Technology, China University of Geosciences (Beijing), Beijing 100083, China

Correspondence should be addressed to Feng-shan Zhou; zhousf@cugb.edu.cn

Received 23 January 2016; Revised 8 June 2016; Accepted 17 July 2016

Academic Editor: Santiago Garcia-Granda

Copyright © 2016 Yang Liu et al. This is an open access article distributed under the Creative Commons Attribution License, which permits unrestricted use, distribution, and reproduction in any medium, provided the original work is properly cited.

Sulfur retention ability of Bayer red mud from alumina plant was investigated. Bayer red mud modified by fusel salt and waste mother liquor of sodium ferrocyanide as the main sulfur fixation agent and the calcium based natural mineral materials as servicing additives; the experimental results showed the following: (1) Through 10 wt% waste mother liquor of sodium ferrocyanide modifying Bayer red mud, sulfur fixation rate can increase by 13 wt%. (2) Magnesium oxide can obviously improve the sulfur fixation performance of Bayer red mud and up to a maximum sulfur fixation rate of 47 wt% at adding 1 wt% magnesium oxide. (3) Dolomite enhanced the sulfur fixation performances with the sulfur fixation rate of 68 wt% in optimized condition. (4) Vermiculite dust reduced sulfur dioxide during the fixed-sulfur process of modified Bayer red mud, and the desulphurization ration could reach up to a maximum 76 wt% at 950°C. (5) An advanced three-component sulfur fixation agent was investigated, in which the optimized mass ratio of modified Bayer red mud, dolomite, and vermiculite dust was 70 : 28 : 2 in order, and its sulfur fixation efficiency has reached to a maximum 87 wt% under its 20 wt% dosage in the coal.

1. Introduction

Since the 1980s, with the rapid development of China's economy, the annual consumption of coal has been increasing by a large margin and China has become the largest producer and consumer of coal [1]. The main pollution of China is derived from emissions of SO₂ and dust caused by coal combustion. Therefore, the control of SO₂ emitted from industrial coal-fired boilers has great significance for air pollution control in our country [2]. Desulfurization technology is the main method to reduce SO₂ pollution [3]. At present, the commonly used desulphurization technology includes desulfurization before combustion, sulfur fixation during combustion, and flue gas desulfurization [4]. Developing a new type of sulfur fixing agents has become the most valuable industrial desulfurization technical way in coal combustion process [5]. At present, the mainly used sulfur-fixing agents at home and abroad include calcium-based, magnesium-based, sodium-based, and potassium-based sulfur-fixing agents [6–9]. Traditional calcium-based sulfur-fixing agent (limestone, dolomite, etc.) generally showed the disadvantages of low

calcium utilization rate and low sulfur fixation rate at high temperature [10].

In recent years, many domestic and foreign researchers found that the sulfur-fixing efficiency of coal combustion could be improved by modifying the fixing agents using sodium chloride [11], ethanol, and acetic acid [12] or adding Fe₂O₃, SiO₂, Al₂O₃, and Na₂CO₃ [13–18] to the sulfur-fixing agents.

In addition to the researches of sulfur-fixing additive, some industrial solid waste is also used as desulfurization agents such as Carbide slag, black liquor of papermaking, and red mud [19–26]. Bayer red mud is an industrial solid waste with high alkalinity and environmental impact, which is discharged during the process of Al₂O₃ extraction from bauxite in alumina plant. Disposal of Bayer red mud occupies large areas of productive land, and it is harmful to the environment due to its high alkalinity, heavy metals, and sometimes radioactivity [27–29]. Red mud is mainly composed of fine particles including Al₂O₃, Fe₂O₃, CaO, MgO, and Na₂O [19, 20]. Owing to its high alkalinity and chemical properties, Bayer red mud could be used as a kind

TABLE I: Chemical composition of Bayer red mud in the present work.

Components	Al ₂ O ₃	CaO	SiO ₂	Fe ₂ O ₃	Na ₂ O	MgO	Water	Loss
Content/wt%	24.35	19.96	18.12	7.79	5.54	1.47	0.87	14.25

of sulfur-fixing agent. This not only opens up a new way for the utilization of red mud but also finds a cheap and efficient sulfur-fixing agent for the coal industry.

In recent years, many domestic and foreign scholars focused their research on red mud slurry for flue gas desulfurization [21, 22]. But the red mud slurry is easy to harden and not conducive for long time use [23]. By adding natural minerals to Bayer red mud, a high performance synergistic sulfur-fixing agent was developed for sulfur fixation during coal combustion in the present work. According to the sulfur-fixing product of sulfur-fixing agent, we will continue to study the preparation of oilfield waste drilling fluid treatment agent using the sulfur-fixing product, which will truly achieve high value-added and clean utilization of red mud.

2. Materials and Methods

2.1. Materials

Raw Coal. Raw coal came from Zouping Weimian Corporation (Shandong, China). The total sulfur content in the coal sample was determined by Eschka method [30]. 0.2 g coal (200 mesh) was mixed with Eschka reagent and burned. The sulfur in the coal reacted with Eschka reagent to produce sulfate. Then, sulfate ions (SO₄²⁻) reacted with barium ions (Ba²⁺) to produce barium sulfate (BaSO₄). The total sulfur content was calculated according to the produced weight of BaSO₄. Experimental results showed that the total sulfur content of the raw coal was 1.685 wt%. According to the classification standard of sulfur coal [31], the raw coal belongs to the middle sulfur coal.

Bayer Red Mud. The red mud in the present work in the form of dried clay was obtained from Zhengzhou Great Wall Alumina Corporation (Henan Province, China). Table I shows the component contents of the red mud. The XRD pattern and its particle size distribution of the red mud sample are shown in Figures 1 and 2. The particle size of the red mud was in the range of 0.1–500 μm (generally finer than 200 mesh after drying and grinding). The mineral compositions of the Bayer red mud were very complicated [32], but the content of Al₂O₃ and SiO₂ was relatively high with 24.35 wt% and 18.12 wt%.

Modification Agents. Modification agents were the byproduct of yellow blood sodium (sodium ferrocyanide) solution from Hebei Chengxin Co., Ltd. (Hebei, China), and fusel alcohol salts from Changchun Dacheng Industry Company (Jilin, China). The chemical composition was shown in Tables 2 and 3.

Sulfur Fixation Additives. Magnesium oxide (MgO, industrial grade, purity more than 95 wt%) was obtained from Beijing

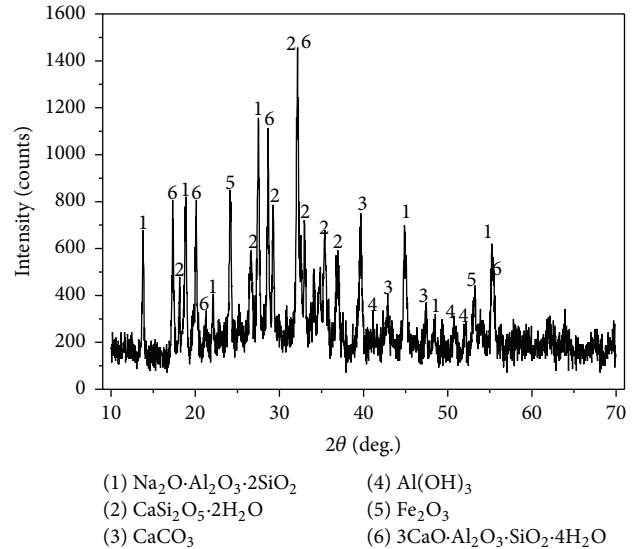


FIGURE 1: XRD of Bayer red mud in the present work.

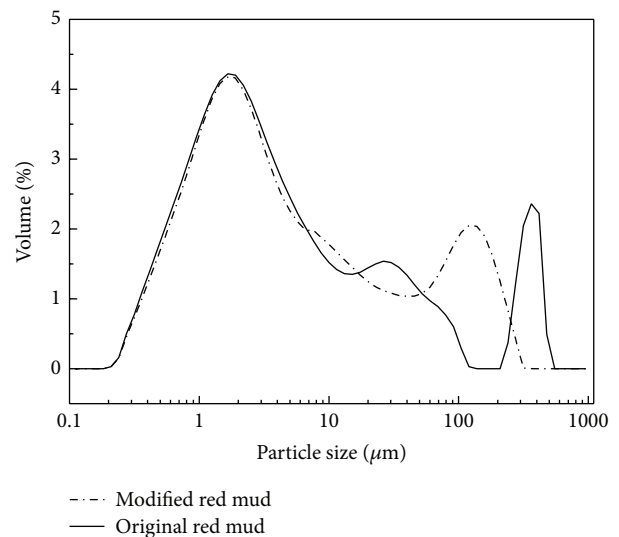


FIGURE 2: Particle size distribution of Bayer red mud in the present work.

Chemical Plant. The natural mineral materials brucite and dolomite were obtained from Dandong Yilong Gaoke New Material Co., Ltd. (Liaoning, China); both of their particle sizes were in the range of 800–1000 mesh.

Sulfur Fixation Promoter. Byproduct dust of vermiculite obtained from Hebei Chenxiang Mineral Materials Research Institute (Hebei, China) has been designated as promoter; its particle size was in the range of 60–200 mesh.

TABLE 2: Chemical composition of waste mother liquor of sodium ferrocyanide.

Components	Na ₂ Fe(CN) ₆	HCOONa	Na ₂ CO ₃	Water
Content/wt%	5.29	39.83	5.27	49.31

2.2. Laboratory Instruments. The pH of red mud suspension in the reaction process was measured by pH500 meter. The chemical analytical methods of Al₂O₃, CaO, and MgO were Karl Fischer titration, SiO₂ by gravimetry, and Fe₂O₃ by colorimetry and K₂O/Na₂O was determined by FP-640 Flame Photometer. The XRD patterns of the samples were determined by X-ray diffractometer with a Cu K α (0.15418 nm) radiation source in a 2 θ range of 10°–70° at a scanning rate of 2° min⁻¹. The morphologies of red mud were analyzed by Hitachi S-4800 high resolution ice emission scanning electron microscopy (SEM) [33].

Both of the SK-G10123K Tube furnace and the SK-G18123 Muffle furnace were purchased from Zhonghuan Experiment Electric Furnace Co., Ltd. (Tianjin, China). Heating rate of the SK-G10123K Tube furnace was 5°C/min at below 500°C, 10°C/min at 500–800°C, 5°C/min at 800–1000°C, and less than 2°C/min at 1000–1200°C. The length of its heating zone was 420 mm, and its constant temperature zone was 200 mm. Muffle furnace SK-G18123 Model with resistance wire heating was used; its heating process was 100°C to the maximum 1200°C in 40 min.

2.3. Experimental Methods

2.3.1. Modification Experiment of Bayer Red Mud. The Bayer red mud was immersed in modification agents with certain concentration for 24 h. Then, it was taken out and dried in an oven at constant temperature of 80°C for 12 h. Finally, it was taken out from the oven, milled, and screened as a reserve. Particle size distribution of original and modified Bayer red mud is shown in Figure 2.

2.3.2. Sulfur Fixation Experiment. Sulfur fixation for combustion coal was carried out in the SK-G10123K Tube furnace. The furnace was heated to 950°C according to its heating rate procedure firstly; then the specified amount of coal sample mixed sulfur fixation agents beforehand was loaded in a combustion boat, the coal sample was pushed slowly to the furnace inside, and finally air was pumped into the furnace to make a full combustion of the coal sample.

2.3.3. The Calculation of Sulfur Fixation Rate and the Utilization Rate of Calcium. The sulfur content was determined by using chemical analysis method. The sulfur fixation efficiency η (see (1)) and the utilization rate of calcium η_{Ca} (see (2)) [26, 34] were determined by testing the total sulfur content in coal ash and the coal sample:

$$\eta = \frac{m_2 \times S_{ad}}{m_1 \times S_{t,ad}} \times 100\%, \quad (1)$$

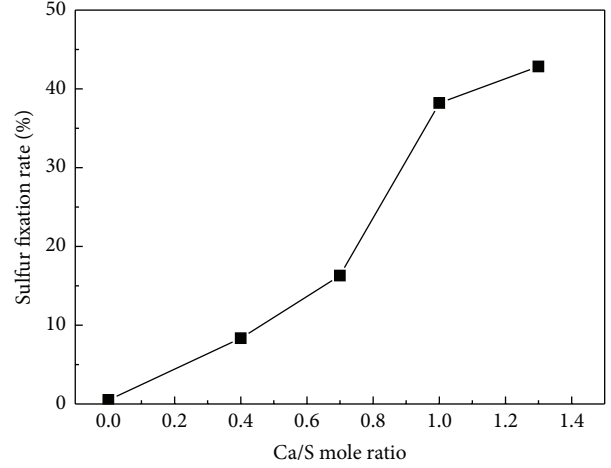


FIGURE 3: Influence of Ca/S mole ratio on the sulfur fixation effect.

where η is sulfur fixation efficiency; m_1 is experimental coal sample mass, g; m_2 is total mass of ash after combustion, g; S_{ad} is the sulfur content of ash, wt%; and $S_{t,ad}$ is total sulfur content of experimental coal sample, wt%. Consider

$$\eta_{Ca} = \frac{S_{ad} \times m_2 \times 56}{32 \times M_{sfa} \times W_{CaO}} \times 100\%, \quad (2)$$

where η_{Ca} is utilization rate of calcium, wt%; m_2 is total mass of ash after combustion, g; S_{ad} is the sulfur content of ash, wt%; M_{sfa} is the mass of adding sulfur fixation agent in the experiment, g; W_{CaO} is percentage content of CaO in the sulfur fixation agent, wt%.

3. Results and Discussion

3.1. Influence of Ca/S Mole Ratio on the Sulfur Fixation Effect. The Ca/S mole ratio is one of the main factors that affect the sulfur fixation effect. Using Bayer red mud as the sulfur fixation agent, the influence of Ca/S mole ratio on the sulfur fixation efficiency was studied. The results were shown in Figure 3.

Figure 3 indicated that the sulfur fixation rate increased with the increase of the Ca/S mole ratio when Bayer red mud was used as sulfur fixation agent. However, the increase of the Ca/S mole ratio would greatly increase the amount of sulfur fixation agent and reduce the heating rate of the coal. So, the doping content of Bayer red mud in the following experiment was optimized to be 10 wt% (the mole ratio of Ca/S was 0.7).

3.2. The Influence of Modification on the Sulfur Fixation Effect

3.2.1. The Influence of Modification on the Sulfur Fixation Efficiency. Experimental results indicated that the maximum sulfur fixation efficiency of original Bayer red mud was only 42.83 wt% when the mass dosage of red mud as sulfur fixation agent was 20 wt% coal sample. Modification activation method was used to improve the sulfur fixation efficiency of red mud. Fusel salt and waste mother liquor of sodium ferrocyanide were used as modification agents. The influence

TABLE 3: Chemical composition of the fusel salt.

Components	Ethylene glycol, propylene glycol, butyl glycol, glycerin, and so forth	Salt mix (sodium formate, sodium acetate and sodium lactate, etc.)	Polyether polyols (low polymerization degree)	Water
Content/wt%	35~45	20~30	25~35	<1

TABLE 4: Effect of the fusel salt on sulfur fixation of modified Bayer red mud.

Amount/wt%	0	10	30	50
Sulfur content in the residue/wt%	0.667	0.877	1.171	1.684
Utilization rate of Ca/wt%	10.20	16.20	21.95	31.61
Sulfur fixation rate/wt%	8.333	12.06	17.87	23.54

TABLE 5: Effect of the waste mother liquor of sodium ferrocyanide on sulfur fixation of modified Bayer red mud.

Amount/wt%	0	10	20	30
Sulfur content in the residue/wt%	0.667	1.876	1.209	1.224
Utilization rate of Ca/wt%	10.20	40.10	26.43	23.64
Sulfur fixation rate/wt%	8.333	29.85	20.58	18.48

of different amount wt% of fusel salt and waste mother liquor of sodium ferrocyanide on the sulfur fixation efficiency of Bayer red mud was studied.

The results of Tables 4 and 5 and Figure 4 indicated that the sulfur fixation efficiency could increase by 7 percentage points after the Bayer red mud was modified by 50 wt% fusel solution. Meanwhile, the utilization efficiency also increased from 22.02 wt% to 31.61 wt%. But the red mud after fusel modification was not easy to be dried and crushed and the mixing was not uniform. For the 10 wt% sodium ferrocyanide modified Bayer red mud, the sulfur fixation efficiency could increase by 13 percentage points and the utilization efficiency increased to 40.10 wt%.

3.2.2. The Influence of Modification on the Surface Morphology of Bayer Red Mud. The results of Scanning Electronic Micrography (SEM) indicated that the morphology of the Bayer red mud modified by fusel salt and sodium ferrocyanide changed after calcination at 950°C (Figure 5). Non-significant structural change was observed in the three samples in Figure 5, but the sodium ferrocyanide modified sample showed a relatively more change in the formation of porous structure. Agglomeration was still noticeable in unmodified and modified red mud. The particles of unmodified Bayer red mud agglomerated more seriously, which was not conducive to the diffusion of SO₂ and the sulfur fixation reaction. In contrast, the secondary pore structure in the modified sample was beneficial to the diffusion of the gases and promoted the sulfur fixation reaction. It was possible that the specific surface area (SSA) and porosity increased the fixation degree. Figure 6 shows the secondary porous structure after sulfur fixation reaction of modified red mud; the SSA has indeed increased (Table 6). As predecessors had proposed that the influence of pore structure characteristics on their sulfur fixation performance was very important, little pores made a significant contribution to alkaline substance utilization

TABLE 6: Specific surface area (SSA) of modified Bayer red mud before and after sulfur fixation reaction.

Sample	Specific surface area with BET method (m ² /g)
Original Bayer red mud	14.100
Bayer red mud modified by 50 wt% fusel solution	99.086
Bayer red mud modified by 10 wt% sodium ferrocyanide solution	142.300
Sulfur fixation ashes formed at 950°C after the sulfur fixation reaction of three-component sulfur fixation agent SFG-2	176.179

in the initial stage of reaction and at lower temperature, while bigger pores took effect in the later stage and at higher temperature. The more the pore in range of effective aperture, the better the sulfur fixation performance [35].

3.3. The Influence of Additives on the Sulfur Fixation Efficiency. Because single modified Bayer red mud showed lower sulfur fixation efficiency, it was necessary to add some additives to improve sulfur fixation efficiency. In this paper, the effects of additives of magnesium containing were mainly studied.

3.3.1. The Influence of MgO on the Sulfur Fixation Efficiency. MgO additives with doping content of 1 wt%, 2 wt%, and 3 wt% were added together with Bayer red mud to the coal samples. Experimental results of Figures 7 and 8 indicated that MgO significantly improved the sulfur fixation efficiency of the combustion coal. With the increase of MgO doping content, the sulfur fixation efficiency showed a decreasing trend after the first increase. The sulfur fixation efficiency was optimized to be 46.56 wt% when the doping content of MgO was 1 wt%.

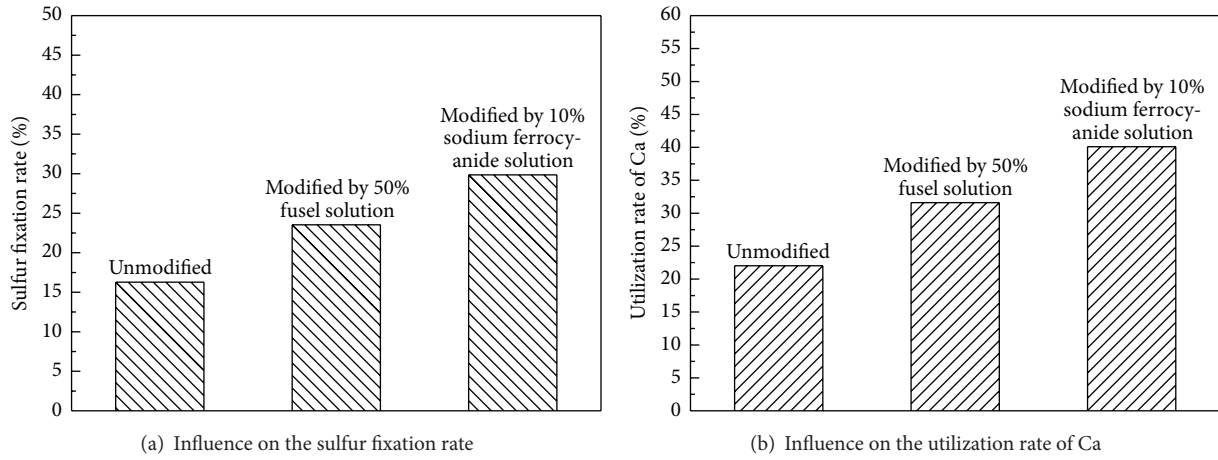


FIGURE 4: Test results for modified Bayer red mud with different solutions.

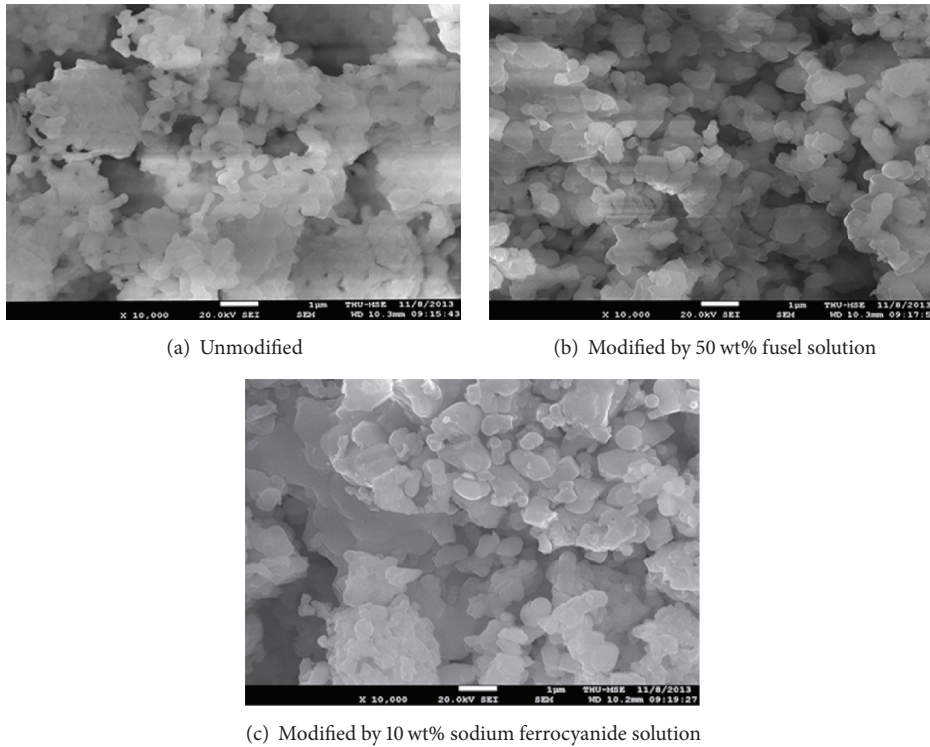


FIGURE 5: SEM photographs of modified Bayer red mud with different solutions.

During the sulfur fixation process, SO_2 transformed into sulfate by reacting with MgO . Meanwhile, MgO showed catalytic effects on sulfur fixation reaction for combustion of coal [36]. So the addition of MgO increased the sulfur fixation efficiency and improved the utilization rate of calcium (the highest utilization rate could reach 56.35 wt%).

3.3.2. The Influence of Natural Mineral Materials Additives on the Sulfur Fixation Efficiency. Both of dolomite and brucite with doping content of 1 wt%, 2 wt%, 3 wt%, and 4 wt% were added together with Bayer red mud to the coal samples.

The influence of dolomite and brucite on the sulfur fixation efficiency of the combustion coal was studied, respectively. The sulfur fixation efficiency increased with the addition of the two natural mineral materials (Figure 9). As an effective sulfur fixation mineral material, dolomite was better than brucite. The sulfur fixation efficiency was optimized to be 67.70 wt% when the doping content of dolomite was 4 wt%. Meanwhile, the paper researched the effect of the mass ratio of brucite and dolomite (4:0, 3:1, 2:2, 1:3, and 0:4) on the sulfur fixation efficiency. According to Figure 10, the results showed that the efficiency of sulfur fixation was different under the same temperature but different dolomite/brucite

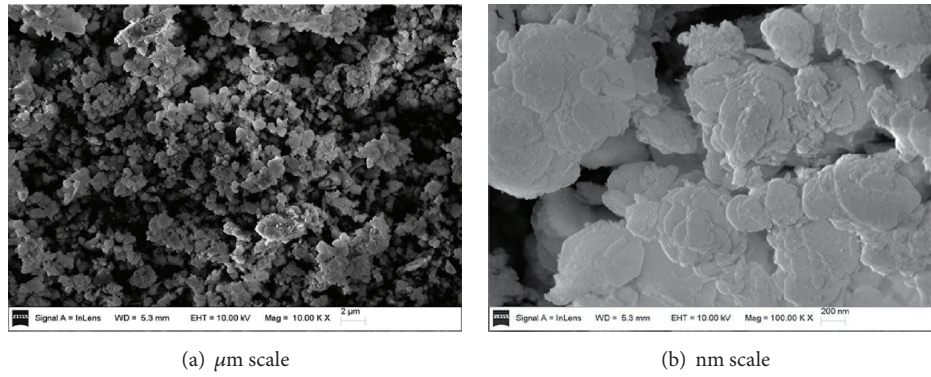


FIGURE 6: SEM photographs of secondary porous structure of sulfur fixation ashes formed after the sulfur fixation reaction of three-component sulfur fixation agent SFG-2.

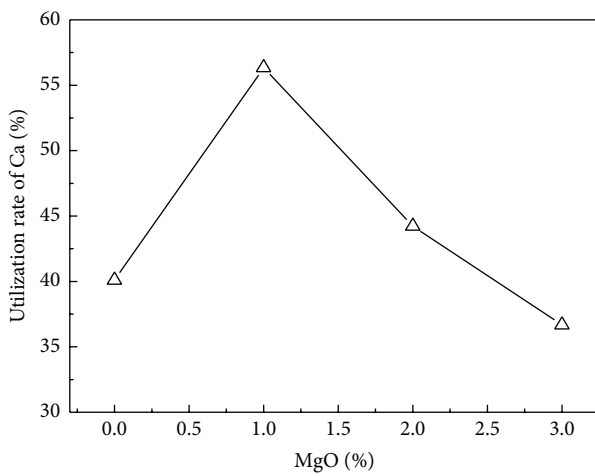


FIGURE 7: Effect of MgO on the utilization rate of Ca.

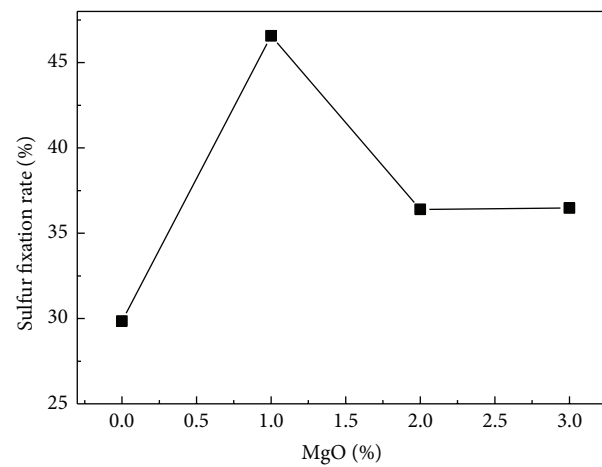


FIGURE 8: Effect of MgO on the sulfur fixation rate.

ratio; with the dolomite increasing or brucite decreasing, the sulfur fixation increased, and the sulfur fixation efficiency was maximum 67.70 wt%; with the only doping content of dolomite was 4 wt%. According to above results, the paper selected dolomite as the additives of sulfur fixation agents and developed a new kind of sulfur-fixed agent named SFG-1 which is composed of modified Bayer red mud and dolomite with the mass ratio of 10:4 in order. At 950°C, CaO and MgO derived from the decomposition of dolomite and brucite could react with SO₂, showed a certain catalytic effect on sulfur fixation reaction, and improved the sulfur fixation efficiency. Besides, adding dolomite could improve pore structure of the red mud after high temperature calcination, accelerate the forming of high temperature stability of sulfide minerals, and restrain the decomposing of CaSO₄ [19], which made the sulfur fixation efficiency improved. And the existence of dolomite can improve the pore structure of red mud in high temperature, which also enhanced the own desulfurization efficiency of Bayer red mud.

3.4. The Influence of Promoter on the Sulfur Fixation Efficiency.
In order to further improve the sulfur fixation effect of

combustion, the promoter added again by experimental design. Although the layered structure and dilatibility of vermiculite promoted the inner oxidation extent of the coal combustion and enhanced the fixed-sulfur efficiency [37], vermiculite was difficult to crush because of its good toughness, so as to increase the cost of crushing. However, the dust from vermiculite industry was mainly composed of fine particles (160–200 mesh) and had high specific surface area. Using the vermiculite dust replacing normal industrial vermiculite as coal-burning sulfur-fixed promoter, the effect of different doping content of vermiculite dust (0.1 wt%, 0.2 wt%, 0.3 wt%, and 0.4 wt%) on fixed-sulfur efficiency was researched.

According to the experimental results (Figure 11), vermiculite dust could promote the fixed-sulfur efficiency. Experimental results showed that vermiculite dust played an important role in reducing SO₂ during the fixed-sulfur process of modified Bayer red mud or SFG-1, and the desulfurization ration could reach up to maximum 76 wt% at 950°C. The main reasons were that further inflating of vermiculite dust at 950°C could make the inner looser and promote the inner oxidation extent of the coal combustion,

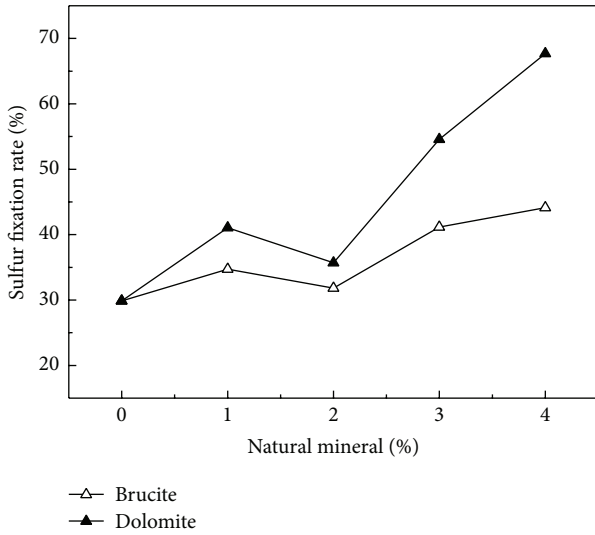


FIGURE 9: Effect of natural minerals on sulfur fixation rate.

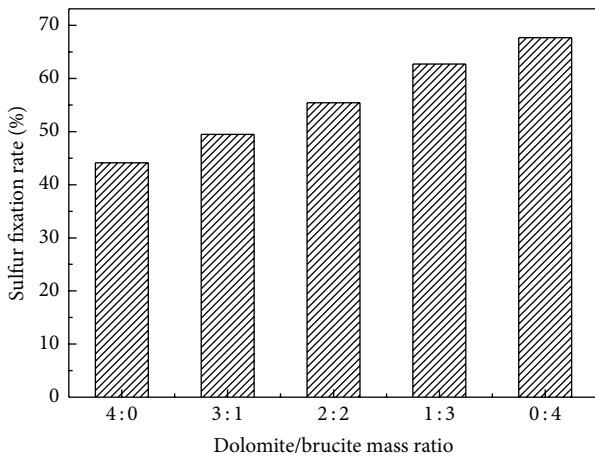


FIGURE 10: Effect of dolomite/brucite ratio on sulfur fixation rate.

which was advantageous to forming CaSO_4 and restraining the decomposing of CaSO_4 [38]. So, an advanced complex sulfur fixation agent named SFG-2 was made successfully by the experimental studies in which Bayer red mud was the main desulphurization composition, dolomite served as additives, vermiculite dust played the inflation role, and the optimized mass ratio of them in order was 70 : 28 : 2.

3.5. The Influence of SFG-2 on the Sulfur Fixation Efficiency. The influence of SFG-2 content ranging in the coal from 10 wt% up to 25 wt% on the sulfur fixation efficiency was studied. Experimental results (Figure 12) showed that SFG-2 achieved desulphurization ration maximum 87 wt% when the doping content of SFG-2 in the coal was up to 20 wt% (i.e., Ca/S mole ratio was 1.3), and it may be inferred that the tricomponent composite SFG-2 was indeed an advanced desulphurization material.

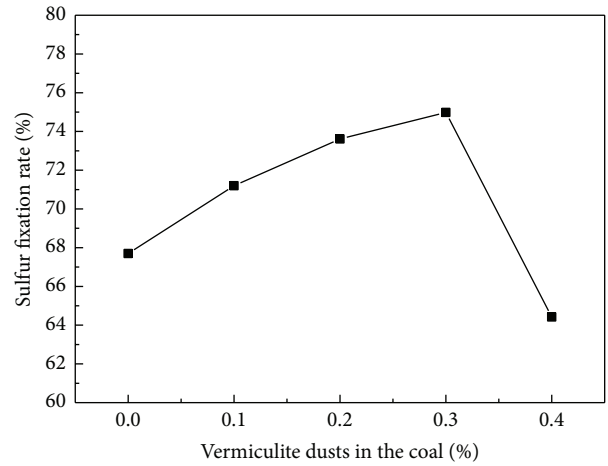


FIGURE 11: Effect of vermiculite dust on sulfur fixation rate under 4 wt% dosage.

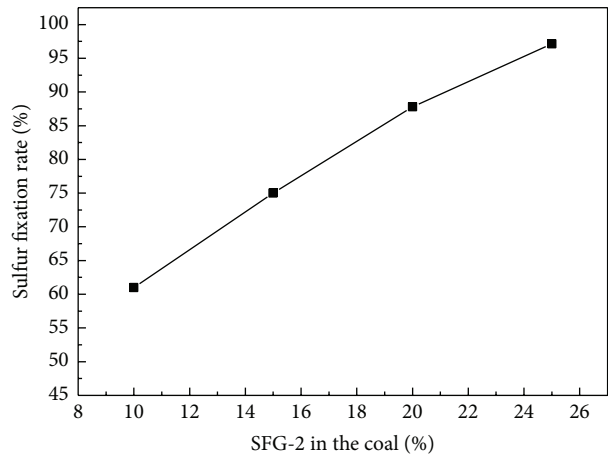
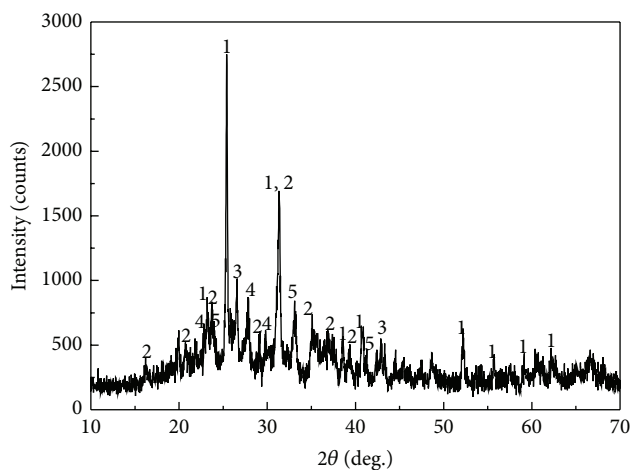


FIGURE 12: Effect of tricomponent composite SFG-2 on sulfur fixation rate under 20 wt% dosage.

3.6. XRD of Desulphurization Produced Ashes. The structural characteristic of desulphurization produced ashes was investigated by X-ray diffraction (XRD), and the analysis results of the produced ashes used SFG-2 as sulfur fixation agent at 950°C were shown in Figure 13. The diffraction structural peaks of CaSO_4 , Fe_2O_3 , $\text{Ca}_2\text{Al}_2\text{SiO}_7$, and $(\text{Na,Ca})\text{Al}(\text{Si,Al})_3\text{O}_8$ could be clearly found, especially CaSO_4 , which showed that CaSO_4 was the main component of sulfur fixation produced ashes at 950°C and the content is more. Besides, the existence of $\text{Ca}_2\text{Al}_2\text{SiO}_7$ and $(\text{Na,Ca})\text{Al}(\text{Si,Al})_3\text{O}_8$ also improved the sulfur fixation efficiency [32].

4. Conclusion

- (1) The sulfur fixation rate of Bayer red mud could be improved by using fusel salt and waste mother liquor of sodium ferrocyanide as the modifying agents. When 50 wt% fusel salt solution was used as



- | | |
|--|---|
| (1) CaSO_4 | (4) $(\text{Na}, \text{Ca})\text{Al}(\text{Si}, \text{Al})_3\text{O}_8$ |
| (2) $\text{Ca}_2\text{Al}_2\text{SiO}_7$ | (5) Fe_2O_3 |
| (3) SiO_2 | |

FIGURE 13: XRD of sulfur fixation produced ashes.

modifying agent, the sulfur fixation rate increased by 7 wt% and the utilization rate of calcium increased from 22.02 wt% to 31.61 wt%. When modified by waste mother liquor of sodium ferrocyanide with the concentration of 10 wt%, sulfur fixation rate could increase by 13 wt%, the highest of which could reach 29.85 wt% and the utilization rate of calcium reached 40.10 wt%.

- (2) Magnesium oxide (MgO) could obviously improve the sulfur fixation performance of Bayer red mud and up to a maximum sulfur fixation rate of 46.56 wt% with the 1 wt% MgO adding.
- (3) The sulfur fixation efficiency increased with the addition of the two natural mineral materials. Dolomite showed better effect than brucite. And the efficiency of sulfur fixation was different at 950°C with different dolomite/brucite ratio. With the dolomite increasing and brucite decreasing, the sulfur fixation increased. The sulfur fixation efficiency was 67.70 wt% when the sulfur fixation agent consisted of 10 wt% Bayer red mud and 4 wt% dolomite.
- (4) Vermiculite dust could promote the fixed-sulfur efficiency. The main reasons were that further inflating of vermiculite dust at 950°C could make the inner looser and promote the inner oxidation extent of the coal combustion, which was advantageous to forming CaSO_4 and restraining the decomposing of CaSO_4 .
- (5) A new kind of tricomponent complex sulfur fixation agent SFG-2 was made successfully, in which modified Bayer red mud was the main desulphurization composition, dolomite served as additives, vermiculite dust played the inflation role, and the optimized mass ratio in order was 70 : 28 : 2. The SFG-2 achieved desulphurization ration maximum 87 wt% when the doping content of SFG-2 in the coal was 20 wt% (i.e.,

Ca/S mole ratio was 1.3), which indeed proved the advanced desulphurization characteristics of SFG-2.

Competing Interests

The authors declare that there is no conflict of interests regarding the publication of this paper.

Authors' Contributions

Yang Liu and Yang Li contributed equally to this work.

Acknowledgments

This research was supported by the National High Technology Research and Development Program of China (863 Program 2012AA06A109).

References

- [1] J. Wang and H. M. Zhang, "Air pollution by sulfur dioxide and its control of coal fired industrial boilers in China," *Electric Power Environmental Protection*, vol. 20, pp. 43–46, 2004.
- [2] H. M. Zhang and J. Wang, "Control of sulfur dioxide pollution from industrial coal fired boiler," *Electric Power Environmental Protection*, vol. 20, pp. 38–42, 2004.
- [3] N. N. Zhang, Y. Jiang, and D. P. Xu, "The research status on sulfur solidifying technique during coal high-temperature combustion," *Coal Quality Technology*, vol. 24, no. 1, pp. 8–10, 2010.
- [4] C. L. Chou, "Geologic characteristics of sulfur in coals and development of the clean coal technologies," *Earth Science Frontiers*, no. 1, pp. 23–27, 1999.
- [5] B. Lin, Y. Z. Ge, and X. L. Zhang, "Introduction of fixed-sulphur technology on calcium-based sorbents," *Coal Chemical Industry*, vol. 74, pp. 48–51, 1996.
- [6] J. H. Li and A. H. Lu, "Effect of Ca-based mineral sulfur-fixing agent on sulfur retention of different kinds of coals," *Techniques and Equipment for Environmental Pollution Control*, vol. 7, pp. 36–40, 2006.
- [7] Z.-S. Yuan, D.-Y. Wu, and S.-D. Wang, "Study on sulfur retention of integrated additive during coal combustion," *Journal of Fuel Chemistry and Technology*, vol. 30, no. 1, pp. 36–40, 2002.
- [8] S.-L. Wang, "Influence of CaO/MgO ratios on efficiency of sulfur fixation," *Coal Geology & Exploration*, vol. 31, no. 2, pp. 4–7, 2003.
- [9] N. Li, W. P. Liu, J. H. Zhou, and K. F. Cen, "Sulfur capture mechanism and application of novel barium-based sorbents at high temperature," *Journal of Chemical Industry and Engineering (China)*, vol. 53, pp. 1198–1201, 2002.
- [10] Z. H. Zhang and X. D. Ma, "Research status of sulfur-fixing agent," *China Resources Comprehensive Utilization*, vol. 27, pp. 13–14, 2009.
- [11] P. Davini, G. DeMichele, and P. Ghetti, "An investigation of the influence of sodium chloride on the desulphurization properties of limestone," *Fuel*, vol. 71, no. 7, pp. 831–834, 1992.
- [12] Y. Fu, G. Z. Lin, and Y. H. Zhuang, "On the role of sodium additives in desulfurization during coal briquette combustion," *Environmental Chemistry*, vol. 13, pp. 492–493, 1994.

- [13] L. R. Chen, L. M. Ge, and A. N. Zhou, "Study on modified calcium hydroxide with sodium alkali used as briquette capturing sulfur agent," *Clean Coal Technology*, vol. 11, pp. 73–75, 2005.
- [14] K.-H. Han, J.-L. Zhao, B. Zheng, C.-M. Lu, and G.-J. Zhao, "Sulfur retention performance and modification of alkaline wastes used in coal combustion," *Journal of the China Coal Society*, vol. 34, no. 12, pp. 1698–1702, 2009.
- [15] C. H. Dai and W. L. Zheng, "Catalytic sulfur retention of the transition-metal oxides under fluidized-bed combustion conditions," *Coal Chemical Industry*, vol. 38, no. 1, pp. 31–34, 2011.
- [16] Z. H. Wu, P. Kou, Y. X. Shi, J. P. Zhang, and J. Wang, "Effects of alkali carbonates on the CaO desulfurization," *Coal Conversion*, vol. 23, pp. 59–62, 2000.
- [17] X. Z. Gong, Z. C. Guo, and Z. Wang, "Reactivity of pulverized coals during combustion catalyzed by CeO_2 and Fe_2O_3 ," *Combustion and Flame*, vol. 157, no. 2, pp. 351–356, 2010.
- [18] Z. Z. Li and B. Q. Xiao, "Study of a newly high-temperated compound sulfur fixation agent for burning-coal," *Science Technology and Engineering*, vol. 7, pp. 3896–3902, 2007.
- [19] G.-J. Zhao, C.-M. Lu, Y. Tian, Z.-Y. Fan, J.-L. Zhao, and Z.-Y. Zhang, "Desulfurization characteristic and mechanism of red mud from alumina plant," *Journal of Fuel Chemistry and Technology*, vol. 36, no. 3, pp. 365–370, 2008.
- [20] S. Wang, H. M. Ang, and M. O. Tadó, "Novel applications of red mud as coagulant, adsorbent and catalyst for environmentally benign processes," *Chemosphere*, vol. 72, no. 11, pp. 1621–1635, 2008.
- [21] S. Z. Yu and R. L. Man, "Application of red mud in flue gas desulfurization from thermal power plant," *Mining and Metallurgical Engineering*, vol. 25, pp. 63–65, 2005.
- [22] Y. N. Chen and J. X. Nie, "Adsorption of SO_2 from flue gas with wastewater in red mud," *Nonferrous Metals*, vol. 59, pp. 153–155, 2007.
- [23] X. Wang, X. H. Bao, and A. X. Zheng, "Study on the sulfur fixation of coal burning by red mud," *Fly Ash Comprehensive Utilization*, no. 6, pp. 23–25, 2010.
- [24] H. T. Liu, K. H. Han, H. Li et al., "Sulfur retention performance of limestone modified by red mud for CFB boiler," *Thermal Power Generation*, vol. 41, no. 9, pp. 7–11, 2012.
- [25] G. X. Yin, C. Ning, and X. F. Fu, "Development of sulfur fixation and combustion-supporting agent for loose coal using red mud and black liquor of papermaking," *Environmental Engineering*, vol. 22, no. 2, pp. 19–22, 2004.
- [26] C. S. Lv, J. W. Wang, and C. Y. Lu, "The summary of the desulfurization process with Bayer red mud," *Guangzhou Chemical Industry*, vol. 40, pp. 20–22, 2012.
- [27] R. K. Paramguru, P. C. Rath, and V. N. Misra, "Trends in red mud utilization—a review," *Mineral Processing and Extractive Metallurgy Review*, vol. 26, no. 1, pp. 1–29, 2005.
- [28] Y.-C. Huang, N. Wang, J. Wan et al., "Comprehensive utilization of red mud and control techniques of radioactive issues," *Bulletin of Mineralogy Petrology and Geochemistry*, vol. 28, no. 2, pp. 128–130, 2009.
- [29] H. N. Gu, N. Wang, and N. C. Zhang, "Study on radioactivity level of red mud and radiological constraints of usability as building materials," *Light Metals*, no. 5, pp. 19–21, 2011.
- [30] "Methods for analysis and testing of coal and coke—ultimate analysis of coal and coke—determination of total sulfur content—eschka method," Tech. Rep. BS 1016-106.4.1-1993, British Standards Institution, 1993.
- [31] China Coal Industry Association & China National Standardization Management Committee, "Classification of quality of coal—part 2: sulfur content," Tech. Rep. GB/T 15224.2, China Standard Press, Beijing, China, 2010.
- [32] K. Q. Wang and S. H. Li, "A study on occurrence mode of rare earth metals in red mud from Bayer process," *Light Metals*, no. 10, pp. 13–16, 2012.
- [33] X. K. Wang, Y. H. Zhang, F. Z. Lv et al., "Removal of alkali in the red mud by SO_2 and simulated flue gas under mild conditions," *Environmental Progress & Sustainable Energy*, vol. 34, no. 1, pp. 81–87, 2015.
- [34] H. Y. Qi, C. F. You, and A. J. Wang, "Influence of temperature on enhancing calcium conversion rate of sorbent and effects of steam reactivation," *Journal of Engineering Thermophysics*, vol. 24, pp. 717–719, 2003.
- [35] G. J. Zhao, F. J. Yin, J. Li, and X. Y. Li, "Study on pore structure and sulfur fixation characteristics of alkali industrial waste," *Advanced Materials Research*, vol. 194–196, pp. 716–721, 2011.
- [36] Y. Tan, *Experiment research of additives on sulfur capture during coal combustion and analysis of mechanism on promoting effect [M.S. thesis]*, Hunan University, Hunan, China, 2005.
- [37] M. Geng, L. Shi, and W. D. Xu, "Experimental research on using vermiculite as coal-burning sulfur-fixed additive," *Non-Metallic Mines*, vol. 29, pp. 28–30, 2006.
- [38] J. H. Li, A. H. Lu, and C. X. Chen, "The application of vermiculite to the desulphurization and dusts clearing during coal combustion," *Acta Petrologica et Mineralogica*, vol. 20, pp. 515–524, 2001.

Research Article

Application of Coal Ash to Postmine Land for Prevention of Soil Erosion in Coal Mine in Indonesia: Utilization of Fly Ash and Bottom Ash

**Shinji Matsumoto,¹ Shunta Ogata,¹ Hideki Shimada,¹ Takashi Sasaoka,¹
Ginting J. Kusuma,² and Rudy S. Gautama²**

¹Department of Earth Resources Engineering, Kyushu University, 744 Motoooka, Nishi-ku, Fukuoka 8190395, Japan

²Department of Mining Engineering, Institute of Technology Bandung, Jalan Ganesha No. 10, Bandung, Jawa Barat 40132, Indonesia

Correspondence should be addressed to Shinji Matsumoto; shinji12@kyudai.jp

Received 21 April 2016; Accepted 17 July 2016

Academic Editor: Guocheng Lv

Copyright © 2016 Shinji Matsumoto et al. This is an open access article distributed under the Creative Commons Attribution License, which permits unrestricted use, distribution, and reproduction in any medium, provided the original work is properly cited.

The increase in the number of coal-fired power plants with the increase in coal production and its consumption has caused the problem of the treatment of a large amount of coal ash in Indonesia. In the past studies, coal ash was applied to postmine land with the aim of improving soil conditions for plant growth; however, heavy rain in the tropical climate may cause soil erosion with the change in soil conditions. This study presents the effects of application of coal ash to postmine land on soil erosion by performing the artificial rainfall test as well as physical testing. The results indicate that the risk of soil erosion can be reduced significantly by applying the coal ash which consists of more than 85% of sand to topsoil in the postmine land at the mixing ratio of over 30%. Additionally, they reveal that not only fine fractions but also microporous structures in coal ash enhance water retention capacity by retaining water in the structure, leading to the prevention of soil erosion. Thus, the risk of soil erosion can be reduced by applying coal ash to topsoil in consideration of soil composition and microporous structure of coal ash.

1. Introduction

Indonesia is one of the largest coal exporters in the world, and the amount of coal production and the export has grown at an annual average rate of more than 10% since 2000 [1]. The increase in domestic demand for coal with economic growth has promoted the energy policy such as the conversion to coal-fired power generation and the construction of new coal-fired plant in Indonesia [2]. This change created the problem of the disposal of a large amount of coal ash [3]. Although coal ash such as fly ash and bottom ash are, generally, disposed of to landfill as industrial waste, the efficient use of them is required due to landfill shortage. 80% of coal ash has ever been reutilized as cement raw materials in Indonesia; however, alternative proposal for effective use of them is needed in consideration of the increase in the amount of coal ash in the future. In the past studies, coal ash was utilized for improvement of soil conditions in revegetation

area [4–7]. Though coal ash was also used for reclamation in mining areas in some cases [8–11], a high annual precipitation and a squall in the tropical climate in Indonesia may cause soil erosion with the change in soil conditions in the area. Evaluation of soil erosion in postmine land to which coal ash is applied is important to verify the applicability of coal ash to postmine land as well as the effects on plant growth. However, soil erosion in postmine land to which coal ash was applied in Indonesia was evaluated in a few studies.

Coal ash is produced with combustion gas by variation of ash composed of SiO_2 and Al_2O_3 after carbon and hydrogen burn in coal-fired power plant. The physical and chemical properties of coal ash are dependent on combustion process and power plant design [12]. Thus, the physical and chemical properties affect the applicability of coal ash in postmine land.

In the tropical climate where annual rainfall exceeds 2,500 mm, heavy rain and/or squall is a major cause of soil erosion [13]. Figure 1 shows the mechanism of soil erosion.

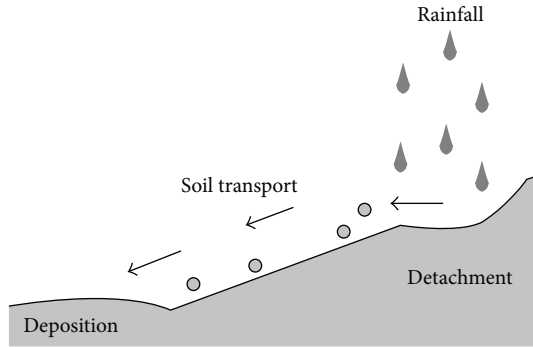


FIGURE 1: Mechanism of soil erosion.

Firstly, soil fractions retain water and are detached by the impact from collision of raindrop. Soil fractions detached from the ground are flown by surface stream water, resulting in the deposition of soil fractions. Soil erosion progresses through this process due to rainfall. The degree of soil erosion is dependent on intensity of rainfall, rain duration, and raindrop energy. Higher intensity of rainfall and that for long term facilitate the transfer of soil fraction [14]. The degree also depends on soil composition, soil permeability, and the Atterberg limits of soils. Soil composition affects permeability and the Atterberg limits of soils [15]. Since a high infiltration rate of water into the ground decreases the development of surface water flow, the soils which show high permeability such as sand and gravel are less likely to cause soil erosion than clay and silt which show low permeability [16, 17]. Moreover, the Atterberg limits indicate the change in physical properties of soils with the change in water content and the resistance to deformation force, and it depends on soil composition. Thus, the Atterberg limits which are influenced by fine fraction in soils affect water retention capacity of soils as well as soil erosion [17, 18]. These characteristics are considered one of the predictive indicators for soil erosion.

For the reasons, the objective of this research is to understand the effects of the application of coal ash to postmine land on soil erosion, aiming at efficient use of coal ash in postmine land in Indonesia. Soil erosion is to be evaluated by performing the artificial rainfall test as well as physical testing with the simulated topsoil mixed with coal ash in this study.

2. Materials and Methods

2.1. Materials. Fly ash and bottom ash were taken in A coal-fired power plant in the K mine in Indonesia: FA1 and BA1. Another type of fly ash was also sampled in B coal-fired power plant in Japan: FA2. The difference in the combustion process and the power plant design between the coal-fired power plants suggests the difference in the physical and chemical properties of the coal ash samples. For the purpose of understanding the chemical and physical properties of them, specific gravity measurement by using pycnometer, X-Ray Fluorescent (XRF), X-Ray Diffraction (XRD), scanning electron microscope (SEM), and water retention test were

TABLE 1: Physical and chemical properties of the coal ash.

Samples	FA1	BA1	FA2
Physical properties			
Specific gravity (g/cm^3)	2.10	1.96	2.07
Chemical composition (mass%)			
SiO_2	30.93	44.56	67.39
Al_2O_3	13.30	16.48	18.70
FeO	5.93	7.60	4.16
MgO	2.24	2.73	1.10
CaO	1.82	2.34	2.87
Na_2O	0.16	0.46	0.67
K_2O	1.54	1.69	1.23
SO_3	1.21	7.22	0.22
H_2O	41.02	22.32	1.97

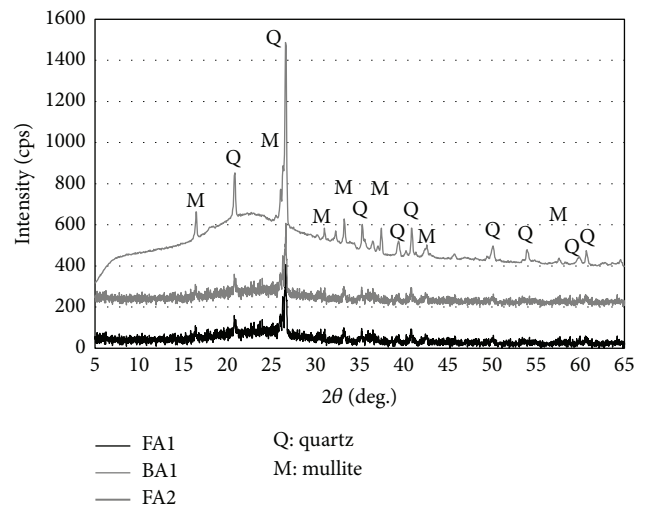


FIGURE 2: XRD patterns of the coal ash.

performed with the samples. The physical and chemical properties of the coal ash samples are summarized in Table 1. Figure 2 shows XRD patterns of them and Figure 3 shows SEM images. The results of water retention test are shown in Figure 4.

2.2. Sample Preparation. Simulated topsoil was prepared by mixing the decomposed granite produced by the Gulin Kita-Kyu Co., Ltd., and the Kyushu Bentonite produced by the Shinagawa Yogyo Co., Ltd., after screening on the basis of soil conditions measured in postmine land in the mine as shown in Table 2. The simulated topsoil was replaced by the coal ash of FA1, BA1, and FA2 at the rates of 0%, 30%, 60%, and 100% in order to evaluate the application of coal ash to topsoil in postmine land. They were named as topsoil (0%) without coal ash, FA1-30, FA1-60, FA1-100, BA1-30, BA1-60, BA1-100, FA2-30, FA2-60, and FA2-100, respectively. The samples were homogeneously mixed by the cone and quartering method. The grain size analysis, the standard test for the Atterberg limits, and the falling head permeability test were performed with the samples in order to understand the effects of

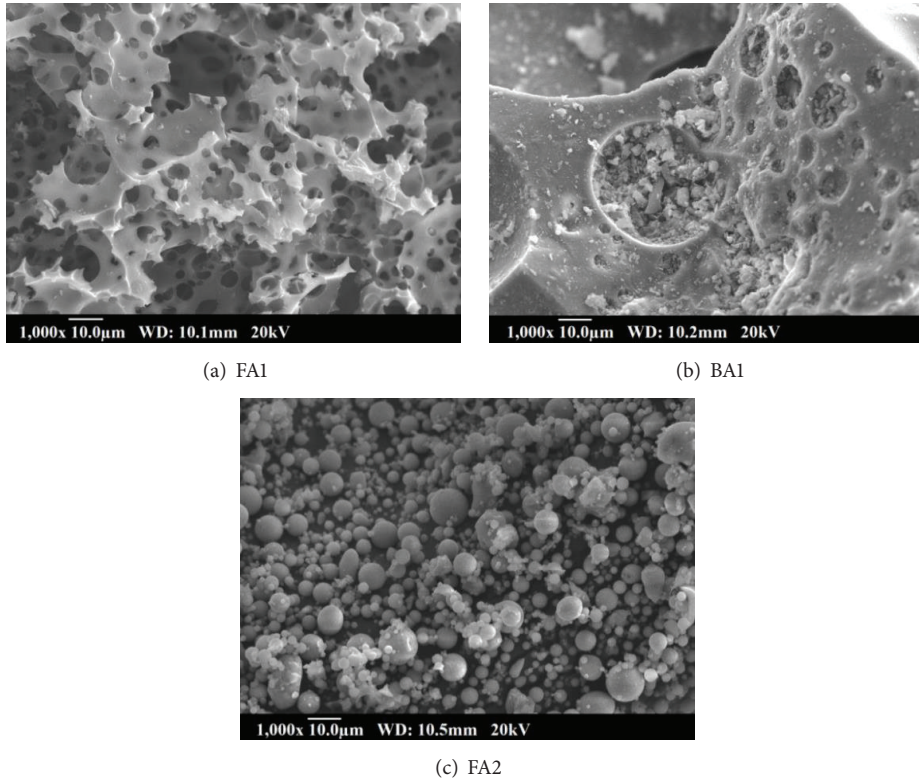


FIGURE 3: SEM images of the coal ash.

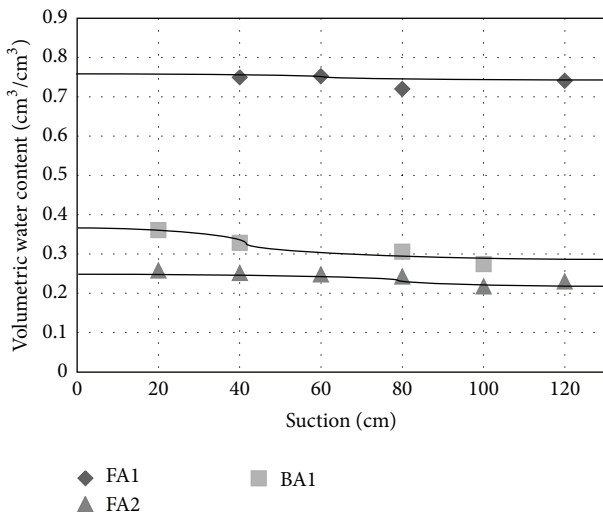


FIGURE 4: Water retention characteristics of the coal ash: curve approximation was drawn by the Van Genuchten model.

the application of coal ash on chemical and physical properties of soils.

2.3. Experimental Methods

2.3.1. XRD Analysis. FA1, BA, and FA2 were supplied to XRD analysis after drying at 80°C for 24 hours in an oven by using

TABLE 2: Soil texture classes of topsoil in the K mine and the simulated topsoil.

Samples	Sand (%)	Silt (%)	Clay (%)
Topsoil in K mine	2.7–48.9	26.6–57.8	24.4–39.6
Simulated topsoil	36.7	26.7	36.6

wide angle goniometer RINT 2100 XRD under the conditions: radiation $\text{CuK}\alpha$, step scanning 0.050° , scan speed $2.000^\circ/\text{min}$, and scan range $2.000\text{--}65.000^\circ$.

2.3.2. SEM Observation. The surface condition of FA1, BA, and FA2 was observed by using KEYENCE VE-9800. The Au-Pd coating was conducted prior to making SEM observations on the surface of the samples with the MSP-1S Magnetron Sputter. The specimens were vacuum-dried using a beam at 20 kV, followed by the beginning of SEM observation.

2.3.3. Physical Properties. Specific gravity of the samples was measured by using pycnometer based on the ASTM D854-14 [19]. Particle size distribution of samples was analyzed based on the ASTM D422-63 [20]. In this test, the samples were categorized into sand, silt, and clay according to the classification. Atterberg limits test, which is to understand the change in mechanical behavior of soils with the change in water content, was also performed according to the ASTM

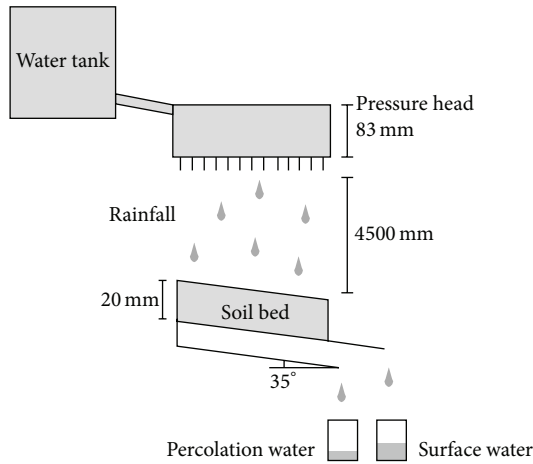


FIGURE 5: Schematic design of the artificial rainfall test.

D4318-05 [21]. Hydraulic conductivity of the samples was measured by conducting falling head permeability test based on the ASTM D5084-10 standard [22].

Additionally, the test for water retention capacity of the samples was conducted based on the standard of JGS 0151-2009 in order to measure the relationship between suction head and volumetric water content [23]. After the test, the web interface of the SWRC Fit was used to draw soil water retention curve by inputting the results and fitting by the Van Genuchten model [24].

2.3.4. Artificial Rainfall Test. The amount of annual soil erosion was measured by performing the artificial rainfall test in which artificial precipitation was supplied for an hour to the simulated topsoil mixed with coal ash. Figure 5 shows the schematic design of the equipment of the artificial rainfall test. After collecting surface stream water, they were dried at 100°C in an oven and the weight of the residue was measured, followed by the calculation of the amount of soil erosion per an hour. We substitute the amount of soil erosion per an hour E , the annual rainfall R , the section area A , the dry density of each sample G , and rain intensity I into the equation to calculate the annual soil erosion H as follows:

$$H = \frac{(R \times E)}{(A \times G \times I)}, \quad (1)$$

where H is the annual soil erosion (cm/year), E is the soil erosion (g/hour), G is the dry density (g/cm^3), A is the section area (cm^2), R is the annual rainfall (mm/year), and I is the rain intensity (mm/hour).

In this test, the rainfall intensity was set at 80 (mm/hour) which was recorded in the postmine land in the mine when concentrated heavy rain occurred and based on the data in the past [25–27]. Moreover, water content was set at 15% which was measured in the postmine land. The slope angle was set at 35° which is maximum slope angle at waste dump in the postmine land according to the standard in the mine. The annual rainfall was set at 3000 (mm/year) as the average value in Indonesia [28]. 240 mm by 155 mm of the case was filled

with the simulated topsoil mixed with each type of coal ash by equalizing the filling rate in each case. The rainfall intensity was adjusted by changing hydraulic head. The surface stream water and the percolation water were collected separately and the volume was recorded during the test. The proportion of surface stream water and the percolation water to the total volume was calculated based on the results. The water content in the simulated topsoil was also measured by drying the soil samples in an oven at the end of the experiment. The rainfall test was conducted under the same conditions with each type of the samples. Besides, the risk of soil erosion was evaluated based on the results according to the risk assessment guideline of soil erosion in Indonesia as shown in Table 4 [26, 27].

3. Results and Discussion

3.1. Characterization of Topsoil Mixed with the Ash Samples.

The physical and chemical properties of the coal ash samples are listed in Table 1. The specific gravity of each type of the coal ash showed similar values: those of FA1, BA1, and FA2 were 2.10, 1.96, and 2.07 (g/cm^3), respectively. Since specific gravity of fly ash is, typically, between 2.1 and 3.1 (g/cm^3), they are typical fly ash samples [29]. Based on the chemical composition of the samples, Si and Al constituted more than half of BA1 and FA2. Additionally, the water content was higher in FA1 and BA1 than that in FA2, indicating that FA1 and BA1 contained unburnt materials. It would appear that the difference in the combustion temperature and/or the combustion efficiency between the coal-fired power plants caused the difference among the samples.

The XRD patterns of the coal ash samples in Figure 2 indicated that they mostly consisted of quartz and mullite, and there was not a large difference in XRD patterns among the samples. This result also suggested that the coal ash samples were typical coal ash due to the content of quartz and mullite in the past studies [30–32]. Meanwhile, the microstructure among the samples varied greatly as seen in the SEM images in Figure 3. FA1 had microporous structures of 1–10 μm in diameter without fine fragments. Angular structure without microporous structures and fine fragments was observed in BA1, whereas the aggregation of 1–10 μm diameters of spherical particles without microporous structure was found in FA2. Thus, the coal ash samples had a completely different microstructure while they consisted of the same minerals.

Figure 4 presents soil water retention characteristic (SWRC) of the coal ash samples. It can be seen that the water content was higher in FA1 than the others at each suction pressure and that of FA2 changed at lowest level. This implied that FA1 contained fine fractions more than in BA1 and FA2 by reason that water retention capacity in soils increases due to fine fraction [17, 18].

The soil composition of the simulated topsoil mixed with 0%, 30%, 60%, and 100% of the coal ash samples is shown in Figure 6. Soil composition of the simulated topsoil mixed with 0% of coal ash was set at 36.7% of sand, 26.7% of silt, and 36.6% of clay based on the data in Table 2. The result indicated that more than 85% of FA1 and BA1 consisted of

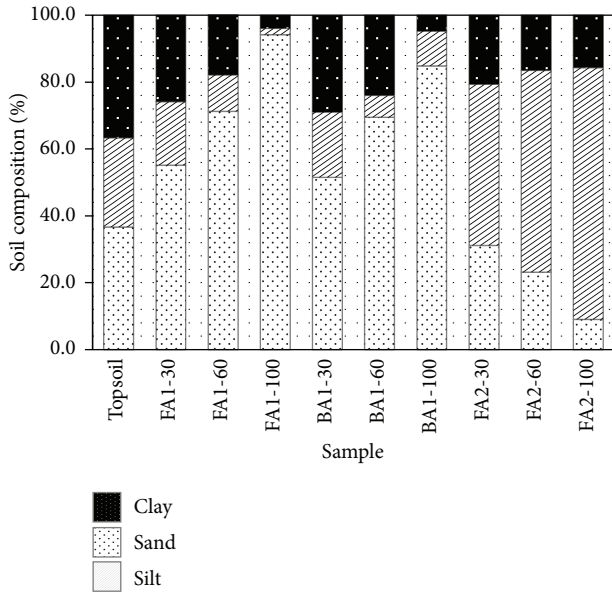


FIGURE 6: Soil composition of the simulated topsoil mixed with the coal ash at the mixing ratio of 0%, 30%, 60%, and 100%.

sand and more than 75% of FA2 consisted of silt. Therefore, the proportion of sand rose and that of silt dropped with the increase in the mixing ratio of FA1 and BA. On the other hand, the percentage of sand and clay decreased and that of silt increased with the increase in the mixing ratio of FA2. The result was not consistent with the result of SWRC. The highest water retention capacity was obtained in FA1 despite a high percentage of sand, and the lowest water retention capacity was recorded in FA2 despite a high percentage of silt considered as fine fractions. It would appear based on the SEM images in Figure 3 that FA1 had the high water retention capacity by retaining water in the microporous structure. Meanwhile, there were no voids which can retain water among the spherical particles in FA2, resulting in low water retention capacity in spite of a high content of silt. Thereby, microstructure of coal ash has to be taken into account in order to evaluate water retention capacity since high water retention capacity is obtained in the coal ash with microporous structures despite a low content of fine fractions.

Figure 7 shows the permeability of the samples and Table 3 presents the summary of the results of the Atterberg limits test. The physical properties were also changed by mixing the simulated topsoil with the coal ash samples. While the permeability of the simulated topsoil increased with the increase in the mixing ratio of FA1 and BA1 which consisted of more than 85% of sand, it decreased by mixing FA2 which consisted of more than 75% of silt. The change in permeability agreed with the soil composition of each sample in terms of the improvement of permeability by mixing sand [17, 18]. In Table 3, liquid limit, plastic limit, and plasticity index were not measured after mixing the coal ash into the simulated topsoil. This was due to a significant decrease in adhesion caused by a high content of sand in FA1 and BA1 and due to a significant increase in adhesion caused by a high content of silt in FA2.

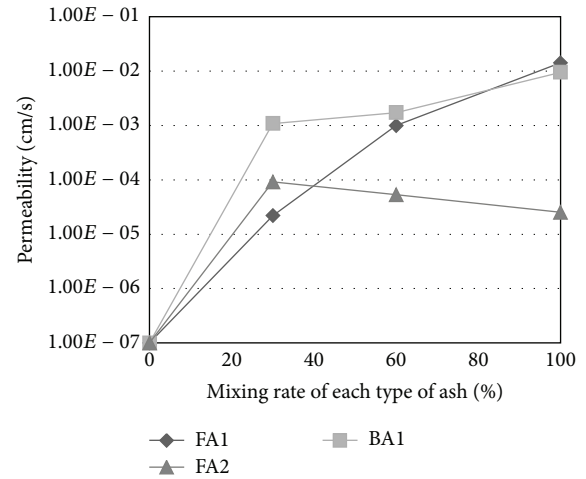


FIGURE 7: Permeability of the simulated topsoil mixed with the coal ash at the mixing ratio of 0%, 30%, 60%, and 100%.

TABLE 3: The Atterberg limits of the simulated topsoil mixed with the coal ash at the mixing ratio of 0%, 30%, 60%, and 100%.

	Liquid limit (W_L)	Plastic limit (W_P)	Plasticity index (I_P)
Topsoil (0%)	18.6	34.4	15.8
FA1-30	ND	ND	ND
FA1-60	ND	ND	ND
FA1-100	ND	ND	ND
BA1-30	ND	ND	ND
BA1-60	ND	ND	ND
BA1-100	ND	ND	ND
FA2-30	ND	14.1	ND
FA2-60	ND	ND	ND
FA2-100	ND	ND	ND

TABLE 4: Risk assessment of soil erosion in Indonesia.

Class	Surface soil loss (cm/year)
Very high	>4.8
High	1.8–4.8
Moderate	0.9–1.8
Low	0.15–0.9
Very low	<0.15

It was impossible to shape the simulated topsoil mixed with FA1 and BA1 owing to detachment of fractions and owing to liquefaction of them in FA2. It suggested that the observation of microstructure of coal ash was useful to evaluate water retention capacity in the case that the Atterberg limits could not be measured.

For the results, the application of FA1 to topsoil is, especially, expected to control soil erosion due to adhesion among fine fractions caused by high water retention capacity [17, 18]. Furthermore, it is expected that surface stream water may easily occur by applying FA2 which shows low

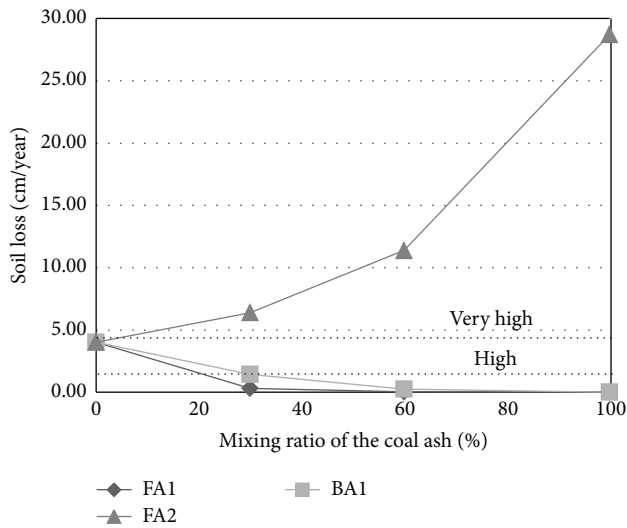


FIGURE 8: Soil loss of the simulated topsoil mixed with the coal ash at the mixing ratio of 0%, 30%, 60%, and 100% in the artificial rainfall test: a range framed by dotted lines indicates high risk of soil erosion.

permeability contrary to FA1 due to a high content of silt, leading to soil erosion.

3.2. Soil Erosion in Artificial Rainfall Test. Figure 8 shows the amount of soil loss at the different mixing ratio of the coal ash into the simulated topsoil in the artificial rainfall test, and Figure 9 shows the change in water content in the samples during the test. The risk of soil erosion based on the standard in Indonesia is drawn with dashed lines in Figure 8 [26, 27]. The percentage of surface stream water and percolation water in the rainfall test is presented in Figure 10. From Figure 8, it was found that soil erosion was prevented significantly by applying FA1 and BA1 to the simulated topsoil. The risk of soil erosion was reduced from the category of “high” to that of “very low” in the standard by applying more than 30% of FA1 or BA1: the risk is considered very low when surface soil loss is less than 0.15 (cm/year). Soil loss was reduced by up to 4.00 (cm/year) by applying FA1 and BA1. On the other hand, the condition was classified into the category of “very high” by applying more than 30% of FA2 to the simulated topsoil. Soil loss increased by up to 24.68 (cm/year) by mixing FA2 with the simulated topsoil. Moreover, these results agree with the discussion of the effects of the application of the coal ash on soil erosion on the basis of physical and chemical properties of the ash mentioned previously. High water content was obtained in Figure 9 in the sample mixed with FA1 which showed high water retention capacity, whereas similar change in water content was obtained in the sample mixed with BA1 and FA2 which showed similar water retention capacity.

Figure 10 demonstrates that the percentage of surface stream water decreased contrary to the increase in the ratio of percolation water by applying FA1 and BA1 with high permeability. When FA2 with low permeability was applied, there was an upward trend in the ratio of surface stream water.

Thus, the risk of soil erosion declined with the increase in the mixing ratio of FA1 and BA1 with high permeability

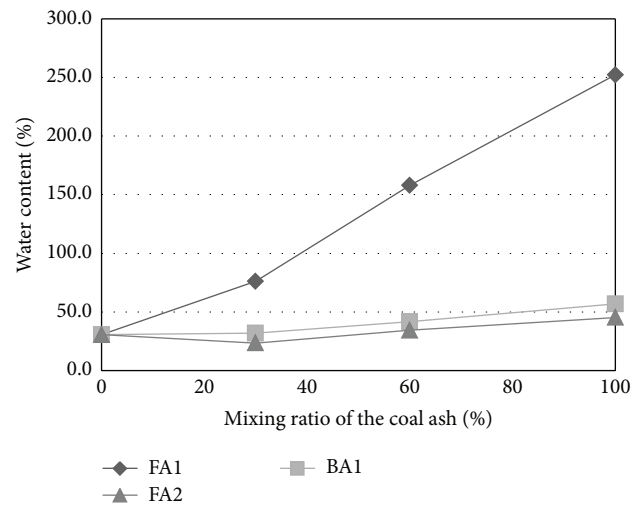


FIGURE 9: Water content of the simulated topsoil mixed with the coal ash at the mixing ratio of 0%, 30%, 60%, and 100% in the artificial rainfall test.

owing to the decrease in surface stream water caused by improving the permeability in the simulated topsoil. The soil loss in the sample mixed with FA1 was, furthermore, less than that with BA1. This was possibly due to adhesion by water retained in microporous structures in FA1. When FA2 with low permeability due to a high content of silt was applied, soil erosion progressed with the increase in the ratio of surface stream water. This result indicated that soil composition which affected permeability in soils was important to predict soil erosion. Soil erosion could not be prevented by applying FA2 which consisted of more than 90% of clay and silt as shown in Figure 6. On the other hand, the risk of soil erosion could be reduced by FA1 and BA1 which consisted of more than 85% of sand at the mixing ratio of over 30%. The mixing ratio, however, should be decided in consideration of the effects of soil composition on plant growth as well as on soil erosion in the case that coal ash is applied to postmine land.

4. Conclusions

In this study, the simulated topsoil mixed with coal ash was prepared to discuss the application of coal ash to postmine land for the purpose of prevention of soil erosion. The artificial rainfall test was performed with the samples in addition to the grain size analysis, the standard test for the Atterberg limits, falling head permeability test, and water retention test, aiming at understanding the change in risk of soil erosion by applying coal ash to topsoil. The main conclusions from the experiments are summarized as follows:

- (i) The risk of soil erosion was significantly reduced by applying coal ash to topsoil which was considered industrial waste with a focus on physical characteristics of the ash.
- (ii) The application of the coal ash which consisted of more than 90% of clay and silt to topsoil promoted

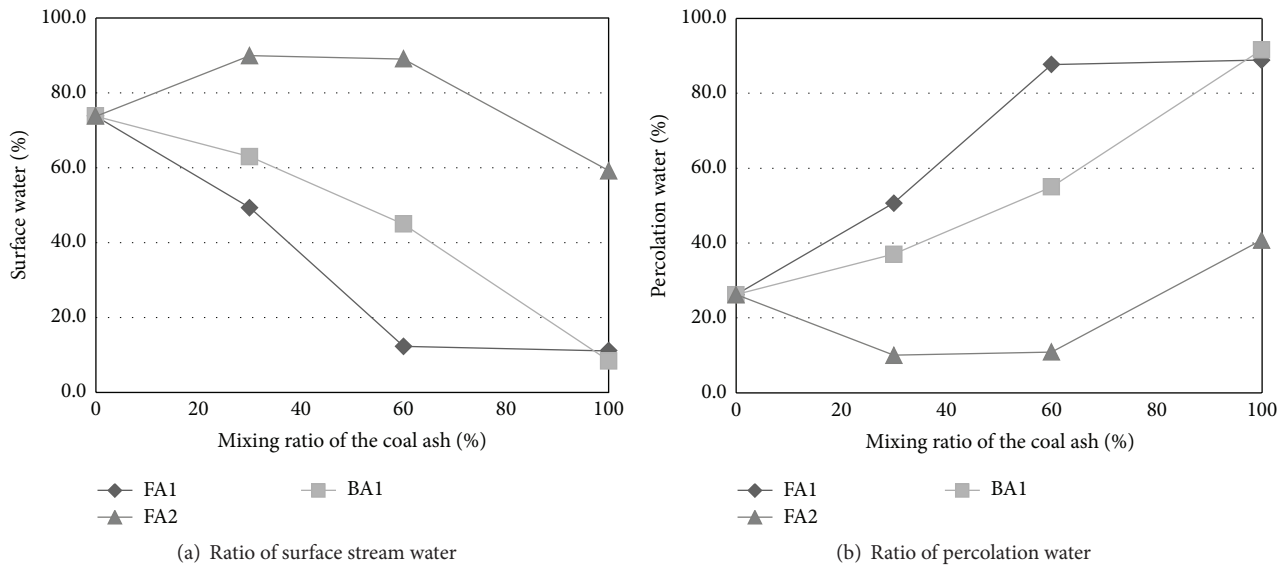


FIGURE 10: Ratio of each type of water flow in the simulated topsoil mixed with the coal ash at the mixing ratio of 0%, 30%, 60%, and 100% in the artificial rainfall test.

soil erosion. Meanwhile, soil erosion was prevented by mixing the coal ash which consisted of more than 85% of sand at the mixing ratio of over 30%. However, the mixing ratio of coal ash to topsoil has to be decided in consideration of the effects of soil composition on plant growth as well as that on soil erosion.

- (iii) Microporous structures in FA1 affected water retention capacity, leading to prevention of soil erosion. The coal ash of FA1 with the structures showed high water retention in spite of low content of clay.
- (iv) For the purpose of prevention of soil erosion by mixing coal ash in topsoil in postmine land, microporous structures in coal ash and soil composition which affect permeability and water retention capacity are useful to select coal ash and to decide the mixing ratio.

Competing Interests

The authors declare that there is no conflict of interests regarding the publication of this paper.

Acknowledgments

This research was supported by grants from the Advanced Graduate Program in Global Strategy for Green Asia, Kyushu University, and the Mitsui Matsushima Co., Ltd. The authors would like to express their gratitude and appreciation to the coal power plants for providing the coal ash samples and to the mine for kind assistance with field work. The authors also acknowledge the work of colleagues in the Laboratory of Rock Engineering and Mining Machinery, Kyushu University.

References

- [1] International Energy Agency, *Coal Information 2015-with 2014 Data*, International Energy Agency, 2015.
- [2] International Business Publications USA, *Indonesia Energy Policy, Laws and Regulation Handbook, Volume 1: Strategic Information and Basic Laws*, International Business Publications, Washington, DC, USA, 2015.
- [3] H. Shimada, T. Sasaoka, K. Matsui et al., "Fundamental study of acid drainage control using flyash," in *Proceedings of the 19th International Symposium on Mine Planning & Equipment Selection*, Fremantle, Australia, 2010.
- [4] J. Skousen, J. E. Yang, J.-S. Lee, and P. Ziemkiewicz, "Review of fly ash as a soil amendment," *Geosystem Engineering*, vol. 16, no. 3, pp. 249–256, 2013.
- [5] A. C. Chang, L. J. Lund, A. L. Page, and J. E. Warneke, "Physical properties of fly ash amended soils," *Journal of Environmental Quality*, vol. 6, no. 3, pp. 267–270, 1977.
- [6] R. J. Haynes, "Reclamation and revegetation of fly ash disposal sites—challenges and research needs," *Journal of Environmental Management*, vol. 90, no. 1, pp. 43–53, 2009.
- [7] S. Jala and D. Goyal, "Fly ash as a soil ameliorant for improving crop production—a review," *Bioresource Technology*, vol. 97, no. 9, pp. 1136–1146, 2006.
- [8] K. C. Haering and W. L. Daniels, "Fly ash: characteristics and use in mineland reclamation, a literature review," *Virginia Coal Energy Journal*, vol. 3, pp. 33–46, 1991.
- [9] J. H. Park, M. Edraki, D. Mulligan, and H. S. Jang, "The application of coal combustion by-products in mine site rehabilitation," *Journal of Cleaner Production*, vol. 84, no. 1, pp. 761–762, 2014.
- [10] C. A. Ríos, C. D. Williams, and C. L. Roberts, "Removal of heavy metals from acid mine drainage (AMD) using coal fly ash, natural clinker and synthetic zeolites," *Journal of Hazardous Materials*, vol. 156, no. 1–3, pp. 23–35, 2008.
- [11] K. C. Vories, "Placement of coal combustion by products at Surface Mining Control and Reclamation Act (SMCRA) mines:

- a short history of OSM technical efforts and responses to environmental concerns,” in *Proceedings of National Meeting of the American Society of Mining and Reclamation*, Breckenridge, Colo, USA, 2005.
- [12] G. J. Kusuma, H. Shimada, R. S. Gautama, K. Matsui, and C. H. Saputra, “An evaluation of fly ash-overburden rock mixtures for a cover layer to prevent acid mine drainage generation in overburden dump,” in *Proceedings of the ISRM International Symposium-8th Asian Rock Mechanics Symposium*, Sapporo, Japan, 2014.
- [13] A. Hamanaka, N. Inoue, H. Shimada, T. Sasaoka, and K. Matsui, “An experimental study for assessment of soil erosion at rehabilitation area in Indonesian coal mine,” in *Proceedings of the International Symposium on Land Reclamation and Ecological Restoration (LRER '14)*, pp. 171–175, Beijing, China, October 2014.
- [14] M. J. M. Römkens, K. Helming, and S. N. Prasad, “Soil erosion under different rainfall intensities, surface roughness, and soil water regimes,” *Catena*, vol. 46, no. 2-3, pp. 103–123, 2002.
- [15] C. A. Igwe and N. Ejiofor, “Structural stability of exposed gully wall in Central Eastern Nigeria as affected by soil properties,” *International Agrophysics*, vol. 19, no. 3, pp. 215–222, 2005.
- [16] R. A. Obashi, “Vulnerability of soil erosion in Okitipupa area of Ondo state, Southwest Nigeria: a climatic problem,” *International Journal of Science and Technology*, vol. 2, no. 4, pp. 326–335, 2013.
- [17] K. Terzaghi, R. B. Peck, and G. Mesri, *Soil Mechanics in Engineering Practice*, John Wiley & Sons, New York, NY, USA, 3rd edition, 1996.
- [18] Y. Taniguchi, H. Komine, and S. Murakami, “Dominant influence of physico-chemical properties of soil to erosion characteristics of fine grain soil in river levee and bank,” in *Proceedings of the 46th Japan National Conference on Geotechnical Engineering*, Kobe, Japan, 2011.
- [19] ASTM, “Standard test methods for specific gravity of soil solids by water pycnometer,” ASTM D854-14, ASTM International, 2014.
- [20] ASTM, “Standard test method for particle-size analysis of soils (withdrawn 2016),” ASTM D422-63(2007)e2, ASTM International, 2007.
- [21] ASTM, “Standard test methods for liquid limit, plastic limit, and plasticity index of soils,” ASTM D4318-05, ASTM International, 2005.
- [22] ASTM, “Standard test methods for measurement of hydraulic conductivity of saturated porous materials using a flexible wall permeameter,” ASTM D5084-10, ASTM International, 2010.
- [23] Japanese Geotechnical Society (JGS), “Test method for water retentivity of soils,” Tech. Rep. JGS 0151-2009, Standards of Japanese Geotechnical Society for Laboratory Soil Testing Methods, 2009.
- [24] K. Seki, “SWRC fit—a nonlinear fitting program with a water retention curve for soils having unimodal and bimodal pore structure,” *Hydrology and Earth System Sciences Discussions*, vol. 4, no. 1, pp. 407–437, 2007.
- [25] National Environment Agency, “Annual weather review 2011,” <http://www.nea.gov.sg/training-knowledge/publications/annual-weather-review-2011>.
- [26] A. Hamanaka, H. Shimada, T. Sasaoka, K. Matsui, I. Miyajima, and Y. Ichinose, “Assessment of soil erosion at the rehabilitation area in Indonesian coal mine,” in *Proceedings of the Spring Annual Symposium on the Mining and Materials Processing*, Tokyo, Japan, 2013.
- [27] A. Hamanaka, N. Inoue, H. Shimada, T. Sasaoka, K. Matsui, and I. Miyajima, “Study on backfilling of soil for revegetation at the rehabilitation area in Indonesian coal mine,” in *Proceedings of the 22nd Mine Planning and Equipment Selection*, C. Drebenstedt and R. Singhal, Eds., Dresden, Germany, 2013.
- [28] L. Dina, “Prospect of keprok orange in kutai timur regency,” *EPP*, vol. 6, no. 1, pp. 36–43, 2009.
- [29] A. A. Klyosov, *Wood Plastic Composites*, John Wiley & Sons, Hoboken, NJ, USA, 2007.
- [30] D. Havlíček, R. Přibíl, and B. Kratochvíl, “Content of quartz and mullite in some selected power-plant fly ash in Czechoslovakia,” *Atmospheric Environment*, vol. 23, no. 3, pp. 701–706, 1989.
- [31] B. G. Kutchko and A. G. Kim, “Fly ash characterization by SEM-EDS,” *Fuel*, vol. 85, no. 17-18, pp. 2537–2544, 2006.
- [32] S. V. Vassilev, C. G. Vassileva, A. I. Karayigit, Y. Bulut, A. Alastuey, and X. Querol, “Phase-mineral and chemical composition of composite samples from feed coals, bottom ashes and fly ashes at the Soma power station, Turkey,” *International Journal of Coal Geology*, vol. 61, no. 1-2, pp. 35–63, 2005.

Research Article

Weathering Influence on Properties of Siltstones from Istria, Croatia

Martina Vivoda Prodan and Željko Arbanas

University of Rijeka, Faculty of Civil Engineering, Radmile Matejčić 3, 51000 Rijeka, Croatia

Correspondence should be addressed to Željko Arbanas; zeljko.arbanas@gradri.uniri.hr

Received 31 March 2016; Revised 3 June 2016; Accepted 7 June 2016

Academic Editor: Jianxi Zhu

Copyright © 2016 M. Vivoda Prodan and Ž. Arbanas. This is an open access article distributed under the Creative Commons Attribution License, which permits unrestricted use, distribution, and reproduction in any medium, provided the original work is properly cited.

Slaking and weathering of weak rocks result in slope instability. Siltstones from flysch rock masses are highly susceptible to weathering, which causes rapid changes in the geotechnical properties and durability. This study investigated siltstone samples of different weathering grades from flysch rock masses from the Istria Peninsula, Croatia, and determined the effects of weathering on their engineering properties. Laboratory testing of siltstone samples of different weathering grades was conducted to determine the specific gravity, grain size distribution, Atterberg limits, and uniaxial compressive strength. The standardized slake durability index is not sufficient to classify the durability of weak rock masses such as siltstones. Therefore, the durability of siltstone samples of different weathering grades was quantified from the fragment size distribution after each of five slaking cycles. The tested samples were classified based on the disintegration ratio, and the modified disintegration ratio was used to determine potential long-term degradation of the tested samples. The results indicated that weathering has a significant influence on the plasticity, uniaxial compressive strength, and durability characteristics and thus affects the landslides and erosion processes in siltstones in the flysch zone of the Istria Peninsula.

1. Introduction

The study area of this investigation is the Pazin Paleogene flysch basin, which is located in the northeastern part of the Istrian Peninsula, Croatia. Numerous landslides and erosion processes occur on the slopes in this area and are most often related to the weathering of flysch rock masses. Weathering is the process of the alteration and breakdown of rock and soil materials at or near the Earth's surface by chemical, physical, and biological processes that generally operate together [1, 2]. Weathering causes mineralogical and lithological changes in rocks and consequently changes in their engineering properties. Many researchers have investigated weathering processes in sedimentary rocks. Chandler [3] and Reißmüller [4] investigated the effect of weathering on the shear strength of marls based on direct shear tests. The effects of chemical weathering of sedimentary rocks were described by Chigira and Oyama [5]. Bhattarai et al. [6] investigated the influence of weathering on the properties of mudstone. Durability is defined as the rock's ability to

resist degradation during its working life [7]. It is considered to be dependent on several parameters, such as permeability, porosity, adsorption, mineralogy, microscopic texture, microfabrics, and the presence of microfractures [8–13]. This makes characterizing the slaking behavior in rocks using a single parameter extremely complex [14]. The slake durability test, which was proposed by Franklin and Chandra [9], is the most widely used test for evaluating the relationship between slaking and the durability of rocks. This test is recommended by both the International Society for Rock Mechanics [15] and the American Society for Testing and Materials [16]. However, the use of the denominated slake durability index in the second cycle (I_{d2}) to quantify a rock's susceptibility to slaking is not satisfactory for characterizing weak rocks [8, 11, 12, 17]. Because the observed weathering of rocks during testing is much greater than what is predicted by the slake durability test, new classifications of weak rocks have been proposed by several authors. Erguler and Shakoor [12] proposed a durability classification for clay-bearing rocks based on the disintegration ratio. This method quantifies

the fragment size distribution of the slaked material by calculating the disintegration ratio for five slaking cycles. A new weathering characterization based on a newly proposed potential degradation index was introduced by Cano and Tomás [18]. This method analyzes changes in the fragment size distribution curves that are obtained from the material that is retained in the testing drum after each slake cycle. Behavior that is observed in the laboratory was compared to the behavior that is observed in the field under natural climatic conditions, investigated by Cano and Tomás [13].

The main aim of this paper is to describe changes in the durability and geotechnical characteristics of siltstones from flysch rock masses in the Istria Peninsula, Croatia, due to weathering processes. The field properties of siltstones of different weathering grades were determined visually, while Schmidt hammer rebound tests were performed to determine the uniaxial strength in the field. Physical and mechanical tests were performed to determine the specific gravity, grain size distribution, Atterberg limits, and point load strength of siltstone samples of different weathering grades. Five cycles of the slake durability test were performed, and the changes in the fragment size distribution curves that were obtained from the material that was retained in the testing drum after each cycle were analyzed. Based on the results of these analyses, the influence of weathering on the geotechnical properties and durability of siltstones of different weathering grades from flysch rock masses was identified and discussed.

2. Geological and Morphological Characteristics of the Study Area

The Istrian Peninsula is located in the northwestern part of the Adriatic Sea and is composed of Paleogene flysch, Cretaceous and Jurassic limestone, and alluvial deposits (Figure 1; [19]). It can be divided into three major regions: (i) Red Istria—Jurassic, Cretaceous, and Eocene plains (southern and western part of the Istria Peninsula); the term originates from the thick Quaternary deposits of so-called “terra rossa,” which overlie the Mesozoic and Tertiary carbonate bedrock; (ii) White Istria—the Cretaceous Eocene carbonate platform and clastic zone (mainly the Čičarija and Učka massifs), which have a characteristically imbricated structure; the term originates from the white color of the weathered Cretaceous and Eocene limestone; (iii) Gray Istria—the Eocene flysch basin (northeastern part of the Istria Peninsula). The term originates from the gray color of the marls, which are interbedded with sandstones and together form the flysch rock mass complex.

The study area includes the Gray Istria area, which is composed of a flysch rock mass that is a sequence of alternating clastic sedimentary rocks of deep marine facies that were deposited during an early stage of orogenesis [20]. The kinematics of the structural elements on the margin between the overthrust carbonate unit, Čičarija Mountain, and the Paleogene flysch basin are based on the relationship between the relatively rigid (limestone carbonate rocks) and relatively ductile (flysch rock mass complex) units during simultaneous deformation. The effects of the deformation are

most distinctive at the contact (overthrust zone) between the limestone and the flysch rock mass complex. The deformation caused the relatively rigid limestone rock blocks to be pushed into the more ductile flysch [21].

In the study area, the flysch rock mass is characterized by lithological heterogeneity because of common vertical and lateral changes in the lithological sequences, which include marls, siltstones, and fine-grained sandstones as well as distinctive calcarenite layers (Figure 2). The flysch rock mass is characterized by high erodibility and low durability of its incompetent members, and it is almost completely covered by weathered surficial material and rock fall talus that are susceptible to sliding [22] except in isolated areas, where the erosion is better expressed [21]. Many small-scale landslides in flysch slopes, primarily rotational and translational slides, tend to occur along slip surfaces that are located at the contact between the surficial deposits and the flysch bedrock, within the colluvial surficial deposits (Figure 3(a)) [23], within the flysch rock mass (Figure 3(b)) [24], or as debris flows (Figure 3(c)) [21]. Intense erosion processes are also observed in the flysch deposits in the study area (Figure 3(d)) [25, 26]. These geomorphological processes occur due to the significant influence of weathering in the flysch deposits and especially in the siltstone component, which has low durability and high susceptibility to weathering. Weathering decreases the residual shear strength of the siltstones, which results in landslide processes in the flysch deposits.

3. Characterization of the Effects of Weathering on the Flysch Rock Mass

Weathering causes changes in the mineralogical composition of a rock that affect its color, texture, composition, firmness, and form. In general, weathering includes two dominant types of processes: physical and chemical weathering processes [7]. Chemical weathering due to chemical reactions leads to the decomposition of the constituent minerals to stable or metastable secondary mineral products [27]. Physical weathering causes disaggregation and strength degradation of rocks. Drying-wetting cycles are likely the primary cause of the degradation of flysch rock masses [28]. A flysch rock mass can have diverse physical and mechanical properties depending on its lithological composition and state of weathering. Weathering processes are particularly expressed in incompetent members, such as claystones, shales, and siltstones. In contrast, sandstones, limestone, and breccioconglomerates are competent members and are considerably more resistant to the influences of exogenetic forces [29]. This study focuses on siltstones, which are the component of the flysch complex that is most susceptible to weathering. Therefore, the mechanical behavior of siltstones has the greatest influence on the behavior of the overall flysch rock mass complex. Figure 4 shows the high degradation of a flysch rock mass due to weathering in flysch pillars that were exposed to atmospheric conditions for seven years. These processes gradually transformed the fresh rock mass to residual soils and caused changes in its mineralogical composition and reductions in its mechanical properties.

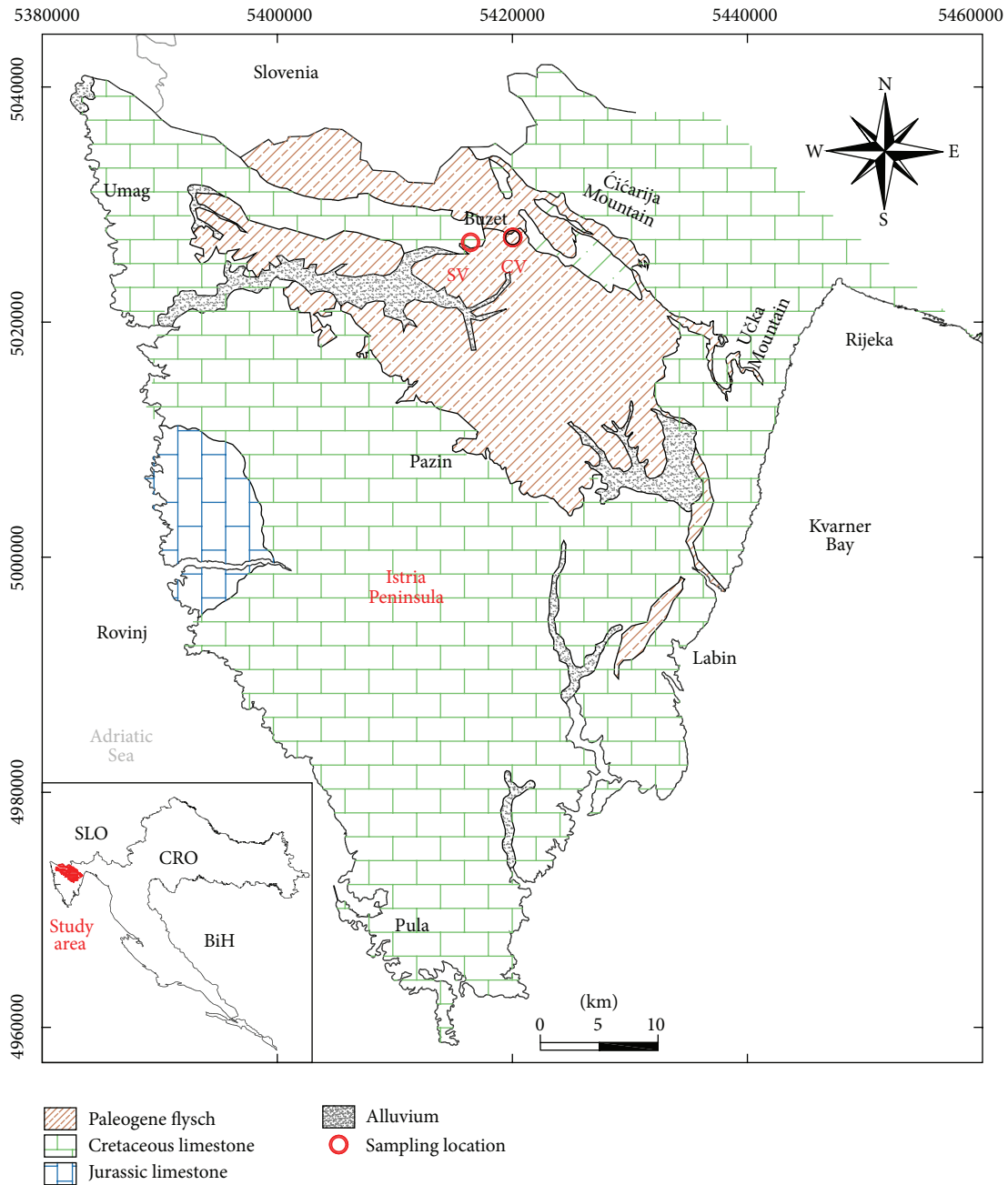


FIGURE 1: Geological map of the Istria Peninsula (based on [19]). CV = Cunj Village, SV = Sovinjak Village.

In this study, six standard grades of weathered siltstone [15] were investigated in a flysch weathering profile (Figure 5(a)). The weathering profile was defined using the following categories: fresh (FR), slightly weathered (SW), moderately weathered (MW), highly weathered (HW), and completely weathered (CW) rock masses and residual soil (RS). The evaluation of the weathering profile in the study area was based on a qualitative description of the colors and discoloration, discontinuities states, the existence or absence of the original rock texture, and the uniaxial compressive strength of the intact rock based on the Schmidt hammer rebound value. Progressive and gradual weakening and

decomposition take place from the ground surface downward to fresh rock, and thus the weathering of the flysch rock material decreases from RS to CW, HW, MW, SW, and FR. Vivoda Prodan et al. [30] performed X-ray diffraction mineralogical analyses of siltstone samples of four different weathering grades, including I (FR), III (MW), V (CW), and VI (RS), that were taken from a flysch outcrop near Cunj Village on the Istria Peninsula. The siltstone samples of the different weathering grades consist of small amounts of quartz and calcite, negligible amounts of plagioclase, and large amounts of clay minerals. Based on dissolution (calcite and chlorite) and a comparison with standard diffractograms,



FIGURE 2: Vertically alternating sandstones and siltstones in the flysch rock mass at the lateral scarp of the Brus Landslide in the Istria Peninsula.



(a)



(b)



(c)



(d)

FIGURE 3: Geomorphological processes at the study area: (a) the rotational Marinci Landslide, (b) the translational Brus Landslide, (c) a debris flow at Krbavčiči, and (d) erosion at Lesiščina.

the following mineralogical composition of the samples (Table 1) was identified: calcite (35–50%), quartz (5–10%), plagioclase (up to 10%), K-feldspar (trace), and clay minerals (40–55%). Calcite, quartz, and phyllosilicates make up 93–97% of the mineralogical composition of the siltstones, and phyllosilicates are the prevalent minerals. The major clay minerals are illite and chlorite, and trace amounts of kaolinite and mixed-layer minerals are present. The different weathering grades of the siltstones in the study area have different mineralogical contents. The clay mineral content of the siltstones increases and the calcite content decreases with increasing weathering grade. The proportions of particular

clay minerals, such as chlorite and illite, also increase with increasing weathering grade.

4. Test Methods

The scope of this study is to discuss and identify changes in the geotechnical properties and durability of siltstones due to long-term weathering processes that affect landslide reactivation. Siltstone samples of different weathering grades that were taken from flysch rock masses were subjected to laboratory testing to obtain data about their geotechnical and



FIGURE 4: View of a landslide body and lateral scarp from the crown of the Brus Landslide in (a) August 2005 and (b) January 2013.

TABLE 1: Mineralogical compositions of siltstone samples of different weathering grades [30].

Sample	Calcite	Quartz	Plagioclase	K-feldspar	Illite	Chlorite	Kaolinite	Mixed-layer clay minerals	Total clay minerals
FR	50	~5	<5	—	15–20	21	*	—	~40
SW	45	~5	5–10	—	15–20	20	*	*	~40
CW	35	5–10	5–10	*	~25	22	*	**	~50
RS	37	5–10	5–10	—	~30	24	*	**	~55

— indicates no presence of minerals.

* Minerals in traces.

** Small amount of minerals.

durability characteristics. Details about the methodology that was used are described in the following paragraphs.

4.1. Geotechnical Properties of Siltstones. Four representative samples of siltstone of different weathering grades, including I (FR), II (SW), III (MW), and V (CW), were collected from a flysch outcrop near Cunj Village in Istria and crumbled before laboratory testing. The siltstone samples of different weathering grades were disturbed and remolded to the engineering soil grade. The state of these siltstone samples matches the material state at the sliding surface, where natural disintegration of the siltstone occurs due to stresses and strains that are caused by sliding. The following geotechnical properties of the treated samples were determined: the grain size distribution according to the ASTM standard D6913-04 [31], the specific gravity of the soil particles following the ASTM standard C188-15 [32], and the Atterberg limits according to the ASTM D4318-10e1 standard [33] and according to British Standards BS1377-2:1990 [34]. The test results of siltstone samples of different weathering grades were compared with the changes of the geotechnical properties of sedimentary rocks due to weathering that were investigated by other researchers (e.g., [3, 6]). The decrease in durability of the flysch rock mass is responsible for slope stability problems due to the rapid disintegration and loss of shear strength. Eberhardt et al. [35] and Mišćević et al. [36] used numerical analyses to demonstrate that landslides occur through beds of weathered marls due to the degradation of shear strength as a result of weathering and saturation of the rock mass by heavy precipitation. Vivoda Prodan et al. [30] determined changes in the residual shear strength due to

weathering based on tests using ring shear and direct shear devices. The measured residual friction angle increases and the residual cohesion decreases with increasing weathering grade of siltstone samples.

4.2. Point Load Test. The point load test (PLT) was used to determine the strength of the siltstone samples of different weathering grade. Tests were performed on siltstone samples of weathering grades I (FR) and III (MW) from the outcrops near Cunj Village and Sovinjak Village in Istria (Figures 1 and 5). The load was applied normal to bedding (perpendicular to any discontinuities) of irregular block samples immediately after sampling to avoid further weathering and resulting strength reduction. The point load strength index, $I_{s(50)}$, is calculated using

$$I_{s(50)} = I_s \times F = \left(\frac{P}{D_e^2} \right) \times F, \quad (1)$$

where P is the load on the point, D_e is the equivalent core diameter calculated from expression (2), and F is size correction factor given by (3):

$$D_e^2 = \frac{(4 \times W \times D)}{\pi}, \quad (2)$$

$$F = \left(\frac{D_e}{50} \right)^{0.45}. \quad (3)$$

The mean value of $I_{s(50)}$ is calculated by deleting the two highest and lowest values from the 10 valid tests and calculating the mean of the remaining values. The uniaxial compressive

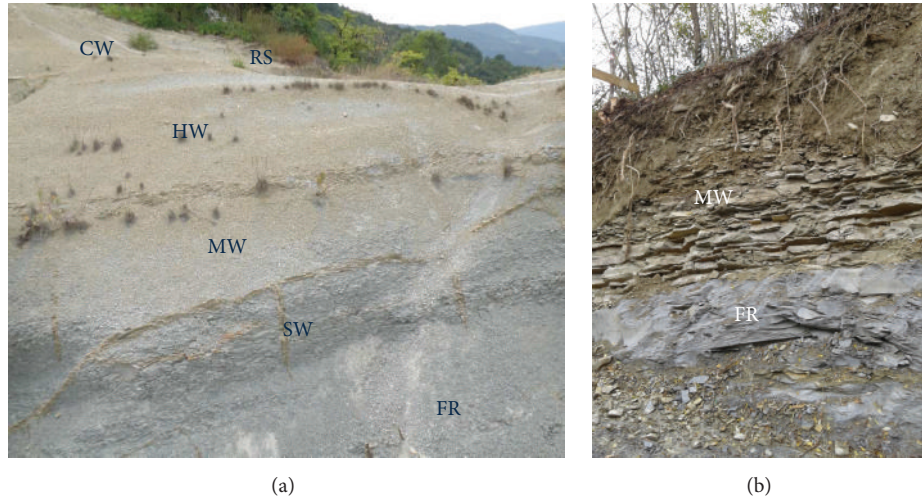


FIGURE 5: Locations of samples that were collected for laboratory testing from flysch outcrops near (a) Cunj Village and (b) Sovinjak Village.

strength of an intact siltstone sample is 24 times point load strength index [25]. The test was performed according to the standards that were proposed by ISRM [37]. The values of the uniaxial compressive strength that were obtained from the PLTs were compared with results from siltstone samples from the Istria Peninsula that were presented by other authors (e.g., [25, 38]).

4.3. Slake Durability Test and Fragment Size Distribution Analysis. The natural conditions of repeated drying and wetting over long periods of time affected the flysch rock and caused signs of weathering and degradation in the outcrop samples. The slake durability test was used to investigate the weathering resistance (i.e., the durability) of the rocks. The tests were performed on siltstone samples of weathering grades I (FR) and III (MW) that were collected from outcrops near Cunj Village and Sovinjak Village in Istria (Figures 1 and 5). The slake durability test was performed in accordance with the [16] standard procedure in five drying-wetting cycles. Ten 45–55 g pieces of intact siltstone were prepared, which resulted in a total sample mass of 470–500 g. The samples were dried for 24 hours in an oven at 105°C, sieved, and then subjected to rotation in a standard slake durability test apparatus for 10 minutes. This procedure was repeated for all five cycles. In addition to the standardized determination of the slake durability index, I_{d2} , the nature of the slaked material that is retained in the drum after each cycle of slake durability test must be quantitatively analyzed. Therefore, the fragment size distribution was used to better define the slaking characteristics of the tested flysch rock samples. The grain size distribution was determined after each drying-wetting cycle. The sieves that were used for the fragment size distribution had aperture sizes of 50, 37.5, 31.5, 28, 20, 14, 10, 6.3, 5, and 2 mm. Fragment size distribution curves after each of the five test cycles were plotted with the percents passing and retained (by weight) on the y -axis. After each cycle, the slake durability index (I_d) was calculated, and the values were compared with the results of two cycles of tests

on similar sedimentary rocks in Croatia (e.g., [25, 39]). The disintegration ratio (D_R) and the modified disintegration ratio (D_{RP}) were also determined to better define the slaking behavior. The disintegration ratio is defined as the ratio of the area under the fragment size distribution curve of the retained fragments to the total area that encompasses the range of fragment size distributions [12]. D_R is equal to 0 for nondurable rocks and to 1 for completely durable rocks. The modified disintegration ratio is a similar parameter and it is equal to the ratio of the area under the fragment size distribution curve of the passed fragments to the total area that encompasses the range of fragment size distributions [18]. Different graphs are used to determine these parameters, so D_{RP} is equal to 1 for the maximum degree of degradation. A rock with a D_R value close to 1 and a D_{RP} value close to 0 will not only exhibit high durability in the field but also not disintegrate into smaller fragments.

5. Test Results

Laboratory tests were conducted to investigate the variability in the geotechnical parameters and the durability of the siltstone samples of different weathering grades. The silt and clay contents vary from 20% in the sample of weathering grade V (CW) to 31% for weathering grade I (FR). The plastic limits of the samples are between 24 and 28% and are not related to the weathering grade. The liquid limits increase with increasing weathering grade. The values that were obtained with the Casagrande device vary between 33% for the sample of weathering grade I (FR) and 43% for weathering grade V (CW), and those from the fall cone test vary from 31% for weathering grade I (FR) to 40% for weathering grade V (CW). There is a good correlation (0.8882) between the liquid limits that were determined with the two tests so both test results can be considered to be relevant. The plasticity index increases with increasing weathering grade from 4% for weathering grade I (FR) to 12% for weathering grade V (CW). The plasticity indexes are low, and the samples are classified

TABLE 2: Geotechnical properties of the siltstone samples of different weathering grades.

Weathering grade	Sampling location	Grain size analysis [%] [30]			Plastic limit (w_p)	Atterberg limits [%]		Plasticity index (PI)	Specific gravity [g/cm^3] [30] (G_s)
		Sand (S)	Silt (M)	Clay (C)		Liquid limit (w_L) Casagrande device	Fall cone test		
I (FR)	Cunj	69	20	11	27	33	31	4	2.65
II (SW)		80		20	23	34	28	5	—
III (MW)		75	15	10	24	35	32	8	2.62
V (CW)		80	13	7	28	43	40	12	2.58

as ML in the plasticity chart. The specific gravity values vary from 2.58 to 2.65 g/cm^3 .

Chandler [3] estimated typical index properties of four weathering stages of Keupler marl and found little difference between the index properties of marls from the unweathered zone I and the partially weathered zones II and III. The fully weathered zone IV was considerably plastic. The influence of weathering on the properties of mudstone was investigated by Bhattarai et al. [6] and they concluded that there is no significant difference in the consistency limits of the soil and rock samples with depth. Table 2 shows the results of the geotechnical properties of the siltstone samples of different weathering grades.

The PLT and the Schmidt hammer test can be applied to siltstone samples of weathering grades I (FR), II (SW), and III (MW). These tests resulted in different uniaxial compressive strengths for the samples of different weathering grades. The uniaxial compressive strengths from the Schmidt hammer rebound values are 22 MPa for sample of weathering grade III (MW), 33 MPa for weathering grade II (SW), and 55 MPa for weathering grade I (FR). Similar values of the uniaxial compressive strength were obtained from the PLTs, including 19 MPa for the sample of weathering grade III (MW) and 48 MPa for weathering grade I (FR). Acceptable values of the uniaxial compressive strength from these two tests must be based on the statistical mean from numerous tests excluding extreme values. The disadvantage of the PLT is the large dispersion of the results, which especially occurs in weak rock masses such as flysch. This dispersion is caused by the layers of the rock mass layers, the layer orientation during sampling, the sample size, and the weathering of the rock mass. However, regardless of its disadvantages, the PLT method is recommended when there is a lack of more reliable tests, where there is a lack of appropriate representative samples, and when it can be used in combination with detailed descriptions of tested samples from the rock mass. Table 3 provides descriptions, typical characteristics, and characteristic uniaxial strength values for the different weathering grades of siltstones. Žufić [25] conducted in situ PLT tests on similar materials, and the point compressive strengths varied from 8 to 36 MPa. Arbanas et al. [38] presented results of PLTs of flysch siltstone samples of different weathering grades. The results from fresh siltstone samples corresponded to uniaxial strengths of 10 to 15 MPa and a maximum of 20 MPa. The corresponding

uniaxial strengths of moderate to slightly weathered samples were less than 2 MPa; these values are not confident and are unacceptable for use in engineering analyses without adequate precautions.

Gamble [8] suggested that slake durability index values that are taken after three or more cycles of slaking and drying may be useful for evaluating rock durability. The slaking behavior of siltstones cannot be described adequately using only two cycles and only a single aperture, such as the 2 mm mesh drum that is used in the standardized slake durability test. Therefore, in this study, 5 cycles were applied to each sample, and the fragment size distribution approach was used to better define the slaking characteristics of the tested siltstones. Figure 6 shows the fractions of the tested samples that were retained in the test drum for the initial conditions and after the second and fifth cycles.

The samples that were retained in the drum were extremely fragmented and appeared highly degraded (Figure 7). However, the fragments were larger than 2 mm, which led to the high I_{d2} values. However, high I_{d2} values do not correlate with this highly degraded state. Therefore, the fragment size distribution of the fragmented siltstone that was retained in the drum after each cycle of the slake durability test was quantified.

Figure 8 shows the fragment size distribution curves of the retained weight, and Figure 9 shows fragment size distribution curves of the passed weight through all of the cycles of the slake durability test of siltstone samples of weathering grades I (FR) and III (MW) that were collected from flysch outcrops near Cunj Village and Sovinjak Village. The fragment size distribution curve of the retained fragments is required to define the disintegration ratio after each of the five cycles of the slake durability test. The modified degradation ratio after each cycle is also determined based on the fragment size distribution curve of the passed fragments of the sample. The slake durability index, disintegration ratio, and modified disintegration ratio after each of the five cycles are presented in Table 4.

Figure 10 shows the number of cycles plotted against the slake durability index. According to the classification of Gamble [8], the samples from the Cunj outcrop can be categorized as highly durable rocks. The I_{d2} values for the siltstone sample of weathering grade I (FR) range from 97.03 to 97.82%, and the I_{d5} values range from 94.01 to 94.24%. The I_{d2} values for the siltstone sample of weathering grade III

TABLE 3: Descriptions, typical characteristics, ranges of field-estimated uniaxial compressive strengths, and point load strength index values for siltstones of different weathering grades in the Istria Peninsula.

Term	Symbol	Description and typical characteristics [15]	Grade [15, 40]	Description and typical characteristics of siltstone in the study area [30]	Uniaxial compressive strength, σ_{ci} (MPa) min.-mean-max. [30, 41]	Point load strength index, $I_{p(50)}$ (MPa) mean
Fresh (unweathered)	FR	No visible sign of rock material weathering. There may be slight discoloration on major discontinuity surfaces.	I R4	Grey, fresh, and intact siltstone. No signs of weathering. Slight discoloration along cracks. Water impermeable. Breaking of sample requires more than one blow of geological hammer. Original rock structure is visible.	46-55-65	2.2
Slightly weathered	SW	Discoloration indicates weathering of rock material and discontinuity surfaces. All the rock material may be discolored by weathering and may be somewhat weaker than its fresh condition.	II R3	Bright grey siltstone with slightly weathered joint surfaces. Water impermeable. Sample cannot be cut with a knife but it can be broken in blocks with one blow of geological hammer. Original rock structure is visible.	27-33-38	—
Moderately weathered	MW	Less than half of the rock material is decomposed and/or disintegrated to a soil. Fresh or discolored rock is present either as a discontinuous framework or as corestones.	III R2	Grey to brown siltstone with brown joint surfaces and low water permeability of discontinuities. Sample can be cut with a knife with difficulty and some blocks can be easily broken with light blows of geological hammer. Original rock structure is visible.	20-22-25	0.9
Highly weathered	HW	More than half of the rock material is decomposed and/or disintegrated to a soil. Fresh or discolored rock is present either as a discontinuous framework or as corestones.	IV R1	Brown siltstone with frequent microcracks and brown weathered surface. High water permeability of discontinuities. Sample disintegrates with light blow of geological hammer and can be cut with a knife. Original rock structure is visible.	* <20 ** NA	** NA
Completely weathered	CW	All rock material is decomposed and/or disintegrated to soil. The original mass structure remains largely intact.	V R0	Light brown silty-clayey soil mixed with remains of siltstone. Pieces can be broken by hand. Original rock structure is visible.		** NA
Residual soil	RS	Rock is completely altered to a soil with the original fabric destroyed.	VI R0	Brown siltstone coarse debris material mixed with clayey, sandy silt. Pieces can be broken by hand.		** NA

* Schmidt hammer results on rocks with a uniaxial compressive strength below 20 MPa are likely to yield highly ambiguous results.

** NA not applicable.

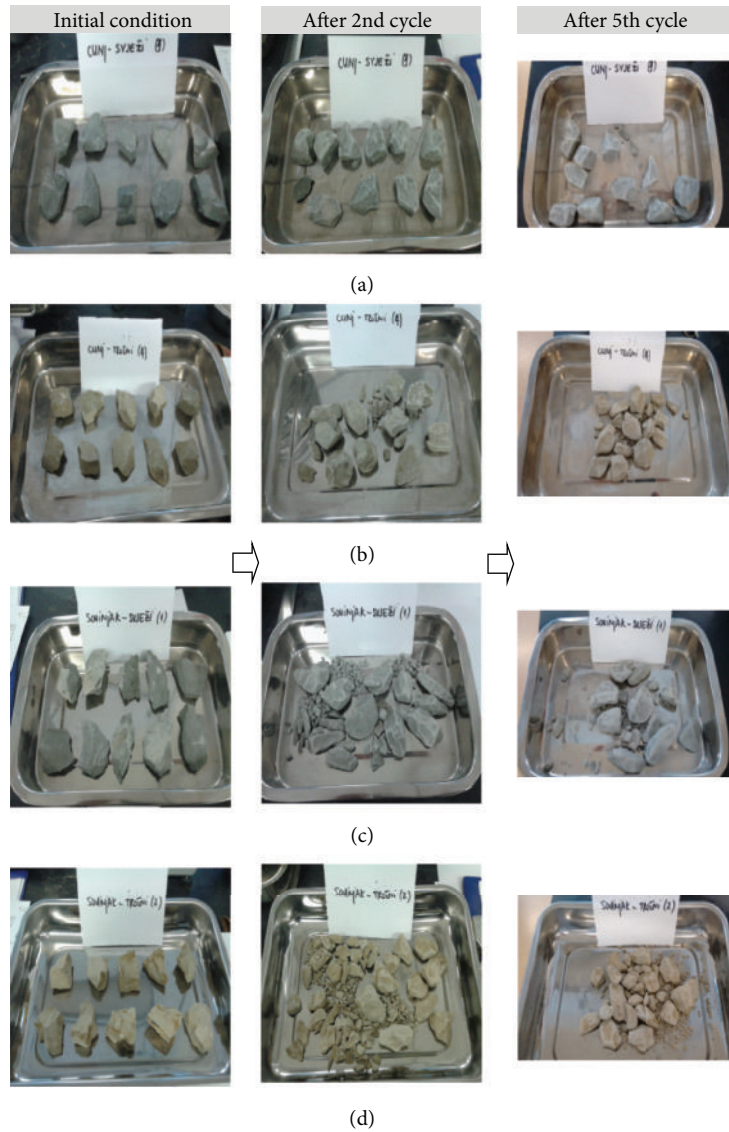


FIGURE 6: Samples taken from flysch outcrops near ((a), (b)) Cunj Village and ((c), (d)) Sovinjak Village, including initial conditions (left), after the 2nd cycle (middle), and after the 5th cycle (right) of the slake durability test.

(MW) range from 95.39 to 97.73%, and the I_{d5} values range from 89.52 to 94.45%. The samples from the Sovinjak outcrop are categorized as medium to highly durable rocks with I_{d2} values of 88.31% for the siltstone sample of weathering grade I (FR) and 89.69% for the sample of weathering grade III (MW). The slake durability indexes of the samples from the Sovinjak outcrop decrease significantly from the second cycle to the fifth cycle. The sample of weathering grade I (FR) has a lower durability index after each cycle than the sample of weathering grade III (MW). Based on a visual inspection and the conditions after the second cycle, the samples should be categorized as a lower class in Gambler's classification.

Žufić [25] performed two cycles of slake durability tests on fresh siltstones from flysch badlands in the Istria Peninsula. The slake durability index after the second cycle varied from 94.17 to 99.09%. These results are quite similar to those

that were obtained from siltstone samples from the Cunj outcrop in this study. Further sample degradation cannot be compared because [25] performed only two slaking cycles. Vlastelica [39] investigated the durability of marls from a flysch rock mass in the Dalmatia region of Croatia through four cycles of slake durability tests. The slake durability index varied from 97.31 to 99.29% after the second cycle and from 94.39 to 98.27% after the fourth cycle. These results are higher than the results that were obtained in this study probably because the mineral composition and textural features of the marls in the Dalmatia region are different than those in this study. Figure 10 shows the relationship between the slake durability index and the number of slaking cycles in this study and in previous investigations of similar sedimentary rocks. However, when they are subjected to the slake durability test, siltstone samples disintegrate to fragments of different

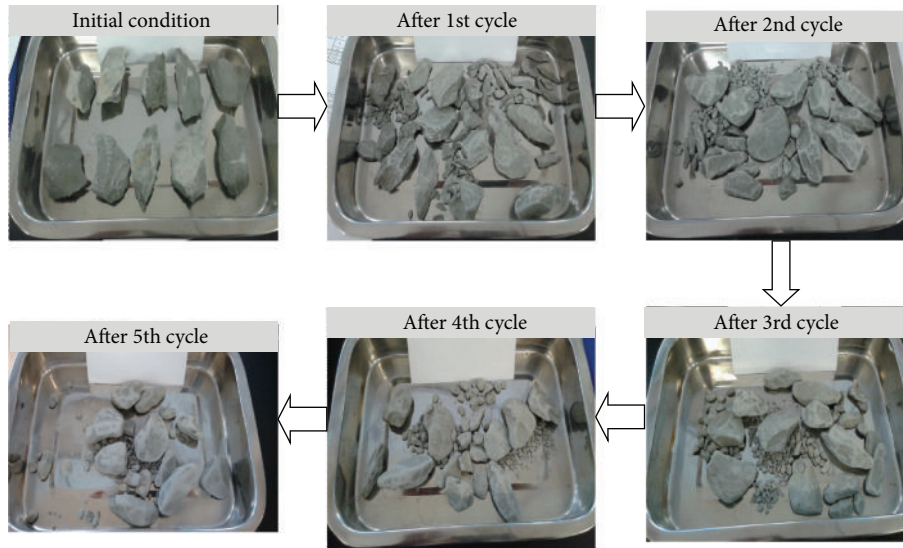


FIGURE 7: Example of a heavily degraded siltstone sample of weathering grade I (FR) (1) taken from a flysch outcrop near Sovinjak Village after five cycles of the slake durability test with $I_{d2} = 88\%$ and $I_{d5} = 73\%$.

TABLE 4: Results of five cycles of the slake durability tests, including the slake durability index, degradation ratio, and modified degradation ratio, for siltstones of different weathering grades in the study area.

Weathering grade	Sample number	Sampling location	First cycle	Second cycle	Third cycle	Fourth cycle	Fifth cycle
			Slake durability index (I_d)				
			I_{d1} [%]	I_{d2} [%]	I_{d3} [%]	I_{d4} [%]	I_{d5} [%]
I (FR)	(1)	Sovinjak	94.71	88.31	82.16	76.75	72.60
III (MW)	(2)		94.35	89.69	85.34	80.97	76.75
I (FR)	(3)	Cunj	98.15	97.03	95.99	94.96	94.01
III (MW)	(4)		97.41	95.39	93.40	91.45	89.52
I (FR)	(5)		98.76	97.82	96.41	95.51	94.24
III (MW)	(6)		98.64	97.73	96.32	95.52	94.45
			Degradation ratio (D_R)				
			D_{R1}	D_{R2}	D_{R3}	D_{R4}	D_{R5}
I (FR)	(1)	Sovinjak	0.69	0.65	0.61	0.58	0.55
III (MW)	(2)		0.69	0.60	0.56	0.53	0.50
I (FR)	(3)	Cunj	0.84	0.81	0.79	0.78	0.76
III (MW)	(4)		0.82	0.79	0.75	0.72	0.69
			Modified degradation ratio (D_{RP})				
			D_{RP1}	D_{RP2}	D_{RP3}	D_{RP4}	D_{RP5}
I (FR)	(1)	Sovinjak	0.30	0.35	0.39	0.42	0.50
III (MW)	(2)		0.31	0.41	0.45	0.47	0.50
I (FR)	(3)	Cunj	0.16	0.20	0.21	0.22	0.24
III (MW)	(4)		0.18	0.22	0.25	0.28	0.31

sizes that do not correspond to the high values of the slake durability index. The graphs in Figures 8 and 9 are used to calculate the degradation ratio and the modified degradation ratio after each slaking cycle (Table 4). Figure 11 shows the changes of these parameters through the slaking cycles. After each cycle, the siltstone sample of weathering grade I (FR) that was taken from the Sovinjak outcrop had a lower durability index than the sample of weathering grade III (MW). The other two parameters indicate that the siltstone

sample of weathering grade III (MW) disintegrated more than the sample of weathering grade I (FR). According to the classification of Erguler and Shakoor [12], based on the disintegration ratio, the samples from the Cunj outcrop can be categorized as medium to highly durable rocks, and the samples from the Sovinjak outcrop can be categorized as medium durability rocks. Therefore, the tested samples are classified in the lower durability class based on the fragmentation during the slake durability test.

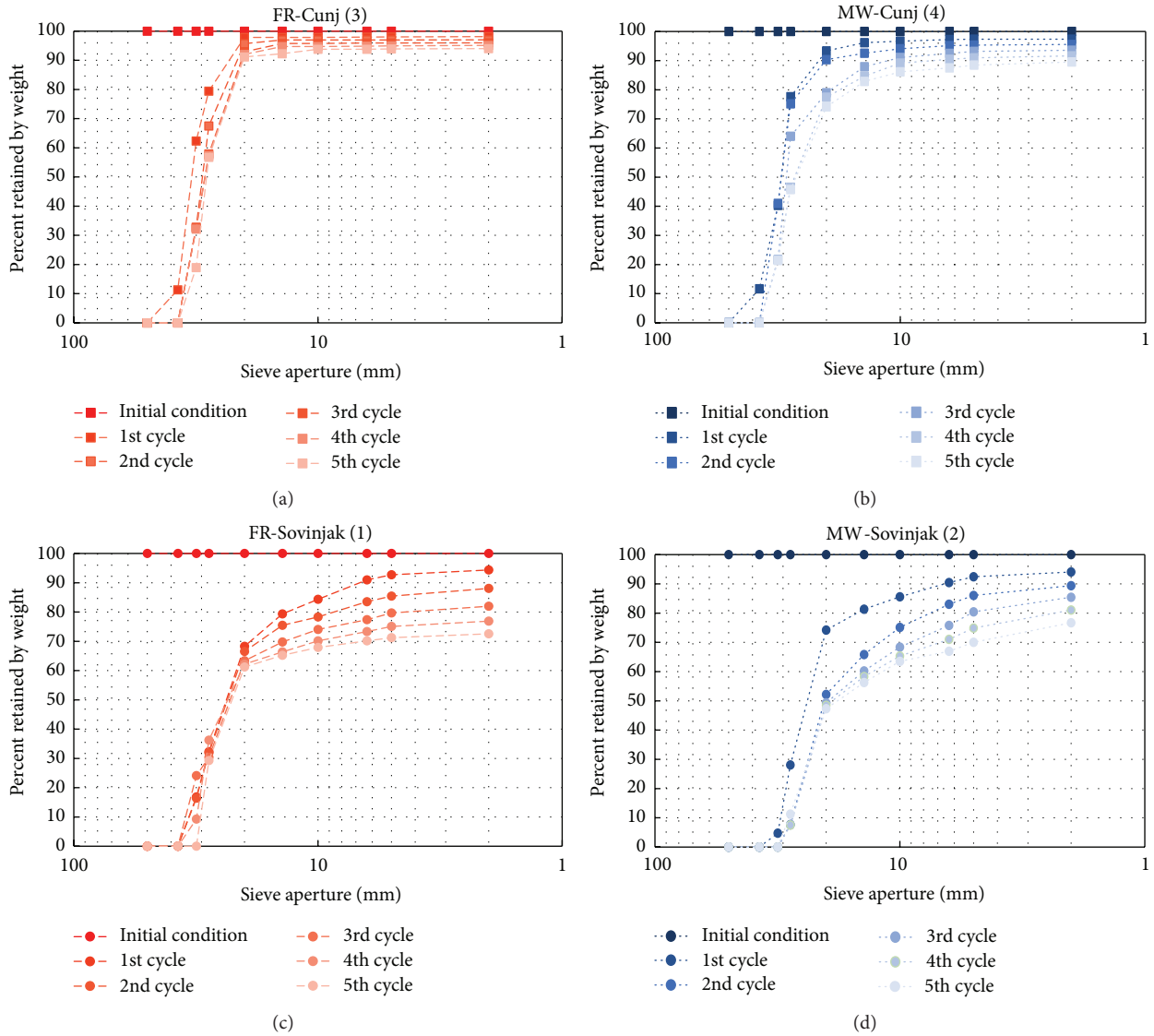


FIGURE 8: Fragment size distribution curves of the retained weight for the siltstone samples of weathering grades (a) I (FR) (3) and (b) III (MW) (4) from a flysch outcrop near Cunj Village and samples of weathering grades (c) I (FR) (1) and (d) III (MW) (2) from a flysch outcrop near Sovinjak Village.

The change in the calculated D_{RP} values between the slaking cycles is also determined to assess the potential long-term degradation of the investigated samples. A logarithmic curve is fitted to the D_{RP} values of each sample, and high R^2 values are calculated (Figure 12). From this curve, the number of cycles that are required for a sample to reach 50% of the maximum possible degradation ($D_{RP} = 1$), N_{50} , is estimated. The siltstone samples from the Sovinjak outcrop are less durable and more susceptible to degradation than those from the Cunj outcrop, and the N_{50} values differ considerably for the same weathering grade. The N_{50} values for the samples from the Sovinjak outcrop are 9 cycles for the sample of weathering grade I (FR) and 5 cycles for the sample of weathering grade III (MW). The samples from the Cunj outcrop have N_{50} values of 1050 cycles for weathering grade I (FR) and 60 cycles for weathering grade III (MW).

6. Discussion and Conclusions

The primary intent of this research is to establish relationship of geotechnical properties and durability with weathering of siltstones from a flysch rock mass in the Istria Peninsula. According to the results obtained by this study, weathering has a significant influence on the plasticity of siltstones. The liquid limit and plasticity index values of silty material increase with increasing weathering grade.

Weathering also has an influence on the uniaxial compressive strengths that are determined with a Schmidt hammer and the PLT. The uniaxial compressive strength decreases with increasing weathering grade. These test methods cannot be applied to highly weathered and more weathered siltstones that have uniaxial compressive strengths of less than 20 MPa because the tests are likely to yield ambiguous results.

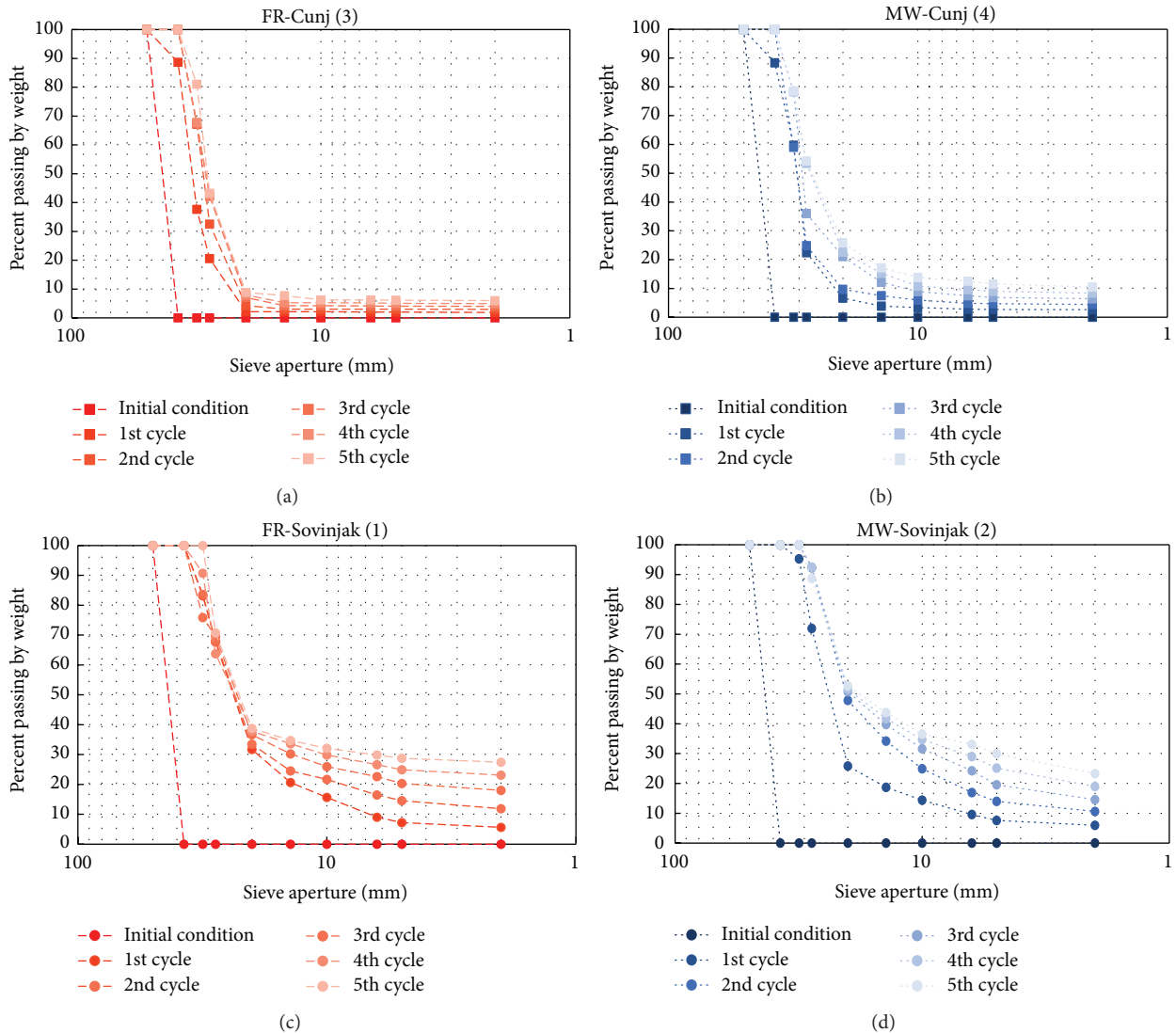


FIGURE 9: Fragment size distribution curves of the passed weight for the siltstone samples of weathering grades (a) I (FR) (3) and (b) III (MW) (4) from a flysch outcrop near Cunj Village and samples of weathering grades (c) I (FR) (1) and (d) III (MW) (2) from a flysch outcrop near Sovinjak Village.

Determination of durability of siltstones using only standardized tests is not sufficient. The use of the slake durability test does not adequately explain the slaking behavior of siltstones because the fragmented samples acquire high slake durability index but are highly degraded. Therefore, additional parameters, such as the degradation ratio and the modified degradation ratio, were calculated to indicate not only the durability but also the manner of disintegration of siltstones of different weathering grades. The siltstone sample of weathering grade I (FR) was more durable and less susceptible to degradation than the siltstone sample of weathering grade III (MW). Fresh samples disintegrated less than moderately weathered samples; therefore, fewer drying-wetting cycles are required to reach the maximum possible degradation. According to the classification based

on the slake durability index the siltstone samples with different weathering grades from Istria are classified in the higher durability class than in classification based on the fragmentation during the slake durability test. The standard slake durability index increases the slaking resistance of the tested siltstone samples by at least one class.

The obtained laboratory results indicate that weathering has a significant influence on the plasticity, uniaxial compressive strength, and durability characteristics of the siltstones. Overall, these test results demonstrated their usefulness of understanding influence of weathering of siltstones from the flysch rock masses on the landslide and erosion occurrences in the Istria Peninsula. The authors suggest that additional tests and studies on siltstones with different weathering grades are needed to widen the obtained results.

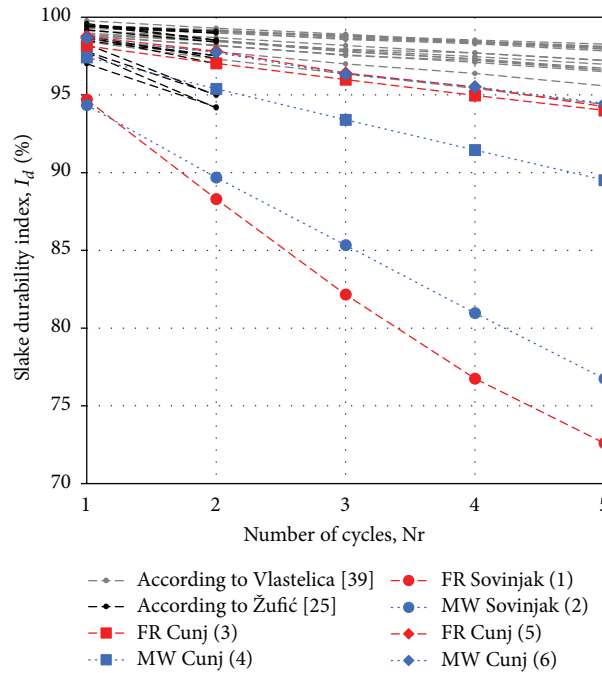


FIGURE 10: Influence of the number of slaking cycles on the slake durability index of the siltstone samples of different weathering grades that were tested in this study and from previous tests of similar samples of fresh siltstone from a flysch rock mass in Istria [25] and marl samples from a flysch rock mass in Dalmatia [39].

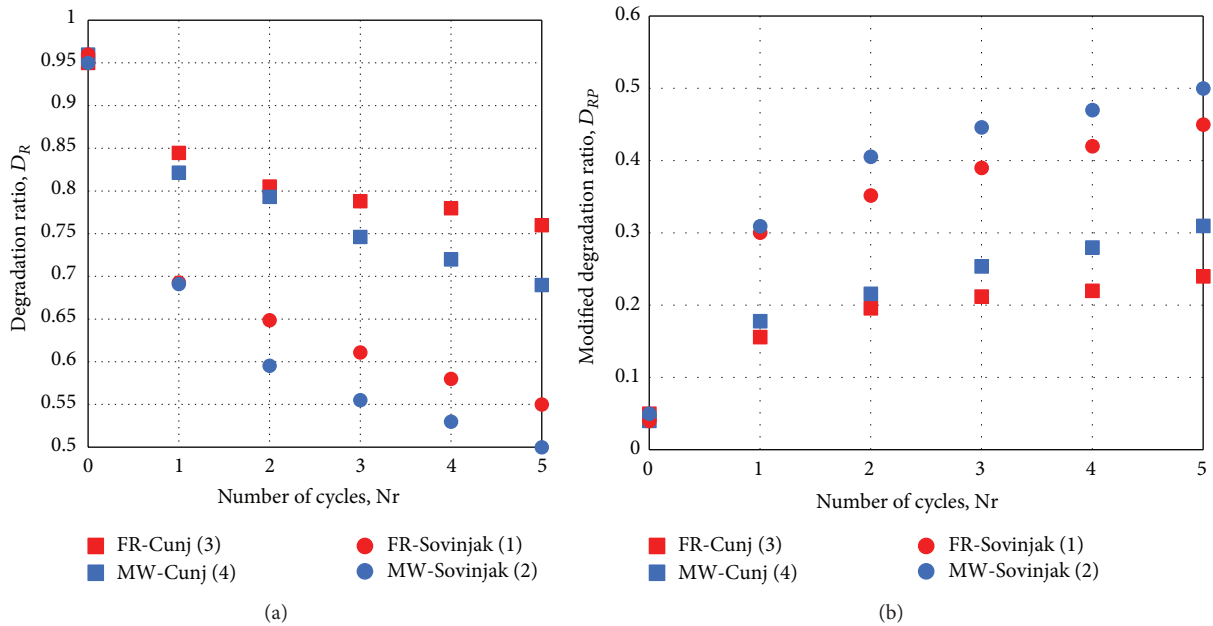


FIGURE 11: (a) Degradation ratio and (b) modified degradation ratio after each slaking cycle for the siltstone samples of weathering grades I (FR) and III (MW) from flysch outcrops near Cunj Village and Sovinjak Village.

Competing Interests

The authors declare that they have no competing interests.

Acknowledgments

This work has been supported in part by the University of Rijeka under Project no. 475, entitled Development of

Landslide Monitoring and Early Warning System for the Purpose of Landslide Hazard Reduction. As well, this work has been supported in part by Ministry of Science, Education and Sports of the Republic of Croatia under the project Research Infrastructure for Campus-Based Laboratories at the University of Rijeka, no. RC.2.2.06-0001. Project has been cofunded from the European Fund for Regional Development (ERDF).

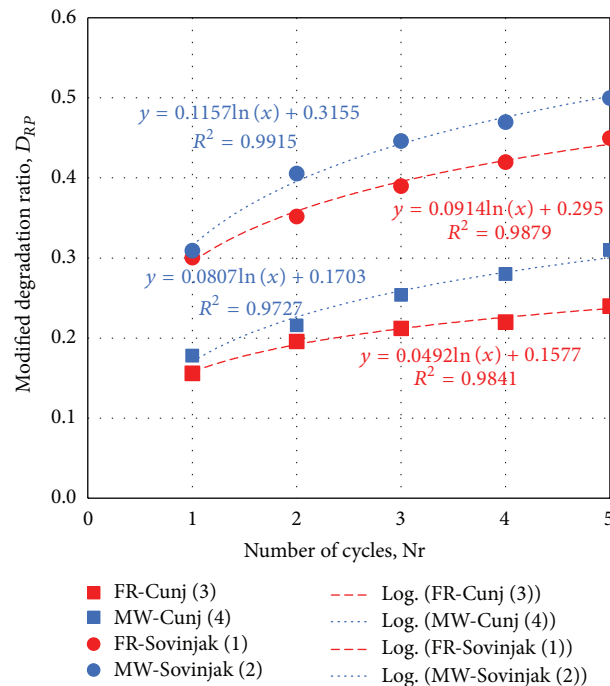


FIGURE 12: Logarithmic curves fitted to the plot of the modified degradation ratio against slake durability test cycles for the siltstone samples of weathering grades I (FR) and III (MW) from the flysch outcrops near Cunj Village and Sovinjak Village.

References

- [1] M. J. Selby, *Hillslope Materials and Processes*, Oxford University Press, 1993.
- [2] Geological Society of London, "The preparation of maps and plans in terms of engineering geology: report by the Geological Society Engineering Group Working Party," *Quarterly Journal of Engineering Geology and Hydrogeology*, vol. 5, no. 4, pp. 293–382, 1972.
- [3] R. J. Chandler, "The effects of weathering on the shear strength properties of Keupler marl," *Geotechnique*, vol. 19, no. 3, pp. 321–334, 1969.
- [4] M. Reißmüller, *Geotechnische Eigenschaften verwitterter Kfssener Mergel [Diploma thesis]*, Technical University of Munich, Munich, Germany, 1997.
- [5] M. Chigira and T. Oyama, "Mechanism and effect of chemical weathering of sedimentary rocks," *Engineering Geology*, vol. 55, no. 1-2, pp. 3–14, 2000.
- [6] P. Bhattarai, H. Marui, B. Tiwari, N. Watanabe, G. Tuladhar, and K. Aoyama, "Influence of weathering on physical and mechanical properties of mudstone," in *Disaster Mitigation of Debris Flows, Slope Failures and Landslides*, pp. 467–479, Universal Academy Press, Tokyo, Japan, 2006.
- [7] P. G. Fookes, C. S. Gourley, and C. Ohikere, "Rock weathering in engineering time," *Quarterly Journal of Engineering Geology*, vol. 21, no. 1, pp. 33–57, 1988.
- [8] J. C. Gamble, *Durability-plasticity classification of shales and other argillaceous rocks [Ph.D. thesis]*, University of Illinois, 1971.
- [9] J. A. Franklin and R. Chandra, "The slake-durability test," *International Journal of Rock Mechanics and Mining Sciences & Geomechanics Abstracts*, vol. 9, no. 3, pp. 325–328, 1972.
- [10] J. C. Dick and A. Shakoor, "Characterizing durability of mudrocks for slope stability purposes," *Geological Society of America Reviews in Engineering Geology*, vol. 10, pp. 121–130, 1995.
- [11] J. Martinez-Bofill, J. Corominas, and A. Soler, "Behaviour of the weak rock cut slopes and their characterization using the results of the slake durability test," in *Engineering Geology for Infrastructure Planning in Europe*, vol. 104 of *Lecture Notes in Earth Sciences*, pp. 405–413, Springer, Berlin, Germany, 2004.
- [12] Z. A. Erguler and A. Shakoor, "Quantification of fragment size distribution of clay-bearing rocks after slake durability testing," *Environmental & Engineering Geoscience*, vol. 15, no. 2, pp. 81–89, 2009.
- [13] M. Cano and R. Tomás, "An approach for characterising the weathering behaviour of Flysch slopes applied to the carbonatic Flysch of Alicante (Spain)," *Bulletin of Engineering Geology and the Environment*, vol. 74, no. 2, pp. 443–463, 2015.
- [14] Z. A. Erguler and R. Ulusay, "Assessment of physical disintegration characteristics of clay-bearing rocks: disintegration index test and a new durability classification chart," *Engineering Geology*, vol. 105, no. 1-2, pp. 11–19, 2009.
- [15] ISRM Commission on Testing Methods, *Rock Characterization, Testing and Monitoring: ISRM Suggested Methods*, Pergamon Press, Oxford, UK, 1981.
- [16] ASTM, "Standard test method for slake durability of shales and similar weak rocks," Tech. Rep. D4644-87, ASTM, Philadelphia, Pa, USA, 2004.
- [17] P. Mišćević and G. Vlastelica, "Durability characterization of marls from the region of dalmatia, croatia," *Geotechnical and Geological Engineering*, vol. 29, no. 5, pp. 771–781, 2011.
- [18] M. Cano and R. Tomás, "Proposal of a new parameter for the weathering characterization of carbonate flysch-like rock masses: the Potential Degradation Index (PDI)," *Rock Mechanics and Rock Engineering*, vol. 49, no. 7, pp. 2623–2640, 2016.

- [19] I. Velić and I. Vlahović, *Geologic Map of Republic of Croatia 1:300.000*, Croatian Geological Survey, Zagreb, Croatia, 2009 (Croatian).
- [20] S. Bergant, J. Tišljar, and M. Šparica, "Eocen carbonates and flysch deposits of the Pazin basin," in *Field Trip Guidebook. 22nd IAS Meeting of Sedimentology*, Institute of Geology, 2003.
- [21] Ž. Arbanas, Č. Benac, and V. Jurak, "Causes of debris flow formation in flysch area of North Istria, Croatia," in *Monitoring, Simulation, Prevention and Remediation of Dense and Debris Flows*, G. Lorenzini and C. A. Brebbia, Eds., WIT Transaction on Ecology and the Environment, pp. 283–292, 2006.
- [22] Ž. Arbanas, M. Grošić, D. Goršić, and B. Griparić, "Landslides remedial works on small roads of Istria," in *Proceedings of the 4th Croatian Roads Congress*, p. 38, 2007.
- [23] Ž. Arbanas, S. Dugonjić, and Č. Benac, "Causes of small scale landslides in flysch deposits of Istria, Croatia," in *Landslide Science and Practice, Volume 1: Landslide Inventory and Susceptibility and Hazard Zoning*, C. Margottini, P. Canuti, and K. Sassa, Eds., pp. 221–226, Springer, Rome, Italy, 2013.
- [24] Ž. Arbanas, S. Mihalić, M. Grošić, S. Dugonjić, and M. Vivoda, "Landslide brus, translational block sliding in flysch rock mass," in *Proceedings of the European Rock Mechanics Symposium (EUROCK '10)*, pp. 635–638, June 2010.
- [25] E. Žufić, *Investigation of geotechnical properties of flysch rock mass in Istria area [M.S. thesis]*, University of Zagreb, 2011 (Croatian).
- [26] V. Gulam, *The erosion of flysch badlands in the central Istria [Ph.D. thesis]*, University of Zagreb, 2012 (Croatian).
- [27] S. Utili, *Evolution of natural slopes subject to weathering: an analytical and numerical study [Ph.D. thesis]*, Politecnico di Milano, Milan, Italy, 2004.
- [28] R. Cardoso and E. E. Alonso, "Degradation of compacted marls: a microstructural investigation," *Soils and Foundations*, vol. 49, no. 3, pp. 315–327, 2009.
- [29] D. Mihljević and E. Prelogović, "Structural—geomorphological characteristic of the mountain ranges Učka & Čičarija," in *Proceedings of the International Symposium Geomorphology and Sea and the Meeting of the Geomorphological Commission of the Carpatho-Balkan Countries*, pp. 13–24, 1992.
- [30] M. Vivoda Prodan, M. Mileusnić, S. Mihalić Arbanas, and Ž. Arbanas, "Influence of weathering processes on the shear strength of siltstones from a flysch rock mass along the northern Adriatic coast of Croatia," *Bulletin of Engineering Geology and the Environment*, 2016.
- [31] ASTM, "Standard test methods for particle-size distribution (Gradation) of soils using sieve analysis," ASTM D6913-04, 2009.
- [32] American Society for Testing and Materials (ASTM), "Standard test method for density of hydraulic cement," ASTM C188-15, American Society for Testing and Materials (ASTM), West Conshohocken, Pa, USA, 2015.
- [33] ASTM, "Standard test methods for liquid limit, plastic limit, and plasticity index of soils," ASTM D4318-10e1, 2010.
- [34] British Standards, "Methods of test for soils for civil engineering purposes. Classification tests," BS 1377-2:1990, 1990.
- [35] E. Eberhardt, K. Thuro, and M. Luginbuehl, "Slope instability mechanisms in dipping interbedded conglomerates and weathered marls—the 1999 Ruffi landslide, Switzerland," *Engineering Geology*, vol. 77, no. 1-2, pp. 35–56, 2005.
- [36] P. Mišćević, D. Števančić, and N. Štambuk-Cvitanović, "Slope instability mechanisms in dipping conglomerates over weathered marls: Bol landslide, Croatia," *Environmental Geology*, vol. 56, no. 7, pp. 1417–1426, 2009.
- [37] ISRM Commission on Testing Methods, "Suggested methods for determining point load strength," in *The Complete ISRM Suggested Methods for Rock Characterization, Testing and Monitoring: 1974–2006*, R. Ulusay and J. A. Hudson, Eds., ISRM, 1985.
- [38] Ž. Arbanas, M. Grošić, and S. Dugonjić, "Behaviour of the reinforced cuts in flysch rock mass," in *Proceedings of the 1st International Conference on Transportation Geotechnics*, pp. 283–291, September 2008.
- [39] G. Vlastelica, *The influence of weathering on durability of cuts in soft rock mass [Ph.D. thesis]*, University of Split, Split, Croatia, 2015 (Croatian).
- [40] P. Marinos and E. Hoek, "Estimating the geotechnical properties of heterogeneous rock masses such as flysch," *Bulletin of Engineering Geology and the Environment*, vol. 60, no. 2, pp. 85–92, 2001.
- [41] R. P. Miller, *Engineering classification and index properties for intact rock [Ph.D. thesis]*, University of Illinois, 1965.

Research Article

The Effects of High Alkaline Fly Ash on Strength Behaviour of a Cohesive Soil

A. Binal

Faculty of Engineering, Department of Geological Engineering, Hacettepe University, Beytepe Campus, 06800 Ankara, Turkey

Correspondence should be addressed to A. Binal; adil@hacettepe.edu.tr

Received 28 February 2016; Revised 3 June 2016; Accepted 7 June 2016

Academic Editor: Guocheng Lv

Copyright © 2016 A. Binal. This is an open access article distributed under the Creative Commons Attribution License, which permits unrestricted use, distribution, and reproduction in any medium, provided the original work is properly cited.

Contemporarily, there are 16 coal-burning thermal power plants currently operating in Turkey. This number is expected to rise to 46 in the future. Annually, about 15 million tons of fly ash are removed from the existing thermal power plants in Turkey, but a small proportion of it, 2%, is recyclable. Turkey's plants are fired by lignite, producing Class C fly ash containing a high percentage of lime. Sulfate and alkali levels are also higher in Class C fly ashes. Therefore, fly ash is, commonly, unsuitable as an additive in cement or concrete in Turkey. In this study, highly alkaline fly ash obtained from the Yeniköy thermal power plants is combined with soil samples in different proportions (5%, 10%, 15%, 20%, and 25%) and changes in the geomechanical properties of Ankara clay were investigated. The effect of curing time on the physicochemical properties of the fly ash mixed soil samples was also analyzed. The soil classification of Ankara clay changed from CH to MH due to fly ash additives. Free swelling index values showed a decrease of 92.6%. Direct shear tests on the cohesion value of Ankara clay have shown increases by multiples of 15.85 and 3.01 in internal friction angle values. The California bearing ratio has seen a more drastic increase in value (68.7 times for 25% fly ash mix).

1. Introduction

Nowadays, fly ash from a power plant is getting to be a more complicated issue for countries due to environmental problems. The number of thermal power plants in Turkey corresponds to energy needs that are increasing day by day. Turkish lignite is typically low-grade coal that has a very low calorific value and high mineral matter content [1–3]. It has been reported in various studies that extreme, high ash yields can range from 23% to 64% [4, 5], which produce vast quantities of coal fly ash to be disposed. According to the latest numbers, the total amount of ash in ponds and landfills has already reached around 100 billion tons in Turkey [3]. Yeniköy power plant uses 4.8 million tons of low-quality lignite and generates 1.2 million tons of ash per year [3]. In contrast, a small quantity of fly ash is used as additives to raw cement or concrete, with far more being stored in the field and ash dam. Therefore, there have been limited studies on the stabilization of cohesive soils with fly ash addition in Turkey.

Bituminous coals have low concentrations of calcium compounds, and the ash produced (Class “F”) exhibits

no self-cementing characteristics. Subbituminous coals have higher levels of calcium carbonate (CaCO_3); thus, the ash (Class “C”) produced during combustion is rich in calcium, resulting in self-cementing characteristics. Since Class “C” fly ash is self-cementing; activators such as lime or Portland cement are not required. Upon exposure to water, Class “C” fly ash hydrates forming cementitious products similar to those produced during the hydration of Portland cement. This property makes self-cementing fly ash a very practical and economic stabilization agent for use in a variety of construction applications [6]. Some studies on the performance of fly ash mixed soil have claimed that Class C fly ashes are accomplished of ameliorating physicochemical properties of cohesive soils [7–11]. Fly ash is used to stabilize fine-grained soils so that a stable working platform can be provided for highway construction equipment [7, 12–14]. Additives with calcium oxide produce flocculation in the layers of clay by the substitution of monovalent ions by Ca^{2+} ions. This balances the electrostatic charges of the layers of clay and reduces the electrochemical forces of repulsion between them. The adhesion of the particles of clay into flocks then occurs, giving

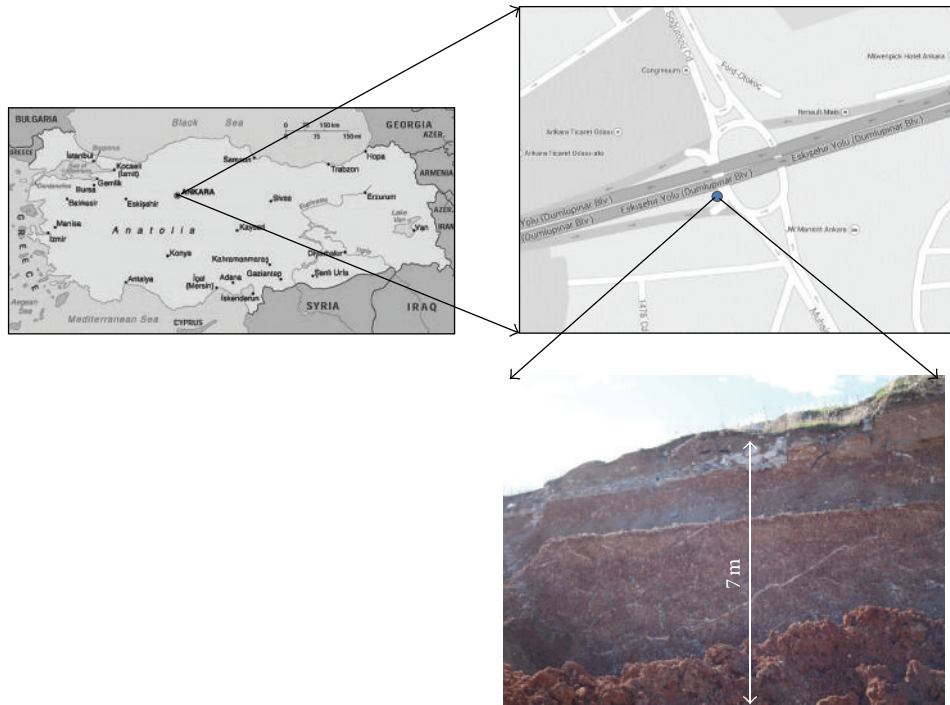


FIGURE 1: The soil sampling area.

rise to a soil with improved engineering properties: a more granular structure, less plasticity, greater permeability, and above all lower expansion [15–22]. Also, the presence of the OH^- ions produces an increase of the soil pH up to values of approximately twelve. In these conditions, pozzolanic reactions take place, when Si and Al which form part of the sheets of the clay dissolve and combine with the available Ca^{2+} giving rise to cementing compounds such as calcium silicate hydrates and calcium aluminate hydrates [18, 21, 23–25].

Akar et al. [3] have studied on short-term leaching manner of Fe, Ca, Cu, Co, Cd, Mn, Ni, Pb, Zn, and Cr (VI) from Yeniköy fly ash using TCLP-1311 [26] and ASTM D3987 [27] tests. According to their results, Ca was found as the most mobile element while Mn and Fe had the lowest mobility. The dissolution of selected trace elements was observed as higher for the particles below $38\ \mu\text{m}$ size. For the leaching tests of original fly ash material, the highest solubility values were found for Ca, Pb, and Cr (VI), respectively. The results suggested that releases of these trace elements were all lower than the allowed limits for solid wastes imposed by the EC Directive [3]. Furthermore, as to the study by Turhan et al. [28], the utilization of the examined all fly ash samples (included Yeniköy fly ash) except Kangal and Soma, in the road, street, roadbeds, and road pavement does not pose any significant source of radiation hazard.

The other material of this study is Ankara clay that includes a sequence of lacustrine sediments that covers the surface of the Ankara Valley. These expansive soils are settled in western, central, and southern parts of Ankara, the capital of Turkey. Due to the expansive nature of this

clay, damage to the roads and low-rise structures caused by differential volume changes of the clay occurs, particularly in the southern part of the city. This damage caused by the swelling has been deliberately ignored in both design and construction, however, because of limited budgets, poor construction methods, inadequate water drainage, and ineffective remedial measures [29].

Finer, reddish-brown clastic of the fluvial-lacustrine deposits is referred to as reconsolidate, stiff, and fissured “Ankara clay” in engineering, geological, and geotechnical studies. Networks of hair cracks and slickensides are often present in Ankara clay, and the surfaces of fragments are usually polished and glossy in nature. Undisturbed sampling is rather difficult, and specimens tend to fail along the fissures and irregular surfaces [30].

This work aims to investigate the possibility of using high alkaline fly ash from Yeniköy lignite-fired power station to ameliorate the geomechanical properties of Ankara clay. The effects of the proportions of the fly ash (FA) and curing time on the physical properties and strength development in Ankara clay have been illustrated in laboratory conditions. Scanning electron microscope (SEM) studies were performed to investigate the factors preventing swelling of Ankara clay. The outcomes of this work are to create new uses for FA in Turkey as well as build a basic mix design for further studies of strength and durability.

2. Materials

2.1. Ankara Clay. Three soil blocks have been supplied from a construction area, from a depth of three meters (Figure 1).

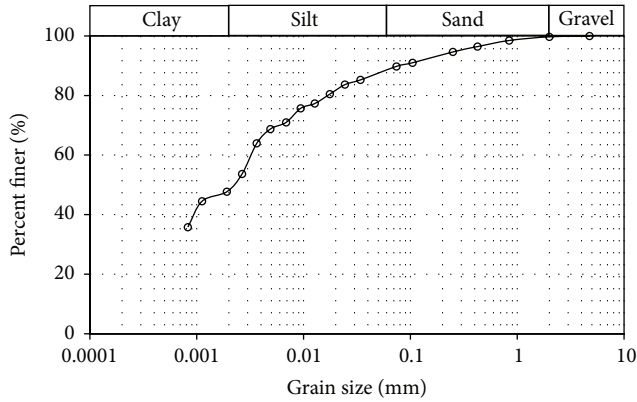


FIGURE 2: The particle-size distribution of AC.

The colour of Ankara clay (AC) in the sampling area is claret red or brown, and it includes lime bands.

AC includes 48% clay, 37.2% silt, 14.5% sand, and 0.3% gravel-sized materials (Figure 2). Regarding index properties, AC has a plastic limit (PL) of 35%, a liquid limit (LL) of 88.7%, and plasticity index (PI) of 53.7%. The soil sample was identified as “CH” by the unified soil classification system.

Smectite, illite, chlorite, kaolinite, quartz, and calcite minerals were determined by the XRD analysis of a bulk sample (range: 5° – 70°) (Figure 3(a)). Besides, types of clay minerals were identified by the XRD analysis on the same sample (Figure 3(b)).

AC has a typical value that is close to active clay ($A_c = 1.12 < 1.2$) and a high swelling potential (free swell index = 50%); therefore, it has been described as expansive soil. Shear strength parameters were calculated as cohesion (c) of 13.9 kPa and internal friction angle (ϕ) of 10.70. Furthermore, the CBR value has been determined as 6.7%. All tests were realized to ASTM standards. Chemical analysis presented that the principal constituents of AC are silica, aluminium, calcium, and iron oxides. Lime bands in AC are the cause of the high calcium content (Table 1).

2.2. Yeniköy Power Plant Fly Ash. In this study, a very high lime fly ash was obtained from the second unit of Yeniköy coal-fired power plant. X-ray fluorescence (XRF) analysis was realized to classify the fly ash. Yeniköy fly ash (YFA) is over 10% reactive lime (21.80%) due to TS EN 197-1 [32] and Class W (calcareous fly ash). In contrast to the standard required in reactive silica, YFA does not comply with the 25% rule. According to ASTM C618 [34] of $\text{SiO}_2 + \text{Al}_2\text{O}_3 + \text{Fe}_2\text{O}_3$, 40.63% of CaO, less than 50% and more than 10% due to Class C (high lime) fly ash provide critical conditions. YFA, $\text{SiO}_2 + \text{Al}_2\text{O}_3 + \text{Fe}_2\text{O}_3$, well below 70% of the amount due, does not comply with the conditions required in TS 639 [33]. For TS EN 450 standards [31], the limit for SO_3 is 3%; the amount of SO_3 in the ash is above this limit (16.63%). Because the percentage of free lime is 1.48%, the 1.00% of the standard limit has been passed. Accordingly, the desired conditions of YFA do not entirely conform to the respective four standards (Table 2).

TABLE 1: The physicochemical properties and the chemical composition of AC.

Index properties		Chemical composition (%)	
Natural water content, w_n (%)	30	SiO_2	56.35
Natural unit weight, γ_n (kN^3)	17.5	Al_2O_3	12.7
Liquid limit, w_L (%)	88.7	Fe_2O_3	5.37
Plasticity index, PI (%)	53.7	MnO	0.09
Specific gravity, G_s	2.69	MgO	1.99
Gravel (%)	0.3	CaO	9.2
Sand (%)	14.5	Na_2O	0.88
Silt (%)	37.2	K_2O	1.37
Clay (%)	48	TiO_2	0.81
Free swell index (%)	50	P_2O_5	0.12
% finer than number 200	89.8	LOI	11.12
Activity, A_c	1.12		
Mechanical properties			
Cohesion (kPa)	13.9		
Internal friction angle ($^{\circ}$)	10.7		
California bearing ratio (CBR, %)	6.7		

The morphological analysis results show that usually semispherical and spherical glass beads have a grain size between 2.1 and $16.89 \mu\text{m}$ (Figure 4) as well as rough surfaces, both perfectly ball-shaped and irregularly shaped particulate (Figure 5). Its irregularly shaped particles are 10–60 microns big.

The natural pH value of fly ash is a valuable property which has a significant effect on the mobility of trace elements in an aqueous environment. Fly ash-water slurry was prepared by mixing 5 g of fly ash with 100 mL of deionized water for the determination of the pH value of the sample [3]. WTW brand (3110) pH meter was used to determine the pH of YFA at one-hour intervals for 24 hours' period. The 24 hours of pH was determined as 12.67. Specific gravity and surface area of YFA were determined as 2.63 and $0.169 \text{ m}^2/\text{g}$ (Table 3).

XRD diffractograms show that YFA includes quartz, unburned clay remains (free lime), anhydrite, gehlenite, hematite, calcite, and sulphide (Figure 6).

3. Methods and Results

This study determined the effects of the fly ash (FA) additives on the strength of clay soil. AC was mixed with fly ash in 5%, 10%, 15%, 20%, and 25% proportions. Atterberg consistency limits, direct shear, the California bearing ratio (CBR), and swelling index tests were used on the cured samples, all tests to ASTM, and Indian standards. At the end of experiments, SEM imaging was realized on the samples.

3.1. Sample Preparation. The samples were prepared by the rules of modified proctor test sample preparation as to ASTM D1557 [35]. In that standard, soil at a selected moulding

TABLE 2: Standards compliance limits.

Oxide mass (%)	TS EN 450 [31]	TS EN 197-1 [32]		TS 639 [33]	ASTM C618 [34]	
		V	W		F	C
SiO ₂	21.85					
Al ₂ O ₃	15.41					
Fe ₂ O ₃	3.36					
S+A+F	40.63			>70.00	>70.00	>50.00
CaO	28.54					
MgO	2.73			<5.00		
SO ₃	16.63	<3.00		<5.00	<5.00	<5.00
K ₂ O	1.02					
Na ₂ O	6.87					
LOI	3.57	<5.00	<5.00	<5.00	<6.00	<6.00
Cl ⁻	0.008	<0.10				

TS EN: Turkish and European standards; TS: Turkish standard.

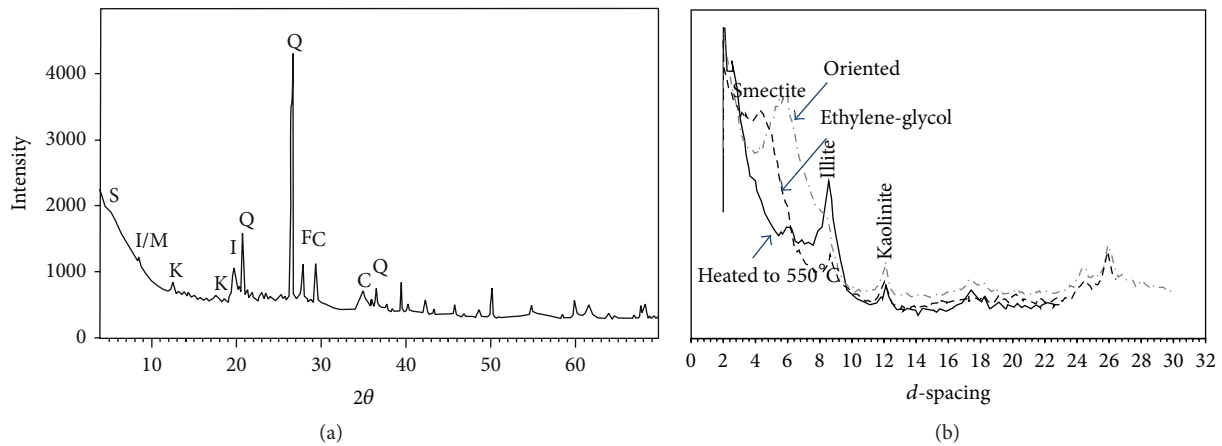


FIGURE 3: Typical XRD patterns of AC: (a) bulk (whole) sample and (b) clay fraction.

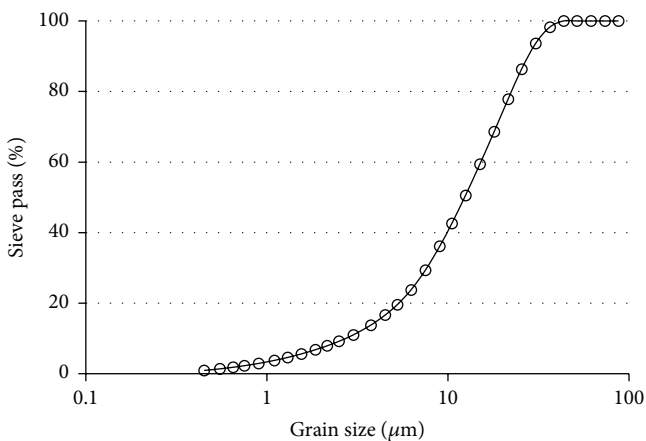


FIGURE 4: The grain size of it was determined by using Sympa Technology Laser Grain Size Analyses System.

water content is put in five layers into a mould, with each layer compacted by 56 blows of a 4.5 kg hammer dropped from a distance of 45 cm. The resulting dry unit weight is determined. The procedure is repeated for an adequate

TABLE 3: Some physical properties of YFA.

Specific gravity (G_s)	Specific surface area (m^2/g)	pH
2.63	0.169	12.67

number of moulding water contents to establish a relationship between the dry unit weight and the moulding water content for the soil. The compaction curve is plotted with the values of the dry unit weight and water content. The values of the highest dry unit weight and optimum moisture content are found from the compaction curve [35]. All CBR tests of samples were realized in optimum moisture content value and about at 98% modified proctor stiffness. Therefore, modified proctor tests were carried out to determine optimum moisture content and maximum dry density of the mixed samples. During sample preparation, firstly, AC samples were ground and after that screened with #4 of a sieve which has 4.75 mm of the aperture. Undersize materials were mixed with 5%, 10%, 15%, 20%, and 25% of FA by weight at the optimum water content (Table 4). Then those mixes were poured into the CBR moulds which have

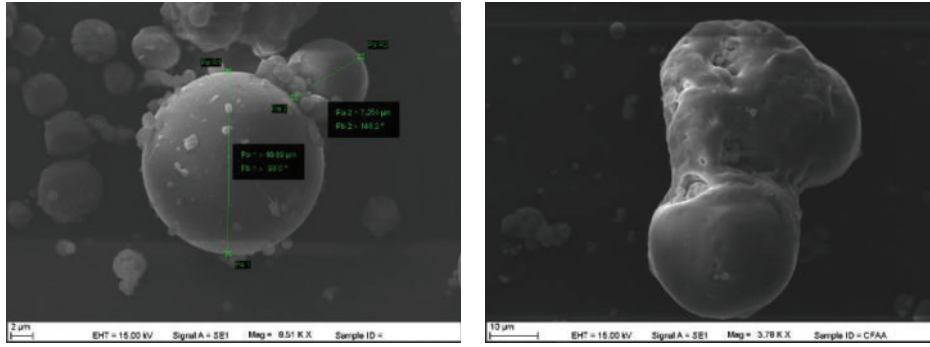


FIGURE 5: The scanning electron microscope (SEM) views of regular and irregular shaped glass beads of YFA.

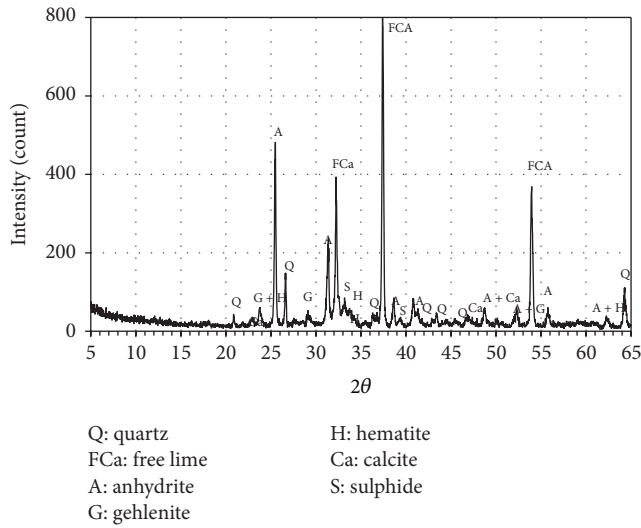


FIGURE 6: The X-ray diffractogram of YFA.

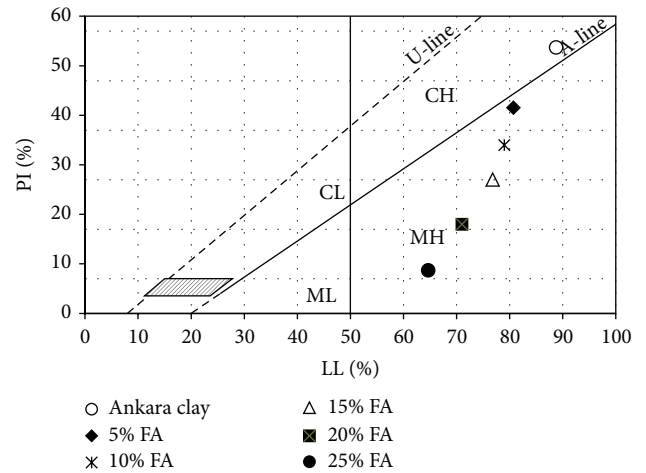


FIGURE 7: Consistency limits of AC and FA mixed soil.

152.4 mm in diameter and 177.8 mm of height. The samples were compacted in the five layers with 25 blows in each layer with using a mechanical compactor which automatically compacts and rotates mould after each blow while keeping track of the number of hammer blows. After that, mixtures were cured at 1, 7, and 28 days in the humidity cabinet which has 21°C of temperature and 90% of RH. During cure periods, prepared CBR samples have waited under load (7 kg), which present overburden pressure of the sampling depth of AC to prevent swelling and stress relaxation. Also, reference CBR samples having no FA were prepared as to the similar method of mixed samples.

3.2. Atterberg Limits. Atterberg limit tests were realized to examine the effects of the FA additive on the soil consistency. The 5%, 10%, 15%, 20%, and 25% fly ashes were mixed with AC. PI and LL tests were carried out to ASTM D4318 [36]. Results show that the FA additive is very active on the consistency limits of the soil. The unified soil classification of the AC was changed from “CH” to “MH.” PI was decreased from 53.75% to 8.76%, and LL was reduced from 88.71% to 64.61% (Figure 7). Furthermore, the plastic limit increased

TABLE 4: Compaction characteristics of testing soil mixed with FA.

FA content (%)	The maximum dry unit weight, γ_d (kN/m ³)	Optimum water content (%)
0	17.85	30
5	16.85	31.5
10	15.84	32.1
15	15.15	32.53
20	14.72	33.33
25	14.17	34.84

from 34.96% to 55.85% with the FA additive. This result shows that the land becomes more pliable with FA’s addition, better equipped for use in the construction of foundations and roads.

3.3. California Bearing Ratio (CBR). Prepared samples were tested as to the standard of the test method for California bearing ratio of laboratory compacted soils [37]. A fully automatic single-speed load frame that has 50 kN of the load cell and 1.27 mm/min speed was used in CBR tests. The values of California bearing ratio (CBR) tests show that the curing

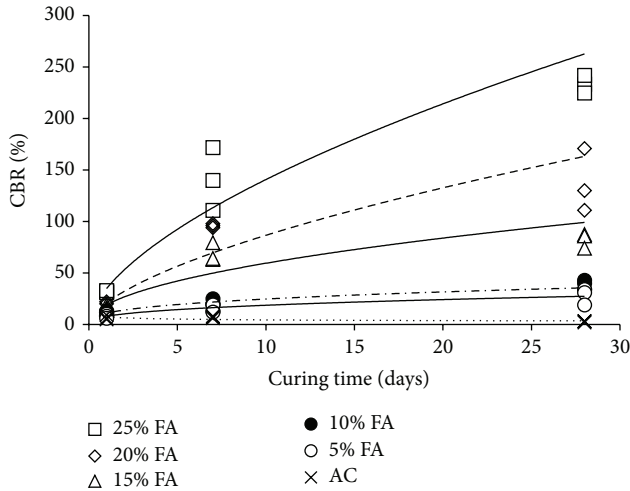


FIGURE 8: The effects of the curing time and FA content on the CBR values.

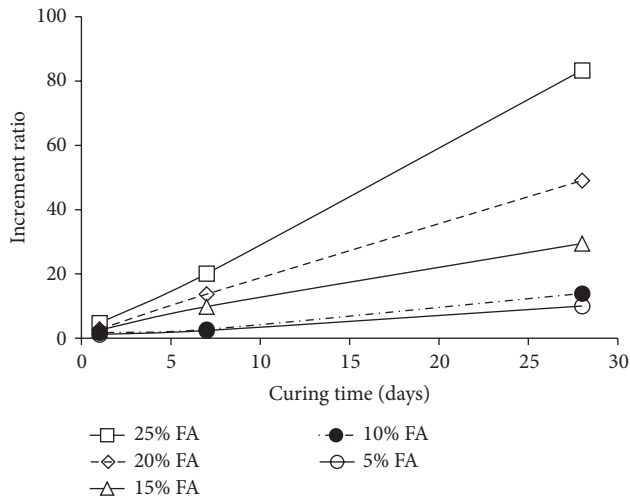


FIGURE 9: Increase at the CBR values with curing time and FA content.

time is critical to CBR values. All samples, including FA, present a high increase in CBR values after seven days curing (Figure 8). However, declines were observed in the CBR results of the samples, not including FA. That behaviour may be related to the curing conditions. Although AC samples were weighted with the load during curing, they started to swell when taking in water in the humidity cabinet. Therefore, they have begun to lose stiffness and CBR after the one-day curing. In contrast, other samples containing FA grew stiffer with curing time. The most increased rates (68.7 of 25% FA at 28 days) of the CBR values were found in the samples that include 25% FA (Figure 9). The increment ratio was calculated by dividing the CBR value of the FA mix by the CBR value of AC.

Furthermore, some physical changes were observed in the 25% FA mixtures. Although the colour of AC is claret red, the 25% FA mix colour was changed to a brownish green. As well, the 25% FA mix samples have shown brittleness (Figure 10).



FIGURE 10: The view of 25% FA mixes sample after the CBR test.

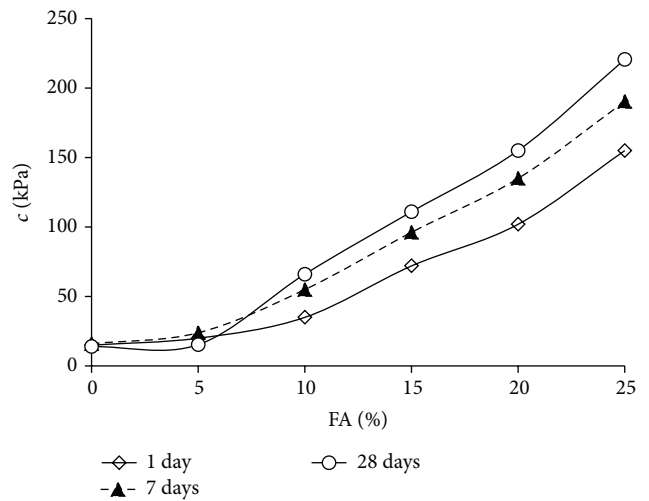


FIGURE 11: Variation of c with FA content and curing time.

3.4. Shear Strength. Shear strength properties of soil and fly ash mixed soil were determined by using direct shear test apparatus. Normal loads were decided as to sampling depth and overburden pressure. Furthermore, all tests were realized on 7- and 28-day cured samples according to standard test methods for a direct shear test of soils under consolidated drained conditions [38]. Due to the longer curing time, an increase in cohesion and angle of internal friction was determined to occur (Figures 11 and 12).

For 28-day curing period, AC's cohesion values increased 15.85 times and internal friction angles increased 3.01 times for the 25% fly ash mixed soil samples (Figure 13). Increment ratio was calculated by the value of the FA mix divided by the value of AC. Also the increase in internal friction angle is very striking. Fly ash additives roughen up to the surface of clay minerals and increase internal friction in that way.

3.5. Free Swell Index. Free swell is the increase in the volume of soil, without any external constraints, on submergence in water. The possibility of damage to structures because of swelling of expansive clays needs to be identified at the outset,

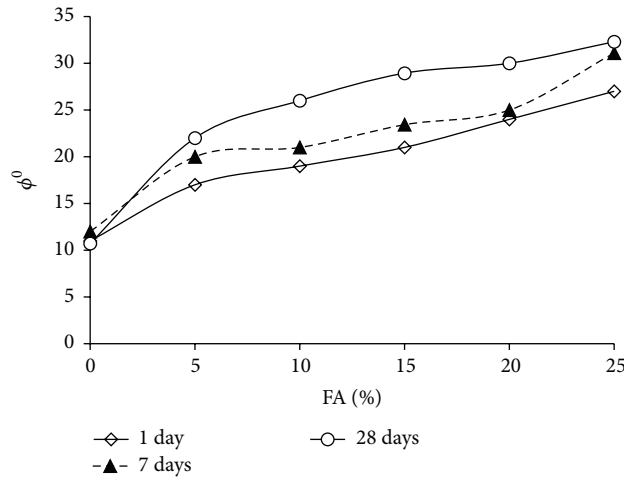


FIGURE 12: Variation of ϕ^0 with FA content and curing time.

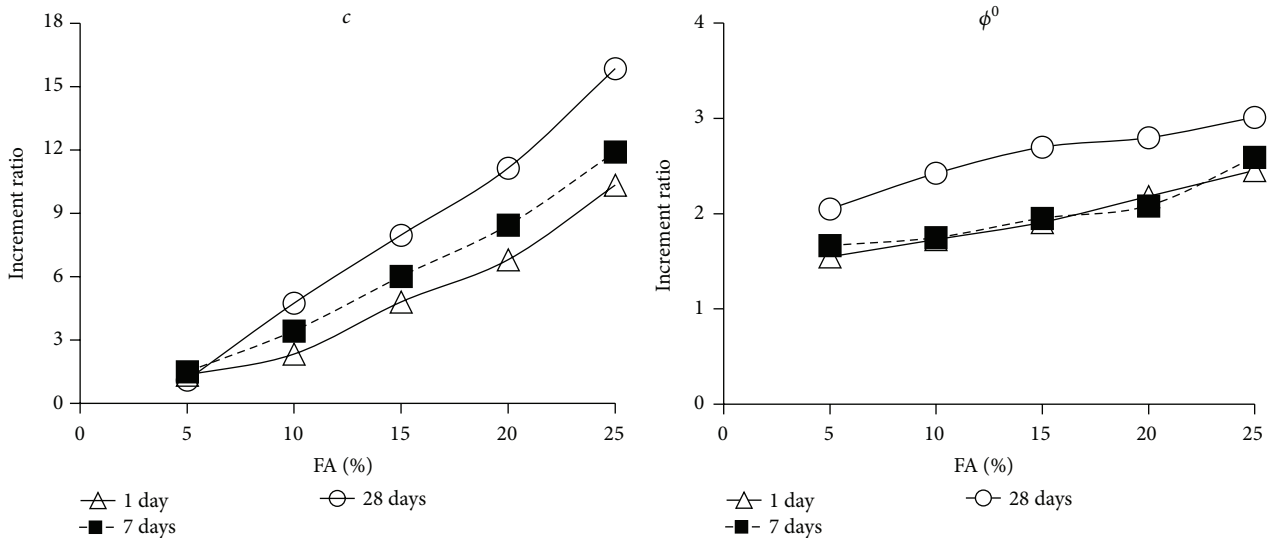


FIGURE 13: The increment ratios of shear strength parameters ($c-\phi$) with FA and curing time.

for an investigation of those soils likely to possess undesirable expansion characteristics. Inferential testing is used to reflect the potential of the system to swell under different simulated conditions. The actual magnitude of swelling pressures developed depends on the dry density, initial water content, surcharge loading, and several other environmental factors. Swelling tests were carried out to the Indian standard [39]. In this procedure, two 10 g soil specimens of oven dry soil passing through a 425-micron IS sieve are taken. If highly swelling soils, such as sodium bentonite, the sample size may be 5 g, alternatively, a cylinder of 250 mL may be used. Each soil specimen shall be poured in each of two glass graduated cylinders (100 mL capacity). One cylinder shall be filled with kerosene oil and the other with distilled water up to a 100 mL mark. Then with removal of entrapped air by gentle shaking, the soils in both the cylinders shall be allowed to settle. Sufficient time which is not less than 24 h shall be allowed for the sample to attain an equilibrium state of the volume

without any change in the volume of the soils. The final volume in each of the cylinders shall be read out. The level of the soil in the kerosene graduated cylinder shall be read as the original volume of the soil samples. The soil level in the distilled water cylinder shall be read as the free swell level [39].

The free swell index of the soil is calculated as follows:

$$\text{Free Swell Index (\%)} = \frac{V_d - V_k}{V_k} \times 100, \quad (1)$$

where V_d is the volume of soil specimen read from the graduated cylinder containing distilled water and V_k is the volume of soil specimen read from the graduated cylinder containing kerosene.

The free swell index values of soil samples decreased with the amount of fly ash in the mix (Figure 14). The free swell value of 25% fly ash mixed soil sample was close to 0%. With 5% FA mixed soil samples, the swelling ratio decreased by

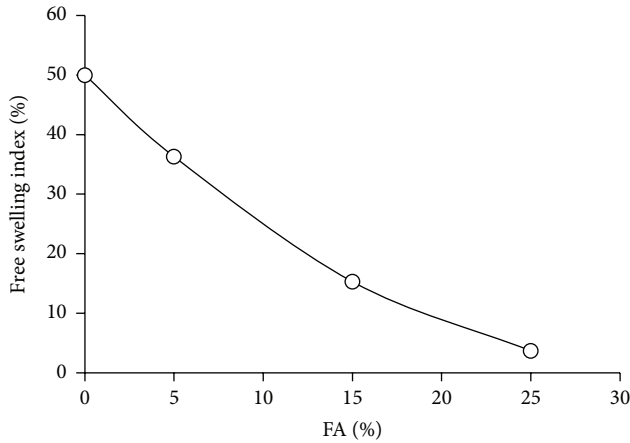


FIGURE 14: Free swelling index versus the amount of FA content.

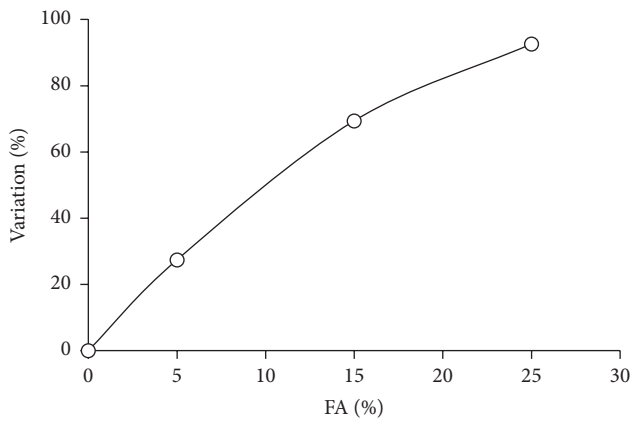


FIGURE 15: Free swelling variation versus the amount of FA content.

27.4% in value; with 25% FA, it declined by 92.6% (Figure 15). Clay soils, even with a very low rate of FA, can considerably reduce their swelling potential.

3.6. Scanning Electron Microscopy Study. After CBR tests, scanning electron microscopy (SEM) images of the samples were taken. In the SEM images, the clay surface was perfectly coated with fly ash among the grains. That explains why the swelling of the clay was prevented. Ash pellets move between the clay minerals with the water molecules and prevent swelling of the clay (Figure 16). Furthermore, FA grains are capable of making bonds among the clay minerals (Figure 17).

4. Statistical Evaluation

Multiple regression analyses were realized to obtain the relationships between shear strength parameters (c and ϕ) and fly ash content (FA, %) and curing time (d , days) as well as CBR values and fly ash content. XLSTAT of Addinsoft

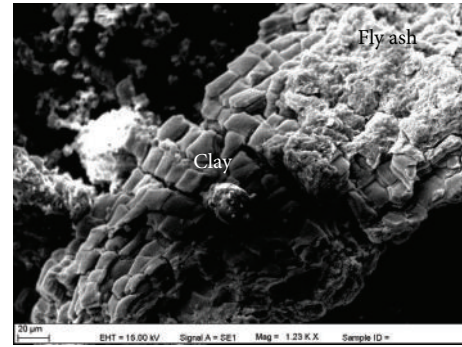


FIGURE 16: The SEM view of coated clay with ash pellets.

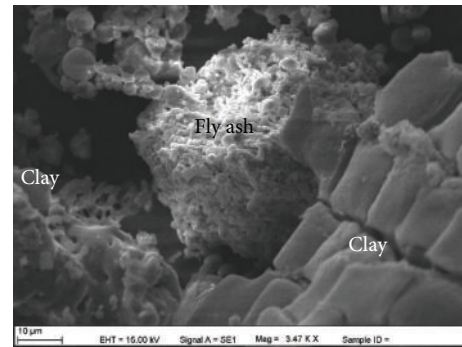


FIGURE 17: The view of ash particles that build the bridge between clay minerals.

was used to create the regression models. The best fit for estimating cohesion (c , kPa) was found as

$$c \text{ (kPa)} = -19.445 + 1.068 * d + 708.642 * \text{FA}, \quad (2)$$

$$\phi^0 = 10.217 + 0.232 * d + 69.095 * \text{FA},$$

where d is curing time (days) and FA is fly ash (%).

As well, the best model for CBR values was presented in

$$\text{CBR} \text{ (%) } = -37.173 + 2.32 * d + 5.039 * \text{FA}, \quad (3)$$

where d is curing time (days) and FA is fly ash (%).

The F -test was carried out to test the overall performance of the regression model (Table 5). Since $F_{\text{model}}(79.776, 50.485) > F_{(0.05, 2, 15)}(3.68)$ for shear strength parameters as well as $F_{\text{model}}(52.921) > F_{(0.05, 2, 51)}(2.79)$ for CBR or the P value is considerably smaller than $\alpha = 0.05$, the null hypotheses are rejected and as a result of that c , ϕ , and CBR related to d and FA.

The proportion between the regression sum of the square (SS_R) and the corrected total sum of squares is called the coefficient of determination (R) and is often used to judge the adequacy of a regression model [40]. R^2 , R_{adj}^2 , the root mean square errors, the mean absolute percentage error, and Akaike's information criterion were used in the evaluation of prediction capacity of MLR models, and these are presented in Table 5.

A model with low RMSE (root mean square error), MAPE (mean absolute percentage error), AIC (Akaike's information

TABLE 5: ANOVA of d and FA for dependent variable (c - ϕ and CBR).

Parameter	Source	DF	Sum of squares	Mean squares	F	Pr > F
c	Model	2	68661.366	34330.683	79.776	<0.0001
	Error	15	6455.049	430.337		
ϕ	Model	2	756.542	378.271	50.485	<0.0001
	Error	15	112.391	7.493		
CBR	Model	2	138925.972	69462.986	52.921	<0.0001
	Error	51	66941.822	1312.585		

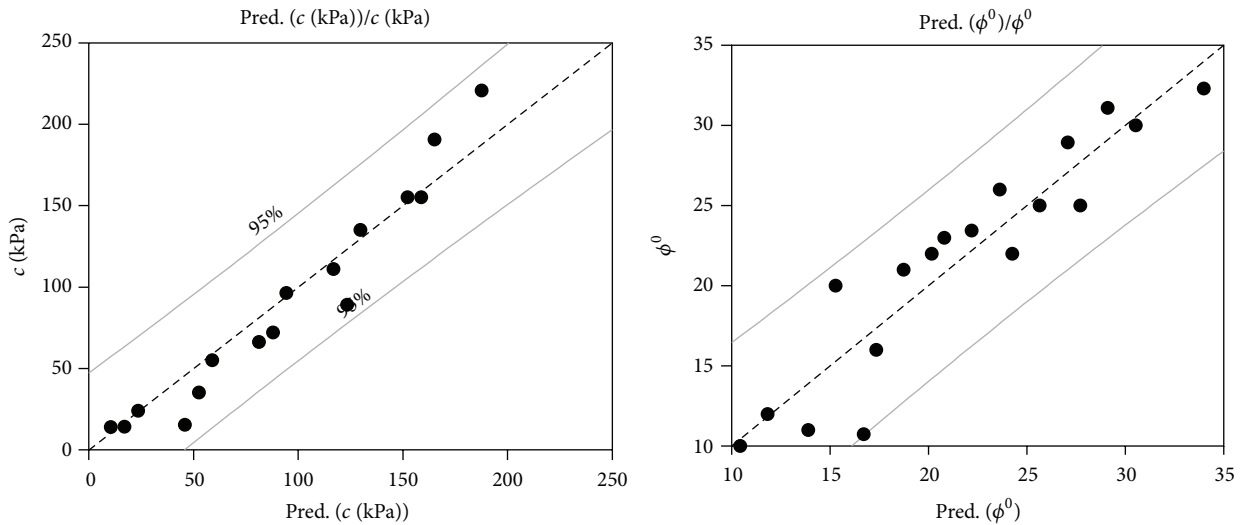


FIGURE 18: Measured and predicted shear strength (c, ϕ) values derived from (2).

criterion), and high R^2 and adjusted R^2 performance indices was defined, and its prediction capacity was accepted as excellent by several researchers [41–44]. By prediction indices, MLR models have shown good performance for independent variables (Table 6).

Furthermore, measured and predicted shear strength parameters and CBR values obtained from MLR evaluation at the 95% confidence intervals are presented in Figures 18 and 19. Predicted values are in good agreement with the measured values in the laboratory.

5. Conclusions

By the work reported in this paper, the following conclusions have been drawn:

- (1) The liquid and plastic limits of AC were decreased with fly ash addition. Furthermore, the soil class of AC is changed from “CH” to “MH.” AC starts showing plastic behaviour when increasing the percentages of FA additives.
- (2) The cohesion and internal friction of AC were increased with FA. Furthermore, curing time is very useful on the shear parameters. Soil samples with 28 days’ curing time have shown the highest cohesion and friction angle.

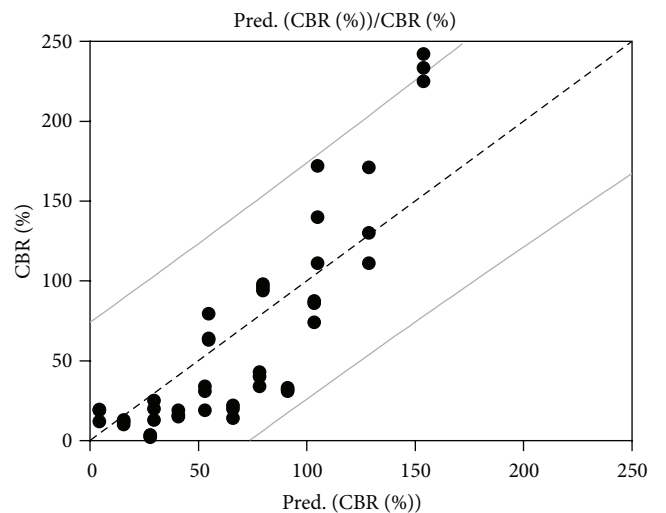


FIGURE 19: Measured and predicted CBR values derived from (3).

- (3) SEM views show that FA particles cover the surfaces of clay minerals and constitute an impervious layer. This phenomenon explains why the soil does not swell when FA has been added to it. Furthermore, FA grains build bridges between clay minerals. Therefore, the shear strength (c, ϕ) starts to increase with the FA

TABLE 6: Goodness-of-fit for MLR.

Dependent variables	Independent variables	R^2	Adj. R^2	RMSE	MAPE	AIC
c	d , FA	0.914	0.903	20.745	47.818	111.880
ϕ	d , FA	0.871	0.853	2.737	11.480	38.969
CBR	d , FA	0.675	0.662	36.23	185.376	390.620

d : curing days; FA: fly ash.

additive increments. Furthermore, there is a robust relationship between shear strength parameters and curing time with fly ash content. Furthermore, the same inference was determined for CBR values.

Competing Interests

The author declares that there are no competing interests.

References

- [1] A. Baba, A. Kaya, and Y. K. Birsoy, "The effect of Yatagan thermal power plant (Mugla, Turkey) on the quality of surface and ground waters," *Water, Air, and Soil Pollution*, vol. 149, no. 1–4, pp. 93–111, 2003.
- [2] H. Haykiri-Acma, S. Yaman, N. Ozbek, and S. Kucukbayrak, "Mobilization of some trace elements from ashes of Turkish lignites in rain water," *Fuel*, vol. 90, no. 11, pp. 3447–3455, 2011.
- [3] G. Akar, M. Polat, G. Galecki, and U. Ipekoglu, "Leaching behavior of selected trace elements in coal fly ash samples from Yenikoy coal-fired power plants," *Fuel Processing Technology*, vol. 104, pp. 50–56, 2012.
- [4] A. I. Karayigit, R. A. Gayerb, X. Querol, and T. Onacak, "Contents of major and trace elements in feed coals from Turkish coal-fired power plants," *International Journal of Coal Geology*, vol. 44, no. 2, pp. 169–184, 2000.
- [5] S. Esenlik, A. I. Karayigit, Y. Bulut, X. Querol, A. Alastuey, and O. Font, "Element behaviour during combustion in coal-fired Orhaneli power plant, Bursa-Turkey," *Geologica Acta*, vol. 4, no. 4, pp. 439–449, 2006.
- [6] S. M. Mackiewicz and E. Glen Ferguson, "Stabilization of soil with self-cementing coal ashes," in *Proceedings of the World of Coal Ash (WOCA '05)*, Lexington, Ky, USA, April 2005.
- [7] G. Ferguson, *Use of Self-Cementing Fly Ash as a Soil Stabilizing Agent Fly Ash for Soil Improvement*, GSP no. 36, ASCE Geotechnical Special Publication, 1993.
- [8] A. Misra, "Stabilization characteristics of clays using Class C fly ash," *Transportation Research Record*, no. 1611, pp. 46–54, 1998.
- [9] J. Prabakar, N. Dendorkar, and R. K. Morchhale, "Influence of fly ash on strength behavior of typical soils," *Construction and Building Materials*, vol. 18, no. 4, pp. 263–267, 2004.
- [10] A. J. Puppala and C. Musenda, "Effects of fiber reinforcement on strength and volume change in expansive soils," *Transportation Research Record*, vol. 1736, pp. 134–140, 2000.
- [11] A. Senol, T. B. Edil, M. S. Bin-Shafique, H. A. Acosta, and C. H. Benson, "Soft subgrades' stabilization by using various fly ashes," *Resources, Conservation and Recycling*, vol. 46, no. 4, pp. 365–376, 2006.
- [12] S. Bin-Shafique, K. Rahman, M. Yaykiran, and I. Azfar, "The long-term performance of two fly ash stabilized fine-grained soil subbases," *Resources, Conservation and Recycling*, vol. 54, no. 10, pp. 666–672, 2010.
- [13] P. G. Nicholson and V. Kashyap, "Fly ash stabilization of tropical Hawaiian soils in fly ash for soil improvement," *ASCE Geotechnical Special Publication*, vol. 36, pp. 1134–1147, 1993.
- [14] S. Koliass, V. Kasselouri-Rigopoulou, and A. Karahalios, "Stabilisation of clayey soils with high calcium fly ash and cement," *Cement and Concrete Composites*, vol. 27, no. 2, pp. 301–313, 2005.
- [15] Y. Du, S. Li, and S. Hayashi, "Swelling-shrinkage properties and soil improvement of compacted expansive soil, Ning-Liang Highway, China," *Engineering Geology*, vol. 53, no. 3–4, pp. 351–358, 1999.
- [16] A. A. Langroudi and S. S. Yasrobi, "A micro-mechanical approach to swelling behavior of unsaturated expansive clays under controlled drainage conditions," *Applied Clay Science*, vol. 45, no. 1–2, pp. 8–19, 2009.
- [17] D.-F. Lin, K.-L. Lin, M.-J. Hung, and H.-L. Luo, "Sludge ash/hydrated lime on the geotechnical properties of soft soil," *Journal of Hazardous Materials*, vol. 145, no. 1–2, pp. 58–64, 2007.
- [18] Z. Nalbantoglu, "Effectiveness of class C fly ash as an expansive soil stabilizer," *Construction and Building Materials*, vol. 18, no. 6, pp. 377–381, 2004.
- [19] Z. Nalbantoglu and E. Gucbilmez, "Improvement of calcareous expansive soils in semi-arid environments," *Journal of Arid Environments*, vol. 47, no. 4, pp. 453–463, 2001.
- [20] S. M. Rao, B. V. V. Reddy, and M. Muttharam, "The impact of cyclic wetting and drying on the swelling behaviour of stabilized expansive soils," *Engineering Geology*, vol. 60, no. 1–4, pp. 223–233, 2001.
- [21] R. N. Yong and V. R. Ouhadi, "Experimental study on instability of bases on natural and lime/cement-stabilized clayey soils," *Applied Clay Science*, vol. 35, no. 3–4, pp. 238–249, 2007.
- [22] A. Seco, F. Ramirez, L. Miqueleiz, and B. Garcia, "Stabilization of expansive soils for use in construction," *Applied Clay Science*, vol. 51, no. 3, pp. 348–352, 2011.
- [23] L. Chen and D.-F. Lin, "Stabilization treatment of soft subgrade soil by sewage sludge ash and cement," *Journal of Hazardous Materials*, vol. 162, no. 1, pp. 321–327, 2009.
- [24] Y. Guney, D. Sari, M. Cetin, and M. Tuncan, "Impact of cyclic wetting-drying on swelling behavior of lime-stabilized soil," *Building and Environment*, vol. 42, no. 2, pp. 681–688, 2007.
- [25] P. Sukmak, S. Horpibulsuk, S.-L. Shen, P. Chindaprasirt, and C. Suksiripattananpong, "Factors influencing strength development in clay-fly ash geopolymer," *Construction and Building Materials*, vol. 47, pp. 1125–1136, 2013.
- [26] TCLP 1311, *Toxicity Characteristic Leaching Procedure*, US Environmental Protection Agency, Washington, DC, USA, 1992.
- [27] American Society for Testing and Materials (ASTM), "Standard test method for shake extraction of solid waste with water," ASTM D3987, American Society for Testing and Materials (ASTM), West Conshohocken, Pa, USA, 1985.
- [28] S. Turhan, A. Parmaksiz, A. Köse, A. Yüksel, I. H. Arıkan, and B. Yücel, "Radiological characteristics of pulverized fly ashes

- produced in Turkish coal-burning thermal power plants,” *Fuel*, vol. 89, no. 12, pp. 3892–3900, 2010.
- [29] E. Avsar, R. Ulusay, and Z. A. Erguler, “Swelling properties of Ankara (Turkey) clay with carbonate concretions,” *Environmental & Engineering Geoscience*, vol. 11, no. 1, pp. 73–95, 2005.
- [30] I. Ordemir, C. Soydemir, and A. A. Birand, “Swelling problems of Ankara Clays,” in *Proceedings of the 9th International Conference on Soil Mechanics and Foundation Engineering*, pp. 243–247, Tokyo, Japan, July 1977.
- [31] TS EN, “Fly ash for concrete—definitions, requirements and quality control,” TS EN 450, National Standard, Turkish Standard Institution, Ankara, Turkey, 1998 (Turkish).
- [32] TS, “Cement—part1: composition, specification and conformity criteria for common cements,” National Standard TS EN 197-1, Turkish Standard Institution, Ankara, Turkey, 2012 (Turkish).
- [33] TS 639, *Fly Ashes-Used In Cement Production. National Standard*, Turkish Standard Institution, Ankara, Turkey, 1998 (Turkish).
- [34] ASTM C618, *Standard Specification for Coal Fly Ash and Raw or Calcined Natural Pozzolan for Use in Concrete*, American Society for Testing and Materials, West Conshohocken, Pa, USA, 2003.
- [35] American Society for Testing and Materials (ASTM), “Standard test methods for laboratory compaction characteristics of soil using modified effort (56,000 ft-lbf/ft³ (2,700 kN-m/m³)),” ASTM D1557, American Society for Testing and Materials (ASTM), West Conshohocken, Pa, USA, 2009.
- [36] ASTM D4318, *Standard Test Methods for Liquid Limit, Plastic Limit, and Plasticity Index of Soils*, American Society for Testing and Materials, West Conshohocken, Pa, USA, 2010.
- [37] ASTM D1883, *Standard of Test Method for California Bearing Ratio of Laboratory-Compacted Soils*, American Society for Testing and Materials, West Conshohocken, Pa, USA, 2014.
- [38] American Society for Testing and Materials (ASTM), “Standard test method for direct shear test of soils under consolidated drained conditions,” ASTM D3080, American Society for Testing and Materials (ASTM), West Conshohocken, Pa, USA, 2004.
- [39] IS 2720 (Part XL), *Methods of Test for Soils, Measurement of Swelling Pressure of Soils*, Indian Standard, Delhi, India, 2002.
- [40] D. Montgomery and G. Runger, *Applied Statistics and Probability for Engineers*, John Wiley & Sons, New York, NY, USA, 1999.
- [41] M. Alvarez Grima and R. Babuška, “Fuzzy model for the prediction of unconfined compressive strength of rock samples,” *International Journal of Rock Mechanics and Mining Sciences*, vol. 36, no. 3, pp. 339–349, 1999.
- [42] J. Finol, Y. K. Guo, and X. D. Jing, “A rule based fuzzy model for the prediction of petrophysical rock parameters,” *Journal of Petroleum Science and Engineering*, vol. 29, no. 2, pp. 97–113, 2001.
- [43] C. Gokceoglu, “A fuzzy triangular chart to predict the uniaxial compressive strength of the Ankara agglomerates from their petrographic composition,” *Engineering Geology*, vol. 66, no. 1-2, pp. 39–51, 2002.
- [44] A. Binal, “Prediction of mechanical properties of non-welded and moderately welded ignimbrite using physical properties, ultrasonic pulse velocity, and point load index tests,” *Quarterly Journal of Engineering Geology and Hydrogeology*, vol. 42, no. 1, pp. 107–122, 2009.

Research Article

Influence of Alkali Treatment on the Surface Area of Aluminium Dross

**N. S. Ahmad Zauzi,¹ M. Z. H. Zakaria,¹ R. Baini,¹ M. R. Rahman,¹
N. Mohamed Sutan,² and S. Hamdan³**

¹Department of Chemical Engineering and Sustainability Energy, Faculty of Engineering, Universiti Malaysia Sarawak, 94300 Kota Samarahan, Sarawak, Malaysia

²Department of Civil Engineering, Faculty of Engineering, Universiti Malaysia Sarawak, 94300 Kota Samarahan, Sarawak, Malaysia

³Department of Mechanical Engineering and Manufacturing, Faculty of Engineering, Universiti Malaysia Sarawak, 94300 Kota Samarahan, Sarawak, Malaysia

Correspondence should be addressed to N. S. Ahmad Zauzi; aznsyuhada@unimas.my

Received 18 March 2016; Accepted 25 May 2016

Academic Editor: Guocheng Lv

Copyright © 2016 N. S. Ahmad Zauzi et al. This is an open access article distributed under the Creative Commons Attribution License, which permits unrestricted use, distribution, and reproduction in any medium, provided the original work is properly cited.

Aluminium dross is an industrial waste from aluminium refining industry and classified as toxic substances. However, the disposal of dross as a waste is a burden to aluminium manufacturer industries due to its negative effects to the ecosystem, surface, and ground water. Therefore the purpose of this study is to evaluate the influence of sodium hydroxide (NaOH) on the surface area and pore size of aluminium dross. There were 3 stages in the treatment activities, which were leaching, precipitation, and calcination process. The optimum result from this study was the surface area of aluminium dross increases from 10.1 m²/g up to 80.0 m²/g at 40°C, 1% NaOH, and 15-minute reaction time. Thus, aluminium dross has a potential to be converted into other useful material such as catalyst and absorbent. The benefit of this research is that the hazardous industrial waste can be turned into wealth to be used in other applications such as in catalytic activities and absorber in waste water treatment. Further investigation on the physicochemical of aluminium dross with different acid or alkali should be conducted to get deeper understanding on the aluminium dross as a catalyst-type material.

1. Introduction

Aluminium dross is one type of the industrial wastes which are generated in a recycle of an aluminium recycle process. There are three types of aluminium dross which are black dross, white dross, and salt cake. White dross is generated in aluminium smelting industries while black dross and salt cake are generated in the aluminium recycling industries. Amount and the formation of these substances depend on several factors such as the type and quality of input materials, operating conditions, the type of technology, and furnace applied. The overall chemistry depends on the alloying elements present in the molten aluminium and the metallurgical process [1]. Generally, this dross may contain Al₂O₃, AlN, Al₄C₃, SiO₂, MgO, Al, and minor quantities of

Si [2]. According to Sultana et al. [3], it was estimated that 15–25 kg of dross is produced per metric tonne of molten aluminium and [4] stated that, throughout the world, it was estimated that 5 million tonnes of an aluminium dross was generated every year.

Aluminium dross is classified as a toxic industrial waste and it requires a proper treatment before it can be discharged. Majority of aluminium dross is disposed in open landfill sites, and this activity can cause harm to the environment due to the toxic ions; there is possibility of toxin ions leached out from the disposed aluminium dross into the ground water, which can cause pollution [4–6]. This substance is usually treated as a landfilled solid waste [6]. The disposal cost of this waste can be expensive; RM 2000.00 per tonne will be charged by the approved local disposal waste company for the disposal in

TABLE 1: Chemical composition of raw aluminium dross.

Composition	SiO ₂	Al ₂ O ₃	Fe ₂ O ₃	MgO	SO ₃	CaO	TiO ₂	Na ₂ O
wt%	1.2	89.8	0.54	0.84	0.15	0.41	0.022	0.31

Malaysia [7]. A large amount of aluminium dross has never been treated properly prior to discharge due to the high cost of treatment and transportation.

Although aluminium dross is a type of waste, several useful usages have been discovered, such as filler in composite, being used in refractories industry, and also being used as adsorbent. Aluminium dross can be leached with copper chloride water solution to obtain aluminium oxychloride, Al(OH)Cl₂, and then can be further treated with aluminium hydroxide to obtain aluminium chloride, Al₂(OH)₅Cl, which can be used as a coagulant in water treatment process [8]. Other than that, aluminium dross can be used as a deoxidizer to remove oxygen in the steel-manufacturing process and used as aggregate in cement processing [4].

More studies on treatment process for aluminium dross are necessary to increase the possibility of recycling this dangerous waste into useful products. Therefore, the aim of this work is to study the possibility of producing commercial catalyst from aluminium dross. In this work, aluminium dross has been treated using different concentration of sodium hydroxide for different temperatures and reaction time.

2. Experimental

Aluminium dross in this study was obtained from aluminium smelting industry, Press Metal Company, which is located in Samalaju Industrial Park, Bintulu, Sarawak. Three processing stages were applied to aluminium dross: leaching with sodium hydroxide, precipitation with hydrogen peroxide, and calcination. The first process was carried out by adding 10 g of aluminium dross with size < 300 μm to a 250 mL of sodium hydroxide (NaOH) with concentrations of 1%, 5%, 10%, and 20%, stirring time of 15 minutes, 30 minutes, 45 minutes, and 60 minutes, and temperatures of 25°C, 40°C, 55°C, and 70°C. The next process was the precipitation with hydrogen peroxide by adding 250 mL of 30% hydrogen peroxide (H₂O₂) to samples. The mixtures were stirred for 30 minutes at room temperature, filtered, and washed with distilled water. In the final stage, the samples were calcined at temperature of 600°C for 3 hours

The chemical composition of raw and treated aluminium dross was analysed using X-Ray Fluorescence Spectroscopy (XRF) equipment (Bruker S4 EXPLORER X-Ray Fluorescence). The surface area and pore size of aluminium dross were determined using BET surface analysis (Quantachrome Instruments Co. Ltd.).

3. Results and Discussion

The chemical composition of aluminium dross (wt%) obtained from XRF is given in Table 1. It was found that almost 90% of the raw material consists of Al₂O₃ and the

TABLE 2: Effect of time on the surface area of aluminium dross at temperature of 25°C and concentration of NaOH at 1%.

Time (mins)	15	30	45	60
Surface area (m ² /g)	79	49	28	28

TABLE 3: Effect of temperature on the surface area of aluminium dross at reaction time of 15 minutes and concentration of NaOH at 1%.

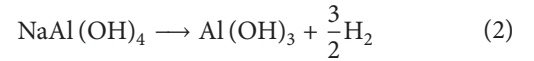
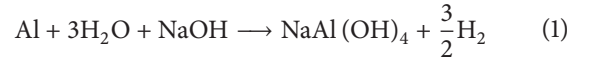
Temperature (°C)	25	40	55	70
Surface area (m ² /g)	79	80	51	47

TABLE 4: Effect of NaOH concentration on the surface area of aluminium dross at reaction time of 15 minutes and temperature at 25°C.

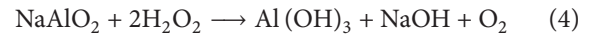
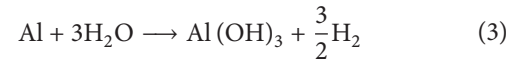
NaOH (%)	1	5	10	20
Surface area (m ² /g)	79	38	74	21

remaining 10% consists of SiO₂, Fe₂O₃, MgO, SO₃, CaO, TiO₂, and Na₂O.

In the first stage of treatment, hydrogen gas was formed during the leaching process with sodium hydroxide. The details of reactions in the first and second stages are given by (1)–(3) and (4), respectively:



The overall reaction can be summarized as follows:



3.1. BET Surface Area. The surface area of the raw aluminium dross analysed using BET surface analysis was found to be 10.061 m²/g, while the surface area for treated samples is given in Tables 2–4. Table 2 represents the effect of time on the surface area of aluminium dross with temperature of 25°C and concentration of NaOH at 1%. Table 3 represents the effect of temperature on the surface area of aluminium dross with time at 15 minutes and temperature at 25°C concentration of NaOH at 1%. Table 4 represents the effect of NaOH concentration on the surface area of aluminium dross with time of 15 minutes at 25°C. Based on Tables 2–4, it was found that all the treated samples have larger surface area up to 700%, compared to untreated one. This occurrence can be explained due to the process of dealumination and it will cause the disintegration surface of aluminium dross [9]. Besides, the increases of BET surface area with the presence of alkali are due to the production of finely dispersed silicon oxides from destruction of mineral structures and removal

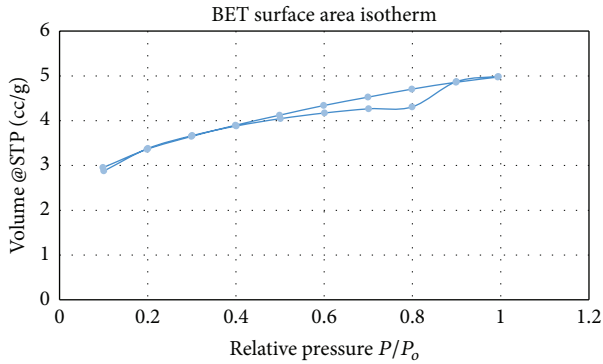


FIGURE 1: Isotherms of raw aluminium dross.

of amorphous of Al or silica components and thus increase the surface pores [10]. A large value of BET surface area will reflect the catalytic activity of the material.

On the effect of time, it shows that the surface area of aluminium dross increases when aluminium dross stirred for 15 minutes but as the time increases until 60 minutes, it may be seen that the surface area of aluminium dross decreases. The catalytic activity may reach a maximum at 15 minutes of reaction time whereas the effectiveness of catalysts could be reducing as the time increases [11].

This experiment was carried out with different temperatures which are 25°C, 40°C, 55°C, and 70°C, respectively. In Table 3, at 25°C, it shows the surface area of aluminium dross increases from 10 m²/g to 79 m²/g. But as the temperature increases up to 70°C, the pattern of the surface area decreases. At higher temperature, aluminium dross was found to be agglomerated; thus the surface of aluminium dross may be ruptured due to high temperature [11, 12].

Table 4 shows the effect of concentration of sodium hydroxide on the surface area of aluminium dross. In this experiment, the concentrations of sodium hydroxide used are 1%, 5%, 10%, and 20%, respectively. With the concentration of 1% of sodium hydroxide, the surface area of aluminium dross increases from 10 m²/g to 79 m²/g. From the table, the surface area of aluminium dross decreases as the concentration of sodium hydroxide increases. Other than that, the maximum concentration for leaching process is at 1% whereas the surface area of aluminium dross decreases when the concentration increases due to saturation of aluminium dross at higher NaOH concentration [11].

Figures 1, 2, 3, and 4 are the nitrogen adsorption and desorption isotherms for raw aluminium dross and treated with 1% concentration of sodium hydroxide, stirring time of 30 minutes, and leaching temperatures of 25°C, 40°C, and 55°C, respectively. Figures show that the amount of N₂ absorbed increases with the relative pressure. The slope of the curve decreases as the relative pressure decreases, which may indicate that the amount of N₂ absorbed is reaching the equilibrium state. According to International Union of Pure and Applied Chemistry (IUPAC), those isotherms can be classified as type I which indicates adsorption and desorption on a microporous solid with pore size below 2 nm. This type of isotherms showed high uptakes of nitrogen gas at

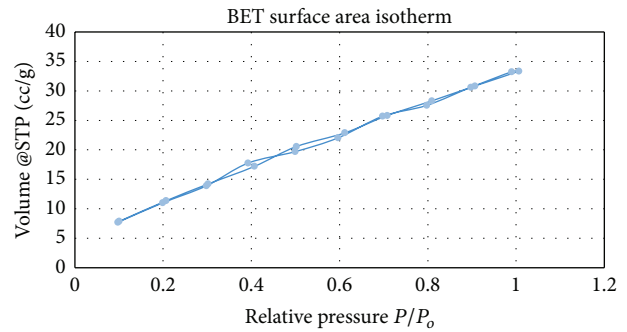


FIGURE 2: Isotherms of aluminium dross treated with 1% of NaOH at 30 minutes and temperature of 25°C.

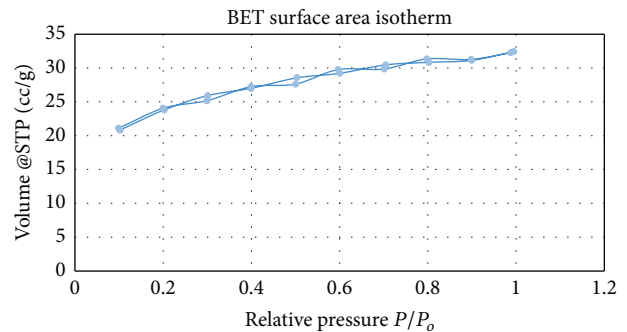


FIGURE 3: Isotherms of aluminium dross treated with 1% of NaOH at 30 minutes and temperature of 40°C.

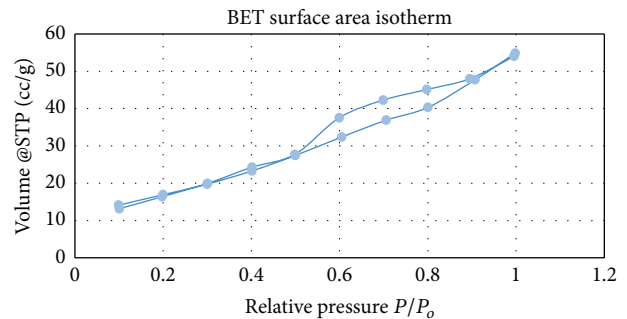


FIGURE 4: Isotherms of aluminium dross treated with 1% of NaOH at 30 minutes and temperature of 55°C.

relatively low pressure due to the narrow pore width and high adsorption potential.

4. Conclusion

The characteristics of aluminium dross after being treated with different concentrations of NaOH, at different reaction time and temperatures, were studied. It shows that, at 15 minutes, the surface area of aluminium dross increases but as the time increases, the surface area decreases. It also shows that at 1% concentration of NaOH, the surface area of aluminium dross increases but it seems to decrease as the concentration of NaOH increases. Surface area of aluminium

dross also reaches a maximum catalytic activity when the temperature is at 25°C but when the temperature increases, it shows decreasing of the surface area of aluminium dross due to the rupture of pores. N₂ adsorption-desorption shows that aluminium dross was type I which is microporous solids. Therefore based on the BET surface analysis, aluminium dross has a potential to be a catalyst-type material and reduce the waste of aluminium dross. For further study, it is recommended to focus on other physicochemical properties of treated aluminium dross.

Competing Interests

The authors declare that the grant, scholarship, and/or funding mentioned in Acknowledgments do not lead to any conflict of interests. Additionally, the authors declare that there is no conflict of interests regarding the publication of this paper.

Acknowledgments

The authors are thankful to the Ministry of Higher Education for funding under FRGS/1/2015/SG06/UNIMAS/03/1 and Universiti Malaysia Sarawak.

References

- [1] H. N. Yoshimura, A. P. Abreu, A. L. Molisani, A. C. De Camargo, J. C. S. Portela, and N. E. Narita, "Evaluation of aluminum dross waste as raw material for refractories," *Ceramics International*, vol. 34, no. 3, pp. 581–591, 2008.
- [2] J. C. E. Bocardo and J. T. Torres, "Development of mulite/zirconia composites from a mixture of aluminum dross and zircon," *Ceramics International*, vol. 35, no. 2, pp. 921–924, 2009.
- [3] U. K. Sultana, F. Gulshan, M. A. Gafur, and A. S. W. Kurny, "Kinetics of recovery of alumina from aluminium casting waste through fusion with sodium hydroxide," *American Journal of Materials Engineering and Technology*, vol. 1, no. 3, pp. 30–34, 2013.
- [4] N. Murayama, I. Maekawa, H. Ushiro, T. Miyoshi, J. Shibata, and M. Valix, "Synthesis of various layered double hydroxides using aluminum dross generated in aluminum recycling process," *International Journal of Mineral Processing*, vol. 110–111, pp. 46–52, 2012.
- [5] B. R. Das, B. Dash, B. C. Tripathy, I. N. Bhattacharya, and S. C. Das, "Production of η -alumina from waste aluminium dross," *Minerals Engineering*, vol. 20, no. 3, pp. 252–258, 2007.
- [6] S.-J. Yoo, D.-H. Kwak, S.-I. Lee et al., "Kinetics of aluminum dross dissolution in sec-butyl alcohol for aluminum sec-butoxide," *Advanced Powder Technology*, vol. 22, no. 5, pp. 617–622, 2011.
- [7] M. S. Meor Yusoff and W. P. Masliana Muslim, "A waste to wealth study on converting aluminium dross schedule waste into γ and α alumina," in *Recent Advances in Environment, Ecosystems and Development*, pp. 17–21, 2009.
- [8] B. Lucheva, T. Tsonev, and R. Petkov, "Non-waste aluminum dross recycling," *Journal of the University of Chemical Technology and Metallurgy*, vol. 40, no. 4, pp. 335–338, 2005.
- [9] S. Kumar, A. K. Panda, and R. K. Singh, "Preparation and characterization of acids and alkali treated kaolin clay," *Bulletin of Chemical Reaction Engineering & Catalysis*, vol. 8, no. 1, pp. 61–69, 2013.
- [10] V. Lakevičs, V. Stepanova, I. Skuja, I. Dušenkova, and A. Ruplis, "Influence of alkali and acidic treatment on sorption properties of latvian illite clays," *Key Engineering Materials*, vol. 604, pp. 71–74, 2014.
- [11] V. R. Choudhary and M. G. Sane, "Effect of preparation conditions of Raney Nickel on its catalytic properties for slurry phase hydrogenation of o-nitrophenol to o-aminophenol," *Indian Journal of Chemical Technology*, vol. 5, no. 4, pp. 199–208, 1998.
- [12] Q. Liu, R. Xin, C. Li, C. Xu, and J. Yang, "Application of red mud as a basic catalyst for biodiesel production," *Journal of Environmental Sciences*, vol. 25, no. 4, pp. 823–829, 2013.

Research Article

Graphite Intended for Green Engineering Developed by Noncontaminant Reverse Abrasion

Roberto Baca Arroyo

Department of Electronics, National Polytechnic Institute, 07738 Mexico City, DF, Mexico

Correspondence should be addressed to Roberto Baca Arroyo; rbaca02006@yahoo.com.mx

Received 13 January 2016; Revised 2 April 2016; Accepted 14 April 2016

Academic Editor: Jianxi Zhu

Copyright © 2016 Roberto Baca Arroyo. This is an open access article distributed under the Creative Commons Attribution License, which permits unrestricted use, distribution, and reproduction in any medium, provided the original work is properly cited.

Graphite intended for green engineering was synthesized by noncontaminant reverse abrasion, which consists of graphite layers assembled with thickness controlled on SiC sandpaper as insulating substrate. Phase formation of the graphite layers was validated by X-ray diffraction studies and its finished profile by Atomic Force Microscopy (AFM). Transport parameters of only three layers were evaluated from current-voltage curves. Mathematical functions such as derivative and modulation of a signal have been built by graphite circuits using different performance principles, compared to those used with silicon devices. The trends related to electronic engineering should be achieved with design of the graphite-based devices to facilitate their mass production in the near future.

1. Introduction

In the last decades, advances in electronic engineering based on circuits of large scale integration (LSI) have found extensive application in communications, automation, and other areas [1]. However, such applications have been implemented by silicon-based architectures and their end life corresponding to the waste electronics which deteriorate the environment at high levels of pollution. By using different performance principles as well as employing earth materials [2], carbon-based architectures intended from elementary mathematical functions could satisfy environmental requirements to the fabrication of novel applications such as control devices and sensors [3–5].

Researchers have synthesized carbon-based devices using chemical vapor deposition (CVD) techniques where volatile compounds of carbon onto nickel or copper surfaces serve to catalyze the conversion of those into graphene by epitaxial growth and annealing of silicon carbide (SiC) at high temperatures [6, 7]. Due to that high cost of production, setback in its scalability, degradation of electronic properties, requirement of specialized equipment, poor mass production, and environmental concerns related to the toxic vapors, the market for carbon-based devices has been blocked. It is known that

excessive levels of carbon gases can exacerbate biological effects with accumulative damage in the health [8, 9].

Graphite is an allotrope of carbon which is the most stable under standard conditions and has been widely recycled from synthetic graphite electrodes of zinc-carbon batteries and electric motor brushes and others [10]. It is difficult for the ignition of the graphite to occur as a result of its higher thermal conductivity of $k = 2000 \text{ Wm/K}$ and electron delocalization within its carbon layers as well as thermal properties highly anisotropic [11], since phonons propagate very quickly along its bound planes but slower for traveling from one plane to another [12]. Ambipolarity phenomena could be a disadvantage to design semiconductor devices by its pure state with a zero-band gap which imply that for both positive and negative bias voltage any current flow does not change, but motion of the charge carries and heat conduction depend on its thickness and dimensions, which can be an advantage for graphite-based devices [7, 13].

Alternatively, an abrasive material as SiC has several advantages to be functional under extreme conditions without breakdown damage. It is well known that SiC substrate is very expensive, but it has higher thermal conductivity of $k = 100\text{--}350 \text{ Wm/K}$ at room temperature. Therefore, SiC sandpaper can be used as an insulating substrate, being easily

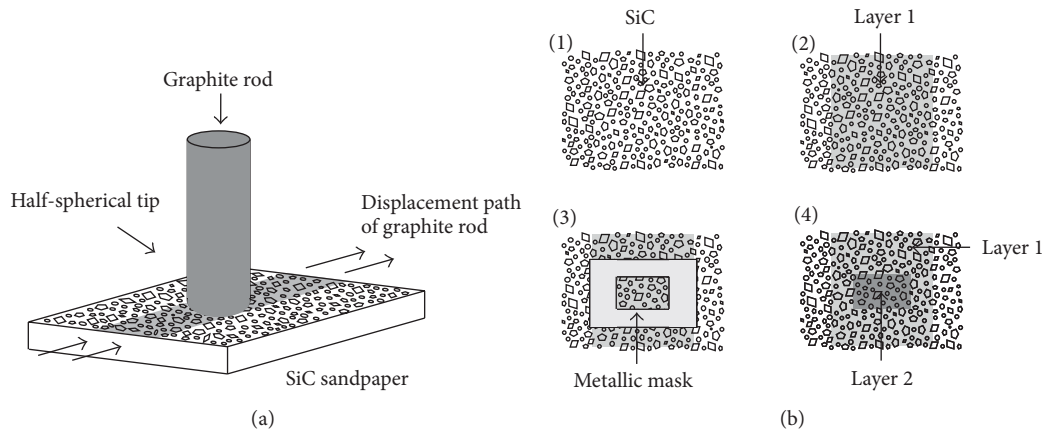


FIGURE 1: (a) Schematic of the reverse abrasion technique. (b) Four steps employed for assembling of the graphite layers.

found on the market at low cost. When it is used as substrate, it must be selected by its grain size and area to get finer finished profiles [13, 14].

This work introduces the fabrication of graphite layers made by noncontaminant reverse abrasion technique. Details of this process are presented in Section 2. Structural and transport parameters of the graphite layers as well as examples of green engineering are covered in Section 3. Finally, conclusions about this research are available in Section 4.

2. Material and Methods

Graphite rods with radii of 1 mm were recuperated from old pencils into their final stage, which can be used to be assembled on SiC sandpaper by friction forces between finer abrasive particles of SiC and graphite atoms to control the amount of graphite assembled on SiC substrate. To know the stability of the assembling, it is explained based on insertion of graphite atoms between layers and their stacking profile in SiC sandpaper which is related to the nucleation phenomena by stronger attractive forces between graphite and SiC atoms at the interface [9].

Figure 1(a) shows the schematic of the process where a graphite rod with a half-spherical tip must be continuously displaced on a SiC surface. Figure 1(b) indicates the four steps for synthesizing of the graphite layers. At the beginning the needed area of SiC sandpaper must be cut off with scissors (step 1). After that, a first graphite layer of smaller thickness can be assembled on SiC sandpaper (step 2). A metallic mask of $1.5 \times 1.5 \text{ mm}^2$, for example, should be placed after (step 3) as pattern of the junction area. Finally, a second layer of greater thickness can be assembled (step 4).

Phase formation of the graphite layers is validated by X-ray diffraction studies (XRD patterns) with a PANalytical diffractometer of CuK_α radiation ($\lambda = 0.15418 \text{ nm}$). Finished profiles of the graphite surface as a function of asperities density and height distribution are studied by Atomic Force Microscopy (AFM) using a Digital Instrument (Veeco) Nanoscope. Transport of the graphite layers is evaluated from current-voltage curves. Graphite circuits are fabricated to demonstrate green engineering and its behavior is confirmed

by waveforms collected with a digital storage oscilloscope (Tektronix, TDS1012C).

3. Results and Discussion

Pencils are still a small but significant source of natural graphite with planar structure of hexagonal form which can be useful by its mechanical properties based on easier slide of either smooth or distorted layers one to the other on SiC sandpaper. For that reason, to satisfy the trends related to electronic engineering of large scale integration (LSI), graphite and SiC are excellent candidates and only three types of graphite layers are synthesized by using the procedure of Figure 1.

3.1. Structural and Transport Parameters of Graphite Layers. Figure 2 shows XRD patterns of the layers synthesized. Samples labeled as GF1, GF2, and GF3 exhibit hexagonal phase of graphite with peak located at 26.60° and plane (002) according to PANalytical Card number 00-025-0284 and other authors [15, 16]. XRD pattern of the SiC substrate is labeled by the SiC sandpaper as reference. Additional peaks are corresponding with SiC, the highest peak being at 35.60° with (111) plane associated with cubic phase, according to PANalytical Card number 00-029-1127, while those peaks positioned at 34.70° , 38.02° , 60.05° , 65.60° , and 71.80° with (101), (102), (110), (106), and (114) planes correspond to hexagonal phase according to PANalytical Card number 00-029-1129. XRD patterns indicate that the peaks heights corresponding to SiC substrate decrease, when hexagonal phase of graphite increases as a function of the assembling on SiC sandpaper.

Surface color of each layer assembled on SiC sandpaper is a first evidence of its finished profile. Nevertheless, a statistical behavior of the graphite surface allows knowing characteristics such as asperity which can be measured by R_a parameter as the variation in profile height (roughness average), and average thickness as a function of the R_p parameter can be analyzed to demonstrate the amount of graphite assembled (surface texture). Therefore, using an AFM analysis the finished profile of the graphite surface can be understood.

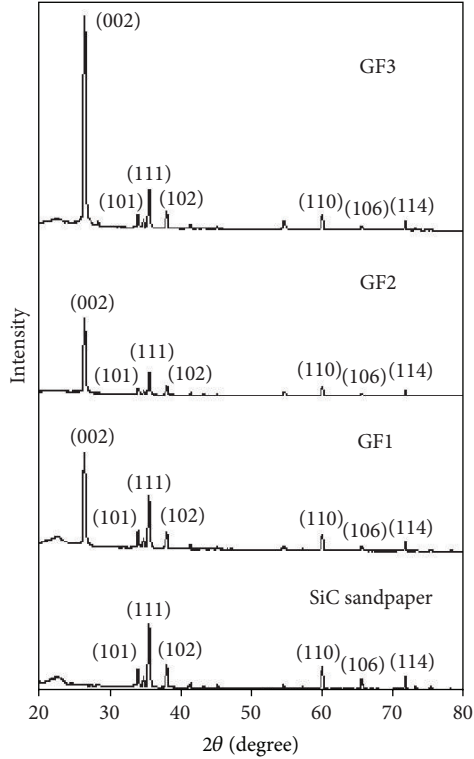


FIGURE 2: XRD patterns of graphite layers as a function of the amount of the graphite assembled on SiC sandpaper as substrate.

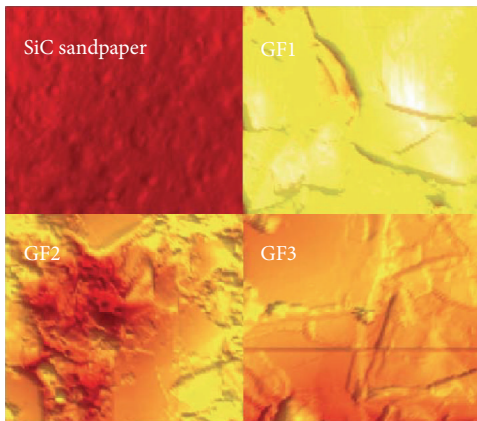


FIGURE 3: AFM images of samples with graphite assembled of different thickness. As reference, the AFM image of SiC sandpaper is shown.

Figure 3 shows AFM images of well-known samples labeled as SiC sandpaper, GF1, GF2, and GF3.

It is well known that a rough surface has the capacity to abrade, if its asperities induce stresses; thus the graphite surface should be measured as a function of density of the asperities and height distribution [14, 17]. Roughness and thickness average as finished parameters are related to the amount of graphite assembled and friction forces involved, which can be studied by a roughness algorithm using the

TABLE 1: Finished parameters from graphite samples.

Parameter	SiC sandpaper	GF1	GF2	GF3
Surface color	Water	Dark gray	Opaque gray	Gray
Scanned area (μm^2)	1.08	1.09	1.10	1.15
R_a (nm)	2.13	15.30	10.32	15.70
R_p (nm)	240.20	309.80	416.20	831.20

TABLE 2: Transport parameters from graphite layers.

Sample	S (cm^2)	dV/dI (k Ω)	σ ($\Omega^{-1}\text{cm}^{-1}$)	μ_n ($\text{cm}^2\text{V}^{-1}\text{s}^{-1}$)
GF1	4.64×10^{-4}	22.72	0.057	255.40
GF2	6.24×10^{-4}	8.33	0.115	289.60
GF3	12.46×10^{-4}	4.54	0.106	285.40

Veeco software. Such finished parameters are listed in Table 1. It is confirmed that the graphite samples assembled on SiC sandpaper have different finished profiles with R_a parameter in the range from 2 to 16 nm, lower than its carrier mean free path of $l = 235$ nm which is a critical parameter for electronic transport in graphite devices [7, 12].

To know the electronic transport of the graphite layers, an electrical circuit of Figure 4(a) has been built to obtain current-voltage curves of well-known samples labeled GF1, GF2, and GF3. Sinusoidal signal must be applied as input voltage and a resistor of 100Ω for monitoring of the output signal was used. Physical diagram of Figure 4(b) was built for measuring of each layer, where two aluminum (Al) electrodes were placed to connect the graphite layer of $l_s = 6$ mm of length. Figure 4(c) shows that each curve had an ohmic behavior from -10 to 10 V which has been previously studied by Ohm's law $dV/dI = l_s/\sigma S$ [12]. From the slope dV/dI of each curve, the conductivity σ as a function of l_s , and cross-sectional area, S equal to the multiplication between *layer thickness* and *metallic mask wide* can be computed.

Because low-field regime ($F < 10^6 \text{ Vcm}^{-1}$) is dominated by thermal scattering of phonons and thermal velocity $v_T = \mu_n F$ is linear in field [18], the average drift mobility, μ_n in graphite as a function of the variation of dimensions, thickness, and lower number of defects gives an indication on stability of the electronic transport. Consequently, μ_n should be calculated as a function of the thickness, which is equivalent to the R_p parameter from AFM analysis (see Table 1) and can be described by $\mu_n = R_p v_T / V$ with $v_T = 4.8 \times 10^7 \text{ cm/s}$ for graphite and V as bias voltage across the layers.

Table 2 gives the transport parameters from the experiment conducted in Figure 4. Current-voltage curves allow knowing that the ambipolar behavior of graphite is dependent on μ_n and σ which can be controlled by device geometry, such as thickness and electrode dimensions, to get stable electronic transport.

3.2. Green Engineering Based on Graphite Circuits. To demonstrate that derivative of a signal based on current injection

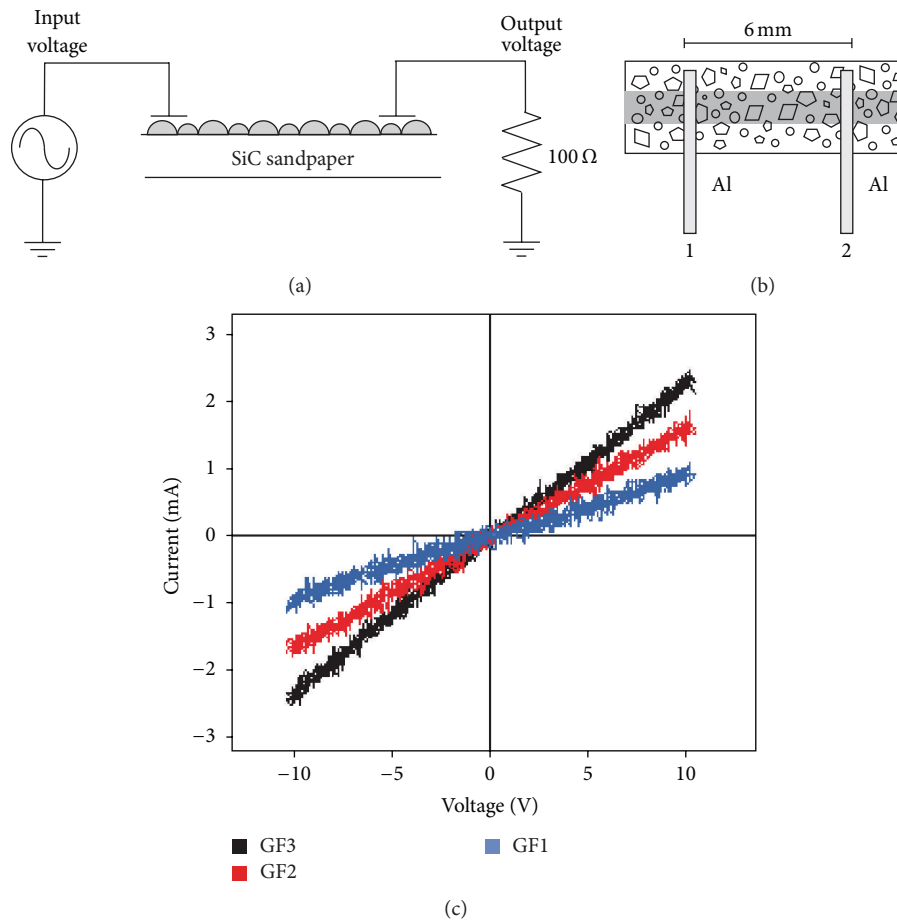


FIGURE 4: (a) Practical circuit implemented. (b) Physical diagram of the experimental procedure. (c) Current-voltage curves.

by a bias voltage can be developed, a schematic diagram of a graphite layer assembled as circuit is shown in Figure 5(a), which consists of the following array: a capacitor connected in series to a first section of the graphite layer with 3 mm of length located between electrodes 1 and 2 to perform a RC circuit, while, between electrodes 1 and 3, a second section with similar length to the first section is used to provide the bias voltage.

It is well known that a typical response of a RC circuit is equivalent to the differentiator circuit [19], but when an additional element is added a special behavior for the RC circuit can be gotten. Figure 5(b) shows a block diagram of the Pulse Width Modulation (PWM) which could be easier implemented by using of the circuit of Figure 5(a), simplifying the well-known silicon-based circuits traditionally fabricated by complex-signal processors [20, 21]. By applying a square signal as input voltage of amplitude 1 V, duty cycle of 30%, and frequency of 100 Hz, the performance of the circuit of Figure 5 can be demonstrated. Figure 5(c) indicates typical derivative of a signal with a slope increased when bias voltage was not applied, while that derivative of a signal with slope decreased under bias voltage of 5 V can be driven (see Figure 5(d)). As a result, if a bias voltage in the range from 0 to 5 V is injected, gradual slope changes can be obtained.

To disclose that a graphite circuit can be used for modulation of signals, a schematic diagram of Figure 6(a) should be realized with two graphite layers of different conductivity GF1 and GF3 (see Table 2). The behavior of this modulator circuit type can be understood by a mathematical function shown in Figure 6(b). Figure 6(c) shows the modulation of a signal monitored from a resistor of 1 kΩ, when a full-rectified signal of amplitude 10 V and frequency of 120 Hz in GF1 layer, as well as square signal of amplitude 1 V, frequency of 600 Hz, and duty cycle of 50% in GF3 layer, has been applied. For example, GF1 has lower conductivity and GF3 higher conductivity; the modulation process can be developed.

To validate the technological importance of the green engineering based on graphite circuits it is explained to compare the physical properties such as μ_n and thermal conductivity of graphite samples with those of GaN and silicon. For GaN the degradation of the heat conduction properties depends on quality, purity, and thickness of its films, because lower thermal conductivity of GaN is in the range of 125 to 225 Wm/K, compared to that of bulk graphite ($k = 2000$ Wm/K) at room temperature [13]. Also, the current conduction of silicon devices has been determined by μ_n in the range of 200 to 1000 cm^2/Vs , which is dependent on the ionized impurity concentration in the range of 10^{15} to 10^{18} cm^{-3}

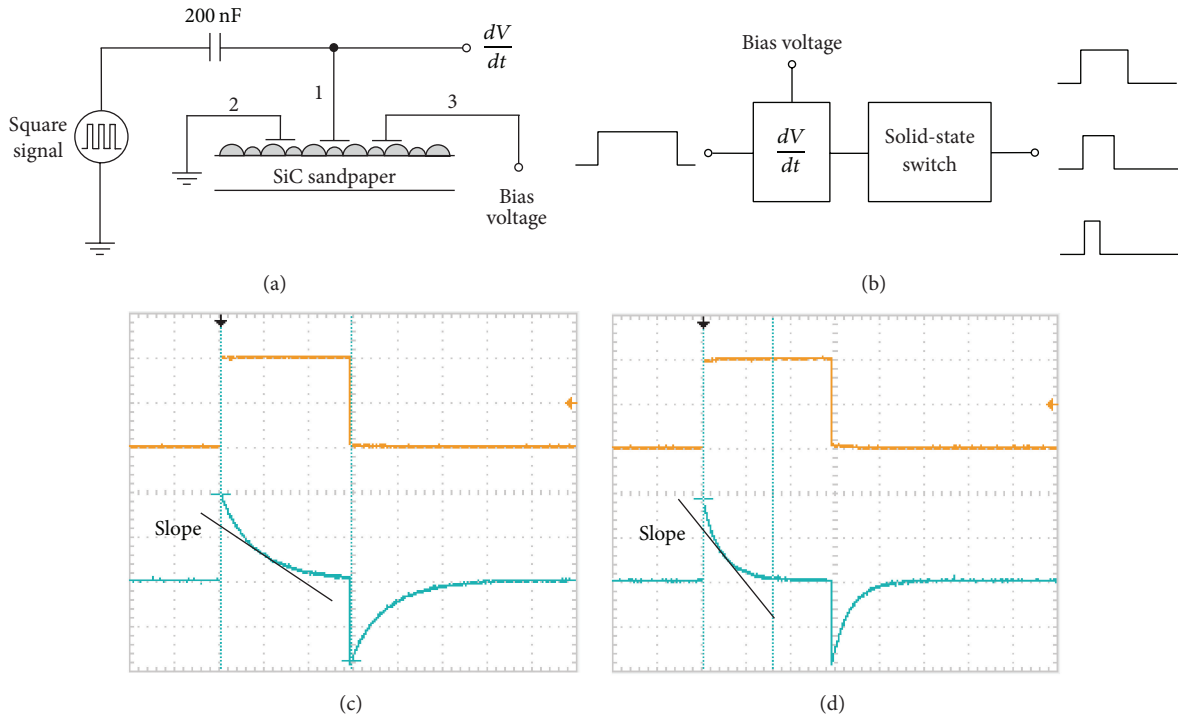


FIGURE 5: (a) Practical circuit implemented for derivative of a signal. (b) Block diagram to realization of a PWM circuit based on graphite architectures. (c) Derivative of a signal without bias voltage. (d) Derivative of a signal with bias voltage.

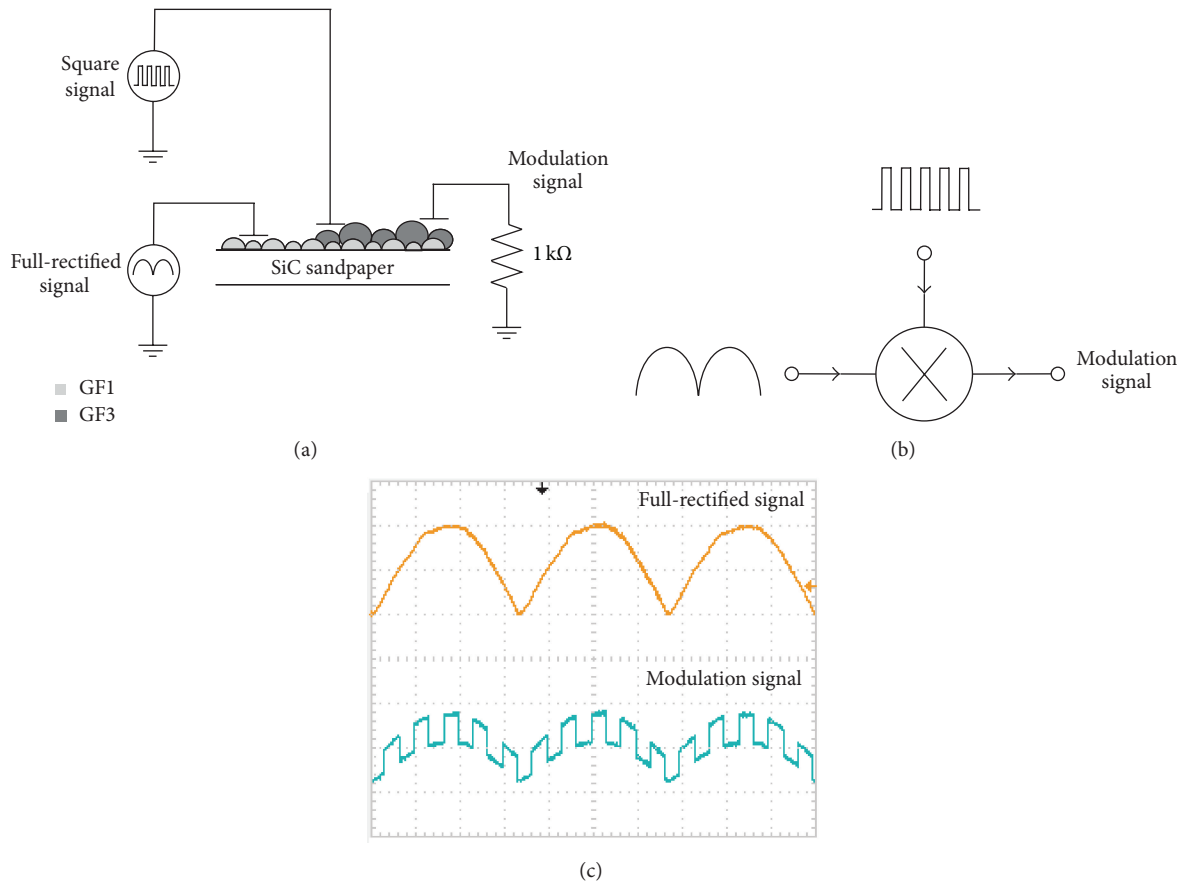


FIGURE 6: (a) Practical circuit implemented for modulation of a signal. (b) Mathematical function of a modulation process. (c) Modulation of a signal when a full-rectified signal was applied.

thermally diffused by planar technology at high temperatures [22].

The proposed graphite devices can become an industrial-scale alternative for electronic engineering applications; because of that graphite circuits have been built with higher junction area around $\sim 10^{-1}$ cm² than that of 10^{-4} to 10^{-3} cm² for silicon and GaN, which allows the fact that heat spreading along graphite layers can be dissipated on SiC sandpaper when higher current conduction in samples of lower thickness than that of 500 nm is attained at μ_n in the range of 250 to 290 cm²/Vs without concentration of donor and acceptor impurities as in silicon devices [18, 22], which means that stacking profile of graphite assembled on SiC sandpaper is associated with lower trap concentration (intrinsic structural defects).

4. Conclusions

Graphite layers synthesized by noncontaminant reverse abrasion have been studied. From graphite rods recuperated by old pencils and SiC sandpaper as an insulating substrate, graphite circuits as an example of green engineering were demonstrated. In spite of graphite limitations as its ambipolar character, design of the graphite-based devices inspired by using different performance principles should be continued in the future. To get stable devices environmentally friendly, automation must be projected for mass production free of toxic sources.

Competing Interests

The author declares that there are no competing interests, but there is a direct interest regarding the publication of this paper: sharing knowledge about green materials and their applications.

Acknowledgments

The collected characterization data of XRD and AFM in this work have been possible thanks to the support of Dr. José Alberto Andraca and Dr. Juan Vicente Méndez from CNMN belonging to the National Polytechnic Institute, Mexico City.

References

- [1] F.-L. Luo, W. Williams, R. M. Rao, R. Narasimha, and M. J. Montpetit, "Trends in signal processing applications and industry technology," *IEEE Signal Processing Magazine*, vol. 12, pp. 171–174, 2012.
- [2] T. R. Dickson, *Understanding Chemistry from Atoms to Attitudes*, LIMUSA, Mexico City, Mexico; John Wiley & Sons, New York, NY, USA, 1st edition, 2006.
- [3] R. Baca-Arroyo, "Nonlinear-electronic transport in Fe₂O₃ thin-films grown from grain-oriented iron foils," *Advances in Materials Science and Engineering*, vol. 2013, Article ID 987572, 8 pages, 2013.
- [4] R. Baca, "Manganese oxide thin-films for current-signal sensing and thermal insulation," *Materials Science in Semiconductor Processing*, vol. 16, no. 5, pp. 1280–1284, 2013.
- [5] R. Baca, "Reliable energy strategy based on incandescent lighting," *Energy and Power Engineering*, vol. 7, no. 5, pp. 174–180, 2015.
- [6] K. E. Whitener Jr. and P. E. Sheehan, "Graphene synthesis," *Diamond & Related Materials*, vol. 46, pp. 25–34, 2014.
- [7] V. Singh, D. Joung, L. Zhai, S. Das, S. I. Khondaker, and S. Seal, "Graphene based materials: past, present and future," *Progress in Materials Science*, vol. 56, no. 8, pp. 1178–1271, 2011.
- [8] W. Soon, S. L. Baliunas, A. B. Robinson, and Z. W. Robinson, "Environmental effects of increased atmospheric carbon dioxide," *Climate Research*, vol. 13, no. 2, pp. 149–164, 1999.
- [9] A. Cotton and G. Wilkinson, *Advanced Inorganic Chemistry*, John Wiley & Sons, New York, NY, USA, 4th edition, 2008.
- [10] M. Reuter and A. V. Schaik, "Opportunities and limits of recycling: a dynamic-model-based analysis," *MRS Bulletin*, vol. 37, no. 4, pp. 339–347, 2012.
- [11] A. A. Balandin, "Thermal properties of graphene and nanostructured carbon materials," *Nature Materials*, vol. 10, no. 8, pp. 569–581, 2011.
- [12] L. A. Pendry, C. Zeller, and F. L. Vogel, "Electrical transport properties of natural and synthetic graphite," *Journal of Materials Science*, vol. 15, no. 8, pp. 2103–2112, 1980.
- [13] Z. Yan, G. Liu, J. M. Khan, and A. A. Balandin, "Graphene quilts for thermal management of high-power GaN transistors," *Nature Communications*, vol. 3, article 827, 2012.
- [14] D. V. De Pellegrin and G. W. Stachowiak, "Sharpness of abrasive particles and surfaces," *Wear*, vol. 256, no. 6, pp. 614–622, 2004.
- [15] G. Venugopal, K. Krishnamoorthy, and S.-J. Kim, "An investigation on high-temperature electrical transport properties of graphene-oxide nano-thinfilms," *Applied Surface Science*, vol. 280, pp. 903–908, 2013.
- [16] C. Xiu-Yun, "Graphene-like nanosheets synthesized by natural flaky graphite in Shandong, China," *International Nano Letters*, pp. 3–6, 2013.
- [17] V. K. Jain, "Magnetic field assisted abrasive based micro-/nanofinishing," *Journal of Materials Processing Technology*, vol. 209, no. 20, pp. 6022–6038, 2009.
- [18] M. Lundstrom, *Fundamentals of Carrier Transport*, Cambridge University Press, New York, NY, USA, 2nd edition, 2000.
- [19] A. S. Sedra and K. C. Smith, *Microelectronics Circuits*, Oxford University in Press, New York, NY, USA, 4th edition, 1988.
- [20] M. H. Rashid, *Power Electronics Circuits, Devices, and Applications*, Prentice Hall Inc, New York, NY, USA, 1st edition, 1995.
- [21] L. Dulau, S. Pontarollo, A. Boimond, J.-F. Garnier, N. Giraud, and O. Terasse, "A new gate driver integrated circuit for IGBT devices with advanced protections," *IEEE Transactions on Power Electronics*, vol. 21, no. 1, pp. 38–43, 2006.
- [22] A. S. Grove, *Physics and Technology of Semiconductor Devices*, John Wiley & Sons, New York, NY, USA, 1st edition, 1967.

Research Article

Soil Erosion Estimation Using Remote Sensing Techniques in Wadi Yalamlam Basin, Saudi Arabia

Jarbou A. Bahrawi,¹ Mohamed Elhag,¹ Amal Y. Aldhebiani,² Hanaa K. Galal,^{2,3}
Ahmad K. Hegazy,⁴ and Ebtisam Alghailani²

¹Department of Hydrology and Water Resources Management, Faculty of Meteorology, Environment & Arid Land Agriculture, King Abdulaziz University, Jeddah 21589, Saudi Arabia

²Biological Sciences Department, Faculty of Science, King Abdulaziz University, Jeddah 21589, Saudi Arabia

³Botany Department, Faculty of Science, Assiut University, Assiut 71515, Egypt

⁴Department of Botany and Microbiology, Faculty of Science, Cairo University, Giza 12613, Egypt

Correspondence should be addressed to Mohamed Elhag; melhag@kau.edu.sa

Received 11 October 2015; Revised 5 February 2016; Accepted 16 February 2016

Academic Editor: Jianxi Zhu

Copyright © 2016 Jarbou A. Bahrawi et al. This is an open access article distributed under the Creative Commons Attribution License, which permits unrestricted use, distribution, and reproduction in any medium, provided the original work is properly cited.

Soil erosion is one of the major environmental problems in terms of soil degradation in Saudi Arabia. Soil erosion leads to significant on- and off-site impacts such as significant decrease in the productive capacity of the land and sedimentation. The key aspects influencing the quantity of soil erosion mainly rely on the vegetation cover, topography, soil type, and climate. This research studies the quantification of soil erosion under different levels of data availability in Wadi Yalamlam. Remote Sensing (RS) and Geographic Information Systems (GIS) techniques have been implemented for the assessment of the data, applying the Revised Universal Soil Loss Equation (RUSLE) for the calculation of the risk of erosion. Thirty-four soil samples were randomly selected for the calculation of the erodibility factor, based on calculating the *K*-factor values derived from soil property surfaces after interpolating soil sampling points. Soil erosion risk map was reclassified into five erosion risk classes and 19.3% of the Wadi Yalamlam is under very severe risk (37,740 ha). GIS and RS proved to be powerful instruments for mapping soil erosion risk, providing sufficient tools for the analytical part of this research. The mapping results certified the role of RUSLE as a decision support tool.

1. Introduction

Evaluating soil erosion risks is a difficult undertaking task due to several concurrent processes, which affects individually other multifaceted interactions and continues at amounts that vary in both time and space [1, 2]. Since the 1960s and on, soil decision-makers and scientists have examined models for calculating soil loss from erosion by water from rainwater, a hill slope, or a minor catchment [3, 4]. With the presence of GIS competencies, the efforts have been directed to be based on spatially distributed models simulating erosion dynamics and surface runoff of more complex and larger catchments [5, 6].

Several models have been developed and used for either research or operational purposes. Some of the most known

soil erosion models are USLE (Universal Soil Loss Equation, 1965), EPIC (Erosion/Productivity Impact Calculator, 1984), EUROSEM (European Soil Erosion Model, 1993), RUSLE (Revised Universal Soil Loss Equation, 1997), Rill Grow (a model for rill initiation and development, 1998), SEMMED (Soil Erosion Model for Mediterranean Regions, 1999), EGEM (Ephemeral Gully Erosion Model, 1999), PESERA (Pan-European Soil Erosion Risk Assessment, 2003), and so forth.

Soil erosion models can be distinguished as mechanistic (or process based) when they simulate the physical erosion processes by specific formulas or empirical when they calculate erosion based on regression of soil loss based on the physical properties of land and climate features [7, 8]. They also can be characterized as dynamic when

the time is a contained parameter. Long-term models are based on accumulated temporal data while event-based models describe single events [9, 10].

The soil erosion estimation models are focused on the identification and quantification of the erosion processes and the controlling factors, resulting in the sequential erosion models development beginning with the universal erosion equation (USLE) realized by Wischmeier and Smith [11], followed by a modified equation (MUSLE) for the quantification of the alluvium resulting from erosion following each rainfall realized by Williams [12], and eventually computerized and more complex equation (RUSLE) developed by Renard et al. [13].

The most important climatic variable in soil erosion processes is rainfall erosivity, which is related to rainfall amount and rainfall intensity [14, 15]. Soil erosion is relatively related to rainfall, partially because of the shedding power of raindrops falls on the soil surface and partially because of the involvement of rainwater to surface runoff [16, 17].

Plants vegetative cover in addition to crop residues reduces soil erosion potential, due to the fact that the vegetation cover protects and leads to slowing down surface runoff movement and enhancing surplus surface water infiltration [18–20]. Type, extent, and quantity of the vegetation cover are the limiting factors of soil erosion effectiveness [21, 22].

The main aim of this research is to quantify the soil erosion in Wadi Yalamlam through examining the soil erodibility K -factor under different levels of soil data availability using the RUSLE model.

2. Materials and Methods

2.1. Study Area. Wadi Yalamlam basin is located about 125 km southeast of Jeddah city and is bounded by latitudes $20^{\circ}26'$ and $21^{\circ}8'N$ and longitudes $39^{\circ}45'$ and $40^{\circ}29'E$ (Figure 1). Wadi Yalamlam basin drained large catchment area of about 180,000 hr. The basin boundary of the lower part is enlarged to include nearly all the flat area in the downstream part. Wadi Yalamlam basin is initiated from high elevation Hijaz escarpment with mean annual rainfall of about 140 mm. The basin elevations greatly vary from upstream and downstream parts and range between 2850 m and 25 m (ASL), respectively. The main course of Wadi Yalamlam has crosscut the highly fractured granitoid, gabbroic, and metamorphic rocks until the coastal plain of the Red Sea. The upper and middle parts of Wadi Yalamlam basin are covered by intense natural vegetation. The lower part is covered mainly by quaternary deposits and sand dunes with small scattered highly altered granitoid and metamorphosed basaltic hills. Several basic dikes are recorded in the lower part of Wadi Yalamlam basin. The thickness of quaternary Wadi Yalamlam deposits increased in the lower part.

2.2. Methodological Framework. The methodology is implemented through several steps which led to the intermediate and the final results. Initially, the C , R , P , and LS factors were calculated in order to be included in the RUSLE formula. Then, the K -factor was estimated from the soil samples

using the USDA nomograph [23]. Later, three interpolation methods (Radial Basis Functions (RBF), Inverse Distance Weighted (IDW), and Ordinary Kriging (OK)) were checked for their accuracy and the K -factor layer (thematic map) was created using the most accurate method. By multiplying the RUSLE factors calculated earlier ($C * R * P * LS$) with the k -layers (thematic map), soil erosion risk thematic map was created. Finally, the erosion risk map was reclassified into five classes of risk. The mathematical expression of RUSLE is

$$A = R * K * LS * C * P, \quad (1)$$

where A is the average annual erosion rate ($t\ ha^{-1}\ yr^{-1}$); R is the rainfall erosivity ($MJ\ mm\ ha^{-1}\ h^{-1}\ yr^{-1}$); K is the soil erodibility ($t\ ha\ h\ ha^{-1}\ MJ^{-1}\ mm^{-1}$); LS is slope length and slope steepness factor (dimensionless); C is the correction coefficient for the effect of vegetation (dimensionless); and P is the correction coefficient for the effect of erosion control measurements (dimensionless).

2.3. Data Description. Meteorological data, especially rainfall data for the last 10 years, were collected from two adjacent weather stations. The first weather station located in the upper stream of the Wadi (latitudes $21^{\circ}48'N$ and longitudes $40^{\circ}55'E$, 1454 m ASL), and the second weather station located in the lower stream (latitudes $19^{\circ}01'N$ and longitudes $41^{\circ}88'E$, 350 m ASL). Thirty-four soil samples were collected from the entire designated study area with a minimum distance of 500 m between the samples locations to avoid data clumping (Figure 1). Soil samples were taken to 30 cm depth and followed stratified random sampling techniques [24]. Physical properties of the soil samples were identified using mechanical mesh with series of pore sizes. Identification of silt as well as clay fractions was carried out following Mitchell [25]. Digital Elevation Model (DEM) data were acquired from the Japanese-American satellite ASTER GDEM. The used DEM is validated by the provider and ASTER GDEM is highly accurate DEM covering all the land on earth with 30 m spatial resolution. Landsat 8 Operational Land Imager (OLI) scene was acquired in 16th of July, 2015. Landsat 8 consists of 9 multispectral bands of 30 m spatial resolution and two thermal bands of 100 m spatial resolution in addition to the panchromatic bands of 15 m spatial resolution. Two Full-Width-Half-Maximum (FWHM) bands of $654.6\ \mu m$ as red band and $864.7\ \mu m$ as infrared band were exercised to drive Normalized Difference Vegetation Index (NDVI).

2.4. Generation of R , K , LS , C , and P Factors. Rainfall erosivity factor (R), estimation of the rainfall erosivity factor (R), is highly based on annual rainfall (mm), and when the annual rainfall is high, erosivity (R) is also high. Estimation of the rainfall erosivity factor was based on the average of the annual rainfall data for twenty-four-year period provided by two meteorological stations in the area. Rainfall erosivity factor (R) was estimated based on total kinetic energy (E) and maximum intensity in 30 minutes (I) in an average year's rain. Barfield et al. [26] condense several measures that have examined relationships between individual storm energies

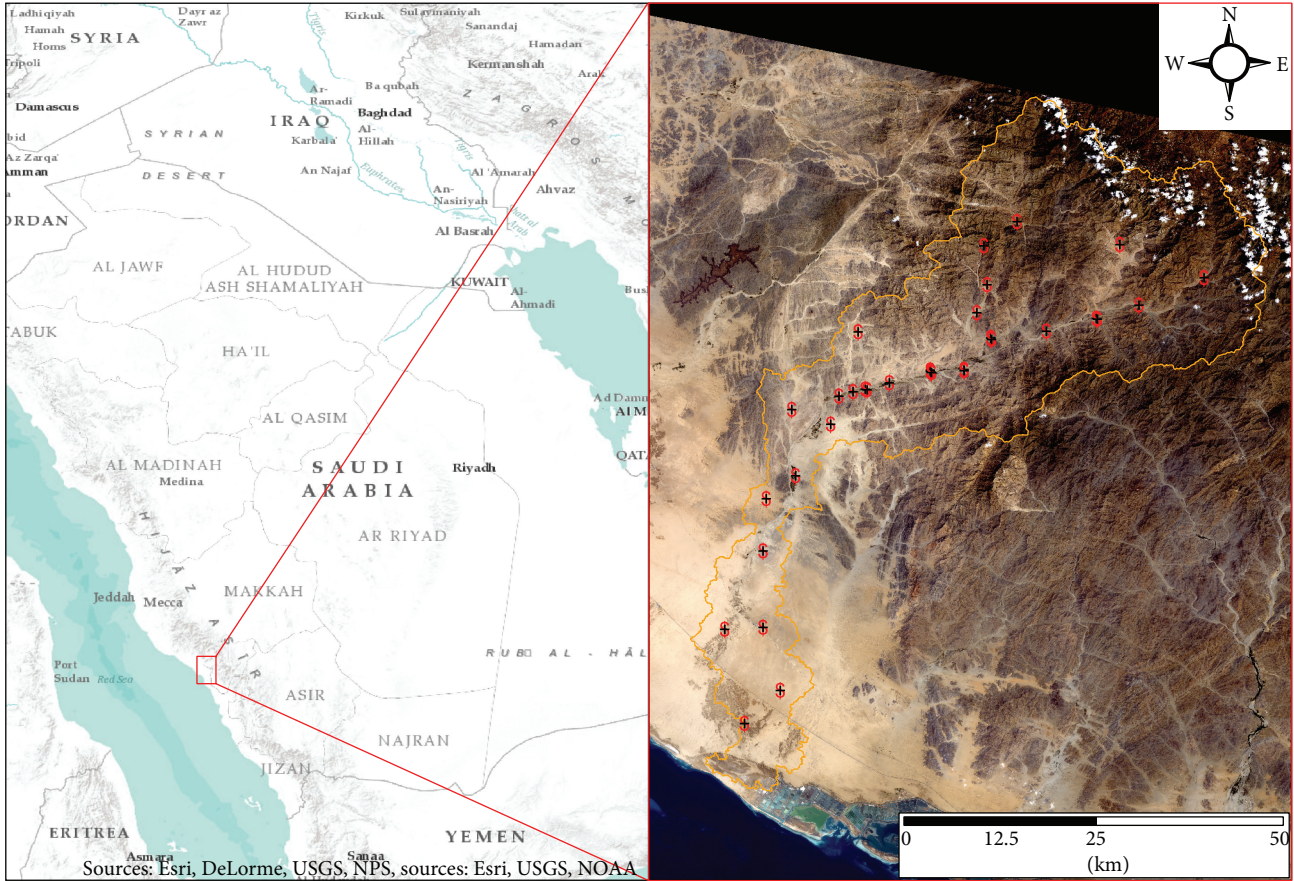


FIGURE 1: Location of the study including sample sites.

and erosion yields. According to Wischmeier [27], the best predictor of R was

$$R = \frac{1}{n} \sum_{j=1}^n \left[\sum_{k=1}^m (E) (I_{30})_k \right], \quad (2)$$

where E is the total storm kinetic energy, I_{30} is the maximum 30-minute rainfall intensity, j is the counter for each year used to produce the average, k is the counter for the number of storms in a year, m is the number of storms n each year, and n is the number of years used to obtain the average R .

Wischmeier [27] also found that the rain kinetic energy (E) could be predicted by

$$E = 916 + (331) \log_{10} (I). \quad (3)$$

K -factor (soil erodibility) is the one that will be mainly examined. Using the stratified random sampling method, thirty-four points, randomly selected and stratified in regard to the geologic formations, were sampled for their necessary topsoil properties. Then, K values were calculated according to the RUSLE formula for these methods following USDA monograph [23]. Finally, the K values were interpolated to produce a surface of K values for the total area. Not only is soil texture the principal component affecting K , but also soil permeability and soil organic content are essential. Rosewell

and Loch [28] described a method to estimate K -factor. Soil physical analysis is indispensable in K -factor determination. Wischmeier and Smith [11] and Renard et al. [29] proposed an algebraic approximation taking into consideration five different soil features (soil organic content, soil permeability, soil texture, soil structure, and soil coarse fragments) as follows:

$$K = \left[\frac{(2.1 \times 10^{-4} M 1.14 (12 - OM) + 3.25 (s - 2) + 2.5 (p - 3))}{100} \right] * 0.1317, \quad (4)$$

where M is the textural factor with $M = (m_{\text{silt}} + m_{\text{vfs}}) * (100 - m_c)$; m_c [%] is clay fraction content (<0.002 mm); m_{silt} [%] is silt fraction content (0.002–0.05 mm); m_{vfs} [%] is very fine sand fraction content (0.05–0.1 mm); OM [%] is the organic matter content; s is the soil structure; and p is the permeability class.

The slope factor (LS) refers to the topographic and/or the relief factor. The slope length factor L computes the effect of slope length on erosion and the slope steepness factor S computes the effect of slope steepness on erosion. The topography related parameters were derived from the Digital Elevation Model (DEM) following Wilson and Gallant

[30]. Based on Wischmeier and Smith [11], LS values were estimated as follows:

$$LS = \left(\frac{\ell}{72.6} \right) m (65.41 \sin^2 \beta + 4.56 \sin \beta + 0.065), \quad (5)$$

where ℓ is the cumulative slope length in feet; β is the downhill slope angle; m is a slope contingent variable, 0.5 if the slope angle is greater than 2.86° , 0.4 on slopes of 1.72° to 2.86° , 0.3 on slopes of 0.57° to 1.72° , and 0.2 on slopes less than 0.57° .

The cover management factor (C) is dimensionless for each grid cell ranging from 0 to 1 under standard fallow conditions. As the surface cover is added to the soil, the C factor value approaches zero. Generally, the C factor is calculated based on derivation of Normalized Difference Vegetation Index (NDVI) and then reclassification of NDVI in order to extract the C factor with higher positive values of NDVI. Red band and infrared band of Landsat 8 were exercised to estimate NDVI as follows:

$$NDVI = \frac{(IR - R)}{(IR + R)}, \quad (6)$$

where IR is the infrared band and R is the red band.

The support practice factor (P) is defined as the ratio of soil loss with a specific support practice to the corresponding soil loss with up- and downcultivation. The lower the P value is, the more effective the conservation practice is deemed to be in reducing soil erosion. Usually, in practice, expert opinion is used to qualitatively assess this factor.

Different interpolation techniques were used to produce adequate thematic maps based on the Root Mean Square Error (RMSE) evaluation. Principally, RBF shows better results rather than the other two interpolation methods in similar arid ecosystems [31]. This could be explained due to the fact that the RBF is considered as an exact interpolation technique, which means that the predicted values are identical to the measured values [32]. The interpolation is based on a mathematical function that smooths the generated surfaces by minimizing the surfaces curvature.

2.5. Integration of Factors for Erosion Risk Mapping. The erosion risk maps were generated by integrating all pre-estimated factors according to the RUSLE to create erosion map using K -factor values derived from soil sampling with interpolation. This was done using map algebra following the RUSLE method, where all layers generated previously were multiplied under GIS environment. The produced soil erosion map was consequently reclassified into five classes of erosion risk after Wischmeier and Smith [11].

3. Results and Discussion

In order to assess the soil erosion risks in the study area, several applications and analyses were implemented. Each generated factor was thus fully described and processed. From the available weather stations located in Wadi Yalam-lam, regression was found between the mean annual precipitation 1983–2010 (mm/year) and the elevation to be read as

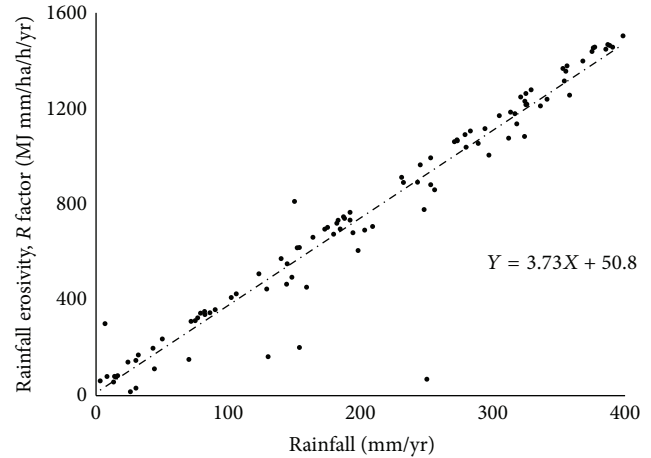


FIGURE 2: Rainfall erosivity factor versus yearly rainfall.

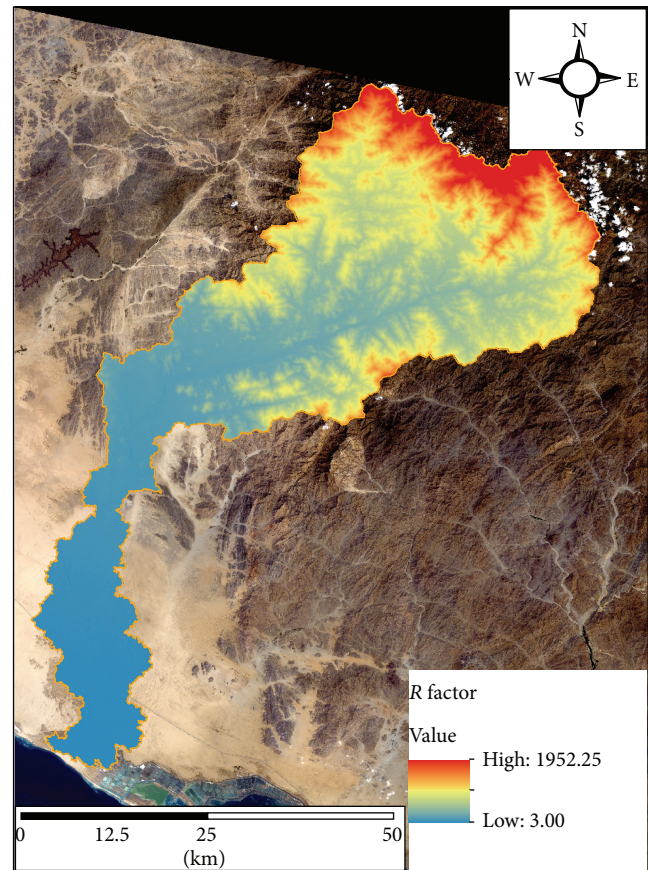


FIGURE 3: Thematic map of rainfall erosivity factor (R) (MJ mm/ha year).

$P = 3.73 * DEM + 50.8$ (Figure 2). The regression relationship was established before estimating the rainfall erosivity index as a function of average annual precipitation and elevation with R^2 of 0.967. The final thematic map for rainfall erosivity factor is shown in Figure 3. The standard error of estimate between the point and the surface K -factor is 0.005 t ha hr/ha MJ mm; K -factor is with an acceptable

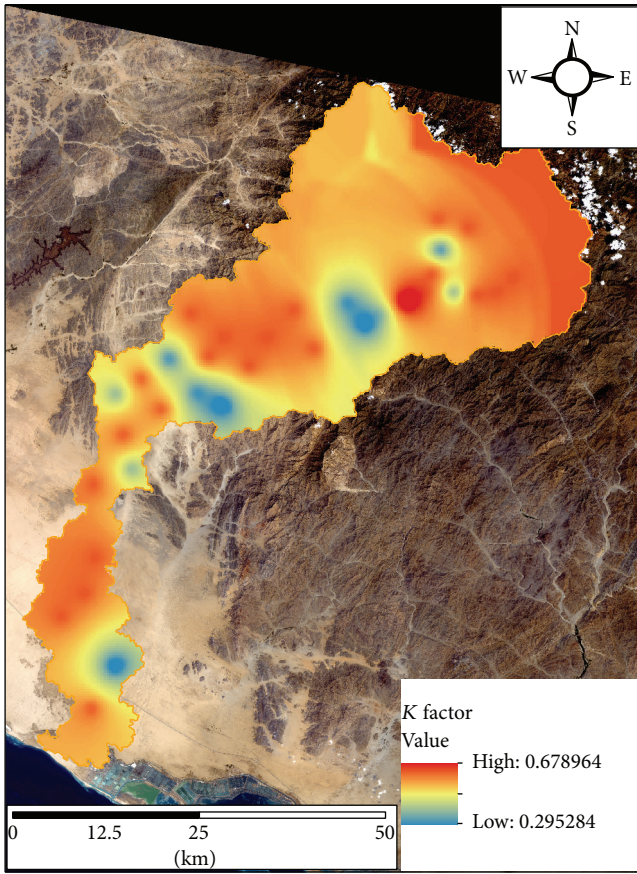


FIGURE 4: Thematic map of soil erodibility factor (K) (t ha hr/ha MJ mm).

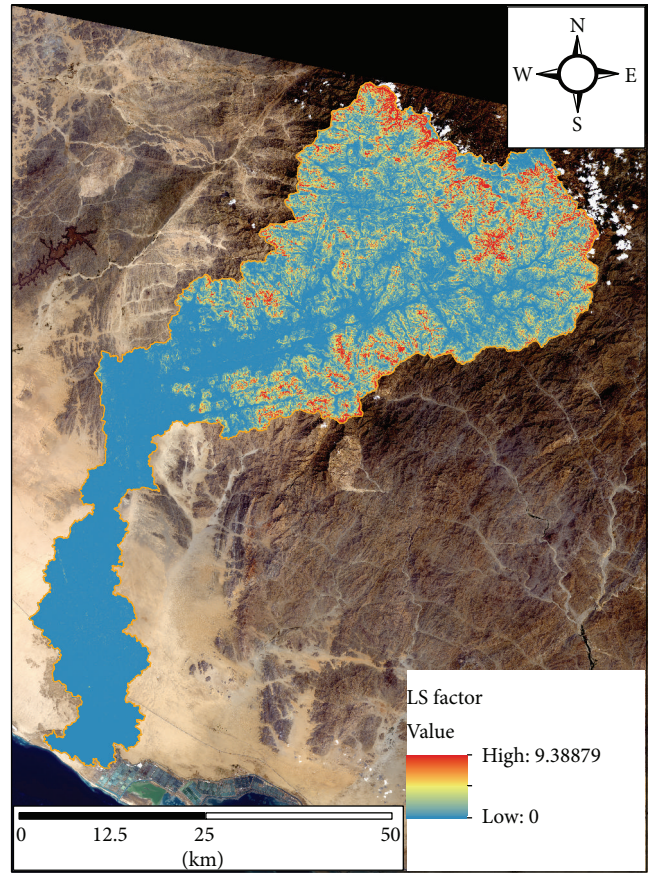


FIGURE 5: Thematic map of the length/slope (LS) factor.

level of accuracy [33]. Thematic map for the soil erodibility factor is shown in Figure 4. To determine LS factor adjusted by Moore and Burch [34, 35] under GIS environment, the slope and flow length for each grid cell were estimated and illustrated in Figure 5. The effectiveness of the plant cover in reducing the raindrop impact depends on the height and the continuity of the canopy and the density of the ground cover. In this study, the C factor was calculated using sigmoidal function derivation of Normalized Difference Vegetation Index (NDVI) to extract the C factor.

The derivation of the NDVI values follows a monotonically decreasing sigmoid function with two control inflection points (0 and 1) which was used in order to define the fuzzy value of C factor as illustrated in Figure 6. However, reclassification of the NDVI values was done in order to assign small values (near zero) for the C factor for vegetated areas which are less risky in terms of erosion potential and big values (close to one) than sparsely vegetated areas and bare ground, which are more prone to erosion as it is shown in Figure 7.

The effect of terraces, contour planting (contouring), and tillage practices on soil erosion is described by the support practice factor P within the RUSLE model. P factor in Wadi Yalamlam is assumed to be 0.9. Such assumption is based on the fact that the wadi is with no agricultural practice in

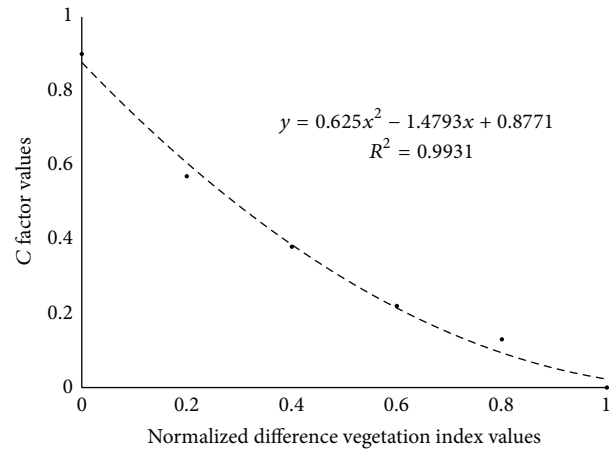


FIGURE 6: C factor function versus Normalized Difference Vegetation Index.

the form of terraces and also the roads infrastructure as well as urban areas is disused due to its neglectability compared to the vast area of the wadi [36].

Standard normal distribution function practiced on the NDVI values indicated that most of the values are around zero value as demonstrated in Figure 8. Several negative

TABLE 1: Erosion risk classes (ERC) following Wischmeier and Smith [11].

Erosion class	ERC 1	ERC 2	ERC 3	ERC 4	ERC 5
Loss t/ha/year	0–5	5–10	10–20	20–40	>40
Classification	Very slight	Slight	Moderate	Severe	Very severe

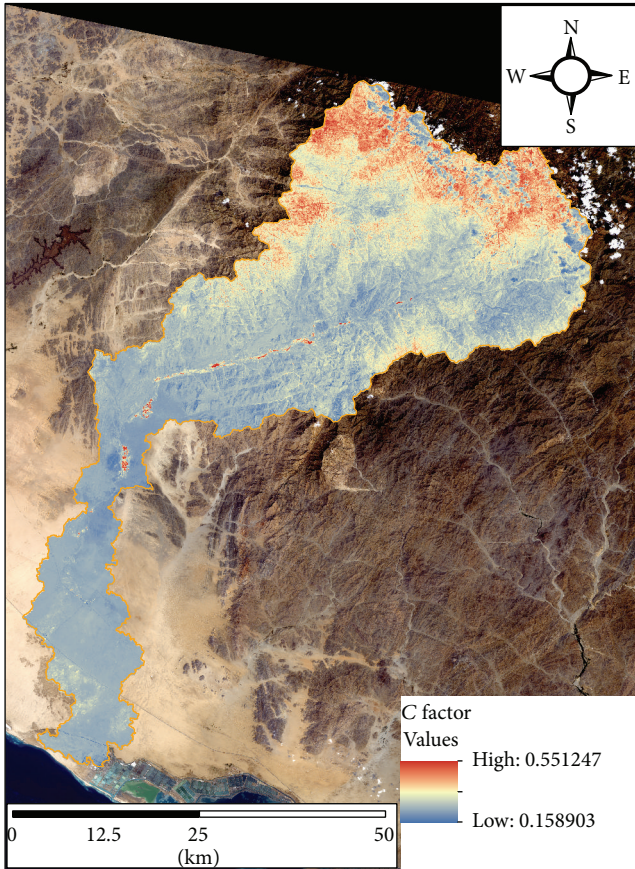


FIGURE 7: Thematic map of the C factor.

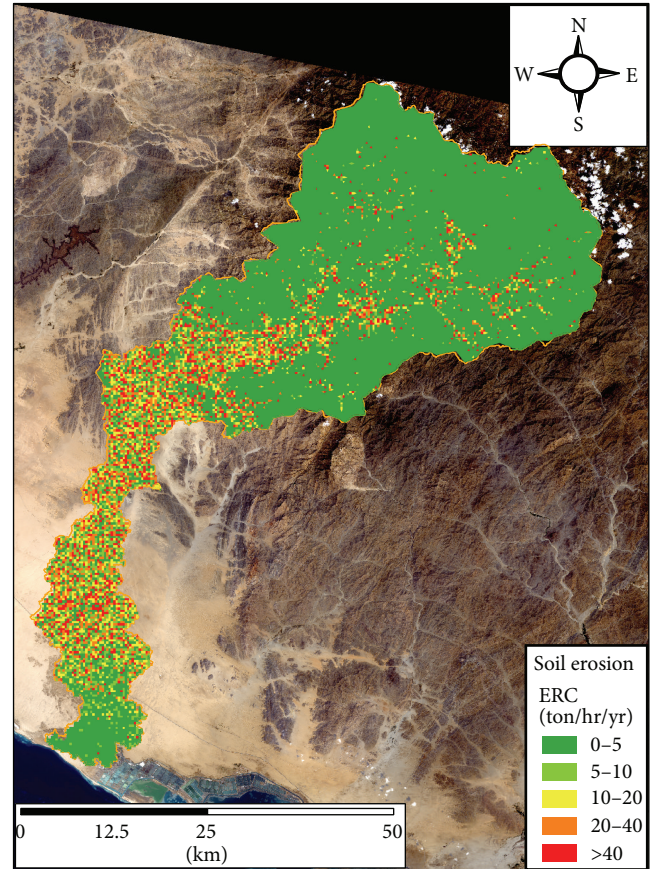


FIGURE 9: Soil erosion classification map.

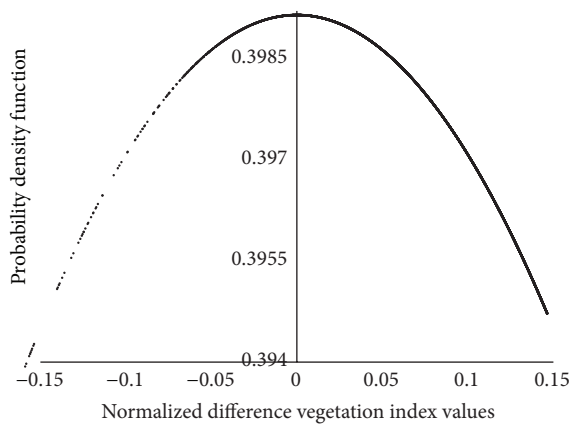


FIGURE 8: Standard normal distribution function of NDVI.

values were reordered but there were more positive values indicating higher organic content [37].

The erosion risk map was generated by integrating all preestimated factors according to the RUSLE equation to create soil erosion map using K -factor values derived from soil sampling with interpolation of RBF with R^2 of 0.89. This was done under map algebra toolbox to fulfill RUSLE method, where all layers generated previously were multiplied under GIS environment. Conducted soil erosion risk map was reclassified into five classes of erosion risk after Wischmeier and Smith [11], as showed in Table 1. The reclassified erosion risk map is shown in Figure 9. The upper part of the wadi, as well as the very lower part, is under the slight condition of erosion, which could be explained by the type of the bedrock material at the upper part and the no slope at the very lower part [38]. The narrow middle part of the wadi is under the very severe condition of soil erosion, which is logically

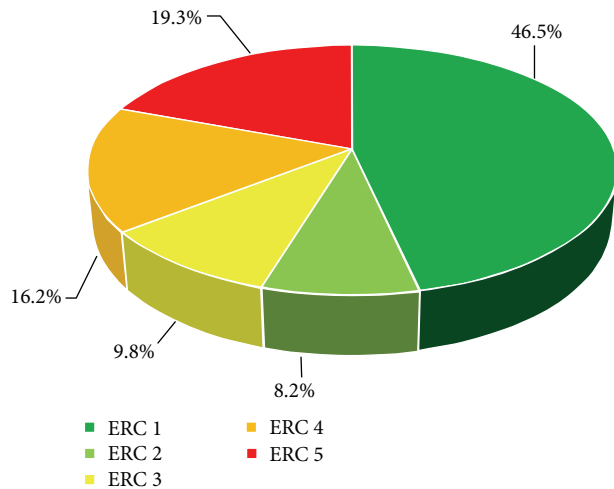


FIGURE 10: Area distribution of erosion risk classes using RUSLE model.

explained due to several geomorphological features including basically the drainage frequency (F_d), drainage density (D_d), and drainage texture (T) of Wadi Yalamlam according to Elhag [37, 39, 40]. In addition, the stream network carves its course and it carries the sediment that erodes as it flows. This gives it more power to erode as there is more friction in the moving water, but it also deposits this material when it flows out of upper stream onto the lower stream [39].

Figure 10 demonstrates the proportion of each erosion risk class to the total basin area of Wadi Yalamlam. Nearly half of the total area is under slight risk (46.5%). On the other hand, considerable areas are under very severe risk (19.3%) and need further attention.

4. Conclusion

Erosion risk values are ranked into classes, which is in accordance with RUSLE standards as it provides better identification of the area most prone to erosion. The dissimilarities discovered earlier seem to fade out. Because the vast majority of erosion risk values in erosion risk map were bigger than 40 tons/ha/year, the reclassification of this map into categories of severity resulted in a concentration of values in the most severe category. Precaution measurements need to be set up in the middle part of Wadi Yalamlam as it is the most subjected parts to severe soil erosion. GIS and Remote Sensing are inevitable technological environments when implementing RUSLE for assessing soil erosion risk in the spatial domain. The adopted approach was based on mapping procedures, such as conversion of categorical into numerical polygons, interpolation of point samples, map algebra, and raster map reclassification. Data quality is a crucial parameter in soil erosion modeling and those errors and uncertainties are propagated to the final erosion results. Denser grid of sampling sites for the soil survey approach would produce a better k layer after interpolation although such a procedure is costly and time-consuming.

Competing Interests

The authors declare that they have no competing interests.

Acknowledgments

This project was funded by the Deanship of Scientific Research (DSR) at King Abdulaziz University, Jeddah, under Grant no. (G-393-155-1436). The authors, therefore, acknowledge with thanks DSR for technical and financial support.

References

- [1] P. M. Driesen, "Erosion hazards and conservation needs as a function of land characteristics and land qualities," in *Land Evaluation for Land-Use Planning and Conservation in Sloping Areas*, W. Siderius, Ed., pp. 32–39, ILRI, Wageningen, The Netherlands, 1986.
- [2] C. Valentin, J. Poesen, and Y. Li, "Gully erosion: impacts, factors and control," *Catena*, vol. 63, no. 2-3, pp. 132–153, 2005.
- [3] J. Wainwright, A. J. Parsons, and A. D. Abrahams, "Plot-scale studies of vegetation, overland flow and erosion interactions: case studies from Arizona and New Mexico," *Hydrological Processes*, vol. 14, no. 16-17, pp. 2921–2943, 2000.
- [4] L. Turnbull, J. Wainwright, and R. E. Brazier, "Changes in hydrology and erosion over a transition from grassland to shrubland," *Hydrological Processes*, vol. 24, no. 4, pp. 393–414, 2010.
- [5] E. G. Gregorich, K. J. Greer, D. W. Anderson, and B. C. Liang, "Carbon distribution and losses: erosion and deposition effects," *Soil & Tillage Research*, vol. 47, no. 3-4, pp. 291–302, 1998.
- [6] C. J. Williams, F. B. Pierson, P. R. Robichaud, and J. Boll, "Hydrologic and erosion responses to wildfire along the rangeland-xeric forest continuum in the western US: a review and model of hydrologic vulnerability," *International Journal of Wildland Fire*, vol. 23, no. 2, pp. 155–172, 2014.
- [7] M. V. K. Sivakumar, "Interactions between climate and desertification," *Agricultural and Forest Meteorology*, vol. 142, no. 2-4, pp. 143–155, 2007.
- [8] I. Z. Gitas, K. Douros, C. Minakou, G. N. Silleos, and C. G. Karydas, "Multi-temporal soil erosion risk assessment in N. Chalkidiki using a modified USLE raster model," *EARSeL eProceedings*, vol. 8, no. 1, pp. 40–52, 2009.
- [9] P. Podwojewski, J. L. Janeau, S. Grellier, C. Valentin, S. Lorentz, and V. Chaplot, "Influence of grass soil cover on water runoff and soil detachment under rainfall simulation in a sub-humid South African degraded rangeland," *Earth Surface Processes and Landforms*, vol. 36, no. 7, pp. 911–922, 2011.
- [10] S. Grellier, J. Kemp, J.-L. Janeau et al., "The indirect impact of encroaching trees on gully extension: a 64 year study in a sub-humid grassland of South Africa," *Catena*, vol. 98, pp. 110–119, 2012.
- [11] W. H. Wischmeier and D. D. Smith, "Predicting rainfall erosion losses from cropland east of the Rocky Mountains," *Agricultural Handbook 2828*, US Government Print office, Washington, DC, USA, 1978.
- [12] R. P. Williams, "Erosion and sediment transport in the Owens River near Bishop, California," *Water-Resources Investigations Report 75-49*, U. S. Geological Survey Water Resources Investigations, 1975.

- [13] K. Renard, G. R. Foster, G. A. Weesies, and J. P. Porter, "RUSLE revised universal soil loss equation," *Journal of Soil and Water Conservation*, vol. 46, pp. 30–33, 1991.
- [14] E. Bochet and P. García-Fayos, "Factors controlling vegetation establishment and water erosion on motorway slopes in Valencia, Spain," *Restoration Ecology*, vol. 12, no. 2, pp. 166–174, 2004.
- [15] V. H. D. Zuazo and C. R. R. Pleguezuelo, "Soil-erosion and runoff prevention by plant covers—a review," *Agronomy for Sustainable Development*, vol. 28, no. 1, pp. 65–86, 2008.
- [16] G. Gyssels, J. Poesen, E. Bochet, and Y. Li, "Impact of plant roots on the resistance of soils to erosion by water: a review," *Progress in Physical Geography*, vol. 29, no. 2, pp. 189–217, 2005.
- [17] S. Cohen, T. Svoray, J. B. Laronne, and Y. Alexandrov, "Fuzzy-based dynamic soil erosion model (FuDSEM): modelling approach and preliminary evaluation," *Journal of Hydrology*, vol. 356, no. 1-2, pp. 185–198, 2008.
- [18] V. H. D. Zuazo, J. R. F. Martínez, C. R. R. Pleguezuelo, A. M. Raya, and B. C. Rodríguez, "Soil-erosion and runoff prevention by plant covers in a mountainous area (SE Spain): implications for sustainable agriculture," *Environmentalist*, vol. 26, no. 4, pp. 309–319, 2006.
- [19] P. K. Shit, G. S. Bhunia, and R. Maiti, "Assessing the performance of check dams to control rill-gully erosion: small catchment scale study," *International Journal of Current Research*, vol. 5, pp. 899–906, 2013.
- [20] A. Psilovikos and M. Elhag, "Forecasting of remotely sensed daily evapotranspiration data over Nile Delta region, Egypt," *Water Resources Management*, vol. 27, no. 12, pp. 4115–4130, 2013.
- [21] V. M. Castillo, M. Martínez-Mena, and J. Albaladejo, "Runoff and soil loss response to vegetation removal in a semiarid environment," *Soil Science Society of America Journal*, vol. 61, no. 4, pp. 1116–1121, 1997.
- [22] V. H. Durán Zuazo, J. R. F. Martínez, C. R. R. Pleguezuelo, A. Martínez Raya, and B. C. Rodríguez, "Soil-erosion and runoff prevention by plant covers in a mountainous area (SE Spain): implications for sustainable agriculture," *Environmentalist*, vol. 26, no. 4, pp. 309–319, 2006.
- [23] USDA. Agricultural Research Service USDA-ARS, "CREAMS, a field scale model for chemicals, runoff, and erosion from agricultural management systems," Conservation Research Report 26, USDA, 1980.
- [24] S. Lohr, *Sampling: Design and Analysis*, Duxbury, Pacific Grove, Calif, USA, 1999.
- [25] J. K. Mitchell, *Fundamentals of Soil Behavior*, John Wiley & Sons, New York, NY, USA, 1976.
- [26] B. J. Barfield, R. C. Warner, and C. T. Haan, *Applied Hydrology and Sedimentology for Disturbed Areas*, Oklahoma Technical Press, Stillwater, Okla, USA, 1983.
- [27] W. H. Wischmeier, "A rainfall erosion index for a universal soil-loss equation1," *Soil Science Society of America Journal*, vol. 23, no. 3, pp. 246–249, 1959.
- [28] C. J. Rosewell and R. J. Loch, "Estimation of the RUSLE soil erodibility factor," in *Soil Physical Measurement and Interpretation for Land Evaluation*, N. McKenzie, K. Coughlan, and H. Cresswell, Eds., pp. 361–369, CSIRO Publishing, Melbourne, Australia, 2002.
- [29] G. R. Renard, G. A. Foster, and D. K. Weessies, "McCool predicting soil erosion by water: a guide to conservation planning with the Revised Universal Soil Loss Equation (RUSLE)," in *Agriculture Handbook*, D. C. Yoder, Ed., p. 703, US Department of Agriculture, Washington, DC, USA, 1997.
- [30] J. P. Wilson and J. C. Gallant, *Terrain Analysis—Principles and Application*, John Wiley & Sons, New York, NY, USA, 2000.
- [31] M. Elhag, "Evaluation of different soil salinity mapping using remote sensing techniques in arid ecosystems, Saudi Arabia," *Journal of Sensors*, vol. 2016, Article ID 7596175, 8 pages, 2016.
- [32] N. Nikolova and S. Vassilev, "Mapping precipitation variability using different interpolation methods," in *Proceedings of the Conference on Water Observation and Information System for Decision Support (BALWOIS '06)*, Ohrid, Macedonia, May 2006.
- [33] W. Drzewiecki, P. Wezyk, M. Pierzchalski, and B. Szafrńska, "Quantitative and qualitative assessment of soil erosion risk in Małopolska (Poland), supported by an object-based analysis of high-resolution satellite images," *Pure and Applied Geophysics*, vol. 171, no. 6, pp. 867–895, 2014.
- [34] I. D. Moore and G. J. Burch, "Physical basis of the length-slope factor in the universal soil loss equation," *Soil Science Society of America Journal*, vol. 50, no. 5, pp. 1294–1298, 1986.
- [35] I. D. Moore and G. J. Burch, "Modelling erosion and deposition: topographic effects," *Transactions of the American Society of Agriculture Engineers*, vol. 29, no. 6, pp. 1624–1630, 1986.
- [36] T. Chen, R.-Q. Niu, P.-X. Li, L.-P. Zhang, and B. Du, "Regional soil erosion risk mapping using RUSLE, GIS, and remote sensing: a case study in Miyun Watershed, North China," *Environmental Earth Sciences*, vol. 63, no. 3, pp. 533–541, 2011.
- [37] M. Elhag, "Remotely sensed vegetation indices and spatial decision support system for better water consumption regime in Nile Delta. A case study for rice cultivation suitability map," *Life Science Journal*, vol. 11, no. 1, pp. 201–209, 2014.
- [38] K. H. Al-Zahrani and M. B. Baig, "Water in the kingdom of Saudi Arabia: sustainable management options," *Journal of Animal and Plant Sciences*, vol. 21, no. 3, pp. 601–604, 2011.
- [39] M. Elhag, "Characterization of a typical mediterranean watershed using remote sensing techniques and GIS tools," *Hydrology: Current Research*, vol. 6, no. 1, pp. 197–204, 2015.
- [40] M. Elhag and J. A. Bahrawi, "Conservational use of remote sensing techniques for a novel rainwater harvesting in arid environment," *Environmental Earth Sciences*, vol. 72, no. 12, pp. 4995–5005, 2014.

Research Article

Effect of Kinetin on Physiological and Biochemical Properties of Maize Seedlings under Arsenic Stress

Haijuan Wang, Biyu Dai, Xiaogang Shu, Hongbin Wang, and Ping Ning

Faculty of Environmental Science and Engineering, Kunming University of Science and Technology, Kunming 650500, China

Correspondence should be addressed to Hongbin Wang; whb1974@126.com

Received 5 September 2015; Revised 24 November 2015; Accepted 25 November 2015

Academic Editor: Zhaohui Li

Copyright © 2015 Haijuan Wang et al. This is an open access article distributed under the Creative Commons Attribution License, which permits unrestricted use, distribution, and reproduction in any medium, provided the original work is properly cited.

The effects of different levels of kinetin (KT) application on the growth, biomass, contents of chlorophyll (Chl a, Chl b, and carotenoid), arsenic uptake, and activities of antioxidant enzymes in maize seedlings under arsenic (As) stress were investigated by a hydroponic experiment. The results showed that KT supplementation increased the biomass in terms of root length, root number, fresh weight, and seedling length, and KT treatments also improved the contents of Chl a, As uptake, and Chl a : b ratio compared to cases with As treatment alone. However, no significant changes were observed in carotenoid content, and a reduction was found in Chl b content of seedlings. KT also increased the activities of catalase (CAT), peroxidase (POD), and superoxide dismutase (SOD) in the leaves of maize seedlings when 0.1 mg/L KT and As were applied, which decreased the content of malondialdehyde (MDA). These results suggested that KT could alleviate the toxicity of As to maize seedlings by keeping the stability of chlorophyll, enhancing the activities of antioxidant enzymes, and inhibiting the lipid peroxidation. In conclusion, the alleviation effect of KT in maize seedlings exposed to As stress was clearly observed in the present study.

1. Introduction

Arsenic (As) has been an element of considerable environmental concern, because of its toxicity and carcinogenic properties [1], resulting from natural geologic activities and anthropogenic sources such as mining, semiconductor manufacturing, forest products, landfill leachates, fertilizers, pesticides, and sewage [2]. Exposure to As (V) caused considerable stress in plants, including disorder of cellular function [3], inhibition of growth [4], biochemical and physiological damage [5], and reduction of crop productivity [3, 6, 7].

In addition, excess As induces oxidative stress in plants by generating reactive oxygen species (ROS), such as superoxide radicals (O_2^-), hydroxyl radical (OH^-), and hydrogen peroxide (H_2O_2) [8]. These species react with lipids, proteins, pigments, and nucleic acids and cause lipid peroxidation, membrane damage, and inactivation of enzymes [9–11]. Plants respond to oxidative stress by increasing the activities of antioxidant enzymes, such as superoxide dismutase (SOD), catalase (CAT), and peroxidase (POD) [4, 10, 12–14].

Cytokinins are a class of phytohormones and can stimulate water uptake, increase cell division, promote organ

development, and lead to the regeneration and proliferation of shoots [15]. Among the cytokinins, KT is the first to be discovered and has been widely used in plants for its growth-promoting, antiaging, and promotion of cell division and differentiation [16–18]. Apart from these effects, KT has an ability to confer resistance to plants against various abiotic stresses [19], such as heavy metal toxicity, drought, and inadequate fertilization [11, 20–23].

The main purpose of this study was to evaluate the effects of KT on growth-promotion and regulation of antioxidant defense in maize seedlings under As stress. The effects of different levels of KT application on growth, seedling biomass, chlorophyll contents, antioxidant enzyme activities, and As uptake in maize seedling were systematically determined under As stress. Our results could be used as indicators to improve plant As tolerance and food safety.

2. Materials and Methods

2.1. Plant Materials and Experimental Design. Maize seeds were washed thoroughly by running tap water and distilled

water and then sown in double distilled water for 24 h. After soaking, 20 healthy and uniformly sized seeds were sown in petri plates that were filled with 130 mL 1/10 Hoagland's solution and 100 mL of 0.5 mg/L As added as $\text{Na}_2\text{HAsO}_4 \cdot 7\text{H}_2\text{O}$ (control) or with 100 mL different concentrations of KT. The concentrations of As and KT were based on the results of previous experiments. The treatments included As (0.5 mg/L) (control), As + KT1 (0.5 mg/L As + 0.1 mg/L KT), As + KT2 (0.5 mg/L As + 0.5 mg/L KT), and As + KT3 (0.5 mg/L As + 1.5 mg/L KT) and each treatment was replicated 3 times. After 12-day growth, the fresh tissues were harvested.

2.2. Determination of Growth Parameters. The harvested seedlings were washed several times by running tap and distilled water and then dried by filter paper. The fresh weight was determined by a digital balance and the root and plant lengths were measured in millimeter. The numbers of the lateral roots were also recorded.

2.3. Determination of As Uptake in Plants. The contents of As in stem and leaves were determined as described previously [24]. The fresh seedlings were thoroughly washed by distilled water and digested with 5 mL of concentrated HNO_3 in a 50 mL digestion glass tube. These tubes were heated at 80~90°C for 30 min, 100~110°C for 30 min, and 120~130°C for 1 h. Later, the tubes were cooled and added with 1 mL of 30% H_2O_2 . The tube contents were mixed and heated at 100~110°C for 30 min and 120~130°C for 1 h. The mixture was filtered and diluted to a total volume of 25 mL. The concentration of As was determined by atomic fluorescence spectrometry (Beijing Rayleigh Instruments Co., AF-610D2). The As content was expressed as $\mu\text{g/g}$ fresh weight.

2.4. Analysis of Antioxidant Enzyme Activities. For the determination of antioxidant enzyme activities, 1.0 g fresh leaf was homogenized in 10 mL of 50 mmol phosphate buffer (pH = 7.0) under cool condition in prechilled mortar and pestle. The homogenate was centrifuged at 20,000 $\times\text{g}$ for 15 min at 4°C, and then the supernatant was stored under cool condition for analysis of SOD, CAT, and POD.

SOD activity was assayed by monitoring the inhibition of photochemical reduction of nitrotetrazolium blue chloride (NBT), according to the method as described by Gao [25]. The reaction solution consisted of 1.5 mL phosphate buffer (pH = 7.0), 0.3 mL DL-methionine (Met), 0.3 mL NBT, 0.3 mL riboflavin, 0.3 mL EDTA- Na_2 , 0.5 mL distilled water, and 0.1 mL raw enzyme. The reaction mixture, which was not exposed to light, did not develop color and served as the control. A control reaction was performed without raw enzyme which was replaced by an equal volume of distilled water. The assay was carried out at 25~35°C and the reaction was measured spectrophotometrically at 560 nm. One unit of enzyme activity was defined as the quantity of enzyme that reduced the A560 of control by 50%.

CAT activity was determined according to Gao [25], and the decomposition of H_2O_2 was evaluated by measuring the decrease in absorbance at 240 nm after 3 min. The reaction mixture contained 1.0 mL Tris-HCl buffer (pH = 7.0), 1.7 mL

distilled water, 0.1 mL enzyme extract, and 0.2 mL 100 mmol H_2O_2 .

POD activity was determined according to Gao [25]. The assay mixture included 1.0 mL KH_2PO_4 (20 mmol/L), 3 mL of reaction solution containing 50 mL of 100 mmol phosphate buffer (pH = 6.0), 28 μL guaiacol, and 19 μL 30% hydrogen peroxide for 3 min (the time interval was 30 s) and 1.0 mL raw enzyme. The change in absorbance at 460 nm was recorded for calculating POD activity.

2.5. Measurement of Malondialdehyde (MDA). The level of lipid peroxidation in fresh tissue was measured in terms of malondialdehyde (MDA) content by the thiobarbituric acid (TBA) reaction method according to Gao [25]. 0.5 g fresh tissues were homogenized in 5 mL 5% trichloroacetic acid (TCA) solution under cool condition and centrifuged at 3,000 $\times\text{g}$ for 15 min at 4°C, and then the clear supernatant was added to 5 mL TBA. The mixture was heated in boiling water for 10 min and then cooled in an ice-bath and centrifuged at 3,000 $\times\text{g}$ for 15 min. The absorbance of the supernatant was recorded at 532, 600, and 450 nm for calculating the content of MDA.

2.6. Determination of Chlorophyll Contents. The contents of leaf chlorophyll were determined according to Gao [25]. 0.2 g fresh leaves were homogenized in 2~3 mL 95% ethanol with some CaCO_3 and SiO_2 . After centrifugation at 4,000 $\times\text{g}$ for 10 min, the absorption of the extracts at 470 nm (carotenoid), 645 nm (chlorophyll b), and 662 nm (chlorophyll a) was recorded for the calculation of the pigment contents.

2.7. Data Analysis. Linear regression was analyzed using SPSS 20 statistical package. One-way ANOVA test was performed followed by Tukey's HSD multiple comparison tests to determine significant differences at significance level $P < 0.05$ or $P < 0.01$ with statistical software SAS 9.2. The figures were drawn by Origin 8.0.

3. Results

3.1. Plant Growth. The growth parameters in terms of fresh weight, shoot length, root length, and root number showed different responses when maize seedlings were exposed to As alone and combined treatment of As and KT. The fresh weight (Figure 1(a)) and root length (Figure 1(c)) were significantly increased when 0.1 mg/L KT was added, compared to the control (As treatment alone). However, no significant difference was found in seedling length and root numbers between 0.1 mg/L KT treatment and control.

A significant increase (12%) in seedling length (Figure 1(b)) was also observed when treated with As + 0.5 mg/L KT. Besides, the application of 1.5 mg/L KT significantly increased the root numbers (Figure 1(d)) by 28% as compared with those at As treatment alone. Moreover, the ameliorative effects were more pronounced on root number than on other growth parameters when exposed to As + 1.5 mg/L KT treatments. Furthermore, the alleviative

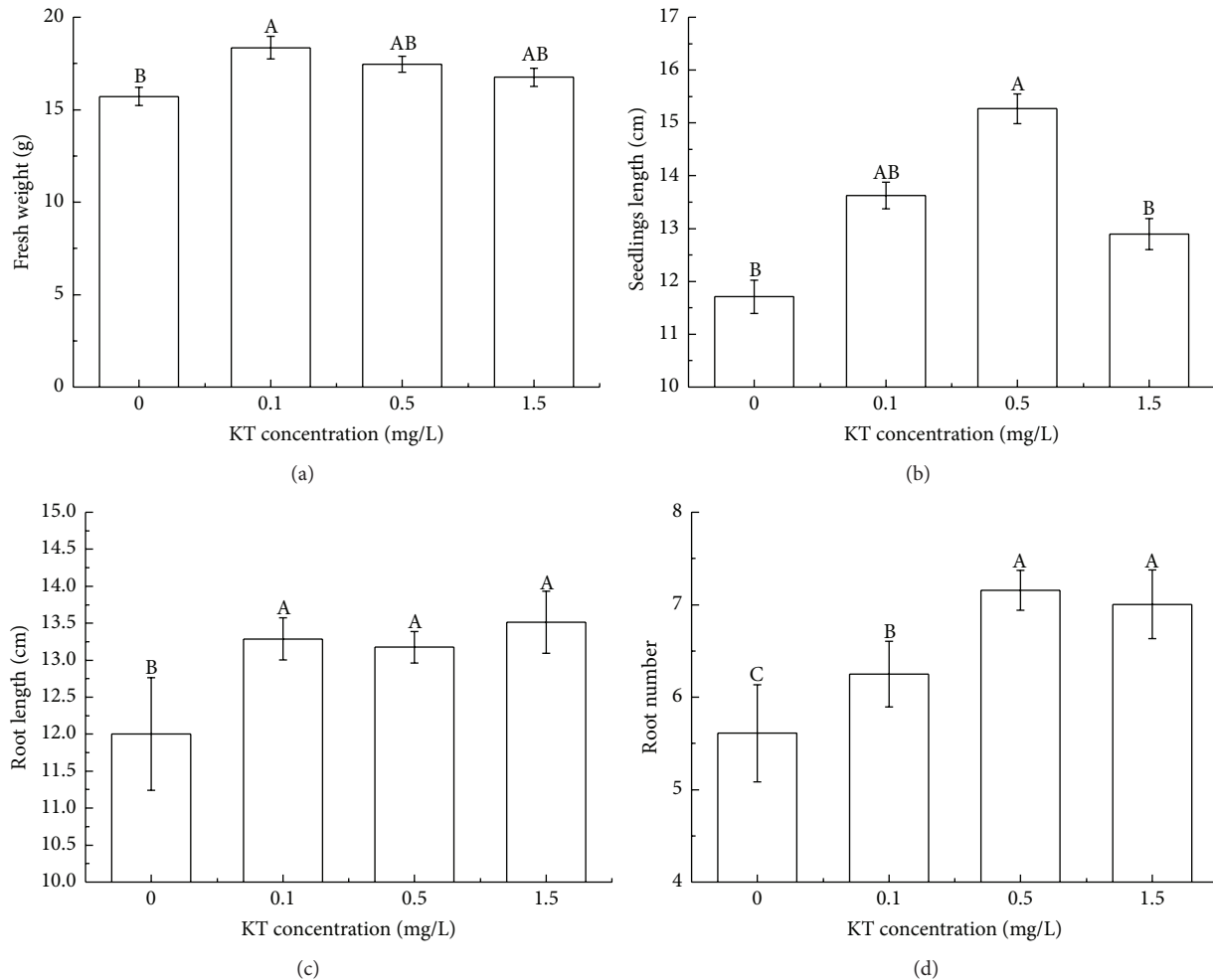


FIGURE 1: Effects of different concentrations of KT on the growth parameters of maize seedlings under 0.5 mg/L arsenic stress. Values with different letters indicate a significant difference ($P < 0.05$).

effects of KT on growth parameters of maize seedlings were related to its concentrations.

3.2. Arsenic Uptake. Arsenic contents had no significant difference at 0.1 mg/L and 0.5 mg/L KT treatment compared to the control. However, a significant increase of As in maize seedlings was observed when 1.5 mg/L KT was added, indicating high concentration of KT could generate adverse effects on maize seedlings (Figure 2).

3.3. Activities of Antioxidant Enzyme and MDA Contents

3.3.1. Activities of SOD. The activity of SOD was significantly increased by 78% with the addition of 0.1 mg/L KT under 0.5 mg/L As stress compared to the control (Figure 3(a)). However, no significant change was found in SOD activity of maize seedlings with 0.5 or 1.5 mg/L KT addition, compared to As treatment alone (Figure 3(a)).

3.3.2. Activities of CAT. CAT activity increased with the increasing concentrations of KT except the 0.5 mg/L KT

treatment. Furthermore, the CAT activity at 1.5 mg/L KT was significantly higher than that at 0.1 mg/L KT (Figure 3(b)).

3.3.3. Activities of POD. A significant increase (60%) of POD activity in maize seedling was noticed when exposed to 1.5 mg/L KT under As stress, compared to the control. However, no significant difference was observed among 0, 0.1, and 0.5 mg/L KT treatments (Figure 3(c)).

3.3.4. MDA Contents. Application of KT at three concentrations (0.1–1.5 mg/L) could significantly reduce the MDA content of maize seedlings compared to the control. However, no significant difference was observed among the three treatments (Figure 3(d)).

3.4. Content of Photosynthetic Pigments. The content of Chl a (Figure 4(b)) and the ratio of Chl a : b (Figure 4(d)) were significantly increased with the 0.5 mg/L KT addition. However, Chl b content (Figure 4(a)) showed a decline trend with an increasing level of KT under As stress. Moreover,

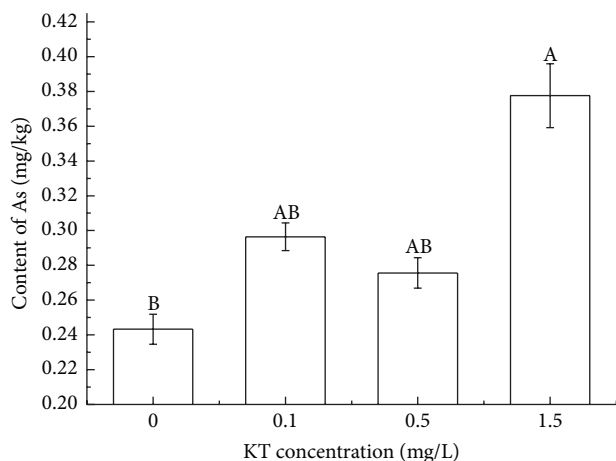


FIGURE 2: Effects of different concentrations of KT on arsenic uptake in maize seedlings under 0.5 mg/L arsenic stress. Values with different letters indicate a significant difference.

the content of carotenoid (Figure 4(c)) showed no variation with KT addition (Figure 4).

4. Discussion

4.1. Effect of KT on Maize Growth Parameters. It is well documented that heavy metals cause several toxic effects on plants, such as inhibition of seedling growth [26], seed germination [23], reduction of shoot length [27], and root length [28]. Therefore, seed germination, root length, root biomass, shoot length, and seedling growth are generally used to describe metal resistance in plants. Several studies have shown that As can inhibit plant growth [29]. In the present study, we mainly investigated the root number, root length, seedling length, and fresh weight of maize exposed to KT and As treatments. Our results showed that the application of KT alleviated the As-induced inhibition of seedling growth by improving the growth parameters in terms of root length, root number, and fresh weight (Figure 1). It has been reported that KT mitigates the adverse effects of salt stress on plant growth [20]. Similarly, KT addition ameliorates the deleterious effects of Mn pollution [11]. After all, our results showed the ability of KT to counter the toxic effects of As on maize seedling growth. However, the inhibition of seedlings when exposed to As and 1.5 mg/L KT may be related to the accelerative accumulation of As in the tested plant.

4.2. Effect of KT on Plant As Uptake. Under our experimental conditions, the contents of As in maize increased with increasing concentrations of KT. It may be attributed to the enhanced root growth and root number, which in turn led to an increasing uptake of As from nutrient media. However, there was no significant difference in plant As uptake between 0.1 mg/L or 0.5 mg/L KT treatment and the control (0 mg/L KT) under As stress (Figure 2), suggesting that a suitable concentration of KT is required to increase plant As uptake.

4.3. Effect of KT on Activities of Antioxidant Enzymes. To cope with the damage caused by oxidative stress, a defensive system in plant is established to decrease the reactive oxygen species, such as the increasing activities of antioxidative enzymes.

SOD is responsible for converting O_2^- into H_2O_2 and O_2 [11]. In the present study, the supplement of 0.1 mg/L KT increased SOD enzyme activity significantly (Figure 3(a)). This may be related to an increasing level of superoxide radicals (O_2^-) induced by As stress, which is consistent with the previous reports [29–31]. However, no significant variation of SOD activity was observed at 0.5 mg/L or 1.5 mg/L KT treatment compared to the control, indicating KT application might have compensated for increased content of superoxide radicals (O_2^-). Prakash et al. [32] have found that KT acts as a direct radical scavenger and downregulates the lipoxygenase activity to prevent the formation of reactive oxygen species.

CAT is one of the H_2O_2 -scavenging enzymes in plants and helps in detoxifying harmful metabolic products [33]. An increasing activity of CAT in maize seedlings suggested a possible method in scavenging H_2O_2 , which in turn decreased the oxidative damage on maize seedling growth (Figure 3(b)).

Excessive H_2O_2 may be further detoxified by POD, which is a common response to oxidative stress [12], and an increase of POD activity has been shown in bean plants under As stress [3]. In the present study, 1.5 mg/L KT application increased the activity of POD significantly in maize seedlings (Figure 3(c)). It is well documented that POD activity increases in radish after supplying of brassinosteroids under cadmium stress [34]. An enhanced activity of CAT (Figure 3(b)) was concomitant with the increasing POD activity (Figure 3(c)), which might be due to the similar protective mechanism such as decomposing H_2O_2 into H_2O and O_2 in maize seedlings under As stress. Moreover, we noticed that an increase of CAT and POD activity and a decrease of SOD activity when exposed to As and 1.5 mg/L KT, which may result from the accelerative accumulation of As in the tested plant, and the adverse effects of oxidative damage might mainly be induced by excess of H_2O_2 .

4.4. Effect of KT on MDA. Malondialdehyde (MDA) is a product of peroxidation of unsaturated fatty acids in phospholipids, which may be ascribed to the level of lipid peroxidation [35], and an increase of MDA accumulation as a result of As stress was observed [3]. In the present study, we found that KT application significantly decreased the contents of MDA under As stress (Figure 3(d)), which might be related to a significant increase of SOD and POD activities, and decreased the lipid peroxidation [36]. According to our results, a decrease of MDA in maize seedlings suggested that KT reduced the As toxicity.

4.5. Effect of KT on Content of Chlorophyll. A high lipid peroxidation coupled with high hydrogen peroxide might have damaged chloroplast and inhibited chlorophyll concentration [14]. Similarly, the photosynthetic pigments are some of the most important internal factors, which are targets of As [7].

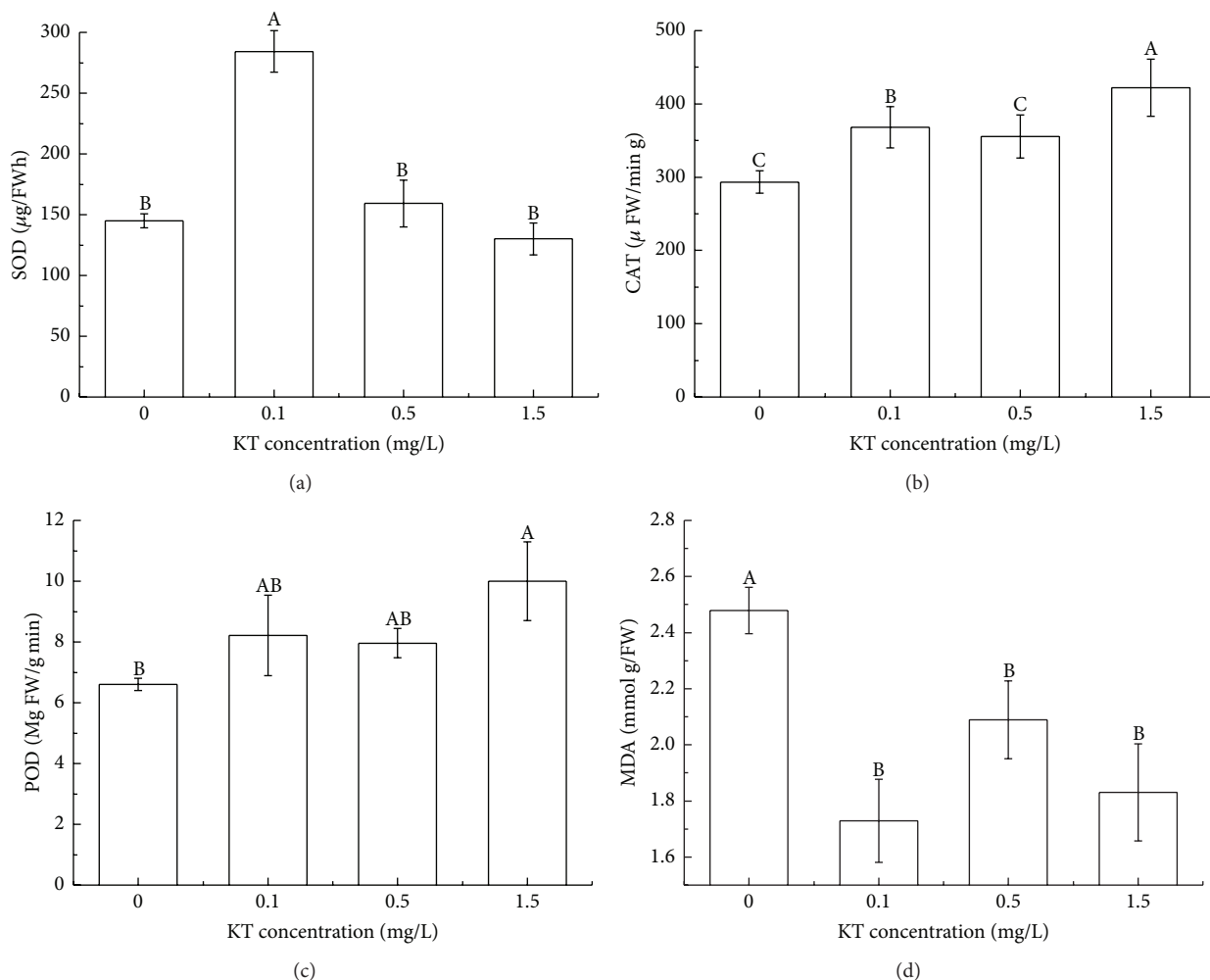


FIGURE 3: Effects of different concentrations of KT on the activity of antioxidative enzymes and MDA contents in maize seedlings under 0.5 mg/L arsenic stress. Values with different letters indicate a significant difference ($P < 0.05$).

It has been shown that As damages the chloroplast membrane and disorganizes the membrane structure [3]. The content of Chl a did not significantly change at 0.1 mg/L KT treatment, but 0.5 mg/L KT obviously increased the content of Chl a (Figure 4(b)). However, 1.5 mg/L KT reversed the increasing trend compared to the control. Therefore, a suitable KT concentration might be responsible for reducing the As-induced toxicity in maize seedlings. In other words, excess of KT concentration may cause damage to chloroplast and the biosynthesis of photosynthetic pigments.

Ebbs and Uchil [37] reported that the Chl b content drops much more drastically than the Chl a content as chlorosis progress, which is induced by Zn and/or Cd. Unlike Chl a, the content of Chl b showed a decline trend with increasing levels of KT under As stress (Figure 4(a)) compared to the control in the present study. A decrease of Chl b content indicated that the toxic effects of As on Chl b are greater than those on Chl a.

The contents of carotenoid (Car) showed no significant change with the application of different levels of KT under As stress (Figure 4(c)), indicating Car was less affected compared

to chlorophyll. A previous reference shows that carotenoid protects chlorophyll from photooxidative destruction [38].

It is apparent that Chl a : b will increase if Chl a content increases and/or Chl b content decreases. As shown in our results, an increase of Chl a : b indicated that the reduction of Chl b was higher than that of Chl a compared to the control (Figure 4(d)). Increasing Chl a : b is usually associated with the improvement of plant photosynthetic capacity [39].

5. Conclusion

KT could mitigate the negative effects of As by enhancing the growth parameters in terms of root length, root number, and fresh weight, improving the activities of antioxidant enzymes (SOD, CAT, and POD), increasing the contents of Chl a and the ratio of Chl a : b, and decreasing the content of MDA.

Conflict of Interests

The authors declare that there is no conflict of interests regarding the publication of this paper.

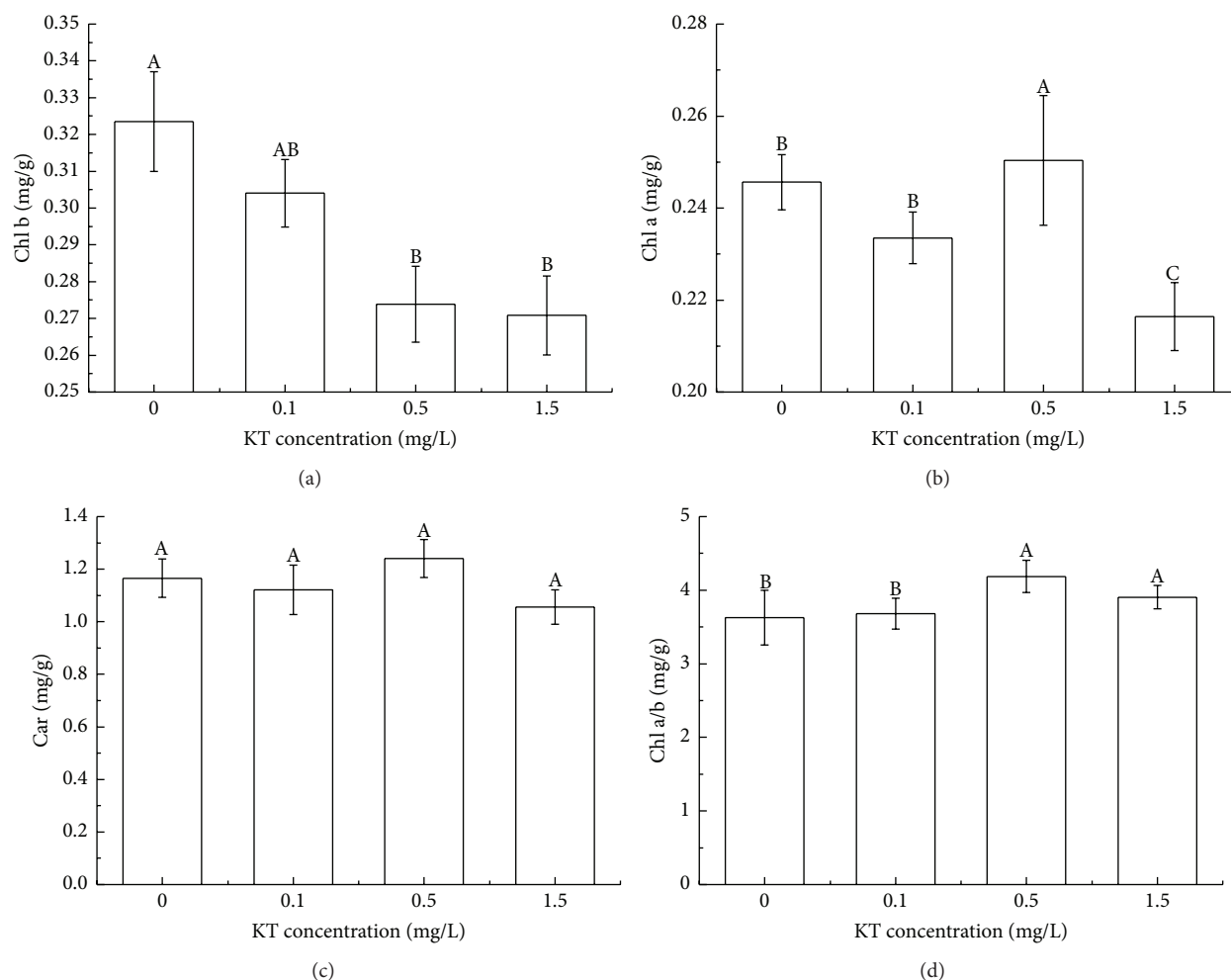


FIGURE 4: Effects of different concentrations of KT on the contents of photosynthetic pigments in maize seedlings under 0.5 mg/L arsenic stress. Values with different letters indicate a significant difference ($P < 0.05$).

Acknowledgments

This work was financially supported by National Natural Science Foundation (no. 31360132), the Department of Environmental Protection in 2010, Heavy Metal Pollution Prevention Projects "Ecological Restoration Technology Demonstration Project of Polluted Farmland in Polymetallic Mining Area, Gejiu, Yunnan," International Cooperation in Science and Technology Project (no. 2014DFA91000), and the Talent Training Fund of Kunming University of Science and Technology (no. KKZ3201222024).

References

- [1] R. D. Tripathi, S. Srivastava, S. Mishra et al., "Arsenic hazards: strategies for tolerance and remediation by plants," *Trends in Biotechnology*, vol. 25, no. 4, pp. 158–165, 2007.
- [2] F. F. Roberto, J. M. Barnes, and D. F. Bruhn, "Evaluation of a GFP reporter gene construct for environmental arsenic detection," *Talanta*, vol. 58, no. 1, pp. 181–188, 2002.
- [3] N. Stoeva, M. Berova, and Z. Zlatev, "Effect of arsenic on some physiological parameters in bean plants," *Biologia Plantarum*, vol. 49, no. 2, pp. 293–296, 2005.
- [4] N. Stoeva and T. Bineva, "Oxidative changes and photosynthesis in oat plants grown in As-contaminated soil," *Bulgarian Journal of Plant Physiology*, vol. 29, pp. 87–95, 2003.
- [5] Y. Li, O. P. Dhankher, L. Carreira et al., "Overexpression of phytochelatin synthase in *Arabidopsis* leads to enhanced arsenic tolerance and cadmium hypersensitivity," *Plant and Cell Physiology*, vol. 45, no. 12, pp. 1787–1797, 2004.
- [6] V. V. Stepanok, "The effect of arsenic on the yield and elemental composition of agricultural crops," *Agrokimiya*, vol. 12, pp. 57–63, 1998.
- [7] E. Miteva and M. Merakchiyska, "Response of chloroplasts and photosynthetic mechanism of bean plants to excess arsenic in soil," *Bulgarian Journal of Agricultural Science*, vol. 8, pp. 151–156, 2002.
- [8] Q. Shi and Z. Zhu, "Effects of exogenous salicylic acid on manganese toxicity, element contents and antioxidative system in cucumber," *Environmental and Experimental Botany*, vol. 63, no. 1–3, pp. 317–326, 2008.

- [9] A. Molassiotis, T. Sotiropoulos, G. Tanou, G. Diamantidis, and I. Therios, "Boron-induced oxidative damage and antioxidant and nucleolytic responses in shoot tips culture of the apple rootstock EM 9 (*Malus domestica* Borkh)," *Environmental and Experimental Botany*, vol. 56, no. 1, pp. 54–62, 2006.
- [10] A. Gunes, D. J. Pilbeam, and A. Inal, "Effect of arsenic-phosphorus interaction on arsenic-induced oxidative stress in chickpea plants," *Plant and Soil*, vol. 314, no. 1-2, pp. 211–220, 2009.
- [11] S. Gangwar, V. P. Singh, S. M. Prasad, and J. N. Maurya, "Modulation of manganese toxicity in *Pisum sativum* L. seedlings by kinetin," *Scientia Horticulturae*, vol. 126, no. 4, pp. 467–474, 2010.
- [12] E. Miteva and S. Peycheva, "Arsenic accumulation and effect on peroxidase activity in green bean and tomatoes," *Bulgarian Journal of Agricultural Science*, vol. 5, pp. 737–740, 1999.
- [13] N. Stoeva, M. Berova, and Z. Zlatev, "Physiological response of maize to arsenic contamination," *Biologia Plantarum*, vol. 47, no. 3, pp. 449–452, 2004.
- [14] C.-X. Li, S.-L. Feng, Y. Shao, L.-N. Jiang, X.-Y. Lu, and X.-L. Hou, "Effects of arsenic on seed germination and physiological activities of wheat seedlings," *Journal of Environmental Sciences*, vol. 19, no. 6, pp. 725–732, 2007.
- [15] D. S. Letham and L. M. S. Palni, "The biosynthesis and metabolism of cytokinins," *Annual Review of Plant Physiology*, vol. 34, no. 1, pp. 163–197, 1983.
- [16] R. Vankova, A. Gaudinova, and M. Kaminek, "The effect of interaction of synthetic cytokinin and auxin on production of natural cytokinins by immobilized tobacco cells," in *Proceedings of the Symposium on Physiology and Biochemistry of Cytokinins in Plants*, pp. 47–51, Federal European Society Plant Physiology, Physiology and Biochemistry of Cytokinins in Plants, 1992.
- [17] D. W. S. Mok and M. C. Mok, *Cytokinins-Chemistry, Activity and Function*, Chemical Rubber Company Press, Boca Raton, Fla, USA, 1994.
- [18] Q. X. Wang, F. Zhang, and D. L. Smith, "Application of Ga³ and kinetin to improve corn and soybean seedling emergence at low temperature," *Environmental and Experimental Botany*, vol. 36, no. 4, pp. 377–383, 1996.
- [19] P. Krishna, "Brassinosteroid-mediated stress responses," *Journal of Plant Growth Regulation*, vol. 22, no. 4, pp. 289–297, 2003.
- [20] M. A. A. Gadallah and A. E. El-Enany, "Role of kinetin in alleviation of copper and zinc toxicity in *Lupinus termis* plants," *Plant Growth Regulation*, vol. 29, no. 3, pp. 151–160, 1999.
- [21] M. M. N. Alla, M. E. Younis, O. A. El-Shihaby, and Z. M. El-Bastawisy, "Kinetin regulation of growth and secondary metabolism in waterlogging and salinity treated *Vigna sinensis* and *Zea mays*," *Acta Physiologiae Plantarum*, vol. 24, no. 1, pp. 19–27, 2002.
- [22] N. Chakrabarti and S. Mukherji, "Effect of phytohormone pretreatment on nitrogen metabolism in *Vigna radiata* under salt stress," *Biologia Plantarum*, vol. 46, no. 1, pp. 63–66, 2003.
- [23] A. M. A. Al-Hakimi, "Modification of cadmium toxicity in pea seedlings by kinetin," *Plant, Soil and Environment*, vol. 53, no. 3, pp. 129–135, 2007.
- [24] L. Ma, H. J. Wang, X. Y. Yang, Y. J. Hu, and H. B. Wang, "The uptake of different arsenic forms in three aquatic plants as affected by Fe³⁺," *Journal of Agro-Environment Science*, vol. 32, no. 6, pp. 1111–1121, 2013 (Chinese).
- [25] J. F. Gao, *Plant Physiology Experimental Guidance*, Higher Education Press, Beijing, China, 2006 (Chinese).
- [26] Y.-J. An, "Soil ecotoxicity assessment using cadmium sensitive plants," *Environmental Pollution*, vol. 127, no. 1, pp. 21–26, 2004.
- [27] S. Verma and R. S. Dubey, "Lead toxicity induces lipid peroxidation and alters the activities of antioxidant enzymes in growing rice plants," *Plant Science*, vol. 164, no. 4, pp. 645–655, 2003.
- [28] J. Strubińska and A. Hanaka, "Adventitious root system reduces lead uptake and oxidative stress in sunflower seedlings," *Biologia Plantarum*, vol. 55, no. 4, pp. 771–774, 2011.
- [29] J. Hartley-Whitaker, G. Ainsworth, and A. A. Meharg, "Copper- and arsenate-induced oxidative stress in *Holcus lanatus* L. clones with differential sensitivity," *Plant, Cell and Environment*, vol. 24, no. 7, pp. 713–722, 2001.
- [30] P. V. Mylona, A. N. Polidoros, and J. G. Scandalios, "Modulation of antioxidant responses by arsenic in maize," *Free Radical Biology and Medicine*, vol. 25, no. 4-5, pp. 576–585, 1998.
- [31] S. Srivastava, S. Mishra, R. D. Tripathi, S. Dwivedi, P. K. Trivedi, and P. K. Tandon, "Phytochelatin and antioxidant systems respond differentially during arsenite and arsenate stress in *Hydrilla verticillata* (L.f.) Royle," *Environmental Science and Technology*, vol. 41, no. 8, pp. 2930–2936, 2007.
- [32] T. R. Prakash, P. M. Swamy, P. Suguna, and P. Reddanna, "Characterization and behaviour of 15-lipoxygenase during peanut cotyledonary senescence," *Biochemical and Biophysical Research Communications*, vol. 172, no. 2, pp. 462–470, 1990.
- [33] S. Gangwar, V. P. Singh, S. K. Garg, S. M. Prasad, and J. N. Maurya, "Kinetin supplementation modifies chromium (VI) induced alterations in growth and ammonium assimilation in pea seedlings," *Biological Trace Element Research*, vol. 144, no. 1–3, pp. 1327–1343, 2011.
- [34] A. Anuradha and S. S. R. Rao, "The effect of brassinosteroids on radish (*Raphanus sativus* L.) seedlings growing under cadmium stress," *Plant, Soil and Environment*, vol. 53, no. 11, pp. 465–472, 2007.
- [35] J. C. Wang, J. Chen, and K. W. Pan, "Effect of exogenous abscisic acid on the level of antioxidants in *Atractylodes macrocephala* Koidz under lead stress," *Environmental Science and Pollution Research*, vol. 20, no. 3, pp. 1441–1449, 2013.
- [36] M. Shri, S. Kumar, D. Chakrabarty et al., "Effect of arsenic on growth, oxidative stress, and antioxidant system in rice seedlings," *Ecotoxicology and Environmental Safety*, vol. 72, no. 4, pp. 1102–1110, 2009.
- [37] S. Ebbs and S. Uchil, "Cadmium and zinc induced chlorosis in Indian mustard [*Brassica juncea* (L.) Czern] involves preferential loss of chlorophyll b," *Photosynthetica*, vol. 46, no. 1, pp. 49–55, 2008.
- [38] E. M. Middleton and A. H. Teramura, "The role of flavonol glycosides and carotenoids in protecting soybean from ultraviolet-B damage," *Plant Physiology*, vol. 103, no. 3, pp. 741–752, 1993.
- [39] L. Feng, M.-J. Gao, R.-Y. Hou et al., "Determination of quality constituents in the young leaves of albino tea cultivars," *Food Chemistry*, vol. 155, pp. 98–104, 2014.